Aging Effects in 319-Type Alloys

by

Neivi Rocío Andrade González

Department of Mining, Metals and Materials Engineering

McGill University, Montreal

A thesis submitted to the Faculty of Graduate Studies and Research
in partial fulfillment of the requirements of the degree of
Doctor of Philosophy

June 2006

Library and
Archives Canada

Published Heritage
Branch

395 Wellington Street
Ottawa ON K1A 0N4
Canada

Bibliothèque et
Archives Canada

Direction du
Patrimoine de l'édition

395, rue Wellington
Ottawa ON K1A 0N4
Canada

Your file Votre référence
ISBN: 978-0-494-27753-9
Our file Notre référence
ISBN: 978-0-494-27753-9

NOTICE:
The author has granted a non-exclusive license allowing Library and Archives Canada to reproduce, publish, archive, preserve, conserve, communicate to the public by telecommunication or on the Internet, loan, distribute and sell theses worldwide, for commercial or non-commercial purposes, in microform, paper, electronic and/or any other formats.

The author retains copyright ownership and moral rights in this thesis. Neither the thesis nor substantial extracts from it may be printed or otherwise reproduced without the author's permission.

AVIS:
L'auteur a accordé une licence non exclusive permettant à la Bibliothèque et Archives Canada de reproduire, publier, archiver, sauvegarder, conserver, transmettre au public par télécommunication ou par l'Internet, prêter, distribuer et vendre des thèses partout dans le monde, à des fins commerciales ou autres, sur support microforme, papier, électronique et/ou autres formats.

L'auteur conserve la propriété du droit d'auteur et des droits moraux qui protège cette thèse. Ni la thèse ni des extraits substantiels de celle-ci ne doivent être imprimés ou autrement reproduits sans son autorisation.

In compliance with the Canadian Privacy Act some supporting forms may have been removed from this thesis.

While these forms may be included in the document page count, their removal does not represent any loss of content from the thesis.

Conformément à la loi canadienne sur la protection de la vie privée, quelques formulaires secondaires ont été enlevés de cette thèse.

Bien que ces formulaires aient inclus dans la pagination, il n'y aura aucun contenu manquant.

Canada

ABSTRACT

The present work was performed on primary A319.2 alloy to investigate the effect of magnesium and strontium additions on the heat treatment behaviour and mechanical properties of the alloy. Samples were cast in permanent mould, then cut in order to obtain coupons which were solution heat treated at 495 °C for 4 and 24 hours, followed by quenching in hot water. Two different artificial aging temperatures were applied at 180 °C and 220 °C for times from 0.5 h up to 24 hours. The investigation consisted of a systematic measurement of macrohardness and matrix microhardness of samples under different heat treatment conditions. Tensile properties were also measured and electron microscopy study of critical samples was done.

It is seen that the alloy does not exhibit the common peak-overaged aging conditions due to the presence of several coexisting phases. It was found that multiple aging peaks are present in the age-hardening curves of Al-Si-Cu-Mg alloys. From the scanning electron microscopy studies, it is seen that addition of magnesium (~0.40 wt %) leads to the precipitation of coarse $Al_5Mg_8Si_6Cu_2$ particles. Strontium modification of the high magnesium alloys leads to segregation of Cu-intermetallics in areas away from the growing Al-Si eutectic regions. It was found that strontium modification retards the precipitation of the silicon out of the matrix.

The effect of aging time and temperature on the structure of the age-hardening precipitates was studied with TEM. TEM observations reveal that the age-hardening behavior is related to the precipitation sequence of the alloy. For the Al-Si-Cu-Mg alloy, the first aging peak is the result from the high-density GP zones, while the subsequent are from metastable phases. The transition from GP zones to metastable phases may be the main reason for the formation of multiple aging peaks.

RÉSUMÉ

Le présent travail est effectué sur un alliage primaire A319.2 pour étudier l'effet des additions de magnésium et de strontium sur le traitement thermique et les propriétés mécaniques de cet alliage. Les échantillons sont coulé dans un moule permanente, d'ailleurs ils sont coupés à fin d'obtenir coupons, lesquels sont homogénéisé à 495 °C pendant 4 et 24 heures, en suivant d'un trempe en eau chaude. Deux températures différentes de vieillissement artificiel étaient essayé soit 180 °C et 220 °C pour temps variant entre 0.5 heures jusqu'à 24 heures. Les recherches ont consisté en la mesure systématique de la macrodureté et de la microdureté de la matrice, d'échantillons ayant subit un traitement thermique, sous différentes conditions. De plus, les propriétés de tension ont été mesurées et une étude des échantillons considérés comme critiques a été réalisée par microscopie électronique.

Il est observé que l'alliage ne montre pas le comportement habituel de maximum-au-dessus-de-vieillissement-limite, à cause de la présence de plusieurs phases coexistantes. Il est trouvé que plusieurs maximums de vieillissement existent dans les courbes d'endurcissement pour vieillissement de l'alliage Al-Si-Cu-Mg. Suite des études faites en microscopie électronique, il est observé que l'addition de magnésium (~0.40 wt %) conduit à la précipitation de grosses particules d'$Al_5Mg_8SiCu_2$. La modification par strontium en alliages avec un haut contenant de magnésium conduit à la ségrégation d'intermétalliques de Cu en zones dans le lointain des régions grandissantes d'eutectique Al-Si. Il est trouvé que la modification par strontium retard la précipitation de Si hors de la matrice d'aluminium.

L'effet du temps de vieillissement et de la température sur la structure du précipitâtes d'endurcissement pour vieillissement est étudié avec microscopie électronique de transmission (MET). Observations par MET ont laissé voir que le comportement d'endurcissement pour vieillissement est rattaché à la séquence de précipitation de l'alliage. Pour l'alliage Al-Si-Cu-Mg, le premier maximum de vieillissement est résultat de la grande densité des zones GP, tandis que les maximums ultérieurs sont résultats de phases métastables. La transition de zones GP à phases métastables peut être la raison principale pour la formation de multiples maximums de vieillissement.

ACKNOWLEDGEMENTS

I would like to express my sincere gratitude to my thesis supervisor Professor John E. Gruzleski and thesis co-supervisor Professor Fawzy H. Samuel for their guidance, support and encouragement throughout the whole course of my studies. Their knowledge in the field of physical metallurgy and material science was of great importance in this research work, their helpful suggestions, patience and personal attitude have been inspiring during my graduate studies.

The financial support of the National Council of Science and Technology of Mexico (CONACYT) in the form of a scholarship throughout my studies is gratefully acknowledged. I will always be indebted to my Mexico.

Thanks to the GM-NSERC-UQAC Industrial Research Chair (TAMLA) of the Université du Québec à Chicoutimi, the Centre Québécois de Recherche et de Développement de l'Aluminium (CQRDA), the Corporativo Nemak in Mexico, for their cooperation in the provision of material, technical assistance and support. Specially thanks to Dr. Salvador Valtierra, Dr. Herb Doty, Dr. Agnes-Marie Samuel and Dr. David Gloria for their helpful recommendations.

My sincere gratitude to Dr. Abdelbaset Elwazri and Dr. Rocco Varano. Thank you for your friendship, help, valuable suggestions, plenty of assistance and plentiful encouragement. You always cheered me up with your positive attitude; I am deeply indebted to you guys.

I would like to thank all the friends I have made during my time at McGill for making it such a pleasant, rich and enjoyable experience.

Special thanks to the Al group: Juan Hernandez, Chunhui Zhang, Kaled Elalem, Lihong Shang, Javier Tavitas, Hujun Zhao and Saed Musmar for their friendship and good times we enjoyed at McGill. Thank you for sharing a little bit of your life with me.

I am deeply grateful to the staff and all professors of the Metals and Materials Engineering Department of McGill University, particularly to Robert Paquette, Edwin Fernandez, Professor Steve Yue, Dr. Florence Paray and Helen Campbell for their aid, cooperation and assistance.

To all the professors, staff and students of McGill, thank you for your classes and your advice during my studies. It was such a real good time at McGill. Special thanks to Dr. Lang Shang and Dr. Kelly Sears for their technical support.

To the city of Montreal and their people, thank you for being such an enjoyable place for studying, growing and continuous learning.

I would like to acknowledge my colleagues at Arvida Research and Development Center of Alcan for their encouragement and understanding in the completion of this work. Thank you for believing in me and helping me shape my professional career.

I would like to thank the Life for the precious time given, where I had the chance to explore and try to understand about the wonders of it.

Later but most importantly, I wish to express my heartfelt deeply gratitude to my family: my dad Felipe, my mom Rosita and my sister Linda, for their guidance, moral support, encouragement, understanding and infinite love. I could never ever pay them back all their efforts and all they have done for me. Without their love none of this would have been possible.

To all of them, thank you, thank you so much….

Neivi Andrade

TABLE OF CONTENTS

CHAPTER 1

CHAPTER 2

CHAPTER 3

CHAPTER 4

CHAPTER 5

CHAPTER 6

CHAPTER 7

LIST OF FIGURES

CHAPTER 2
LITERATURE REVIEW

CHAPTER 3
EXPERIMENTAL TECHNIQUES

CHAPTER 4
METALLOGRAPHIC STUDY & MECHANICAL PROPERTIES RESULTS

CHAPTER 5
ELECTRON MICROSCOPY RESULTS

CHAPTER 6
DISCUSSION

LIST OF TABLES

CHAPTER 2
LITERATURE REVIEW

CHAPTER 3
EXPERIMENTAL TECHNIQUES

CHAPTER 4
METALLOGRAPHIC STUDY & MECHANICAL PROPERTIES RESULTS

CHAPTER 5
ELECTRON MICROSCOPY RESULTS

CHAPTER 6
DISCUSSION

CHAPTER 1

INTRODUCTION

Aluminum-silicon foundry alloys possess the essential characteristic of good castability, corrosion resistance, and machinability, which make them excellent candidates for automotive and aerospace applications. Cast 319 aluminum (7.2-7.7 wt % Si, 3.3-3.7 wt % Cu, 0.25-0.35 wt % Mg, 0.4 max. wt % Fe, 0.2-0.3 max. wt % Mn, 0.25 max. wt % Zn, 0.25 max. wt % Ti) is an important automotive alloy used for engine blocks and cylinder heads. The microstructure of the as-cast material consists of aluminum dendrites, a eutectic structure containing aluminum and silicon, a variety of well-known strengthening precipitates (such as $CuAl_2$, $MgCuAl_2$, Mg_2Si) and intermetallic phases (like α-$Al_{15}(Fe, Mn)_3Si_2$), β-Al_5FeSi and $Al_5Mg_8Cu_2Si_6$).

In order to enhance the alloy properties, modification of eutectic silicon is carried out usually by strontium addition, to convert the silicon morphology from coarse-flake like to fine-fibrous. Magnesium is often added to improve the strength via Mg_2Si precipitation following heat treatment to refine the silicon eutectic.

Important parameters which affect the mechanical properties of this alloy are the solidification rate and subsequent heat treatment. The solidification rate determines the dendrite arm spacing and the size of the intermetallic phases, whereas heat treatment affects the density, size and distribution of age-hardening precipitates. The age-hardening mechanism responsible for strengthening is based on the formation of intermetallic compounds during decomposition of a metastable supersaturated solid solution obtained by solution treatment and quenching (precipitation hardening).

The heat treatment helps to obtain a desired combination of mechanical properties (strength and ductility). The T6 temper consists of a solution heat treatment, water quenching and artificial aging. The solution heat treatment is carried out at a temperature slightly under the eutectic temperature at about 495 °C for about 4 to 8 h. During solution treatment, hardening agents are dissolved in the matrix, the casting is homogenized and the eutectic silicon spheroidized.

Quenching creates a supersaturated solid solution at room temperature and avoids precipitation of dissolved elements. Natural aging takes place at room temperature between quenching and artificial aging. Although natural aging effects are not well understood, they seem to be detrimental to the Al-Si alloys [1]. During artificial aging, the hardening elements precipitate and improve the strength.

In recent years, the process of heat treatment for Al-Si base alloys containing Cu and/or Mg has been investigated in certain aspects, but the effects of Mg and its strengthening precipitates are not well documented. Despite the widespread and long term commercial application of this alloy, the information available on its strengthening is so meager, with respect to their formation, structure, morphology and stability of precipitates, that there is no guidance for a fundamental understanding of current processing practices and their impact on mechanical properties.

Other studies [2-6] have shown that the formation of precipitates plays a dominant role in determining the strength of many aluminum alloys; namely, their composition, structure, and crystallographic relationship to the host aluminum lattice, such as the parameters controlling their effectiveness in impeding dislocation motion.

A common approach to study fine precipitation in aluminum casting alloys is by transmission electron microscopy. However, this technique is time consuming and sample preparation is more involved than that for electron probe microanalyzer (EPMA) or scanning electron microscopy samples.

This work is part of an ongoing program covering the development and properties of 319 type alloys in relation to automotive applications, where the effects of Mg and Sr have been studied in different contexts. The present study was undertaken to investigate the individual and combined roles of Mg and Sr on the hardness and tensile properties of the 319-type alloy at normal cooling rates. Hardness and tensile results are reported as well as their relation with the different T4 and T6 tempers, in order to identify the many types of precipitates that are present in this complex alloy in sufficient concentrations to control the strength of the alloy.

The present work reports that double aging peaks are strongly present in the age-hardening curves of the Al-Si-Cu-Mg alloy, but not in Al-Si-Cu alloys. However, there are little published data describing these double aging peaks phenomena [2, 7, 8]. Therefore, the age-hardening behavior of Al-Si-Cu alloys has been investigated by means of hardness, tensile, optical and electron microscopy observation.

The particular objectives of this work are summarized as:

- To study the effect of Mg content (0.02 wt % and 0.40 wt %), Sr content (0 and 165 ppm), solution heat treatment time (4 h and 24 h at 495 °C) and aging treatment on the hardness and tensile properties of 319 alloys
- To understand the heat treatment process in terms of the phases formed in these alloys
- To present a better understanding of the precipitation as a function of chemical composition of A319.2 alloys

CHAPTER 2

LITERATURE REVIEW

In this chapter, the metallurgical concepts relevant to heat treatment are reviewed. The mechanisms during melt treatment are first considered and the precipitation hardening mechanisms are described. The correlation between microstructure and mechanical properties is then reviewed.

2.1. Aluminum Alloys

The properties of aluminum alloys depend on several factors, particularly other elements, which are always present, either as alloying additions or residual elements. Aluminum alloys usually contain several alloying elements besides the base metal aluminum [9]:

- The main alloying elements are copper (Cu), silicon (Si), magnesium (Mg), zinc (Zn) and manganese (Mn).
- Some elements are frequently present in small quantities, either as impurities or additions, including iron (Fe), chromium (Cr), titanium (Ti), nickel (Ni), cobalt (Co), silver (Ag), lithium (Li), vanadium (V), zirconium (Zr), tin (Sn), lead (Pb), and bismuth (Bi) which are added in special alloys.
- Elements such as beryllium (Be), boron (B), sodium (Na), strontium (Sr) and antimony (Sb) can be added as trace elements.

2.2. Classification of Aluminum Alloys

Casting alloys should be pourable and have good mold-filling characteristics, whereas workability is of primary importance with wrought alloys. Hence, significant differences in alloy content between wrought and cast alloys takes place. Typically, the alloying content of casting alloys is 10-12 %; whereas for wrought alloys it is 1-2 % (although in some particular cases can be up to 6 or 8 %) [10]. Figure 2.1 summarizes the wide range of alloys that are available for use.

A subdivision of aluminum alloys takes place depending on whether or not an alloy can be hardened by the addition of alloying elements, as is the case with precipitation-hardenable alloys that can be strengthened by ageing. Non-precipitation-hardenable alloys are only work-hardenable and cannot be hardened by aging [9].

2.2.1. Aluminum-Silicon Casting Alloys

Aluminum-silicon alloys constitute 90 % of the total casting alloys. This is due to their excellent casting properties, corrosion resistance, machinability and weldability when combined with the Al-Si eutectic and the alloying elements (such as Cu, Mg, Zn, and Mn among others). Mechanical properties of these alloys are enhanced by various mechanisms in the production process, including:

- The treatment of the liquid metal by reducing the hydrogen content and the removal of inclusions,
- The addition of alloying elements,
- Grain refinement by adding Ti and/or B,
- Modification of the Al-Si eutectic (by addition of Sr, Na, or Sb),
- Reduction of the secondary dendrite arm spacing by increasing the solidification rate and the formation of intermetallic compounds that precipitate during the heat treatment.

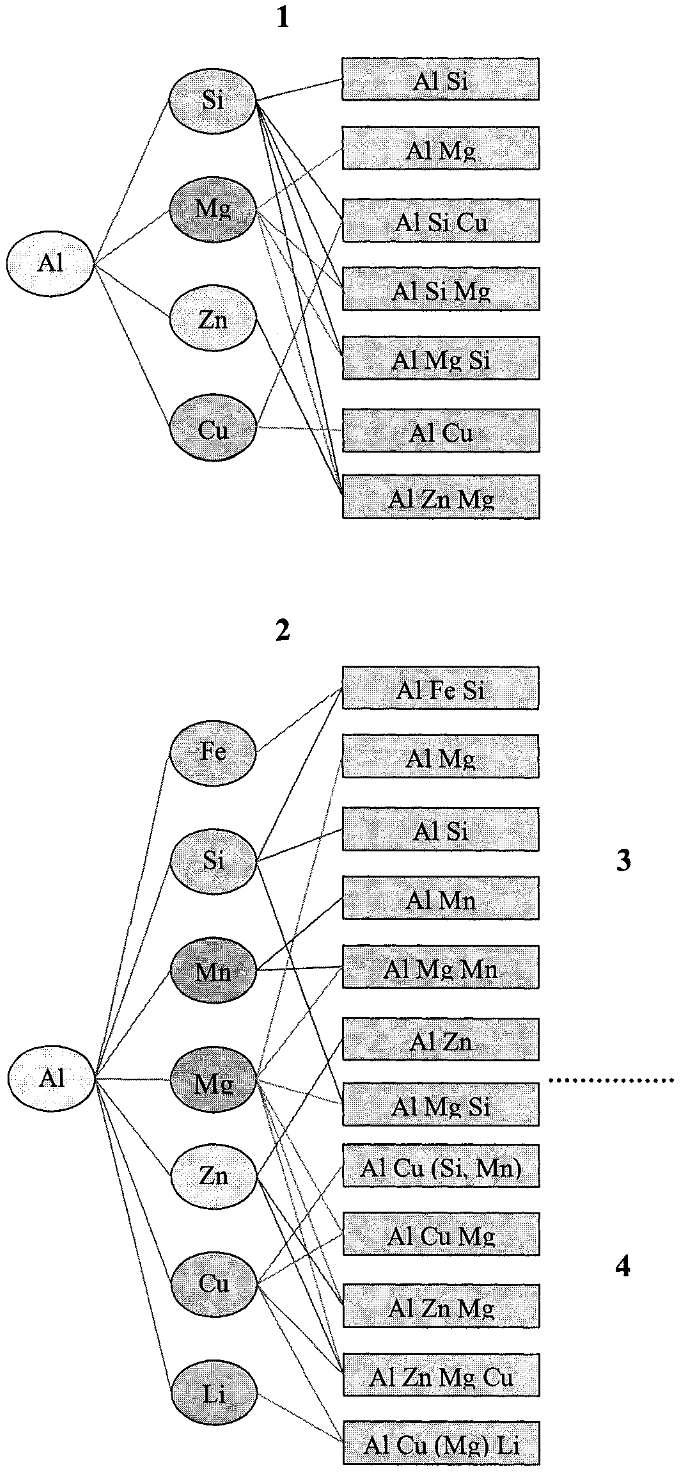

Figure 2.1 – Schematic Arrangement of Cast and Wrought Aluminum Alloys: (1) Casting Alloys, (2) Wrought Alloys, (3) Work-Hardenable Alloys and (4) Age-Hardenable Alloys [9]

Depending on the silicon content Al-Si casting alloys are classified into three groups [11]:

- Hypoeutectic alloys (5-11 % Si), in which the aluminum solidifies forming a dendritic net and the eutectic Al-Si precipitates interdendritically.
- Eutectic alloys (11-13 % Si), in which the final structure is completely eutectic.
- Hypereutectic alloys (13-20 % Si), in which the primary solidification reaction involves the precipitation of primary Si particles until the eutectic temperature is reached, and the remaining solidifies as a eutectic.

Hypoeutectic and near-eutectic Al-Si alloys are used when good castability and corrosion resistance are required. The alloy composition includes major and minor alloying elements, such as Si, Cu, Mn, Mg, Cr, Ni, Zn, Pb and Sn. These elements originate from the processes for producing primary and secondary metal, supplemented by master alloys added in the production of foundry ingots. The microstructure and properties are determined largely by the alloy composition.

In this family of alloys of hypoeutectic composition, silicon provides good casting properties. However, the presence of large, brittle, acicular flakes and plates of eutectic silicon leads to a substantial decrease of the strength and elongation of the castings. To overcome this effect in sand or permanent mold castings, it is necessary to modify the eutectic to improve strength, ductility, pressure tightness, and machinability. Modification is accomplished by adding a small amount of Na or Sr (0.001 to 0.030 %) to the melt [12-14].

Small additions of Mg and Cu enhance the response to heat treatment. However, the higher strength achieved is accomplished with some sacrifice in ductility and corrosion resistance [10]. Minor alloying elements such as Fe, Zn, Ni, and Ti are important because of their specific effects as described below.

Higher iron levels in Al-Si alloys lead to the formation of Al-Fe and Al-Fe-Si phases. The intermetallic compound takes the form of platelets and needles, reducing the strength and ductility. As a result, the iron content is limited to 1 %, and when higher strength is required to a maximum of 0.2 % [15, 16].

Zinc is present in solid solution. Additions of Mg reduce the solubility of Zn, forming $MgZn_2$ and Al_2Zn_3Mg phases. Such phases make the alloy heat-treatable and in conjunction with solid solution hardening they form the basis for increased strength in these alloys. Nickel has low solubility in the solid solution and leads to phases such as Al_3Ni, AlFeNi and Al_3CuNi. At high temperature, the strength of the material improves due to the formation of Al_3Ni, which promotes precipitation hardening. It has been reported that Ni additions have negative effects on corrosion resistance [17].

Titanium refines the grain of the aluminum solid solution. It is added either by means of one of the grain refiner compounds, Al_3Ti, TiB_2 or TiC, or by dissolving Ti at concentrations of 0.1 to 0.2 % [18].

2.2.1.1. Alloy A319.2

The 319 alloy belongs to the series 3xx.x, and is a heat-treatable alloy. It has Si and Cu as the major alloying elements, and other elements to a lesser extent. The digit following a decimal indicates the form of the product [19]:

- A “0” following the decimal indicates the chemistry limits applied to an alloy casting,
- A “1” following the decimal indicates the chemistry limits for ingot used to make the alloy casting.
- A “2” following the decimal also indicates ingot but with different chemical limits, typically tighter but still within the limits of the ingot.

Some alloy names include a letter that precedes an alloy number. These letters distinguish alloys that differ slightly in percentage of impurities or minor alloying elements, for example, 319.0, 319.1, A319.0, A319.2, B319.0 and B319.1.

Alloy A319.2 exhibits very good castability, weldability, and pressure tightness and moderate strength. Typical applications for sand castings of these alloys are internal combustion and diesel engine crankcases, gasoline and oil tanks, and oil pans. Permanent mold cast parts include water-cooled cylinder heads, and engine parts. Tables 2.1 and 2.2 show the typical composition and mechanical properties, respectively, of these alloys [19, 20].

Table 2.1 - Chemical Composition of 319 Alloys [19, 20]

	Elements (wt %)								
Alloy	Si	Fe	Cu	Mn	Mg	Ni	Zn	Ti	Others
319.0	5.5-6.5	1.0	3.0-4.0	0.50	0.10	0.35	1.0	0.25	0.50
A319.0	5.5-6.5	1.0	3.0-4.0	0.50	0.10	0.35	3.0	0.25	0.50
B319.0	5.5-6.5	1.2	3.0-4.0	0.80	0.1-0.5	0.50	1.0	0.25	0.50

Table 2.2 – Mechanical Properties of 319 Alloys [19, 20]

	Tensile Properties			Brinell
Casting Process & Temper	Ultimate Strength (MPa)	Yield Strength (MPa)	Elongation (% in 50.8 mm or 2 in.)	Hardness (500 kg load on 10 mm ball)
Sand Mold				
As-Cast	185	150	2.0	70
T6	250	200	2.0	80
Permanent Mold				
As-Cast	235	165	2.5	85
T6	280	185	3.0	95

2.3. Melt Treatment

In order to assure high quality castings, it is important to create a defined microstructure. The materials making up the charge, the melting practices, the cleaning and degassing methods used, all affect nucleation and crystal growth; thereby crystallization behavior and its effects on solidification behavior, shrinkage, and feeding. Consequently, it is necessary to have good melt treatment to ensure good melt quality. Among the objectives of the melt treatment are a suitable microstructure, including fine grain size and modification.

2.3.1. Eutectic Modification in Al-Si Alloys

Al-Si alloys are characterized by the presence of Al-Si eutectic. The microstructure of this eutectic consists of coarse silicon needles embedded in a matrix of aluminum solid solution (Figure 2.2). These needles are in reality plates, which act as internal stress raisers, making the alloy brittle. In order to overcome this, a morphological change of the eutectic Si is possible [21].

Modification can be defined as the transformation from coarse platelets to fibrous, seaweed like form. Microstructurally a modified eutectic appears as rounded islands of Si surrounded by a sea of aluminum, whereas in three dimensions its morphology resembles that of coral (Figure 2.3 a and b).

Thermally, modification can be achieved by increasing the solidification rate or during heat treatment. Figure 2.4 shows the effect of heat treatment on unmodified samples at high solidification rates, whereas Figure 2.5 shows the same effect at lower solidification rates. The effect of heat treatment on modified samples is shown in Figure 2.6 at high solidification rates, whereas Figure 2.7 shows the same effect at lower solidification rates.

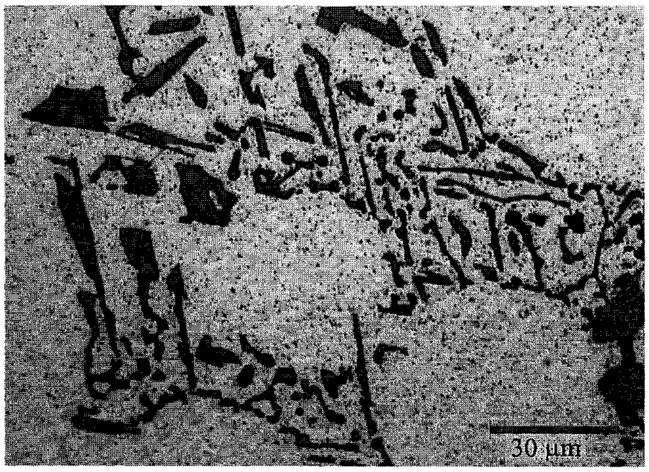

Figure 2.2 – Unmodified Microstructure of the Cast Al-Si Eutectic in a 319 Aluminum Alloy (0.0004 wt % Sr) [37]

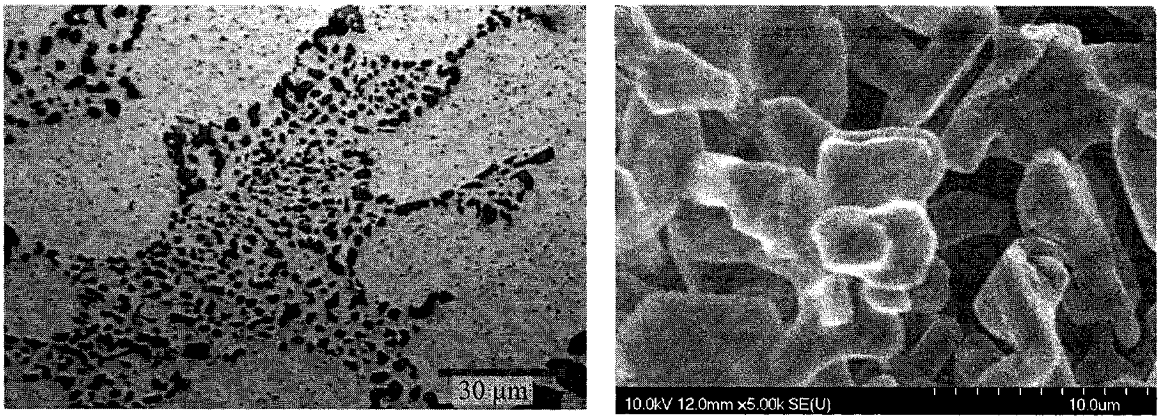

(a) Optical Structure

(b) FE-SEM Sample

Figure 2.3 – Modified Microstructure of the Cast Al-Si Eutectic in a 319 Aluminum Alloy (0.0125 wt % Sr) [37]

(a) As-Cast Sample (EDS 25μm)

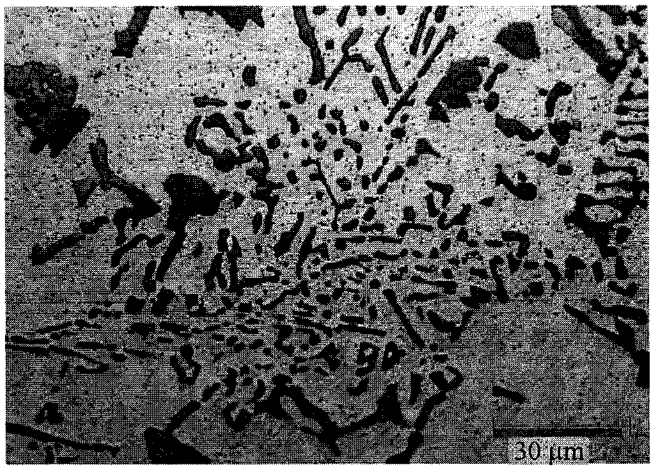

(b) Heat Treated Sample (EDS 25μm)

Figure 2.4 – Unmodified Structure of the Al-Si eutectic in a 319 Aluminum Alloy, Which Shows the Effect of Heat Treatment in the Modification of the Al-Si Eutectic at Higher Solidification Rates [37]

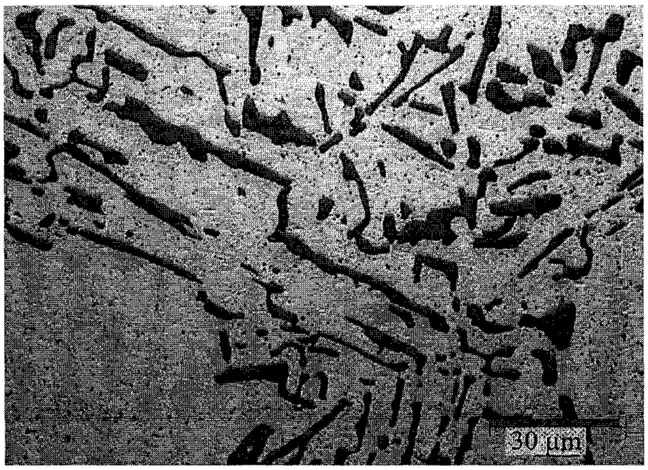

(a) As-Cast Sample (EDS 50µm)

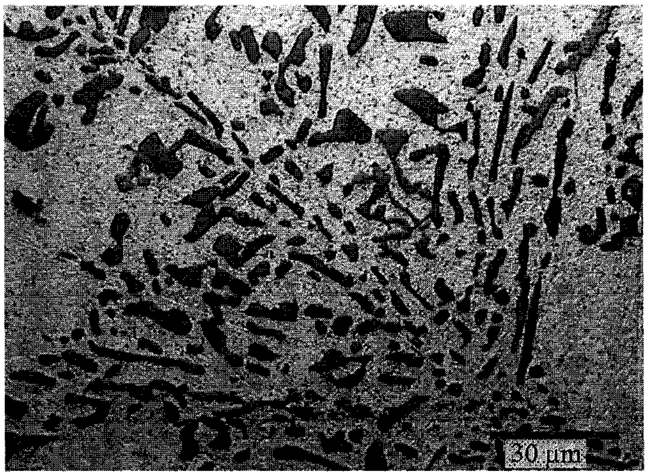

(b) Heat Treated Sample (EDS 50µm)

Figure 2.5 – Unmodified Structure of the Al-Si eutectic in a 319 Aluminum Alloy, Which Shows the Effect of Heat Treatment in the Modification of the Al-Si Eutectic at Lower Solidification Rates [37]

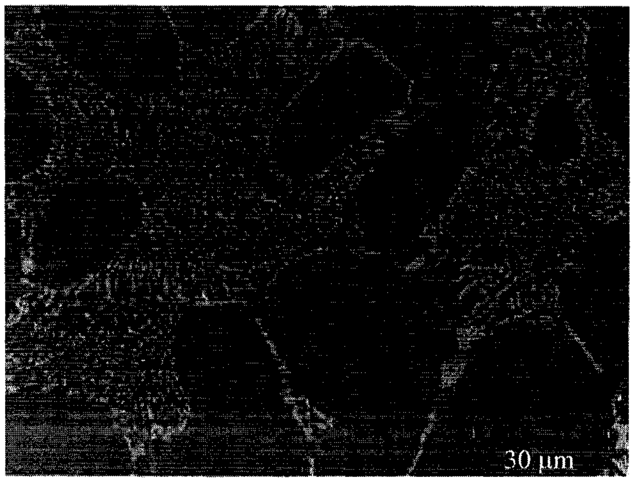

(a) As-Cast Sample (EDS 20μm)

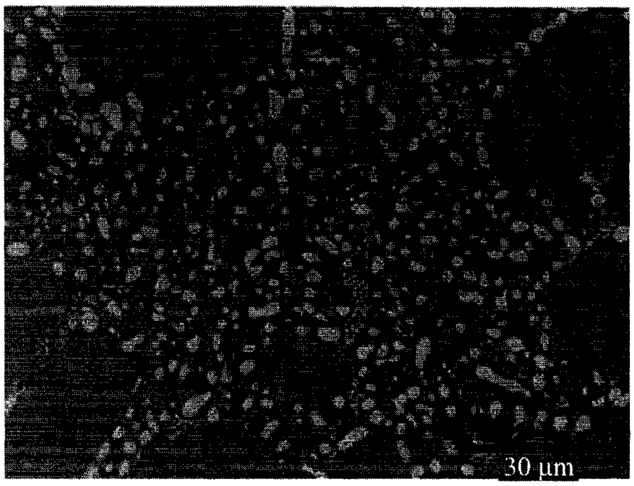

(b) Heat Treated Sample (EDS 20μm)

Figure 2.6 – Modified Structure of the Al-Si eutectic in a 319 Aluminum Alloy, Which Shows the Effect of Heat Treatment in the Modification of the Al-Si Eutectic at Higher Solidification Rates [37]

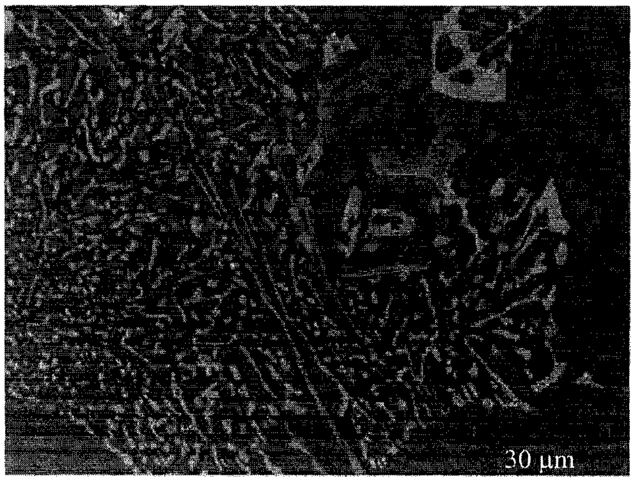

(a) As-Cast Sample (EDS 50µm)

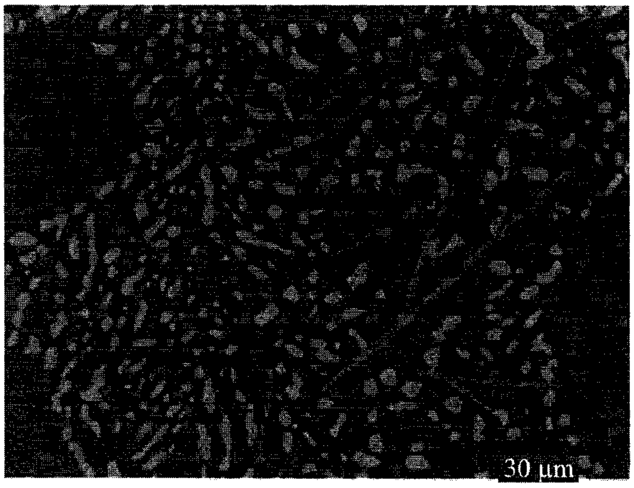

(b) Heat Treated Sample (EDS 50µm)

Figure 2.7 – Modified Structure of the Al-Si eutectic in a 319 Aluminum Alloy, Which Shows the Effect of Heat Treatment in the Modification of the Al-Si Eutectic at Lower Solidification Rates [37]

Chemically, modification can be achieved by additions of elements such as Na, Sr, Sb, Ca or lanthanides to the melt [22]. Among them Na and Sr are preferred due to their strong effect at low addition levels. The degree of modification depends on the amount of Sr added, as well as the time between the addition and casting. Modification improves ductility and toughness, but also increases tensile strength, while hardly affecting the yield strength; although hardness decreases somewhat (Table 2.3) [17]. The effect of modification on the tensile strength is reduced by heat treatment because of the more globular and coarser Si grains that are formed.

Table 2.3 – Mechanical Properties of AlSi7Mg (Chill Casting)
for Different Forms of the Al-Si Eutectic [17]

Type of Modification	Microstructure	Tensile Properties					
		As-Cast			Heat Treated *		
		Ultimate Strength (MPa)	Yield Strength (MPa)	Elongation (% in 2 in.)	Ultimate Strength (MPa)	Yield Strength (MPa)	Elongation (% in 2 in.)
None	Grainy	82	180	6.8	228	304	11.8
With Na	Modified	85	195	16.4	213	292	15.1
With Sr	Modified	87	196	15.9	226	301	14.4
With Sb	Fine lamellar	89	201	11.9	211	293	16.5

* Solution Heat Treated for 10 h at 540 °C, Quenched in Water and Artificially Aged for 6 h at 160 °C

To explain the modification mechanism, several theories have been developed, which can be classified in two main groups: theories based on nucleation mechanisms and theories based on growth mechanisms [23].

Crossley and Mondolfo [24] have proposed a theory based on nucleation mechanisms to explain modification. They assumed that Si grows at a faster rate than Al in unmodified alloys, leading to sharp acicular Si particles. Hence, when adding a modifier agent the growth of Si is hindered, and that of Al is promoted because its surface tension is reduced.

Another theory based on nucleation mechanisms is the one developed by Shamsuzzoha et al. [25]. They have stated that the growth of Si occurs in a ledge-wise manner; leading the {111} Si planes to encroach along the <112> directions. With slow solidification rates twinning is present, promoting a small angular distortion along the twinning planes, which is responsible for branching. When the solidification rates increase, Si atoms do not have time to accommodate in the ledges, promoting a twinning but at a higher rate, increasing distortion and branching.

Shu-Zu and Hellawell [26] developed a theory based on growth mechanisms. They proposed an enrichment of the modifying atoms at the Si-liquid interface. This absorption distorts the ledges, and promotes twinning and branching.

2.3.1.1. Strontium Modification

Strontium is usually introduced directly into the melt in the form of an Al-10 wt % Sr master alloy. Pure Sr is not used as a modifier because it forms an oxide layer that prevents dissolution [27, 28]. The amount of Sr necessary to achieve modification depends on the Si level, on the concentration of the minor alloying elements (which can act as inhibitors) and on the cooling rate. In contrast with Na, Sr modification depends more on the solidification rate [17]. For this reason, Sr is preferred in permanent mold castings, rather than sand mold castings.

Sr is preferred over Na as a longer-lasting modifier, because its loss is appreciably less after several hours of its addition into the liquid. It has been seen that as the Mg content increases, less Sr is needed to achieve modification. In order to check the degree of modification achieved, metallographic analyses are required. However, since Sr reduces the eutectic temperature, modification verification can be done by thermal analysis.

2.3.2. Grain Refining

Grain refining is one of the inoculations made late in the melting operation to alter the structure of the cast metal. It is done to produce a finer, equiaxed grain size structure that improves most mechanical properties and surface finish characteristics. With reduction in grain size, the resistance to hot tearing due to the decrease in the coherency temperature results in a low cracking tendency [29]. In 319 alloys, the combination of a large volume fraction of eutectic liquid and low coherency temperature results in a low cracking tendency [30].

Porosity due to hydrogen is reduced as the grain is refined [31] although in practice grain refinement is achieved by addition, before the casting operation, of chemical aggregates such as Ti and/or B. It can be done as well by increasing the cooling rate or by mechanical agitation of the melt during cooling to detach dendrite arms.

Ti and B are very efficient grain refiners. They provide a surface at or just above the liquidus temperature of the alloy, to form nuclei or seeds of Al_3Ti or $(Ti, Al)B_2$ throughout the mass of molten metal. These nucleate fine, equiaxed grains as the casting solidifies. Ti is soluble in liquid aluminum and it is required to have at least 0.15 % Ti in the alloy. With normal operating temperatures, the usual amounts of refiners added are 0.05-0.15 % Ti, 0.04 % B, or 0.01-0.08 % Ti + 0.003 % B. For high-Si aluminum alloys, such as piston alloys, an addition of 0.003-0.008 % B is preferred [17]. The use of master alloys containing Ti-3-10 % B and TiB ratio of 3:50 are commonly used. Larger additions of refiners result in gravity segregation of intermetallic complexes.

As long as the nuclei do not coalesce, the grain refining effect of Ti and B persists. When the level of Ti exceeds 0.25 %, coarse primary crystals of Al_3Ti are formed, reducing the mechanical properties. If the grain refined melts are held at high temperatures (above 750 °C), the effectiveness of the refinement is diminished.

Moreover, adding more grain refiner will not solve this situation, but it can be rectified by solidifying the metal and remelting. Because of the high cost of this operation, it is necessary to have a tight melt control.

2.3.3. Porosity

Porosity in aluminum castings is associated either with the presence of hydrogen (trapped while liquid and expelled as the metal solidifies, due to its drop in solubility Figure 2.8) or with the volumetric contraction occurring as the liquid metal freezes. When these two factors are combined, irregular porosity forms. Based on their distribution and morphological aspects, it is possible to determine the origin of certain pores [9].

Macroscopic shrinkage cavities are assumed to be due to contraction and are associated with faulty feeding designs, and the inability of liquid metal to flow into already solidified regions [23].

Three different contraction stages are exhibited in a molten alloy, Figure 2.9 [32]. The first one (liquid) does not have a dramatic effect in castings, and normally is seen as a reduction in height of the liquid held in the feeder. The second stage (contraction during solidification) is due to the change from a random open liquid structure into a more compact solid one. Most of the small gaseous pores in aluminum castings are thought to be caused by the decrease of solubility of hydrogen.

Several models [33-36] have been developed to explain the formation of these pores based on nucleation and growth mechanisms, models that require geometrical consideration and the knowledge to measure parameters like surface tension and supersaturation pressure.

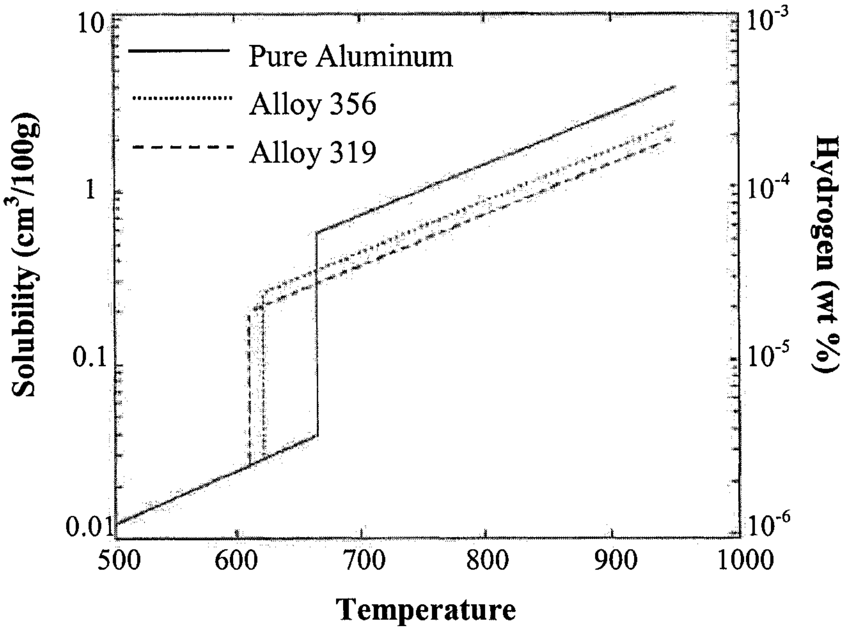

Figure 2.8 – Solubility of Hydrogen in Aluminum at One Atmosphere [14, 24]

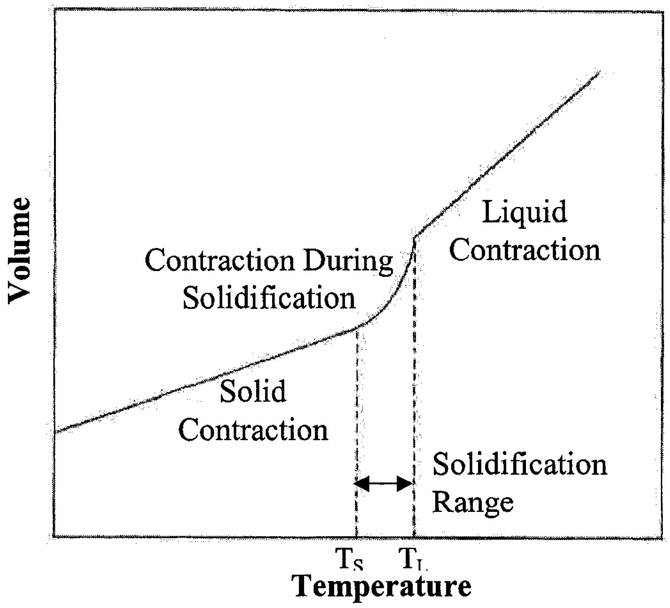

Figure 2.9 – Schematic Illustration of Three Shrinkage Regimes: In the Liquid, During Freezing and in the Solid [24]

2.3.4. Secondary Dendrite Arm Spacing

Solidification in hypoeutectic aluminum-silicon alloys proceeds by formation of dendrites of primary aluminum from the liquid. Figure 2.10 shows the various intermediate stages in dendrite development [21]. The distance between the different dendrite arms is measured on the secondary branches, rather than on the primary ones [21]. Figure 2.11 shows the difference in size obtained by cooling an A319 alloy at two different rates [37].

The larger the dendrite arm spacing, the coarser the microconstituents and the more pronounced their effects on properties. Mechanical [38-49] and physical properties [50, 51] of engineering castings are enhanced when dendritic arm spacing (DAS) diminishes. Figure 2.12 shows the effect of the DAS on mechanical properties of an A319 alloy, whereas Figure 2.13 represents the thermal conductivity as a function of DAS.

Cooling rates directly control dendrite arm spacing, which influences property development and substantially improves ductility. In order to obtain information related to the rate or time involved during solidification at different places within a complex casting, microstructural examination can be done by reference to data obtained in controlled unidirectional solidification trials [22].

2.4. Heat Treatment of Al-Si-Cu Alloys

Heat treatment reduces or eliminates the inhomogeneity originating during casting and solidification [17]. Castings are usually thermally processed under different heating and cooling cycles to improve their properties. For Al-7 % Si-0.3 % Cu alloy, one of the common heat treatment practices is the T6, which involves a sequence of solution heat treating, rapid cooling (quenching) in water and precipitation hardening (artificial aging).

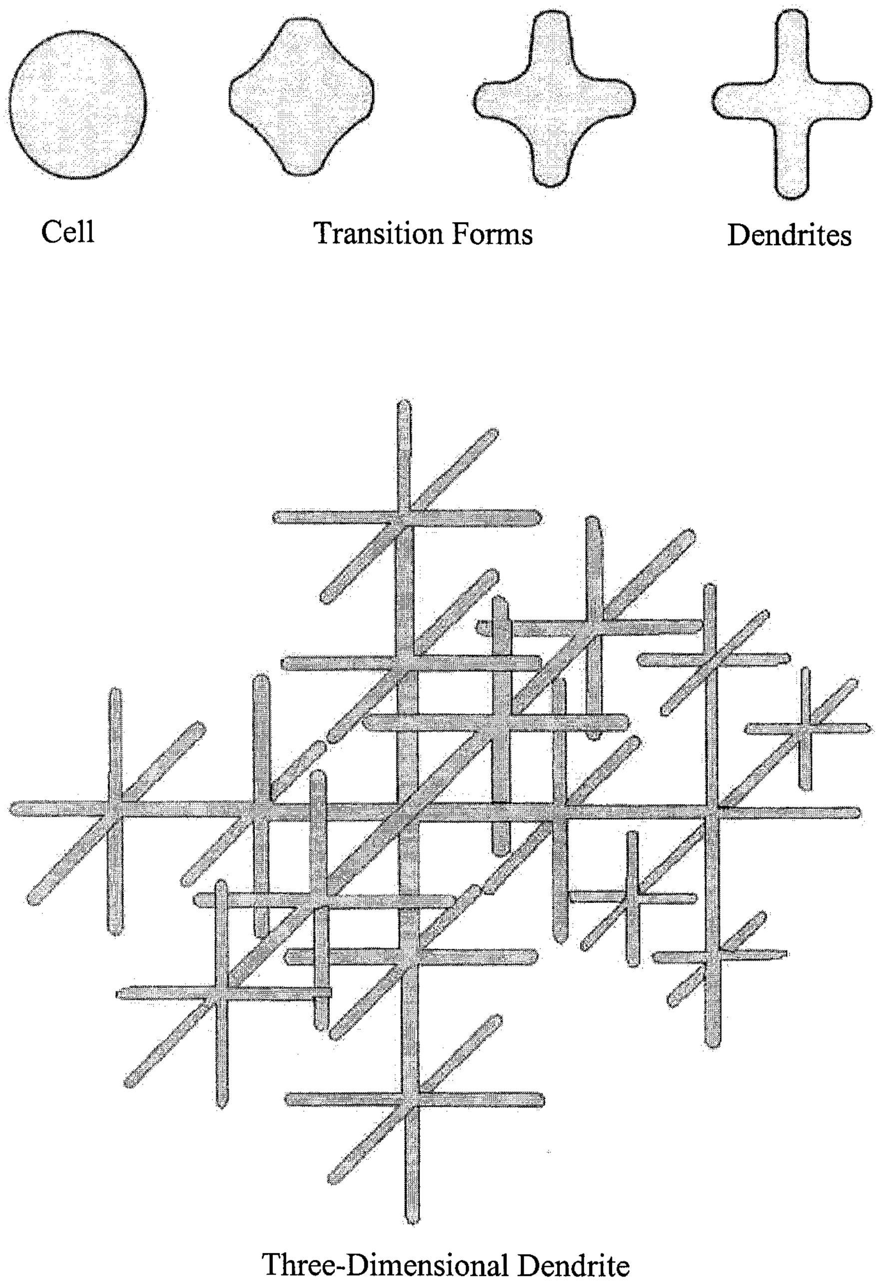

Figure 2.10 – A Schematic Interpretation of the Cell to Dendrite Transition is Presented

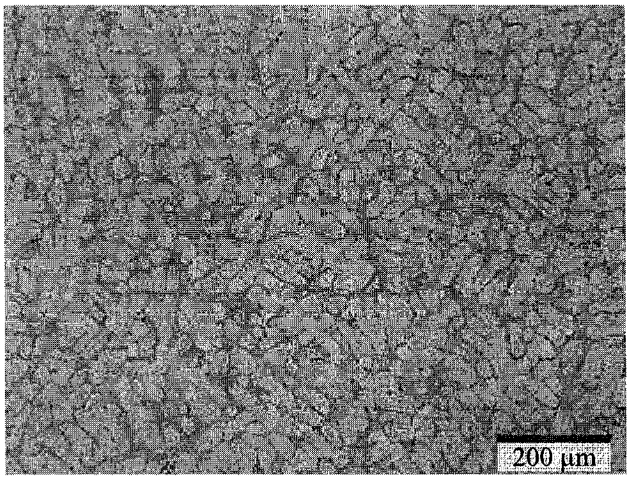

(a) As-Cast Sample EDS ~20 μm
Solidification Time 13 s and Solidification Rate 5.3 °C/s

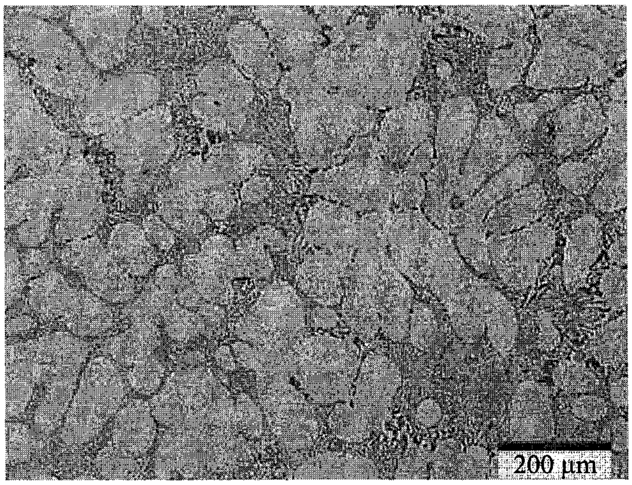

(b) As-Cast Sample EDS ~50 μm
Solidification Time 110 s and Solidification Rate 0.9 °C/s

Figure 2.11 – Micrographs of Dendrites Obtained from Samples Solidified at [37]: (a) High and (b) Low Rates

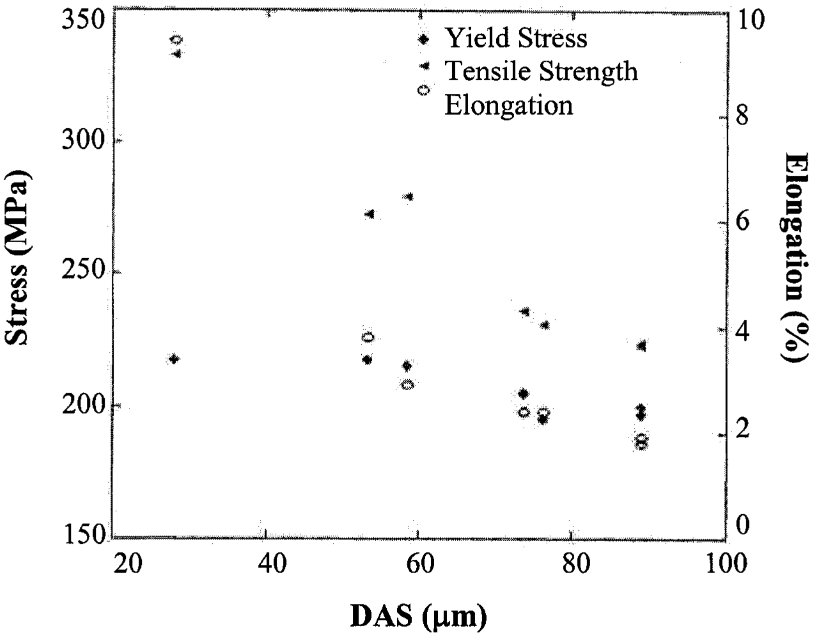

Figure 2.12 – Mechanical Properties of a C355-T6 Alloy as a Function of DAS [40]

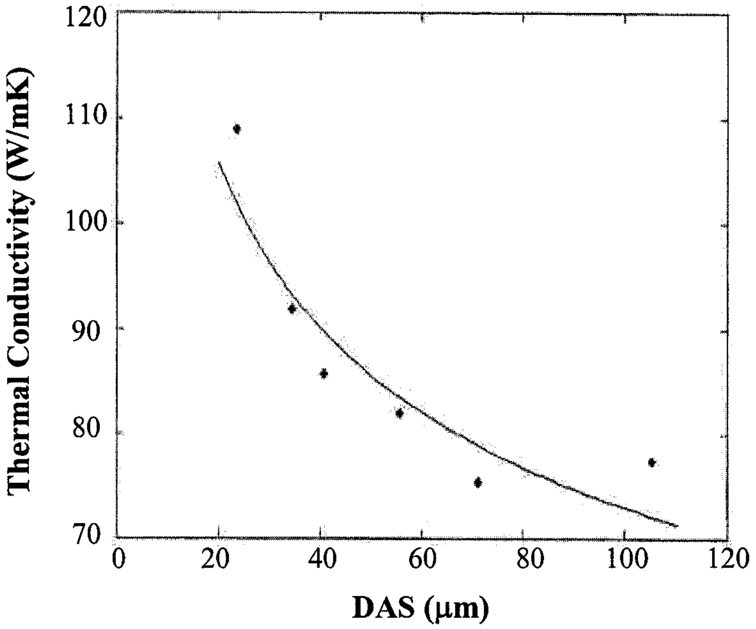

Figure 2.13 – Thermal Conductivity in an A319 Alloy as a Function of DAS [43]

Besides the phase and morphology changes associated with heat treatment, other (sometimes desirable) effects can occur. Microsegregation and residual stresses due to solidification or solutionizing are minimized, insoluble phases may be physically altered, and susceptibility to corrosion may be affected [52].

2.4.1. Solution Heat Treatment

The purpose of solution treatment is to produce a homogenous α-Al phase solid solution. The solid solution becomes enriched in alloying elements responsible for age hardening by diffusion processes. Solution treatment consists of soaking the alloy at a sufficiently high temperature to dissolve the hardening particles (Mg_2Si, $CuAl_2$) into the α-Al.

Thermal analysis obtained during solidification of a 319 alloy (Figure 2.14), shows the presence of a complex $Al_5Mg_8Cu_2Si_6$-$CuAl_2$ eutectic [22]. In order to dissolve the 3.6 wt % Cu of this alloy, the material should be heated above 490 °C, overstepping it will result in melting the complex eutectic. Unfortunately, when the solution temperature decreases, there is a detrimental effect on the mechanical properties (Figure 2.15).

The risk of incipient melting of the lowest melting point constituents, such as Fe- and Cu- containing particles, in Al casting alloys, can sometimes be reduced by pre-solutionizing at lower temperatures than the optimum, with subsequent treatment at a higher temperature. This process is known as “step solutionizing”.

The solution heat treatment time used represents a compromise between the mechanical properties achieved and the economic efficiency. Shorter solution times are required in permanent mold castings than in investment or sand mold casting. Nevertheless, thin-walled sand castings produced with extensive chills can display finer microstructures than parts produced with heavy-section permanent mold. These finer microstructures will exhibit in general greater mechanical properties.

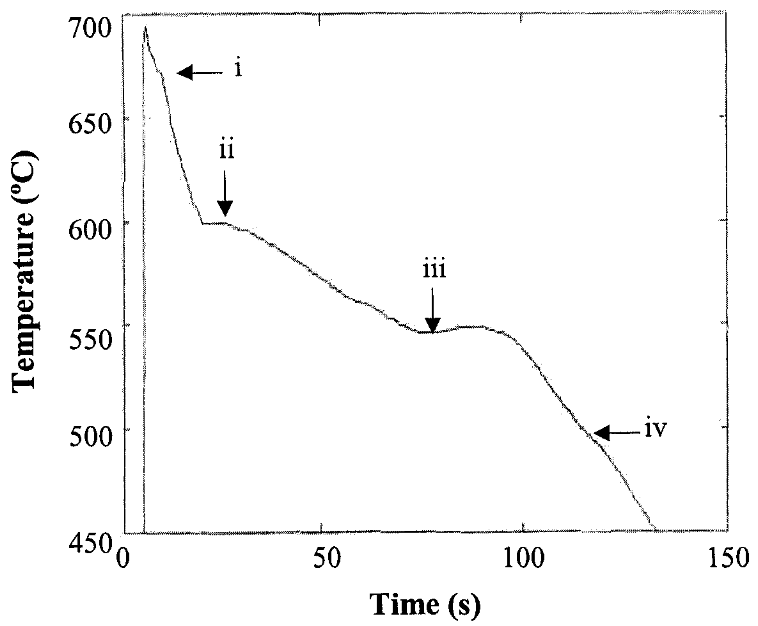

Figure 2.14 – Solidification Curve of a Modified and Refined Type 319 Alloy [22]:

(i) Peritectic Precipitation of Al_3Ti,
(ii) Formation of Primary Aluminum Dendrites,
(iii) Eutectic Al + Si Reaction, (iv) Solidification of
Complex Eutectic of the Type $Al_5Mg_8Cu_2Si_6 - CuAl_2$

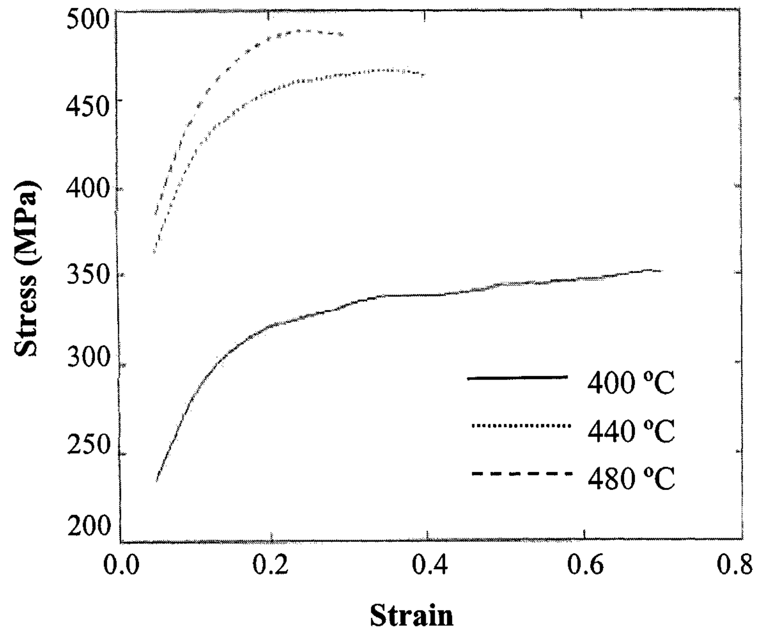

Figure 2.15 – Stress-Strain Curve Obtained in Compression of T4 Samples From a 319 Alloy Solubilized at Three Different Temperatures [22, 29]

During the solution treatment of the 319 alloys, three metallurgical events take place: the dissolution of hardening particles ($CuAl_2$, Mg_2Si) into α-Al, the homogenization of the casting, and the spheroidization of the undissolved constituents (eutectic Si).

2.4.1.1. Dissolution of the Cu, Mg and Si Into the Aluminum Matrix – Soluble phases and precipitates formed during solidification are dissolved into the matrix by diffusion-controlled processes. Typically, the standard practice [20, 53, 54] solution heat treatment temperatures for the 319 aluminum alloys are around 505 °C for times from 4 to 12 hours. At this temperature the solid solubility of silicon and Cu in the Al matrix are 1.38 wt % [55] and 3.8 wt % [56] respectively. Therefore, dissolution of these precipitates takes place.

2.4.1.2. Homogenization – In castings in the as-cast state, alloying and impurity elements tend to segregate into networks of eutectic constituents. Therefore, the microstructure is not homogeneous. By solution treatment, the elements in constituent phases are redistributed when they dissolve and segregation is minimized. Some constituent phases, particularly iron-rich intermetallics, contain insoluble elements and are changed little by solution treatment [17].

Parameters such as solution temperature and solidification cooling rate (i.e. finer or coarser microstructure) of the casting will play a very important role in the time required to achieve complete homogenization.

2.4.1.3. Morphological Change of the Eutectic Silicon – The morphology of the eutectic silicon plays a very important role when determining mechanical properties. Along with the particle size, the shape and the spacing are important factors that characterize the silicon morphology. Under normal cooling conditions, the Si particles are present in the form of coarse needles. These needles act as crack initiators and affect mechanical properties such as toughness and ductility.

The solution treatment tends to spheroidize constituents that are present in quantities that cannot be fully dissolved. In 319 alloys, excess silicon is always present. As a result, during solution heat treatment spheroidization and coarsening of the eutectic silicon takes place in an effort to reduce the surface energy [57].

At the beginning of the solution treatment, the acicular silicon platelets in the unmodified structure begin to break down into smaller fragments and gradually spheroidize. In modified structures, the spheroidization takes place at an early stage. Li et al. [58] reported that in modified alloys spheroidization was complete after 1 hour of solution treatment, while in unmodified alloys even after 12 hours some coarse needles of Si were visible. Figure 2.16 shows a schematic of the spheroidization and coarsening process [37, 59].

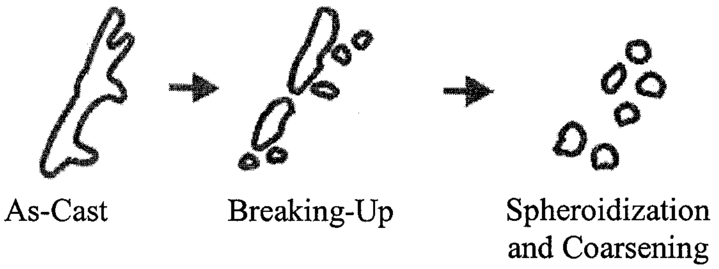

(a) Unmodified Silicon

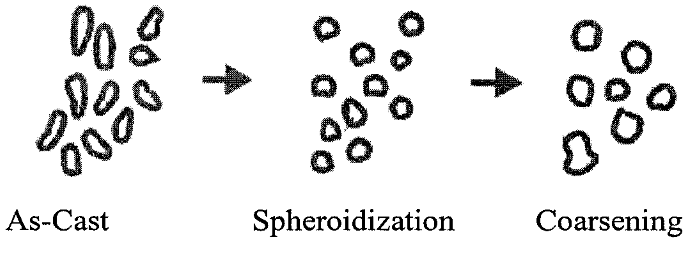

(b) Modified Silicon

Figure 2.16 – Schematic Characterization of the Three Stages of Spheroidization and Coarsening of the Eutectic Silicon Phase

The globularization and coarsening process of the silicon particles is known as Ostwald ripening, which is the process that involves the growth of larger particles at the expense of smaller ones. This explains why during the solution heat treatment, the number of silicon particles decreases as their average size increases. The coarsening involves mass transfer by the detachment of atoms from smaller particles, and their diffusion through the matrix to join onto larger particles. The driving force for this process is the concentration gradient which exists from larger to smaller particles. This difference in concentration will cause the preferential dissolution of smaller particles [60].

Although modification of the Al-Si eutectic will contribute to improved physical [22, 49, 61, 62] and mechanical [22, 25-27, 32, 63-65] properties, difficulties may arise during machining if the morphology of the silicon phase is fully rounded during heat treatment.

2.4.2. Quenching

The rapid cooling process following the solution heat treatment is called quenching. This ensures that age-hardening precipitation from the supersaturated solution will result in a suitable size range and uniform distribution of the precipitates.

Rapid quenching increases response to age hardening, but it also creates residual stresses and distortion. Slow quenching rates result in precipitation during quenching, localized overaging, loss of corrosion resistance in grain boundaries and lower response to age hardening [66, 67]. The ASTM standard B-917 [54], suggests that during quenching cooling proceeds rapidly through the 400 °C to 260 °C range in order to avoid premature precipitation that is detrimental to tensile properties and corrosion resistance. For castings alloys, the quench delay should not exceed 45 s. Most commercial quenching is accomplished in water near the boiling point.

Experimental trials should be conducted to find a critical cooling rate, above which no increase of hardness is found to occur. Figure 2.17 shows, for a 319 alloy, the maximum value of hardness in samples aged at 160 °C plotted as a function of the average cooling rates in the 400-480 °C range. From the figure, it can be seen that cooling rates of 10 °C/s or somewhat higher are optimum [22].

2.4.3. Precipitation Hardening

After solution-heat treatment and quenching, the solid solution will be supersaturated in vacancies and solute atoms. It will try to attain equilibrium conditions by precipitation of the supersaturated solute atoms. This involves diffusion of the solute atoms and the presence of an excess number of vacancies which promotes the movement of atoms through the crystal lattice [9]. Because the process is temperature and time dependent, precipitation is achieved either by natural (i.e. at room temperature) or artificial (i.e. at elevated temperature) aging. Natural or artificial precipitation hardening following solution heat treatment and quenching determines to a major extent the properties of cast aluminum products. The precipitation sequence in these alloys is shown in Table 2.4 [17].

In the case of Al-Si-Cu alloy the purpose of this treatment is to precipitate out of solution the hardening elements ($CuAl_2$) that were dissolved during the solution heat treatment. At temperatures above 100 °C, GP zones that formed by diffusion of copper atoms in the supersaturated solid solution (s.s.s.) are replaced by θ", referred to as GP II with a three-dimensional atomic arrangement [52]. As the diffusion continues, it leads to the formation of the transition phase θ', which is coherent with the matrix and has the same composition and structure as the stable θ phase. Finally, θ' transforms to stable, non coherent equilibrium θ. The precipitates formed act as obstacles to dislocation movement, so the strength increases. Pre-precipitation may occur depending on the precipitation temperature, forming metastable phases. These metastable phases increase the strength depending on their type, size and distribution.

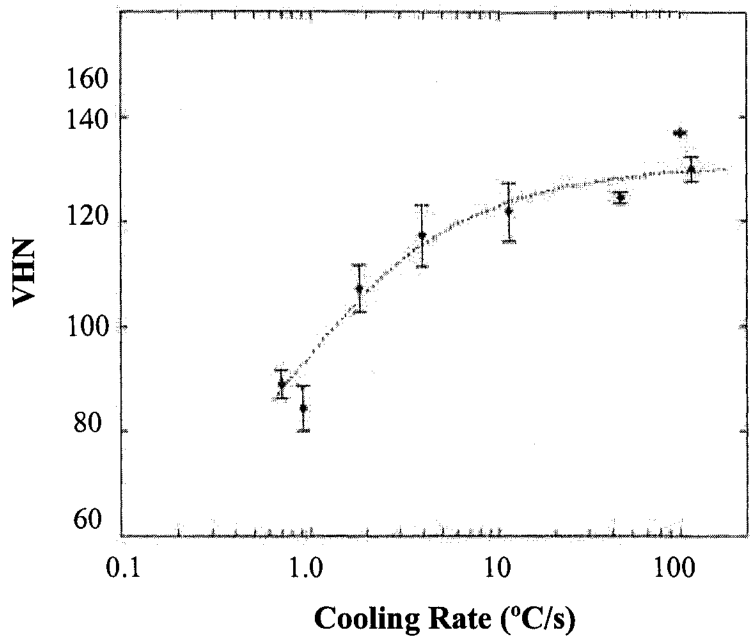

Figure 2.17 – Variation of the T6 Hardness Achieved in a 319 Alloy as a Function of the Cooling Rate Averaged in the 400-480 °C Range [14, 22]

Table 2.4 – Precipitation Hardening System of Al-Si-Cu Alloys [17, 24]

α-Al$_{s.s.s.}$	→	Vacancy-Rich	→	θ"	→	θ'	→	θ
		G.P. Zones		Disk-Like		Disk-Like		$CuAl_2$
				Coherent		Coherent / Non Coherent		Equilibrium
				Tetragonal		Tetragonal 2		BC Tetragonal

Notes:
s.s.s. = Super Saturated Solid Solution
G.P. = Guinier-Preston Zones
Tetragonal 2 = Tetragonal with Different Composition
BC = Body-Centered

2.4.3.1. Natural Aging – After quenching, most aluminum alloys harden to some extent. The extent of change is highly alloy dependent. For instance, alloys A356 and 355 age within 48 h, with negligible changes afterwards; whereas alloy 520 hardens over a period of year [9]. Aging at room temperature or slightly elevated temperatures, is a result of Guinier-Preston (GP) zone formation within the lattice structure. With coherent precipitates, the crystal lattice is strongly distorted (Figure 2.18).

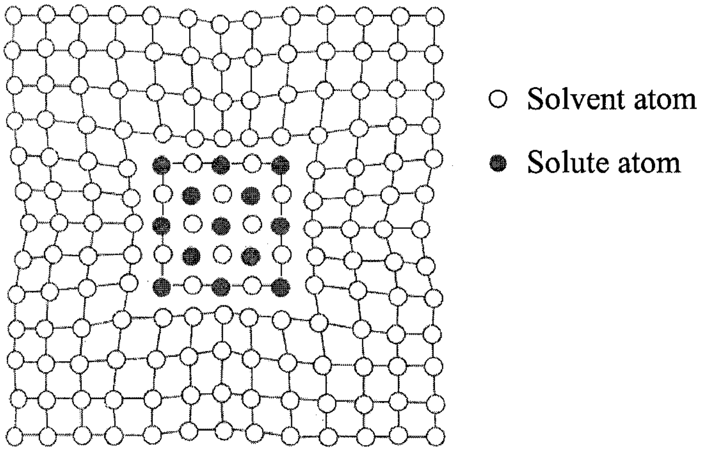

(a) Coherent

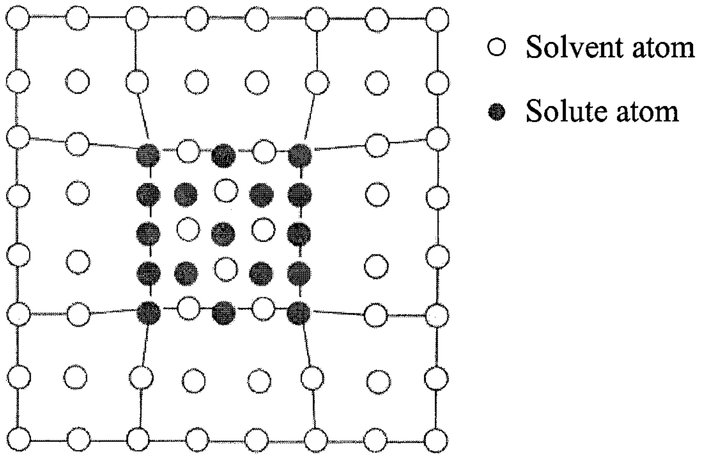

(b) Incoherent

Figure 2.18 – Types of Phase Boundaries Between Matrix and Particle:
(a) Coherent and (b) Incoherent

A marked increase in hardness, strength and 0.2 % proof stress is a result of the extra force that is required to move the dislocations, along with the formation of GP zones. During natural ageing, strength and ductility reach a steady value with longer ageing times. The higher the natural aging temperature, the shorter are the ageing times needed to reach the steady value [68].

2.4.3.2. Artificial Ageing – Aging at a moderately elevated temperature such as point W in Figure 2.19 causes the solute atoms to precipitate out of solid solution. A range of partially coherent metastable phases forms at higher ageing temperatures (about 100 °C to 200 °C), accompanied by hardening effects (Figure 2.18). In part, the stresses are reduced by partial dislocations leading to a less pronounced coherency strain region. Consequently, in theory there is only a small increase in strength. However, due to the fact that the metastable phases are larger than the coherent phases that result from natural ageing, the strength increases [9].

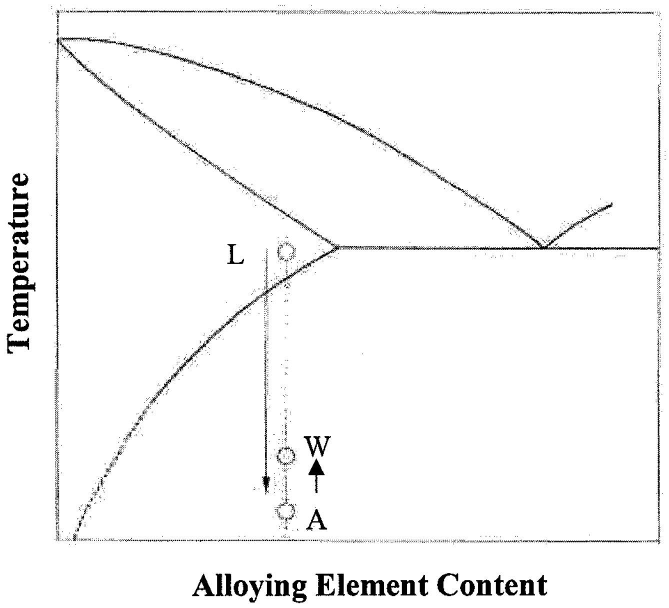

Figure 2.19 – Schematic of Binary System Suitable for Age-Hardening, Where:

L = Solution Treatment Temperature
W = Artificial Ageing Temperature
A = Quenching Temperature

These metastable phases form instead of the coherent precipitates that form at lower temperatures (natural ageing). As time increases, the coherent precipitates tend to disappear and the incoherent precipitates predominate. At higher temperatures, in the artificial ageing range of 100 °C to 250 °C, the partially-coherent phases form quicker. Artificially aged samples exhibit a greater increase in strength and hardness than with natural ageing [69].

The maximum hardness will be reduced with an increase of temperature as coarser and more dispersed precipitates will be formed (Figure 2.20) [2, 22, 69]. Artificially aged castings are air cooled to ambient temperature after the ageing period. Castings aged immediately after quenching will give entirely different mechanical properties than castings from the same batch that have been sitting at room temperature (after solutionized and quench) and then returned to the furnace-ageing stream [70, 71].

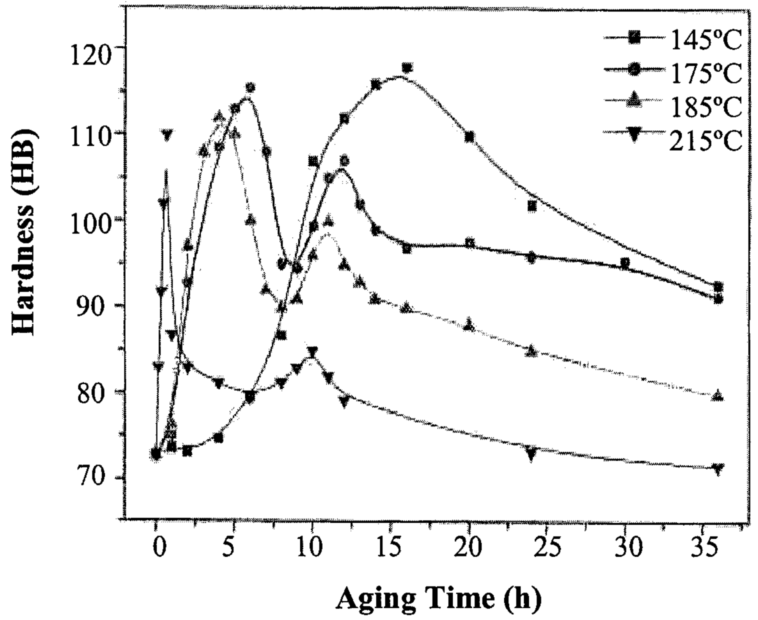

Figure 2.20 – Age-Hardening Curves of Al-Si-Cu-Mg Alloy Aged at Different Temperatures [70]

2.4.3.3. Overaging – The stabilization (T7) treatment is conducted at higher temperatures (20-240 °C) than T6 (150-180 °C) [22]. At higher temperatures and longer ageing times, the formation of incoherent equilibrium phases (i.e. $CuAl_2$, Mg_2Si) increases, leading to a reduction in the hardening effect. The loss of strength is a result of the removal of coherency strains which causes a fluent dislocation movement. With the stabilization treatment, some advantages over the T6 treatment exist, among them, is the reduction in residual stresses. In the case when service of the casting involves exposure at elevated temperatures and to thermal fatigue, the overaged treatment results in increased stability and performance [72].

In aluminum casting alloys, there is no clear division between natural ageing, artificial ageing and overageing. When aging temperature and time increase, the supersaturated solid solution approaches an equilibrium condition and several coherent, incoherent and partially-coherent phases form. A schematic of the hardening process is shown in Figure 2.21 [9, 52].

2.5. Precipitation Studies Using Electron Microscopy

2.5.1. Electron Microscopy

Electron microscopy is a powerful tool to analyze the microstructure, chemistry and crystal structure of materials from areas smaller than 1µm. In general, electron microscopy is divided into two different areas: surface scanning electron microscopy (SEM) and transmission electron microscopy (TEM) [73, 74].

The fundamental difference is that an image from a scanning electron beam instrument is built up by scanning a focused, highly convergent electron probe (much more smaller than the area being imaged) over an area of the sample and measuring a signal produce from the interaction of the electron beam with the specimen [74, 75].

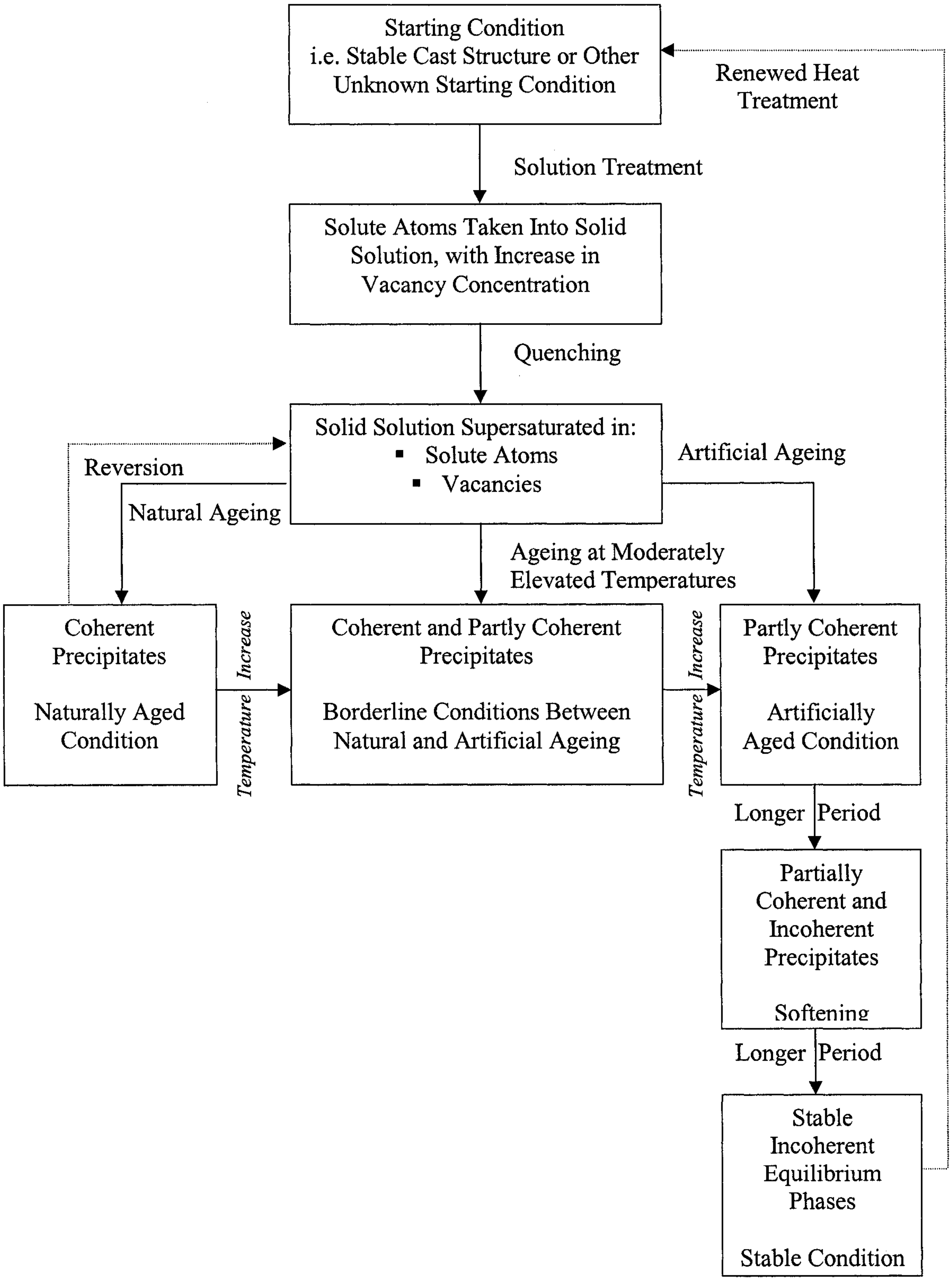

Figure 2.21 – Schematic of the Hardening Process [9]

On the other hand, a transmission electron microscope uses a parallel (coherent) stationary beam of electrons illuminating an area of the sample and forming an image using some portion of the electrons which pass through the specimen [75].

In this regard, images from scanning electron beam instruments are sometimes referred to as virtual images because the image is comprised of a signal different than that of the incident electron beam. Images from a transmission electron microscope can be classified as a real image.

All surface scanning electron microscopy techniques utilize a focused (1 μm to 0.15 nm) electron beam incident on a sample. The size of the electron probe depends on the electron gun configuration (thermionic versus field emission) and the amount of current in the electron probe selected by the operator (typically < 500 nA) [76]. Several types of signals are the result of the interactions between the sample and the electron probe, including secondary electrons (SEs), backscattered electrons (BSEs) and characteristic X-rays.

Resolution for the BSEs and X-ray images is dependent on the size of the electron interaction volume (typically between 0.5 and 5 mm), which is a function of the accelerating voltage, the average atomic number and the density of the sample [76]. For SE imaging, resolution is usually dependent on the size of the electron probe and the inherent contrast of the sample [73, 76].

Modern electron probe microanalyzers (EPMA) and scanning electron microscopes (SEM) are scanning electron beam instruments which differ by the type of detector used to perform chemical analyses [75]. The EPMA has three or more wavelength-dispersive X-ray (WDX) spectrometers to provide highly accurate chemical analysis, whereas the SEM is usually only equipped with an energy-dispersive X-ray (EDX) spectrometer.

The EDX spectrometer provides “quick” identification of most elements, is easy to use and is relatively inexpensive, EPMAs are also equipped with EDX spectrometers. Another advantage of the EDX spectrometer over the WDX spectrometer is its small size, which permits it to be used close to a specimen inside a TEM, where the amount of X-rays generated is limited by the limited sample thickness.

Samples for the transmission electron microscopy are required to be thin so that electrons with energies of 100 keV or higher can pass through the sample to provide a magnified image of the sample or an electron-diffraction pattern. Specimen contrast in the TEM arises due to scattering of the beam electrons as they pass through the specimen. An image is formed by unscattered electrons, elastically scattered electrons or a combination of unscattered and elastically scattered electrons [77].

Diffraction contrast can use either the unscattered electrons to form a bright-field (BF) image or the elastically scattered electrons to form a dark-field (DF) image. Mass-absorption contrast arises where two or more phases are present which have different abilities (due to atomic number differences) to absorb the incident electron beam. This contrast arises from inelastically scattered electrons [78].

2.5.2. Electron Microscopy Studies on the Age Hardening Precipitates

Many authors have studied the precipitation of Mg_2Si and $CuAl_2$ in wrought alloys by TEM [6, 79-84], but little research work involving TEM in Al-Si-Cu casting alloys has been done [2, 5, 74, 85].

Information about the crystal structure, size, shape and distribution of precipitates is provided by TEM. This information is necessary to understand the precipitation hardening.

A study by Donlon et al. [74] on the precipitates responsible for age-hardening of an Al-7.5 % Si-3.5 % Cu revealed that the first precipitates formed were needle-shaped G.P. zones, aligned along <100> directions of the matrix, which were coherent with the matrix along their major axes. As aging continues, the elongated precipitates appear together with smaller equiaxed precipitates. As these coarsen following aging, θ'-$CuAl_2$ thin plates lying on {011] planes [74] are formed. Finally, the equilibrium phase ($CuAl_2$) is formed with a body-centered crystal structure.

The precipitation of θ", θ' due to the presence of copper and S' and β" (Mg_2Si) due to the addition of magnesium in an Al-Si-Cu alloy has been reported [85, 86]. The identification of precipitates is very complicated, since θ', S' and β' are all needle-like particles forming along the <100> directions of the matrix [86].

Li et al. [2, 74] showed that besides the θ ($CuAl_2$) and β (Mg_2Si) phases, some other precipitate phases exist in aged Al-Si-Cu-Mg alloys, such as W ($Al_xCu_4Mg_5Si_4$) and S ($CuAl_2Mg$) phases.

As Kang et al. [7] reported, the θ' phase preferentially precipitates on dislocations introduced around eutectic Si particles in the Al-Si-Cu base alloys; while the λ' ($Al_5Cu_2Mg_8Si_5$) phase homogeneously precipitates in the α matrix, regardless of the sites of dislocations and therefore significantly raises the age-hardening ability. As suggested by Zafar et al. [8], the Q ($Al_5Cu_2Mg_8Si_6$) phase may exist in the aged Al-Si-Cu-Mg alloys, which can be responsible for the age-hardening.

Eskin et al. [85, 86] concluded that the best combination of mechanical properties corresponds to the presence of all hardening phases, such as θ', S' and β". However, this statement was not supported by the electron diffraction identification of phases, but was based only on the precipitation morphology.

The precipitation of Al-Si-Cu-Mg alloys requires further studies to explain the mechanism of hardness increase due to Mg addition to Al-Si-Cu alloys. In the ternary alloys, only binary θ' phases contribute to the hardening and no ternary silicon containing phases were found [6]. The hardness increase due to precipitation of β" [86] is not much different from that of S' and therefore it cannot give a hint concerning the mechanism of hardening.

CHAPTER 3

EXPERIMENTAL TECHNIQUES

The experimental procedure was designed to investigate the effect of Sr modification, Mg additions and metallurgical parameters such as solution heat treatment time, and artificial aging time and temperature on the properties and precipitation of $CuAl_2$, Mg_2Si during the heat treatment of Al-7 % Si-0.35 % Cu alloys. This chapter focuses on describing and illustrating the instrumentation and experimental setups utilized.

A summary of all operations performed is shown in Figure 3.1. The experimental work can be divided into several steps as:

- Fabrication and heat treatment of the samples
- Metallographic examination
    - Secondary dendrite arm spacing (SDAS)
    - Grain size measurements
- Mechanical properties testing
    - Micro~ and macro~ hardness measurements
    - Tensile properties
- Electron microscopy analysis
    - Electron probe microanalyzer (EPMA)
    - Field emission scanning electron microscopy (FE-SEM)
    - Transmission electron microscopy (TEM)

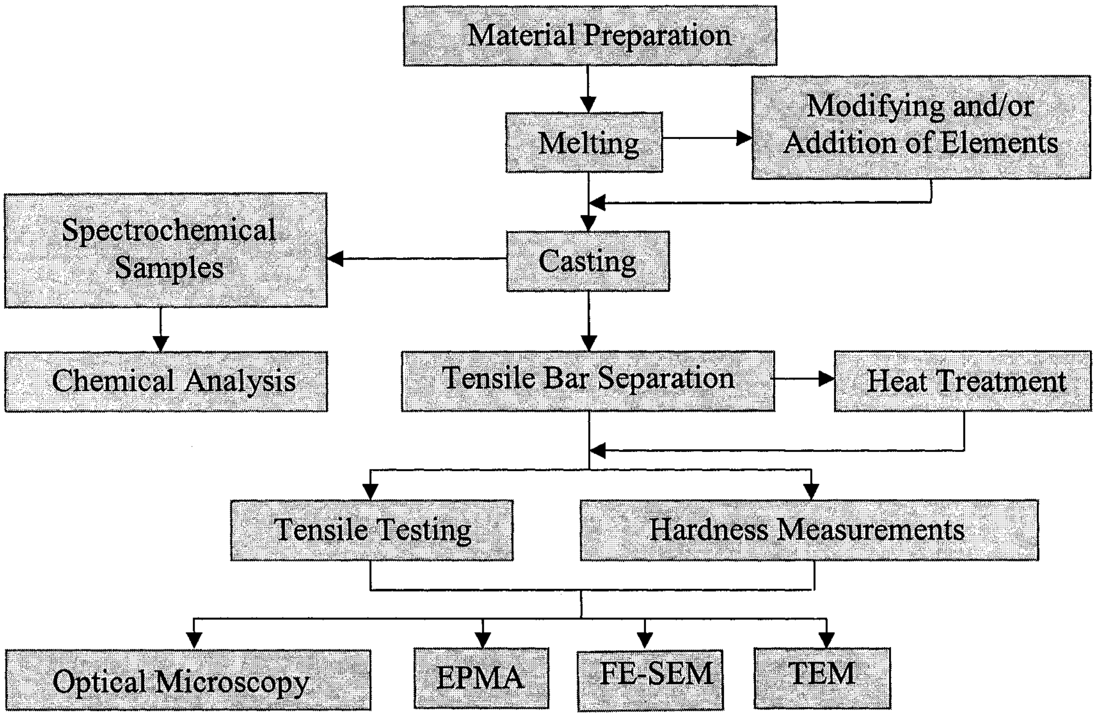

Figure 3.1 – Experimental Procedure

3.1. Sample Fabrication

Cast bars from which coupons were obtained for further heat treatment and evaluation were produced, along with cast bars for tensile testing. The production characteristics are described in the following paragraphs.

The casting was carried out at the Université du Quebec à Chicoutimi. The specimens were all made from commercial A319 alloy. The chemical compositions of the four 319-type alloys that were used are shown in Table 3.1.

Table 3.1 - Chemical Composition of the Samples

	Elements (wt %)					
A319.2	Si	Cu	Mg	Fe	Ti	Sr
A	6.18	3.59	0.02	0.12	0.15	0.0003
S	6.12	3.53	0.02	0.12	0.15	0.0167
M	6.20	3.59	0.42	0.09	0.15	0.0015
MS	6.18	3.62	0.39	0.10	0.15	0.0164

The experimental base alloy (composition A listed in Table 3.1) was supplied in the form of ingots. The supplied ingots of the as-received alloy were cut into smaller pieces, dried, and melted in a 30 kg capacity SiC crucible heated by means of an electric resistance furnace. The melting temperature was kept at 750 ± 5 °C. Measured quantities of Sr or Mg additions were made at this temperature, using a perforated graphite bell. Strontium was added in the form of an Al-10 wt % Sr master alloy, while magnesium was added as pure metal.

The melt was stirred for 15 minutes to ensure homogeneous mixing of the added material, and then degassed with pure argon (using a graphite impeller, 200 rpm speed) for 15 min, followed by filtration using 15 ppi. Two minutes before the end of degassing, grain refiner (TiB_2 30 ppm B) and Sr modifier were added.

The molten metal was then poured into a standard Stahl mold [ASTM-B108-85a (160) permanent mold]. Each casting gave two bars whose dimensions are given in Figure 3.2.

To drive out moisture, prior to melting, the mold was preheated to 350 ± 5 °C. The pouring temperature was 725 ± 5 °C, the humidity level was between 11 to 15 % and the hydrogen level was 0.1 ml H_2/100 g Al. For each pouring, samples for spectrochemical analysis were taken.

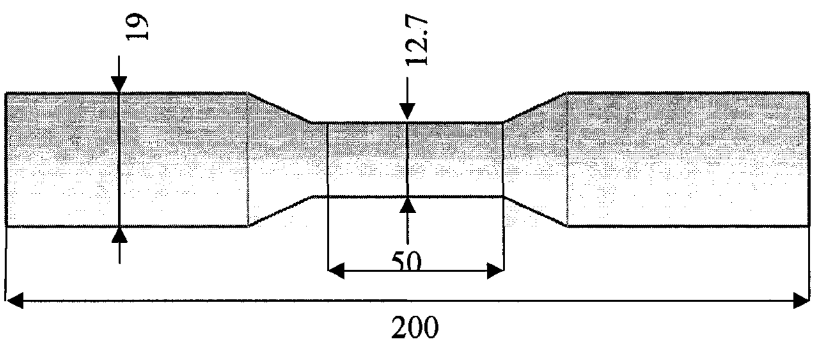

Figure 3.2 – Dimensions in mm of the Permanent Mould Tensile Bar

All bars were taken in batches to Robert Mitchell Cie., to be X-rayed. The setting parameters of the apparatus were 100 kV, 8 mA and 25s. Thus, all bars were radiographically examined in order to facilitate the selection of sound samples. Few bars were rejected due to the presence of defects. Finally, the selected specimens were either tested in the as-cast or heat treated condition.

3.2. Heat Treatment

The effect of different heat treatment parameters such as solution heat treatment time, artificial aging time and temperature were studied, with respect to their relation to Sr modification and Mg addition on precipitation in A319 alloys.

All the heat treatments were carried out in an electric furnace (Hayes Certain Curtain Type LR 62) equipped with a set-point program/controller (West 2050, two instruments in one microprocessor-based technology). The furnace was calibrated through an adequate tuning of the controller to improve the control characteristics.

The calibration of the furnace temperature was carried out with 3 thermocouples at different places in the furnace, and at different temperatures. The results obtained from the calibration indicated a maximum variation of ± 3 °C at any of the treatment temperatures used in the zone where the heat treatments took place.

The inside dimensions of the furnace were 85 cm in length, 35 cm in width and 20 cm in height. The heating elements were located on the top and the sides over a length of 60 cm from close to the back of the furnace.

The greatest temperature variation (12 °C) occurred between the back and the front of the furnace. The selected temperature was found in the middle position. For each heat treatment condition, all the samples were placed on a rack coated with alumina, such that they did not touch each other in order to have air circulation and uniform heating. The rack was always placed in the central position of the furnace, where the temperature was in the range of ± 2 °C.

For each given condition, except those in which the solution time was the variable, all the samples were solutionized and quenched at the same time, leaving only the other conditions, such as artificial aging time and temperature, as variables.

The solution treatment was just below that at which the last liquid of the eutectic solidifies (495 °C for 4 h). At this temperature the maximum concentration of Cu is dissolved in the aluminum. ASTM standards [54] recommend for the 319.0 alloy a solution heat treatment of 505 °C for 4 to 12 hours. Other authors [12, 45, 88] consider a temperature of 495 °C and a time of 4 h as the optimum. In this research work a solution heat treatment time of 4 hours was usually used to evaluate the precipitation in these alloys. Evaluations at 24 hours of solutionizing time were also done. It is very important to mention that the evaluation of the properties and precipitation in this work is focused on the as-cast, T4 (solution heat treated and quenched) and T6 (solution heat treated, quenched, and artificially aged).

Quenching was performed by immersion of the samples in water with a quench delay no longer than 5 seconds. The water bath used was a modified domestic hot-water tank. The temperature was set to 90 °C. The artificial aging treatment was carried out at 180 °C and 220 °C. Time was a variable in the precipitation hardening treatment, and ranged from 0.5 h up to 24 h. In all of the heat treatment stages, the soaking time did not begin to be counted until the furnace reached the desired temperature.

A summary of the heat treatment schedules of the coupons is given in Table 3.2. For the tensile test bars only a few heat treatment experiments, considered as critical, were done. A summary of those heat treatments is shown in Table 3.3.

Table 3.2 – Heat Treatment Schedules of the Coupons *

Cycle	Solution Treatment		Quenching	Natural	Artificial Aging	
	Temperature (°C)	Time (h)	Temperature (°C)	Aging (h)	Temperature (°C)	Time** (h)
W	495	4	90	0	180	½ - 24
X	495	4	90	0	220	½ - 24
Y	495	24	90	0	180	½ - 24
Z	495	24	90	0	220	½ - 24

* Unmodified and modified, with Mg and without Mg additions
** Artificial aged at ½, 1, 2, 3, 4, 5, 6, 8, 10, 12, 14, 19, 24 h

Table 3.3 – Heat Treatment Schedules of the Tensile Test Bars *

Cycle	Solution Treatment		Quenching	Natural	Artificial Aging	
	Temperature (°C)	Time (h)	Temperature (°C)	Aging (h)	Temperature (°C)	Time** (h)
W	495	4	90	0	180	½ - 24
X	495	4	90	0	220	½ - 24

* For all chemical compositions
** Artificial aged at ½, 1, 2, 3, 4, 5, 6, 8, 10, 12, 14, 19, 24 h

3.3. Metallographic Examination

Metallographic examination is here meant to include sample preparation and studies in image analysis, secondary dendrite arms spacing (SDAS) measurements and grain size measurements.

3.3.1. Metallographic Preparation

Coupons were cut from the gage length and shoulders of the tensile bars. Coarse grinding was carried out using 120 grit silicon carbide papers. This was followed by fine grinding using successively #120, # 240, #320, #400, #600, #1200 and #2400 grit papers with water as the polishing medium. Subsequently, polishing was performed with alumina powder suspended in water as the polishing media, 5 μm and 0.3 μm powders were used for rough and fine polishing respectively. Finally, to produce a mirror-like surface, the final polishing was done with 0.05 μm colloidal silica.

3.3.2. Secondary Dendrite Arm Spacing (SDAS)

On selected samples, secondary dendrite arm spacing was measured using the line intercept method performed using CLEMEX Vision ^{TM}. Before the measurements, samples were polished and etched using Nital (100 ml of methanol and 3 ml of HNO_3).

For the four chemical compositions, samples were prepared from the as-cast and heat-treated coupons at conditions that were considered of critical importance. A summary of the heat treatment conditions of the samples chosen for SDAS examination is given in Table 3.4.

On dendrites with at least six arms, ten SDAS measurements on dendrites were taken from each coupon (five on each side) and averaged. Figure 3.3 shows the line intercept method.

Table 3.4 – Conditions of the Coupons Used for SDAS Examination

Condition	Solution Treatment Temperature (°C)	Solution Treatment Time (h)	Quenching Temperature (°C)	Natural Aging (h)	Artificial Aging Temperature (°C)	Artificial Aging Time (h)
As-Cast	-	-	-	-	-	-
T4	495	4	-	-	-	-
	495	24	-	-	-	-
T6 (W)	495	4	90	0	180	2
	495	4	90	0	180	4
	495	4	90	0	180	12
	495	4	90	0	180	24
T6 (X)	495	4	90	0	220	2
	495	4	90	0	220	4
	495	4	90	0	220	12
	495	4	90	0	220	24
T6 (Y)	495	24	90	0	180	2
	495	24	90	0	180	4
	495	24	90	0	180	12
	495	24	90	0	180	24
T6 (Z)	495	24	90	0	220	2
	495	24	90	0	220	4
	495	24	90	0	220	12
	495	24	90	0	220	24

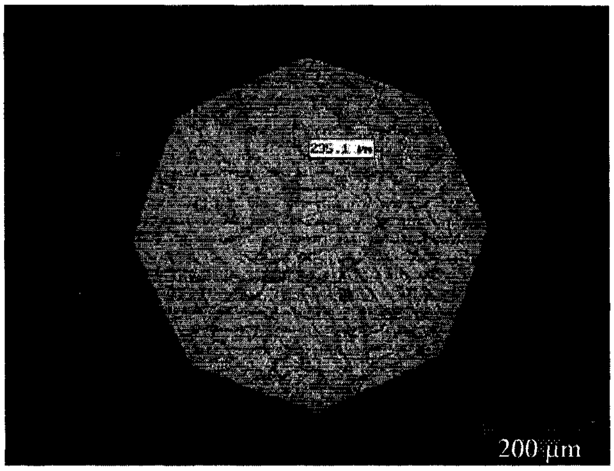

Figure 3.3 – SDAS Measurement Using Line Intercept Method
Length of the Dendrite 235.1 µm/10 Dendrite Arms = 23.51 µm SDAS

3.3.3. Grain Size

On selected samples, grain size measurements were measured using the line intercept method performed using CLEMEX Vision ™. Before the measurements, samples were polished and etched using a solution with 35 g of $FeCl_3$ dissolved in 200 ml of distillated H_2O for 5 min. The polished surface was swabbed until the contrast in revealed grains was high enough.

To better highlight the grain structure, filtered lights at different incident angles were used. A combination of red, green, blue and yellow light gave an enhanced contrast to the grain structure.

For the four chemical compositions, samples were prepared from the as-cast and heat-treated coupons at conditions that were considered of critical importance. A summary of the heat treatment conditions of the samples chosen for grain size examination is given in Table 3.5. At least 5 measurements were taken from each coupon and averaged.

Table 3.5 – Conditions of the Coupons Used for Grain Size Examination

Condition	Solution Treatment Temperature (°C)	Solution Treatment Time (h)	Quenching Temperature (°C)	Natural Aging (h)	Artificial Aging Temperature (°C)	Artificial Aging Time (h)
As-Cast	-	-	-	-	-	-
T4	495	4	-	-	-	-
	495	24	-	-	-	-
T6 (W)	495	4	90	0	180	2
	495	4	90	0	180	4
	495	4	90	0	180	12
	495	4	90	0	180	24
T6 (X)	495	4	90	0	220	2
	495	4	90	0	220	4
	495	4	90	0	220	12
	495	4	90	0	220	24
T6 (Y)	495	24	90	0	180	2
	495	24	90	0	180	4
	495	24	90	0	180	12
	495	24	90	0	180	24
T6 (Z)	495	24	90	0	220	2
	495	24	90	0	220	4
	495	24	90	0	220	12
	495	24	90	0	220	24

3.4. Mechanical Properties

Mechanical properties were obtained from microhardness measurements, macrohardness measurements and tensile tests. They were monitored as functions of heat treatment time and chemical composition.

3.4.1. Microhardness

Microhardness measurements were done to assess the changes occurring in the aluminum matrix (α-Al) due to modification and heat treatment. The testing was done using a Vickers hardness tester, with a diamond indenter with an angle of 136° and a load of 50 gf. For each cast bar, seven coupons, each 2.5 cm long were obtained. The coupons were ground and polished by typical metallographic polishing, to obtain a flat and parallel surface on both sides. No chemical etching was performed on the mirror-like polished coupons.

The inclination of the sample with respect to the indenter has an influence when obtaining symmetrical microhardness. For this reason, the coupons were placed in a universal clamp and leveling device when tested. Twelve microhardness readings were taken from each coupon (six on each side) and averaged.

The size of the indentation was measured with a micrometer integrated to a microscope at 400X. The value of the indentation was then transformed to a microhardness value using the following formula [89]:

$$VH = 1.854 \times 10^3 (F/d^2)$$

Where: "F" is the load (in g) and "d" is the indentation average length (in μm). A typical microhardness indentation is shown in Figure 3.4.

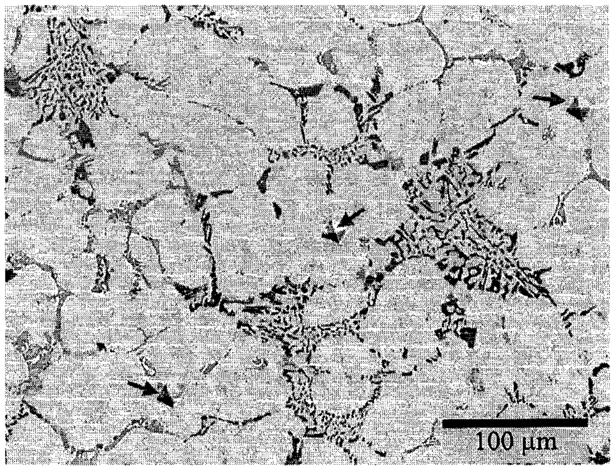

Figure 3.4 – Typical Microhardness Indentation

3.4.2. Macrohardness

Macrohardness measurements were done to assess the changes occurring in the microstructure (aluminum matrix and eutectic silicon) due to modification and heat treatment. The testing was done using a Vickers hardness tester, with a diamond indenter with an angle of 136° and a load of 5 kgf. The hardness tester was calibrated by taking 10 hardness readings on the standard test block. All the values fell within the range. The coupons were ground and polished, to obtain a flat and parallel surface on both sides.

Six microhardness readings were taken from each coupon (three on each side) and averaged. For each heat treatment condition, the average of three different coupons was calculated (18 measurements per condition). Hardness indentations were made across the sample diameter and were well separated to ensure that there was no overlap of the deformation. A typical microhardness indentation is shown in Figure 3.5.

3.4.3. Tensile Testing

The influence of Sr and Mg additions and heat treatment conditions on mechanical properties was investigated by pulling a very large number of tensile bars.

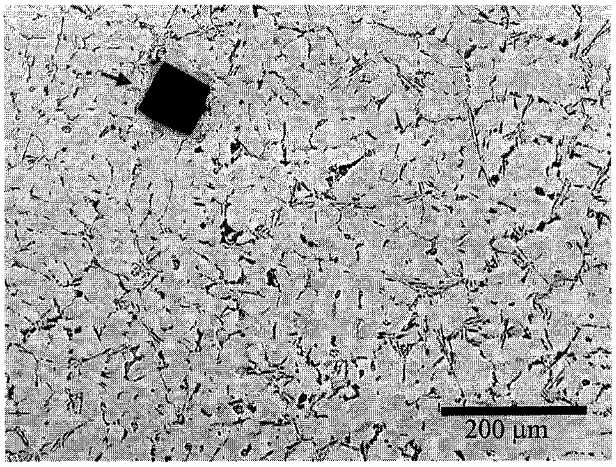

Figure 3.5 – Typical Macrohardness Indentation

The tensile properties of samples produced at certain heat treatment conditions considered as critical, were evaluated in order to obtain information related to the precipitation in the alloy. The as-cast, T4 and T6-treated test bars were pulled to fracture in an MTS Universal testing machine at a strain rate of 4 x $10^{-4}s^{-1}$. Mechanical properties, such as yield strength (YS) at 0.2 % offset strain, ultimate tensile strength (UTS), and elongation (% el.), were obtained from the data acquisition system of the machine. A strain gage extensometer (MTS 634-2SE-51) was attached to the test specimen to measure elongation as the load was applied (Figure 3.6). Both signals were sent to an X-Y recorder to get the load-elongation curve.

3.5. Electron Microscopy Analysis

Optical microscopy was conducted to examine specimens with as-cast and heat treated structures and slightly different secondary dendrite arm spacing, silicon eutectic constituents and microporosity. Further examination at finer scales was conducted using an electron probe microanalyzer (EPMA), field-emission scanning electron microscopy (FE-SEM) and transmission electron microscopy (TEM), which revealed precipitates and their variations with the heat treatment.

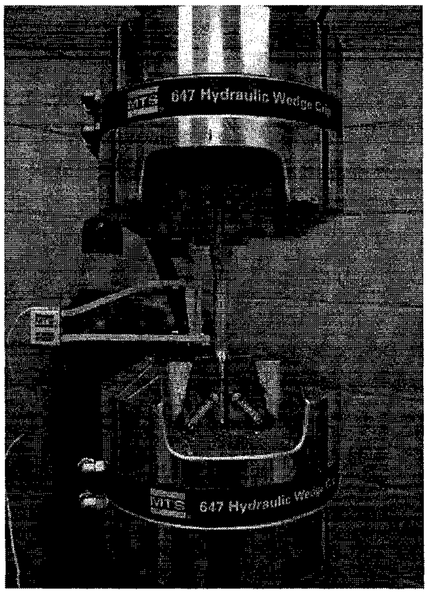

Figure 3.6 – Position of the Extensometer During Testing of the Specimens

3.5.1. EPMA Sample Preparation and Observation

Dissolution behavior was studied using an electron probe microanalyzer (EPMA) equipped with energy dispersive X-ray (EDX) and wavelength dispersive spectrometer (WDS) facilities, operating at 20 kV and 30 nA. The beam size was around ~2 μm. Samples were prepared from the as-cast and heat-treated coupons at conditions that were considered of critical importance. A summary of the heat treatment conditions of the samples chosen for EPMA examination is given in Table 3.6. The coupons were etched using a solution of 48 % HF and 52 % water at room temperature by immersion for 30 s.

Quantitative analysis of the volume fractions of the various phases and Cu following the different solution treatment times was carried out. On the polished sample surfaces, mapping was also done to determine the distribution of alloying elements. In order to understand the effect of solution treatment on age-hardening, the distribution of copper and other solute elements was measured within the aluminum dendrites, as a function of solution time (4 h and 24 h) and artificial aging temperatures (180 °C and 220 °C) at constant solution treatment temperature at 495 °C and aging time of 4 h.

Table 3.6 – Conditions of the Coupons Used for EPMA Examination

Composition	Condition	Solution Treatment Temperature (°C)	Solution Treatment Time (h)	Quenching Temperature (°C)	Natural Aging (h)	Artificial Aging Temperature (°C)	Artificial Aging Time (h)
M	As-Cast	-	-	-	-	-	-
	T4	495	4	90	-	-	-
	T4	495	24	90	-	-	-
	T6	495	4	90	0	180	4
	T6	495	4	90	0	220	4
	T6	495	24	90	0	180	4
	T6	495	24	90	0	220	4
MS	As-Cast	-	-	-	-	-	-
	T4	495	4	90	-	-	-
	T4	495	24	90	-	-	-
	T6	495	4	90	0	180	4
	T6	495	4	90	0	220	4
	T6	495	24	90	0	180	4
	T6	495	24	90	0	220	4

3.5.2. FE-SEM Sample Preparation and Observation

Field Emission Scanning Electron Microscopy (FE-SEM) is a high resolution imaging technique that provides topographic and structural information in plan view or within the cross-section [90]. The X-ray microanalysis by an energy dispersive spectroscopy (EDS), allows the FEG-SEM to analyze qualitatively and quantitatively the elements present in a selected area of a secondary or backscattered electron image.

In this work, the Hitachi S-4700 FEG-SEM was used with a mixed detection system using lower and upper detectors. The upper detector was used for its high resolution and high signal to noise ratio ability for secondary electron imaging. The system can be adjusted, with the voltage bias, to give images consisting of pure secondary electrons to pure backscattered electrons, and anywhere in between. This provides a great flexibility in overcoming charging and in optimizing imaging contrast.

FE-SEM conventionally involves the analysis of bulk specimens; however, there is a problem of the interaction volume lowering the resolution of the microscope. This is overcome by reducing the accelerating voltage. However, features below 100nm can be difficult to characterize with respect to X-ray microanalysis using EDS because the X-ray signal is low. This limitation in the FE-SEM can be alleviated by using thin specimens which would normally be used in the TEM, such as carbon extraction replicas or thin foils, since the interaction volume effect is greatly reduced.

Therefore, the aim for using FE-SEM in this work was to develop a technique to examine fine precipitates in thin foils. Sample preparation of the thin foils is described in the next section.

A summary of the heat treatment conditions of the samples chosen for FE-SEM examination is given in Table 3.7.

Table 3.7 – Conditions of the Coupons Used for FE-SEM Examination

Composition	Condition	Solution Treatment		Quenching	Natural	Artificial Aging	
		Temperature (°C)	Time (h)	Temperature (°C)	Aging (h)	Temperature (°C)	Time (h)
M	As-Cast	-	-	-	-	-	-
	T4	495	4	90	-	-	-
	T4	495	24	90	-	-	-
	T6	495	4	90	0	180	0.5
	T6	495	4	90	0	180	2
	T6	495	4	90	0	180	4
	T6	495	4	90	0	180	6
	T6	495	4	90	0	180	12
	T6	495	4	90	0	180	24
MS	T6	495	4	90	0	180	4

3.5.3. TEM Sample Preparation and Observation

Thin foils were prepared from the as-cast and heat-treated coupons at conditions that were important for the information they could provide to this research work. A summary of the heat treatment conditions of the samples chosen for TEM examination is given in Table 3.6.

The thin foils were prepared by electropolishing using a Struers Tenupol 3 machine, a solution of 30 % nitric acid and 70 % methanol at -30 °C with a current of ~0.12 A. The steps taken for thin foil preparation are summarized in Figure 3.7.

Samples were studied in a fully computerized TEM Jeol JEM-2011 at an acceleration voltage of 200 keV. The images were then acquired with a Gatan Dual View 300 W 1.3k x 1k CCD camera attached to the microscope.

Table 3.6 – Conditions of the Coupons Used for TEM Examination

		Solution Treatment		Quenching	Natural	Artificial Aging	
Composition	Condition	Temperature (°C)	Time (h)	Temperature (°C)	Aging (h)	Temperature (°C)	Time (h)
M	As-Cast	-	-	-	-	-	-
	T4	495	4	90	-	-	-
	T4	495	24	90	-	-	-
	T6	495	4	90	0	180	0.5
	T6	495	4	90	0	180	2
	T6	495	4	90	0	180	4
	T6	495	4	90	0	180	6
	T6	495	4	90	0	180	12
	T6	495	4	90	0	180	24

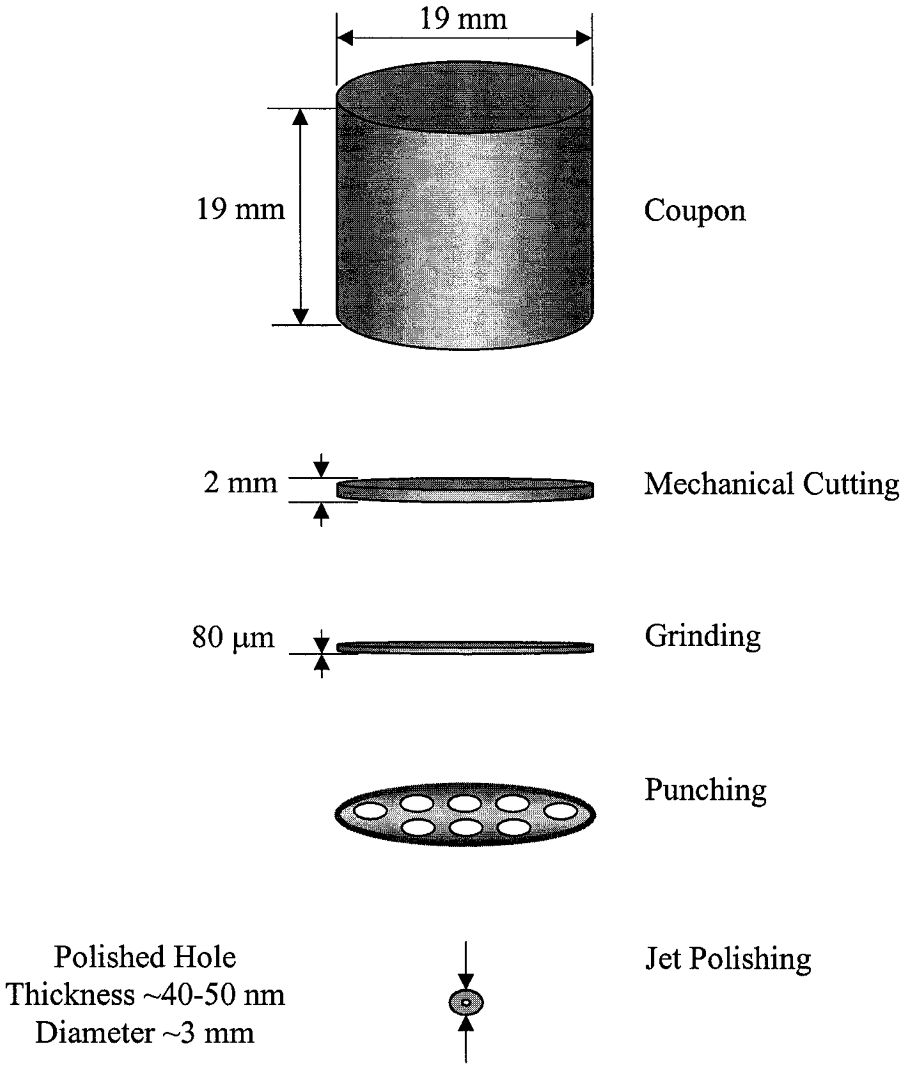

Figure 3.7 – Sample Preparation of Thin Foils for TEM

CHAPTER 4

METALLOGRAPHIC STUDY & MECHANICAL PROPERTIES RESULTS

The overall purpose of the present research was to study the effect of metallurgical parameters, such as solution heat treatment time, artificial aging time and temperature on the properties and precipitation during the heat treatment of 319 alloys.

Metallographic studies were conducted to examine, from the point of view of microstructure and chemical composition, the specific changes due to heat treatment. This was done to achieve the first objective of the present research. Due to the very large number of samples and conditions investigated, only selected photographs are shown.

Another primary purpose of this work was to investigate the importance of Sr and Mg additions on the mechanical properties, particularly after heat treatment. The mechanical properties were evaluated through the tensile test. Hardness and microhardness measurements were also taken on all samples.

Metallographic and mechanical properties results are presented in the following sections. The microstructure of this alloy is presented at first, followed by the results concerning the hardening curves and casting soundness. Finally, tensile results are described.

4.1. Microstructural Results

4.1.1. Microstructure

The microstructure of the "as-cast" material consists of aluminum dendrites and a eutectic structure containing aluminum, silicon, and intermetallic particles of $CuAl_2$, $Al_{15}(Fe, Mn)_3Si_2$ and $Al_5Mg_8Cu_2Si_6$ (Figure 4.1).

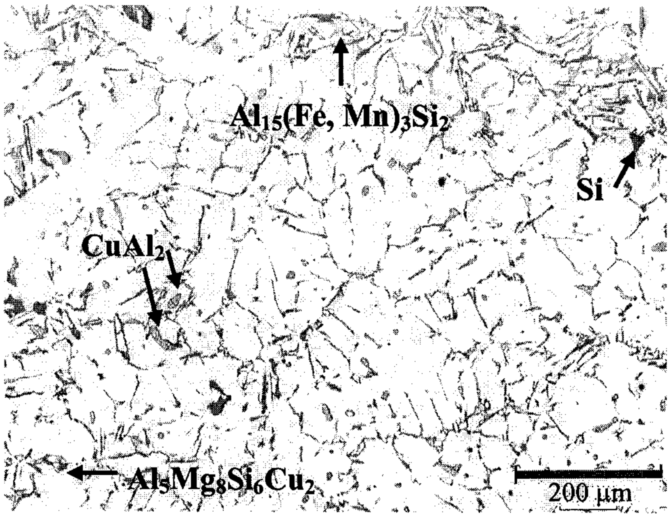

Figure 4.1 – Optical Micrograph of the As-Cast Alloy Showing: Aluminum Dendrites, Al-Si Eutectic, Si Particles, and Intermetallic Particles of $CuAl_2$ and $Al_{15}(Fe, Mn)_3Si_2$

Microporosity is very small if present, hence is negligible. All cast bars were X-rayed to verify their soundness. When samples were heat-treated, a slight modification of the eutectic Si is observed, whereas the $CuAl_2$ and $Al_{15}(Fe, Mn)_3Si_2$ phases do not show a perceptible dissolution.

The high-magnification micrograph of Figure 4.2a reveals that the silicon particles (or flakes) are unmodified. However, the relatively higher cooling rate associated with permanent mold casting (~ 8 °C·s^{-1}, corresponding to a dendrite arm spacing ~ 20-30 μm) leads to smaller silicon particles. Increasing the magnesium content to ~ 0.40 wt % (alloy M) results in the formation of thick plates of $Al_5Mg_8Si_6Cu_2$ (dark grey, arrowed) growing out of the $CuAl_2$ phase particles (Figure 4.2b).

Modification of the high-Mg alloys with 150 ppm of Sr, i.e. alloys S and MS, leads to two main observations: (a) modification of the eutectic silicon particles and their segregation in the form of isolated colonies, (b) severe segregation of both $Al_5Mg_8Si_6Cu_2$ and $CuAl_2$ phase particles in areas away from the advancing interfaces of the eutectic silicon colonies (Figure 4.2c). As a result of such segregation, $CuAl_2$ is mostly in the form of blocky phase with high copper concentrations, which makes their dissolution in the aluminum matrix during solution treatment very slow.

Dissolution of $CuAl_2$ phase is evident when alloys are solution treated at 495 °C, for 4 h leaving behind tiny particles, circled in Figure 4.3a. Thick plates of $Al_5Mg_8Si_6Cu_2$ are still seen in Figure 4.3b, while blocky particles of $CuAl_2$ phase in alloy MS remain as yet undissolved (Figure 4.3c).

The copper intermetallics, present in bulk form, melt at solution temperatures above 500 °C, leading to the formation of spherical liquid droplets within the dendrites and grains, as shown in Figure 4.4.

When the unmodified alloys are solution treated for longer times (24 h), most of the $CuAl_2$ phase remains in solution (Figures 4.5a and 4.5c). In modified alloys, $CuAl_2$ particles are present (Figure 4.5b). In modified alloys with high Mg content, plates of $Al_5Mg_8Si_6Cu_2$ are still present, along with blocky particles of $CuAl_2$ (Figure 4.5d).

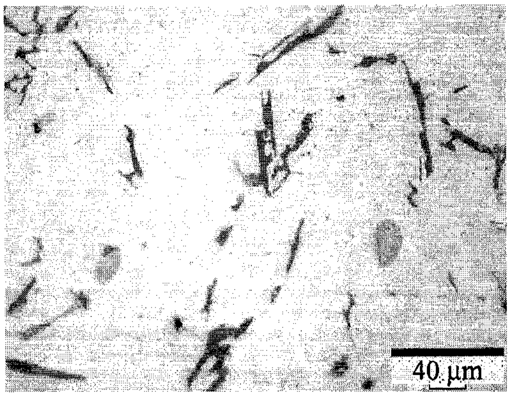

(a) Alloy A

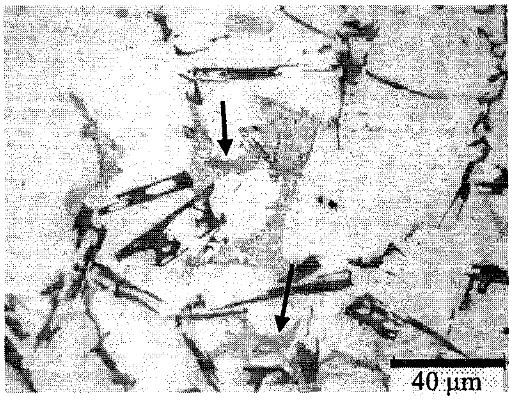

(b) Alloy M

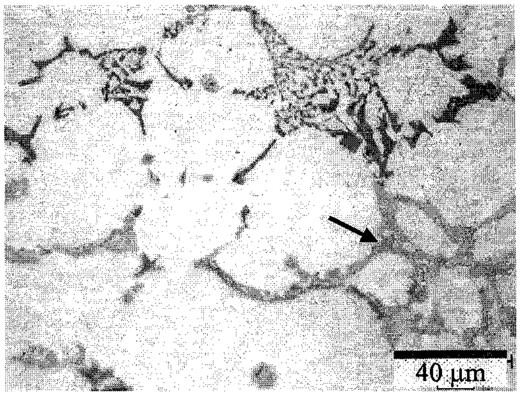

(c) Alloy MS

Figure 4.2 – High Magnification Micrographs in the As-Cast Condition, Showing:

(a) Effect of Permanent Mold Casting and $CuAl_2$ Phase Precipitates in the 319 Alloy
(b) Formation of Thick Plates of $Al_5Mg_8Si_6Cu_2$ Dark Grey Arrowed, With Mg Additions
(c) Segregation of $Al_5Mg_8Si_6Cu_2$ and $CuAl_2$ Due to Modification of the High-Mg Alloy

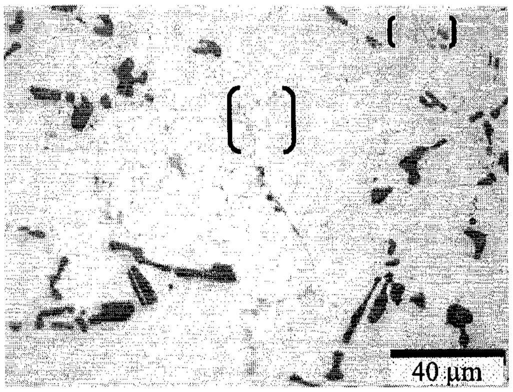

(a) Alloy A

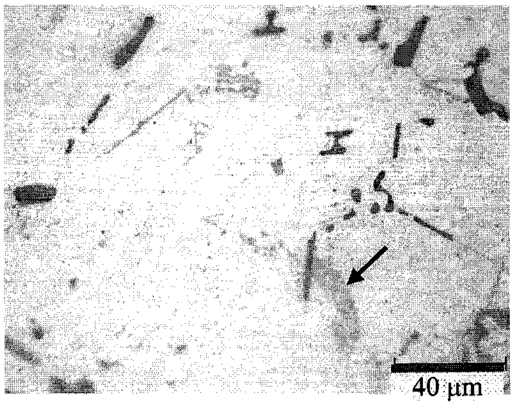

(b) Alloy M

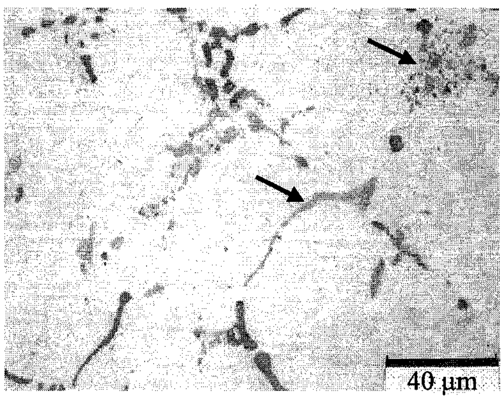

(c) Alloy MS

Figure 4.3 – Microstructure of 319 Alloy Coupons Treated at 495 °C for 4 h, Showing:

(a) Dissolution of $CuAl_2$ Phase in 319 Alloy
(b) Thick Plates of $Al_5Mg_8Si_6Cu_2$ Seen in the High-Mg Alloy
(c) Presence of $Al_5Mg_8Si_6Cu_2$ and Block-Like $CuAl_2$ in Modified High-Mg Alloy

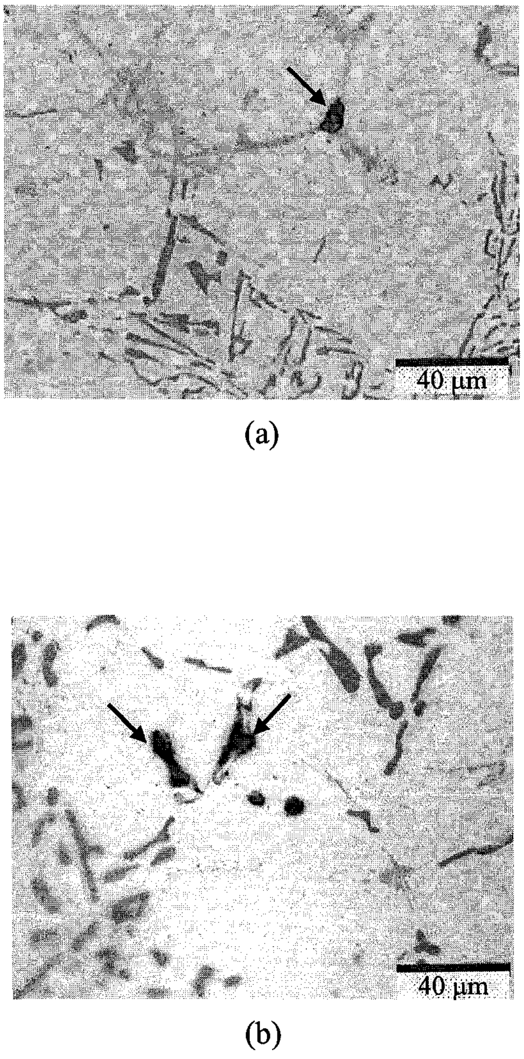

Figure 4.4 – Incipient Melting of Copper-Base Intermetallics in High-Mg Alloy (Alloy M) Solution Treated Above 500 °C

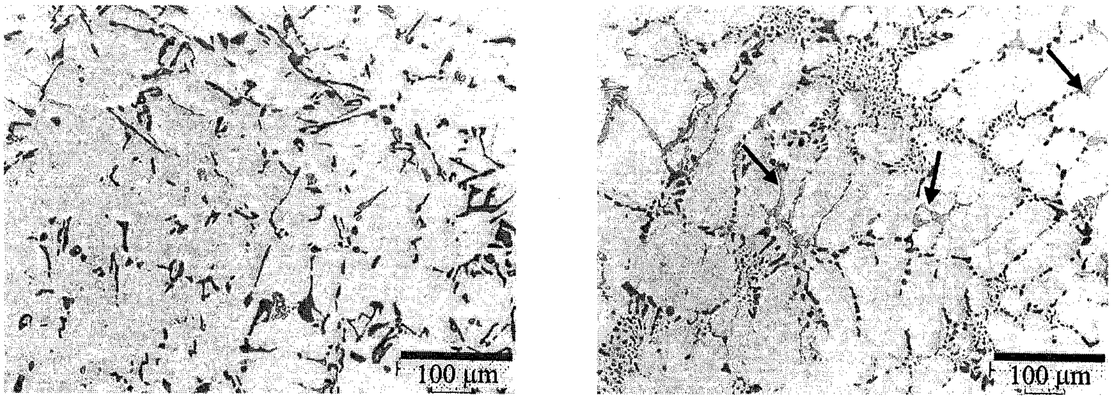

(a) Alloy A (b) Alloy S

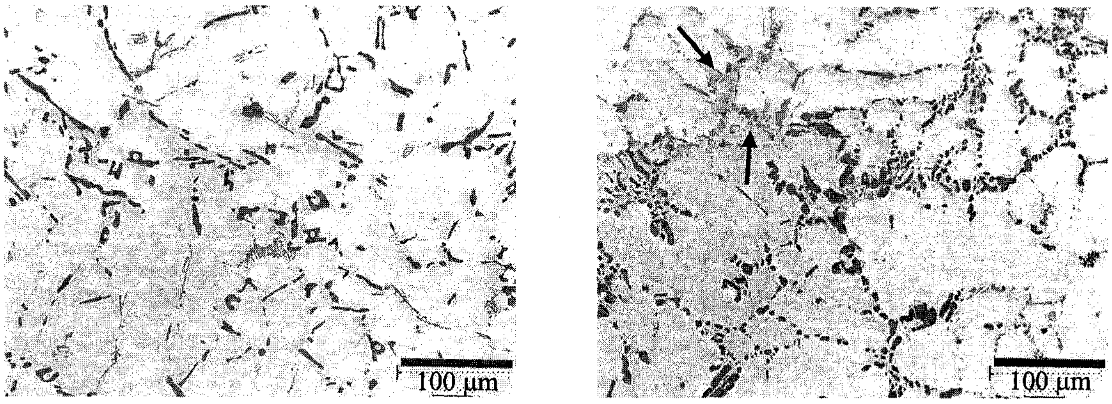

(c) Alloy M (d) Alloy MS

Figure 4.5 – Microstructure of 319 Alloy Coupons Treated at 495 °C for 24 h, Showing:

(a, c) Dissolution of $CuAl_2$ in 319 Unmodified Alloys
(b) Presence of Block-Like $CuAl_2$ in the Modified Alloy
(d) Presence of $Al_5Mg_8Si_6Cu_2$ and $CuAl_2$ in Modified High-Mg Alloy

4.1.2. Secondary Dendrite Arm Spacing (SDAS)

For each sample 5 different dendrite arms with at least 6 arms were measured, then averaged. Tables 4.1 to 4.4 show the SDAS corresponding to the different heat-treatment conditions.

Table 4.1 – Secondary Dendrite Arm Spacing in Alloy A

Condition	Solution Time (h)	Artificial Aging		Average SDAS (μm)
		Temperature (°C)	Time (h)	
As-Cast	-	-	-	25.0
T4	4	-	-	27.7
	24	-	-	35.0
T6 (W)	4	180	2	22.2
			4	22.5
			12	23.7
			24	24.1
T6 (X)	4	220	2	34.9
			4	35.1
			12	36.5
			24	39.7
T6 (Y)	24	180	2	33.0
			4	34.4
			12	36.6
			24	37.5
T6 (Z)	24	220	2	52.3
			4	54.8
			12	54.9
			24	55.6

Table 4.2 – Secondary Dendrite Arm Spacing in Alloy S

Condition	Solution Time (h)	Artificial Aging Temperature (°C)	Artificial Aging Time (h)	Average SDAS (μm)
As-Cast	-	-	-	28.6
T4	4	-	-	33.3
	24	-	-	38.0
T6 (W)	4	180	2	22.4
			4	22.9
			12	25.6
			24	28.6
T6 (X)	4	220	2	29.5
			4	30.5
			12	34.3
			24	36.8
T6 (Y)	24	180	2	34.4
			4	36.8
			12	37.3
			24	37.6
T6 (Z)	24	220	2	54.3
			4	55.5
			12	55.5
			24	55.8

Table 4.3 – Secondary Dendrite Arm Spacing in Alloy M

Condition	Solution Time (h)	Artificial Aging Temperature (°C)	Artificial Aging Time (h)	Average SDAS (μm)
As-Cast	-	-	-	24.0
T4	4	-	-	28.2
	24	-	-	38.5
T6 (W)	4	180	2	29.9
			4	30.8
			12	33.4
			24	33.8
T6 (X)	4	220	2	33.7
			4	36.4
			12	37.2
			24	38.8
T6 (Y)	24	180	2	34.6
			4	37.7
			12	42.3
			24	46.8
T6 (Z)	24	220	2	36.9
			4	43.1
			12	43.4
			24	44.2

Table 4.4 – Secondary Dendrite Arm Spacing in Alloy MS

Condition	Solution Time (h)	Artificial Aging Temperature (°C)	Artificial Aging Time (h)	Average SDAS (μm)
As-Cast	-	-	-	28.0
T4	4	-	-	34.4
	24	-	-	39.4
T6 (W)	4	180	2	26.8
			4	28.9
			12	33.4
			24	35.3
T6 (X)	4	220	2	26.3
			4	31.5
			12	33.5
			24	36.5
T6 (Y)	24	180	2	38.5
			4	41.2
			12	42.9
			24	43.5
T6 (Z)	24	220	2	42.4
			4	42.3
			12	45.0
			24	49.8

4.1.3. Grain Size

The average grain sizes for the as-cast and heat-treated samples are given in Tables 4.5 to 4.8. Typical grain size micrographs are seen in Figures 4.6 to 4.9.

Table 4.5 – Grain Size Distribution in Alloy A

Condition	Solution Time (h)	Artificial Aging Temperature (°C)	Artificial Aging Time (h)	Average Grain Size (μm)	Grain Size Classification ASTM E112
As-Cast	-	-	-	391.5	Extra Fine
T4	4	-	-	374.5	Extra Fine
	24	-	-	423.3	Fine
T6 (W)	4	180	2	386.0	Fine
			4	515.8	Medium
			12	689.2	Large
			24	751.2	Large
T6 (X)	4	220	2	510.4	Medium
			4	650.4	Large
			12	680.8	Large
			24	785.2	Large
T6 (Y)	24	180	2	478.5	Medium
			4	654.0	Large
			12	698.4	Large
			24	812.3	Coarse
T6 (Z)	24	220	2	613.2	Large
			4	639.0	Large
			12	706.8	Large
			24	810.5	Coarse

Table 4.6 – Grain Size Distribution in Alloy S

Condition	Solution Time (h)	Artificial Aging Temperature (°C)	Artificial Aging Time (h)	Average Grain Size (μm)	Grain Size Classification ASTM E112
As-Cast	-	-	-	450.3	Medium
T4	4	-	-	465.4	Medium
	24	-	-	505.1	Medium
T6 (W)	4	180	2	417.8	Medium
			4	621.8	Large
			12	720.4	Large
			24	839.9	Coarse
T6 (X)	4	220	2	566.8	Medium
			4	663.6	Large
			12	847.1	Coarse
			24	867.5	Coarse
T6 (Y)	24	180	2	587.8	Medium
			4	677.8	Large
			12	720.4	Large
			24	839.9	Coarse
T6 (Z)	24	220	2	649.4	Large
			4	715.4	Large
			12	815.3	Coarse
			24	1524.8	ExtraCoarse

Table 4.7 – Grain Size Distribution in Alloy M

Condition	Solution Time (h)	Artificial Aging Temperature (°C)	Artificial Aging Time (h)	Average Grain Size (μm)	Grain Size Classification ASTM E112
As-Cast	-	-	-	363.3	Fine
T4	4	-	-	370.8	Fine
	24	-	-	480.0	Medium
T6 (W)	4	180	2	468.7	Medium
			4	480.0	Medium
			12	493.5	Medium
			24	520.8	Medium
T6 (X)	4	220	2	418.5	Medium
			4	484.3	Medium
			12	518.3	Medium
			24	539.3	Medium
T6 (Y)	24	180	2	419.3	Medium
			4	426.8	Medium
			12	457.5	Medium
			24	576.1	Medium
T6 (Z)	24	220	2	465.5	Medium
			4	474.8	Medium
			12	641.8	Large
			24	633.3	Large

Table 4.8 – Grain Size Distribution in Alloy MS

Condition	Solution Time (h)	Artificial Aging		Average Grain Size (μm)	Grain Size Classification ASTM E112
		Temperature (°C)	Time (h)		
As-Cast	-	-	-	443.0	Medium
T4	4	-	-	470.7	Medium
	24	-	-	515.1	Medium
T6 (W)	4	180	2	460.7	Medium
			4	535.9	Medium
			12	650.5	Large
			24	741.2	Large
T6 (X)	4	220	2	505.2	Medium
			4	655.2	Large
			12	690.3	Large
			24	764.3	Large
T6 (Y)	24	180	2	549.6	Medium
			4	594.7	Medium
			12	701.0	Large
			24	810.8	Coarse
T6 (Z)	24	220	2	620.1	Large
			4	654.4	Large
			12	717.8	Large
			24	825.0	Coarse

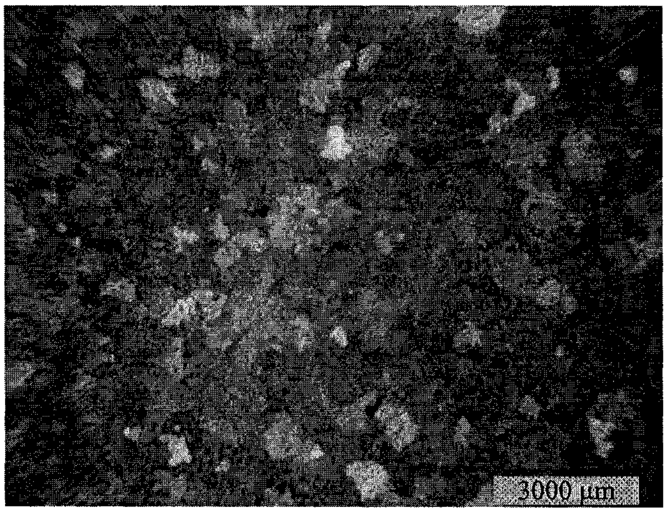

Figure 4.6 – Extra Fine Grain Size (382 µm) in Alloy A
(Solution Temperature 495 °C for 4 hours)

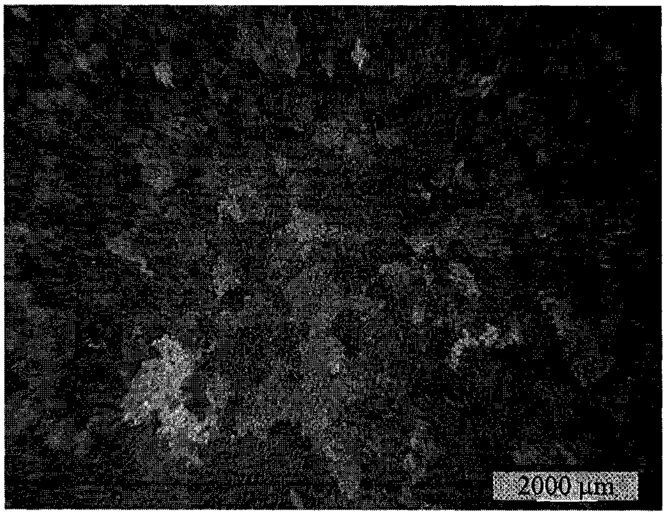

Figure 4.7 –Fine Grain Size (451 µm) in Alloy A
(Solution Temperature 495 °C for 4 hours – Aging Temperature 180 °C for 2 h)

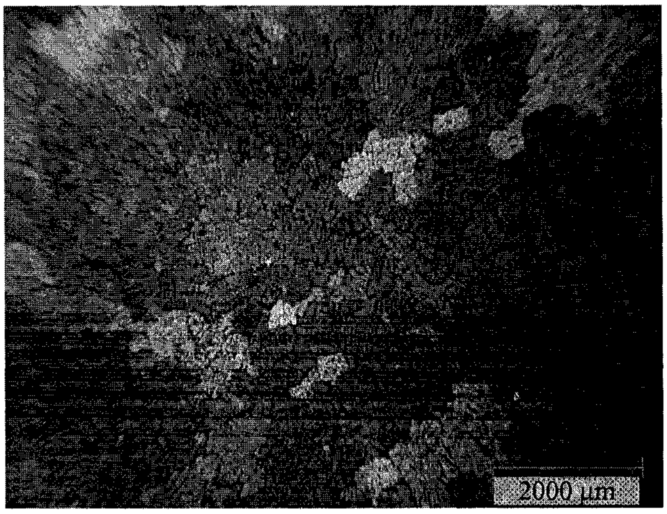

Figure 4.8 –Medium Grain Size (540 µm) in Alloy A
(Solution Temperature 495 °C for 4 hours – Aging Temperature 220 °C for 2 h)

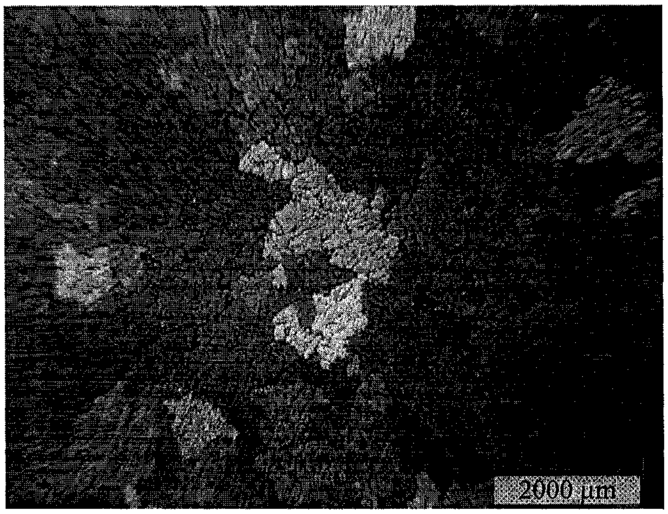

Figure 4.9 –Large Grain Size (812 µm) in Alloy A
(Solution Temperature 495 °C for 24 hours – Aging Temperature 180 °C for 24 h)

4.2. Mechanical Properties

4.2.1. Casting Soundness

Radiography was used to detect the presence of defects in the tensile bars. The samples were X-rayed and the films were examined in order to facilitate the selection of sound castings. The bottom grips of the tensile bars often exhibited defects associated with shrinkage. Nevertheless, the most important part of the test bars was the gage length and the selection of the sound samples was done based on the soundness of this section. This portion of the samples was examined carefully for any variation in the density of the X-ray film which indicated the presence of flaws such as porosity or inclusions.

Figures 4.10 and 4.11 show some X-rays of unmodified and Sr-modified tensile bars. The defects in the unmodified test bars (Figure 4.10) were very localized and well defined. Sr modification caused an increase in the defects detected, as well as changes in their shape and size (Figure 4.11).

For each alloy composition, all test bars were X-ray examined to determine the type and intensity of casting/solidification defects. Most of the test bars were sound with negligible gas porosity (rated "slight" according to ASTM standards).

4.2.2. Hardness

Coupons were taken from the Stahl mold bars prepared from each alloy melt composition. For each heat treatment condition (i.e. aging temperature), sixty-five coupons were used (five samples x 13 different aging times). Hardness and microhardness measurements were taken from samples in the as-cast condition, as well as in the T4 and T6 conditions.

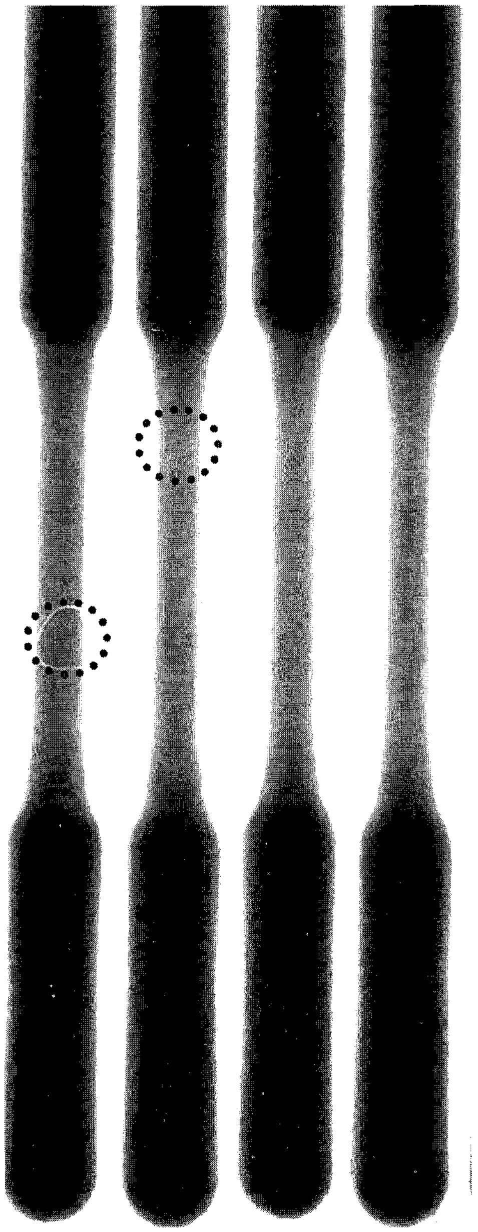

Figure 4.10 –Radiograph of Some Unmodified Tensile Bars
In Red Dotted Circles Defects are Shown

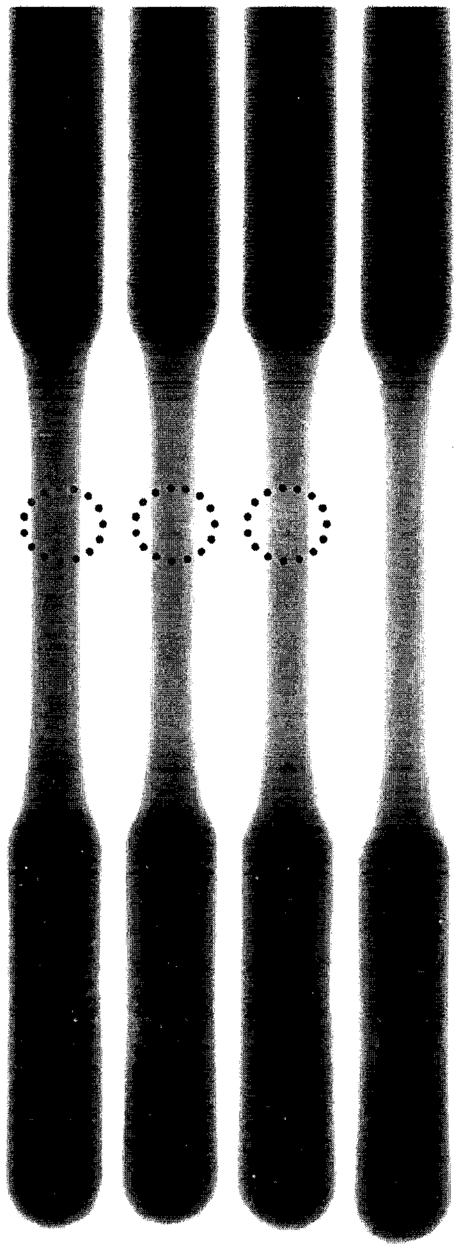

Figure 4.11 –Radiograph of Some Modified Tensile Bars
In Red Dotted Circles Defects are Shown

The results for the as-cast and T4 measurements with the corresponding standard deviations are shown in Figures 4.12 and 4.13. The hardness results of the heat-treated coupons can be seen in Figures 4.14 to 4.17. The modified high Mg alloy apparently displays slightly lower hardness parameters compared to those obtained from the high Mg alloy, but the consistency in the data is better.

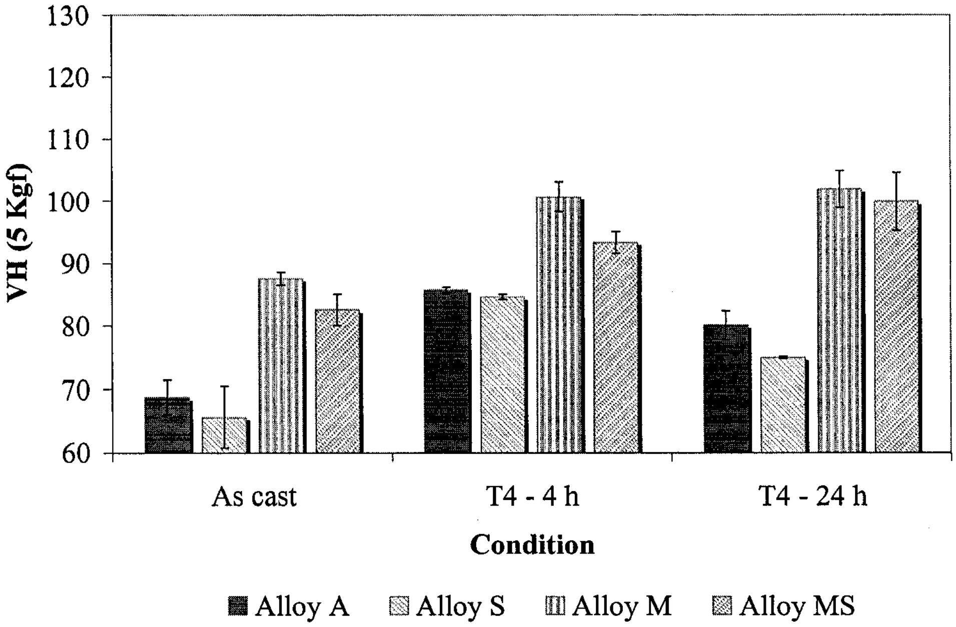

Figure 4.12 – Vickers Hardness Obtained from the Coupons in the As-Cast and T4 Condition

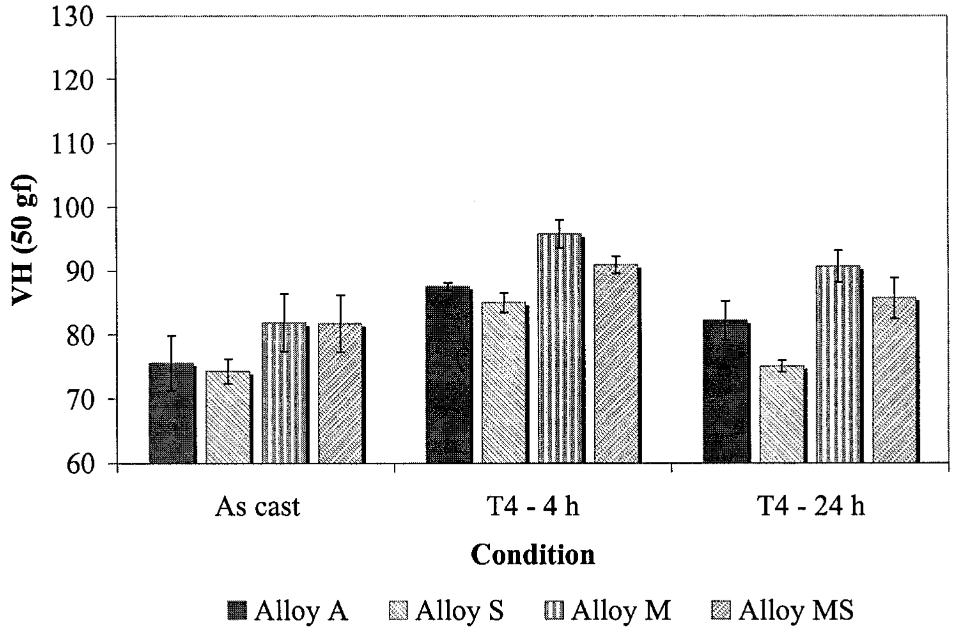

Figure 4.13 – Microhardness Obtained from the Coupons in the As-Cast and T4 Condition

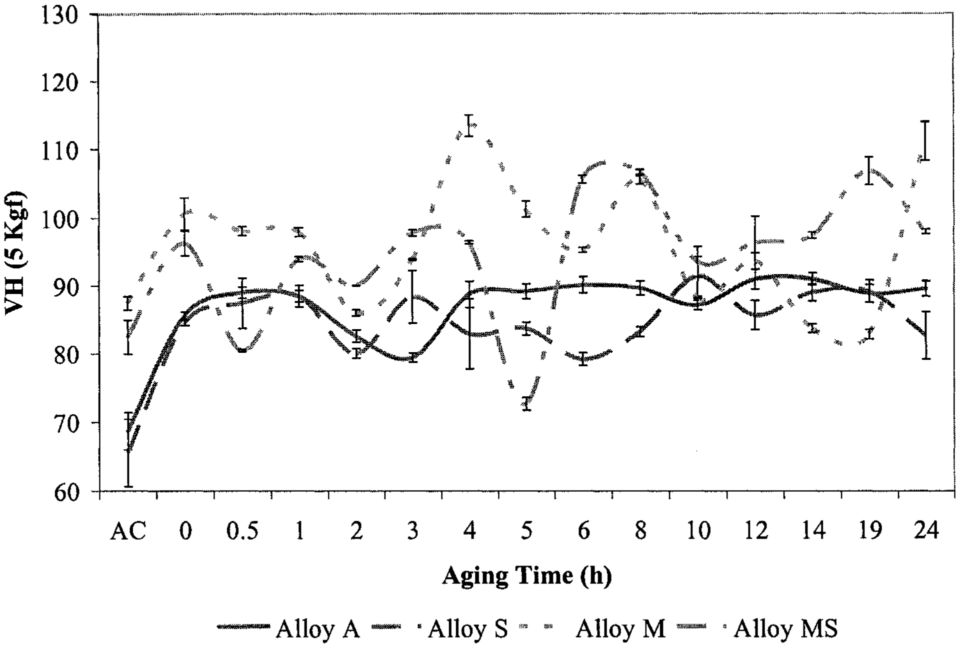

Figure 4.14 – Vickers Hardness Obtained from the Coupons
(Solution Temperature 495 °C for 4 hours – Aging Temperature 180 °C)

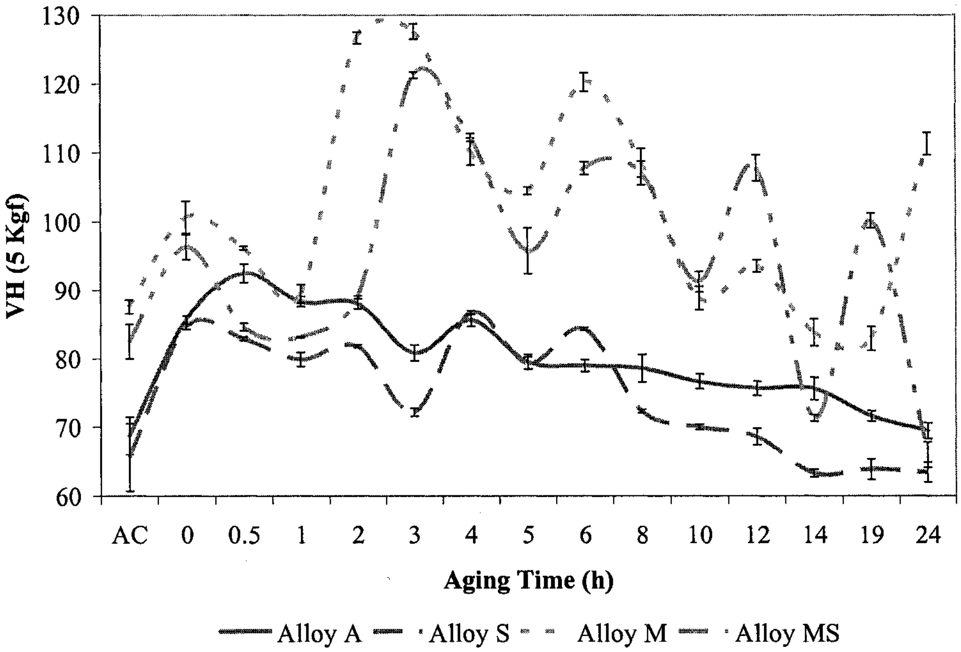

Figure 4.15 – Vickers Hardness Obtained from the Coupons
(Solution Temperature 495 °C for 4 hours – Aging Temperature 220 °C)

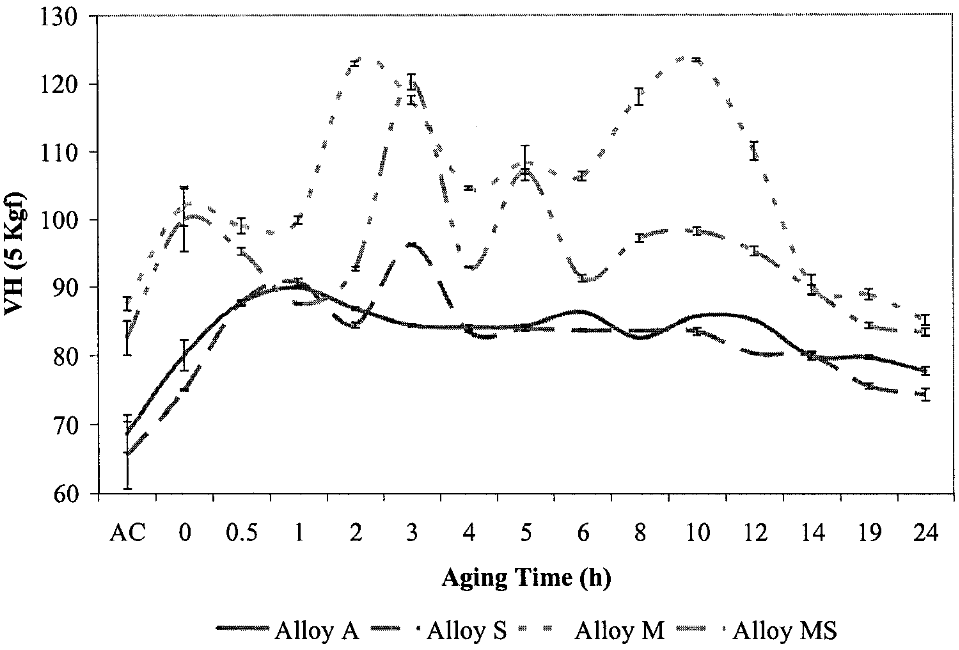

Figure 4.16 – Vickers Hardness Obtained from the Coupons
(Solution Temperature 495 °C for 24 hours – Aging Temperature 180 °C)

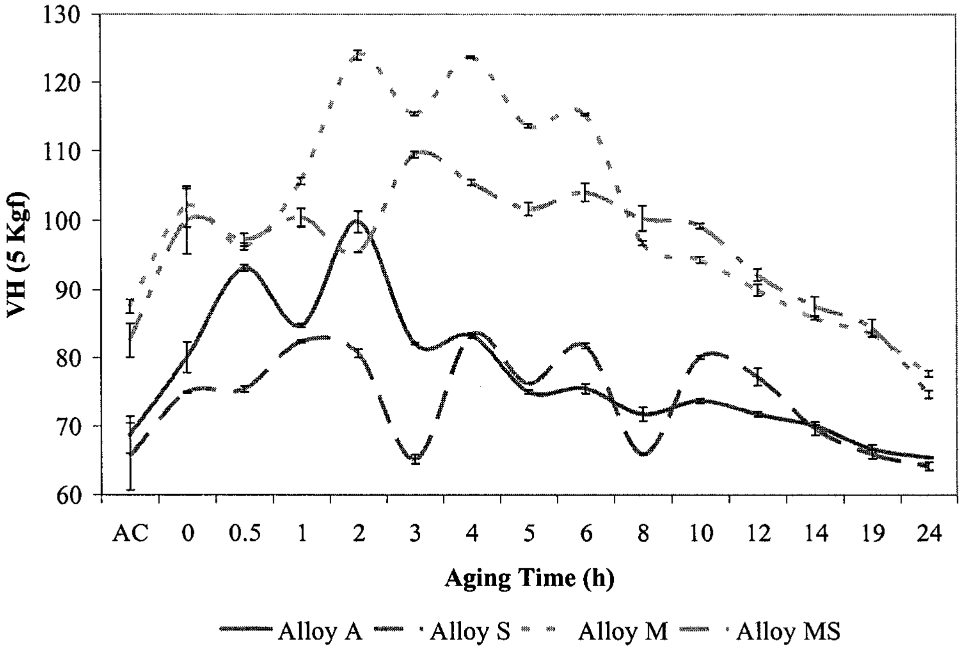

Figure 4.17 – Vickers Hardness Obtained from the Coupons
(Solution Temperature 495 °C for 24 hours – Aging Temperature 220 °C)

In order to determine more precisely the effectiveness of aging temperature and time on the hardness of alloy M with Mg additions (high Mg content, high volume fraction of intermetallics) 15 coupons were treated similarly (i.e. same solution heat treatment conditions and aging times). Table 4.9 shows the results obtained. Prolonged aging treatment at 220 °C brought about significant changes in hardness. When the aging treatment temperature is raised from 210 to 220 °C, a remarkable aging response is exhibited by the unmodified high Mg-containing alloys.

Table 4.9 – Effect of Aging Temperature on the Hardness Measurements of the Alloy M Solution Treated at 495 °C for 4 h and with 2 h of Aging Time

Condition	Aging Temperature (°C)	Microhardness (50 gf)	Macrohardness (5 Kgf)
As-Cast	---	81.9 ± 4.5	87.5 ± 1.0
T4 – 4 h	---	95.8 ± 2.2	100.7 ± 2.4
T6	180	110.5 ± 4.0	86.1 ± 0.4
	210	115.2 ± 0.8	137.5 ± 3.1
	215	121.2 ± 0.1	124.0 ± 2.2
	220	116.9 ± 1.2	126.7 ± 0.8

4.2.3. Tensile Properties

Figure 4.18 and 4.19 show the effect of solution time and aging temperature on hardness and tensile properties for samples solutionized at 495 °C and aged at different times. It can be seen that there is an obvious age-hardening phenomenon for each curve. However, other small hardening peaks were observed following the first one in the age-hardening curves (180 °C and 220 °C). At an intermediate stage of aging, after a small decrease the strength increases again and reaches subsequent peaks. At the final stage of aging, the hardening of the alloys decreases as a result of over-aging, except for unmodified high Mg alloys.

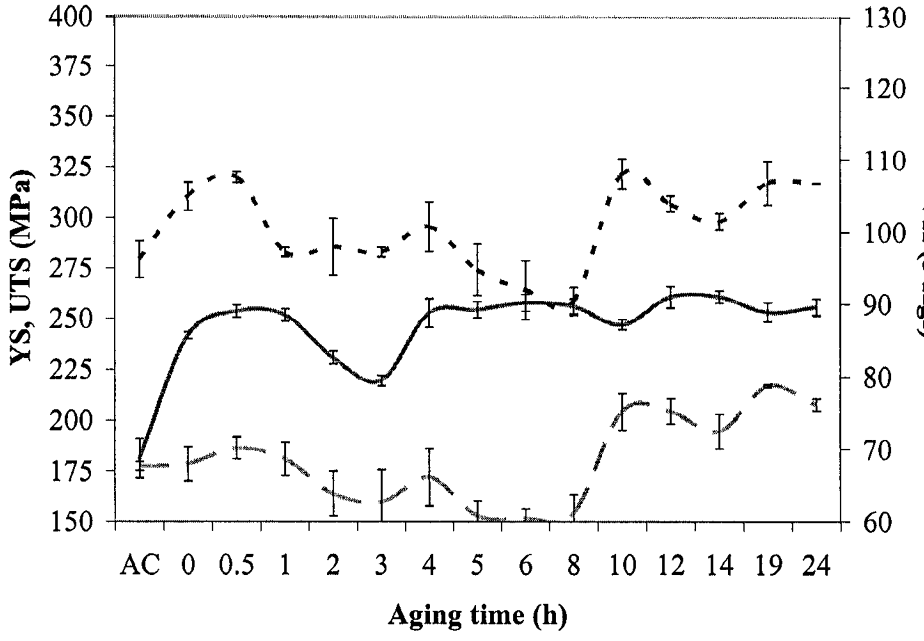

(a) Alloy A (A319.2)

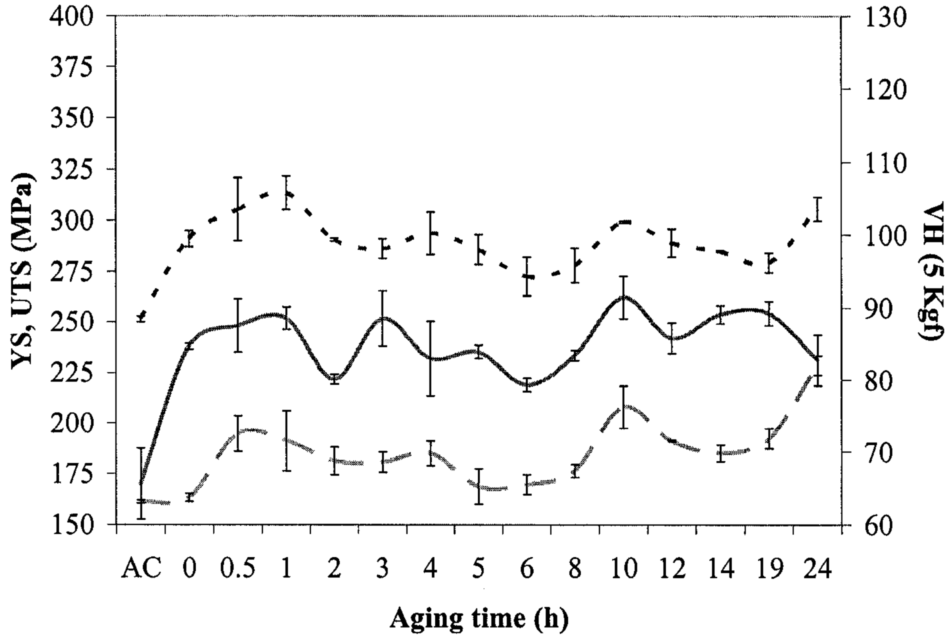

(b) Alloy S (A319.2 + 160 ppm Sr)

Figure 4.18 – Tensile Properties and Vickers Hardness (VH) Obtained from the Heat-Treated Samples (Solution Temperature 495 °C for 4 h – Aging Temperature 180 °C) (Continued)

- - - - UTS ——— VH — — — YS

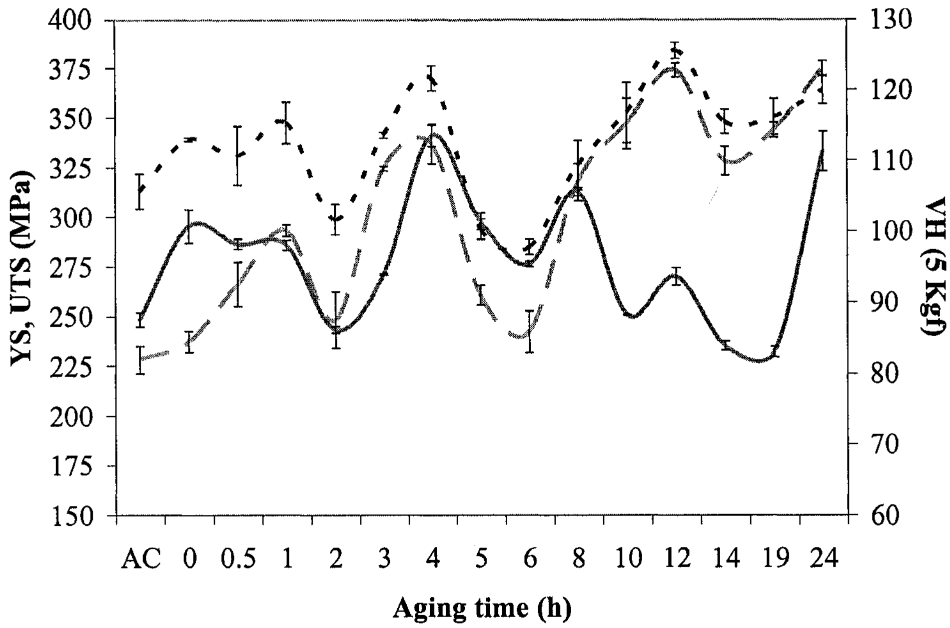

(c) Alloy M (A319.2 + 0.40% Mg)

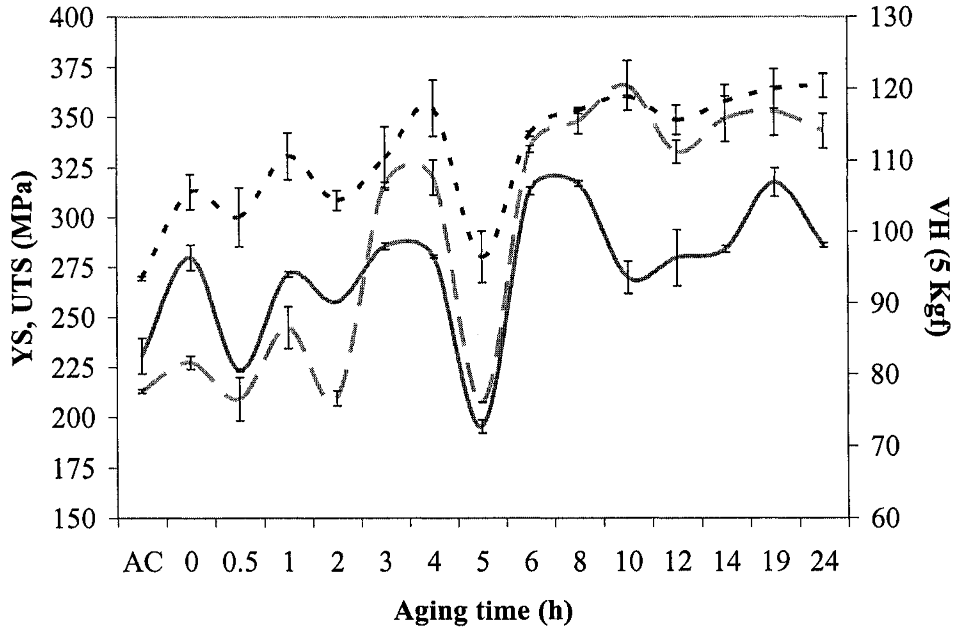

(d) Alloy MS (A319.2 + 0.40% Mg + 160 ppm Sr)

Figure 4.18 – (Continued)

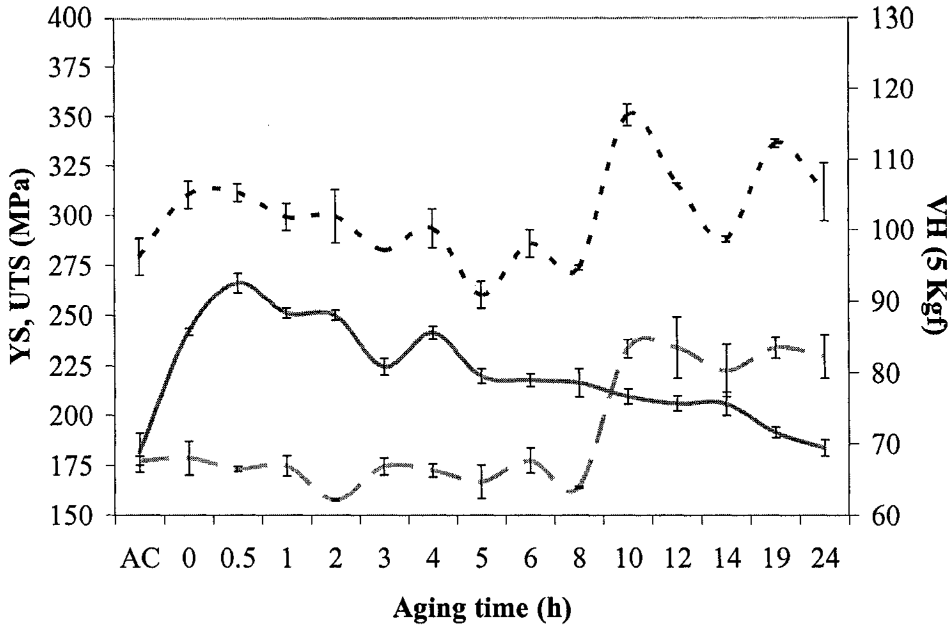

(a) Alloy A (A319.2)

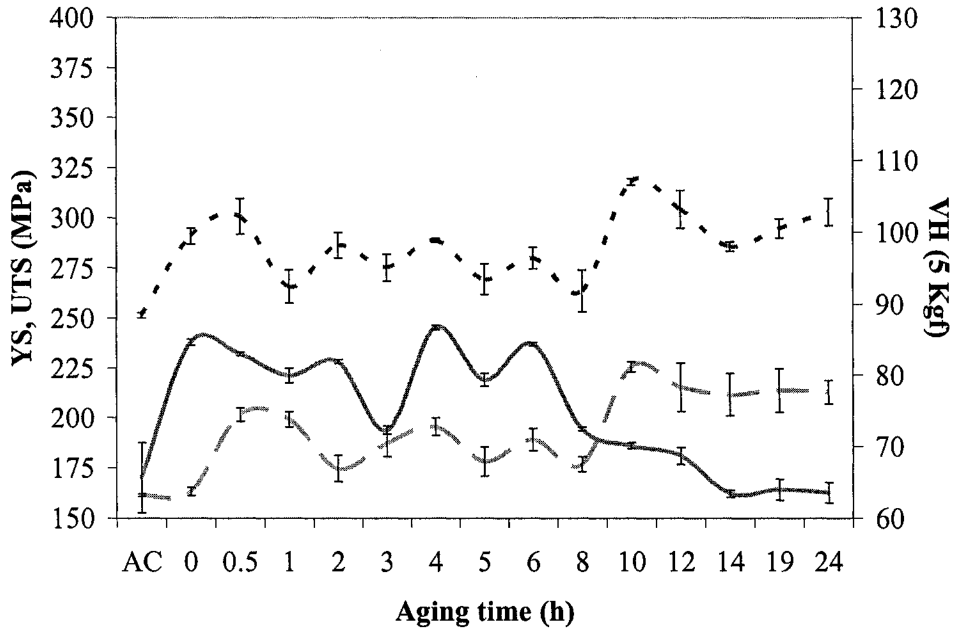

(b) Alloy S (A319.2 + 160 ppm Sr)

Figure 4.19 – Tensile Properties and Vickers Hardness (VH) Obtained from the Heat-Treated Samples (Solution Temperature 495 °C for 4 h – Aging Temperature 220 °C) (Continued)

- - - - UTS —— VH — — — YS

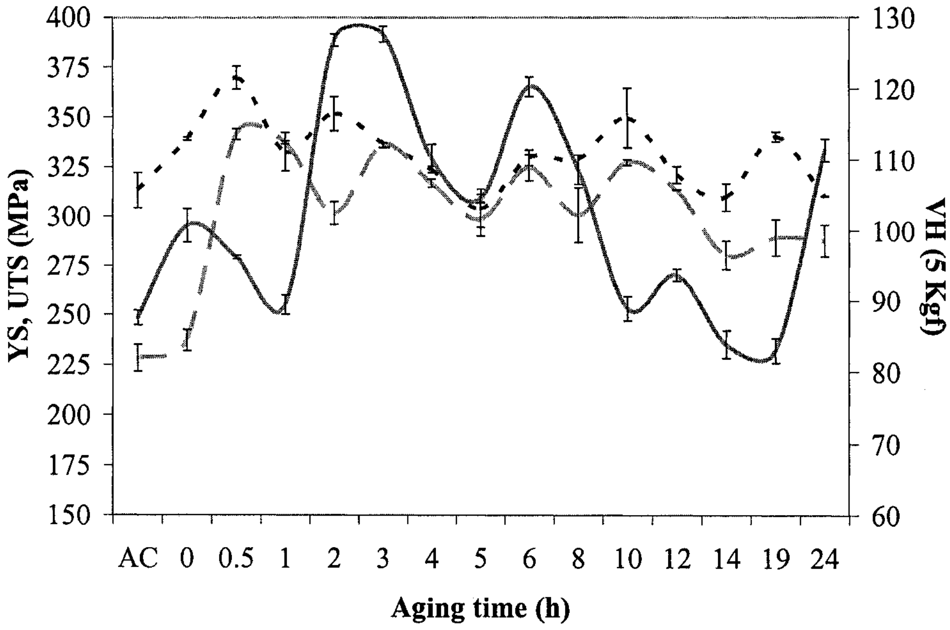

(c) Alloy M (A319.2 + 0.40% Mg)

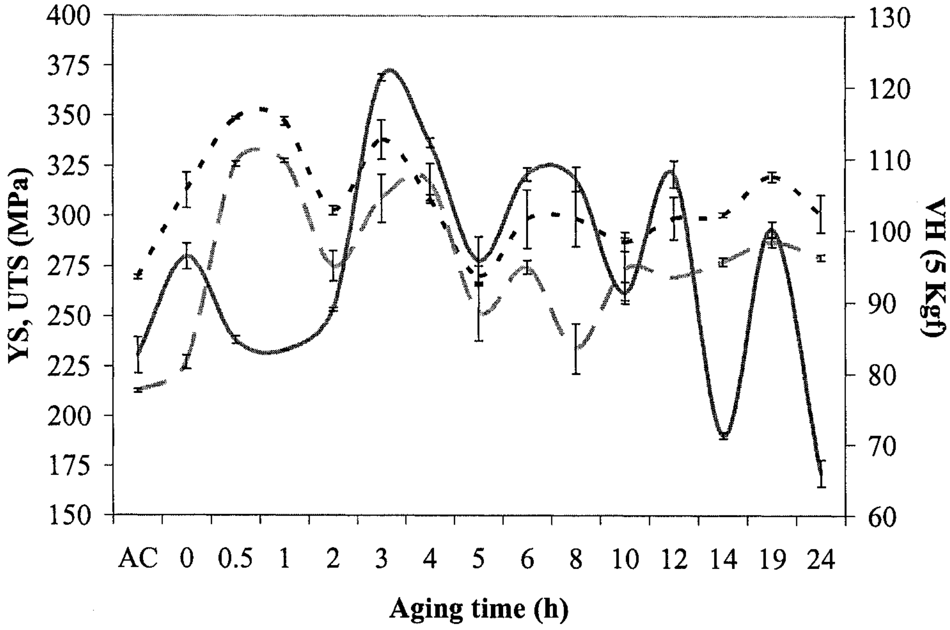

(d) Alloy MS (A319.2 + 0.40% Mg + 160 ppm Sr)

Figure 4.19 – (Continued)

- - - - UTS —— VH — — – YS

CHAPTER 5

ELECTRON MICROSCOPY RESULTS

Electron microscopy was used to analyze the microstructure, chemistry and crystal structure of precipitates from areas smaller than 1 μm. The use of electron microscopy techniques had the objective of presenting a better understanding of the precipitation process as a function of the composition and heat treatment of A319.2 alloys.

In this chapter, electron microscopy results are presented. Microstructures related to the mechanical tests are introduced. The results are divided into two different areas:

- Electron probe microanalyzer (EPMA)
- Transmission electron microscopy

Due to the very large number of samples and conditions investigated, only selected photographs are shown.

5.1. Electron Probe Microanalyzer (EPMA) Results

In Figure 5.1, the Cu concentration is a minimum (1.09 wt %) near the center of the dendrites (point C), whereas the Cu concentration increases to 2.5-3.7 wt % at the edges of the dendrites (point B and A, respectively). The Cu concentration in the matrix around the $CuAl_2$ particles is ~4 wt % after 4 h solution treatment, which is higher than the Cu concentration (~ 3.5 wt %) in the aluminium matrix after 24 h solution heat treatment.

Li et al. [91-93] have reported a Cu concentration of ~2 wt % after 100 h solution heat treatment. The Cu atoms diffuse in the matrix far away from the remaining $CuAl_2$ during the solution heat treatment.

The distribution of various elements within the aluminium dendrites was determined by performing quantitative point analysis using WDS (Table 5.1).

The effect of solution treatment time and aging temperature on the element content at the centers of dendrites for alloys M and MS is summarized in Table 5.2. The error represents the range of element concentrations due to microsegregation.

The line scans corresponding to alloy M in the as-cast and following 4 h and 24 h solution heat treatment times are presented in Figure 5.2 a-c. Note that after 24 h solution heat treatment in high Mg content samples, $CuAl_2$ phase was very small and dispersed, thus it is was undetectable by the electron beam.

The line scans for alloy MS are shown in Figure 5.3 a-c. These scans reveal the concentration gradients of Cu and Mg across the area containing the Cu and Mg phase particles, respectively.

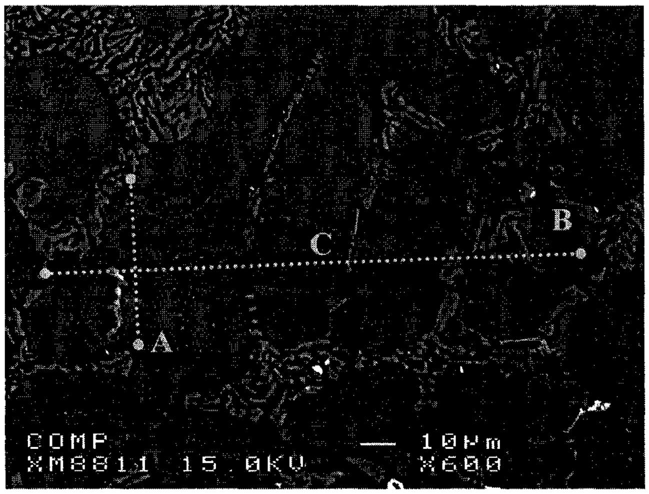

Figure 5.1 – Backscattered Image of Alloy MS in the As-Cast Condition, Showing the Locations of the Quantitative Line Scans Along the Major and Minor Axes of Dendrites. Cu Concentration is a Minimum (0.9 wt %) in Point C, whereas Cu Concentration Increases at the Edges of the Dendrites (2.5-3.7 wt %) in Point B and A, Respectively

Table 5.1 – Element Concentration in the Matrix

Alloy	Solution Time (h)	Cu (wt %)	Mg (wt %)	Si (wt %)
M (A319.2+0.4 %Mg)	0	0.95 ± 0.09	0.15 ± 0.02	1.17 ± 0.03
	4	3.84 ± 0.17	0.34 ± 0.01	0.84 ± 0.05
	24	3.76 ± 0.08	0.32 ± 0.01	0.81 ± 0.05
MS (A319.2+0.4 %Mg + 160 ppm Sr)	0	0.91 ± 0.09	0.22 ± 0.02	1.19 ± 0.07
	4	3.77 ± 0.29	0.34 ± 0.02	0.89 ± 0.06
	24	3.62 ± 0.20	0.33 ± 0.01	0.88 ± 0.04

Table 5.2 – Effect of Solution Treatment Time at 495 °C on the Dendrite Element Concentration*

Alloy	Solution Time (h)	Aging Temperature (°C)	Cu (wt %)	Mg (wt %)	Si (wt %)
M (A319.2 + 0.4%Mg)	4	180	3.19 ± 0.18	0.23 ± 0.02	0.56 ± 0.07
		220	4.37 ± 0.15	0.33 ± 0.02	0.89 ± 0.06
	24	180	4.25 ± 0.18	0.37 ± 0.01	1.15 ± 0.10
		220	4.20 ± 0.17	0.30 ± 0.01	0.87 ± 0.11
MS (A319.2 + 0.4%Mg + 160 ppm Sr)	4	180	3.81 ± 0.19	0.41 ± 0.08	0.81 ± 0.04
		220	2.65 ± 0.13	0.32 ± 0.10	0.62 ± 0.13
	24	180	3.62 ± 0.11	0.37 ± 0.06	0.71 ± 0.05
		220	3.44 ± 0.12	0.58 ± 0.27	1.03 ± 0.25

* After Artificially Aged for 4 h

In modified high-Mg alloys, there is a segregation of both $Al_5Mg_8Si_6Cu_2$ and $CuAl_2$ phase particles in areas away from the advancing interfaces of the eutectic silicon colonies (Figure 5.4). As a result of such segregation, $CuAl_2$ is mostly in the form of blocky phase, which makes their dissolution in the aluminium matrix during solution treatment very slow (Figure 5.5).

A general view of the microstructure of alloy MS (0.40 wt % Mg + 160 ppm Sr) is seen in Figure 5.6 in the as-cast and T4 conditions. After 24 h of solution treatment at 495 °C, there is an achievement of almost complete dissolution of the $CuAl_2$ phase, although a few particles are still observed in the matrix.

Figure 5.7a, shows the backscattered image of Alloy MS in the as-cast condition obtained from the X-ray image of Figure 5.5d. The EDX spectra of the corresponding phases are shown in Figure 5.7b to 5.7d. Figure 5.8a and 5.9a show the backscattered image of Alloy MS in the T4 conditions obtained from the X-ray images of Figure 5.5e and 5.5f respectively. The EDX spectra of the corresponding phases are shown in Figure 5.8b and 5.8c and Figure 5.9b and 5.9c.

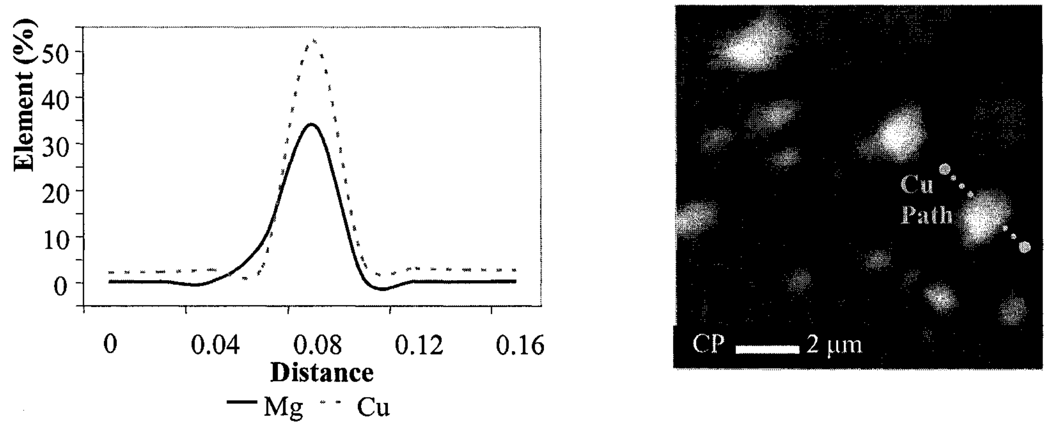

(a) As-Cast

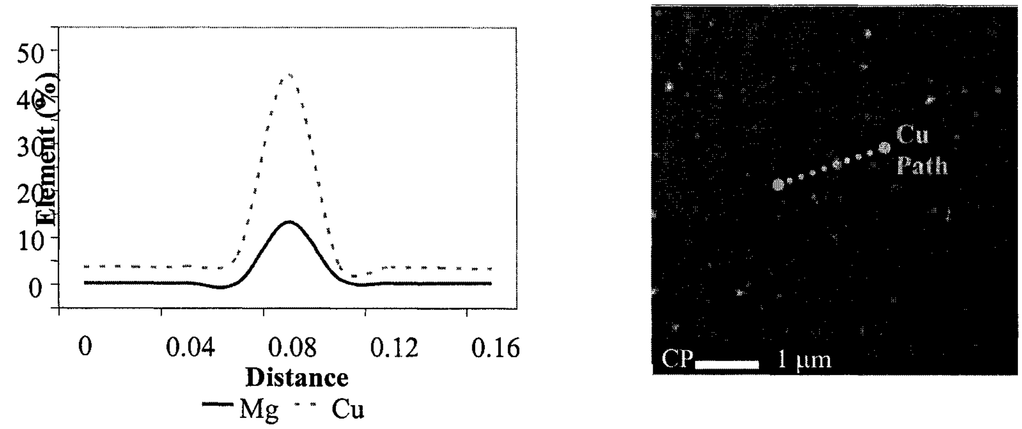

(b) After 4 h Solution Heat Treatment

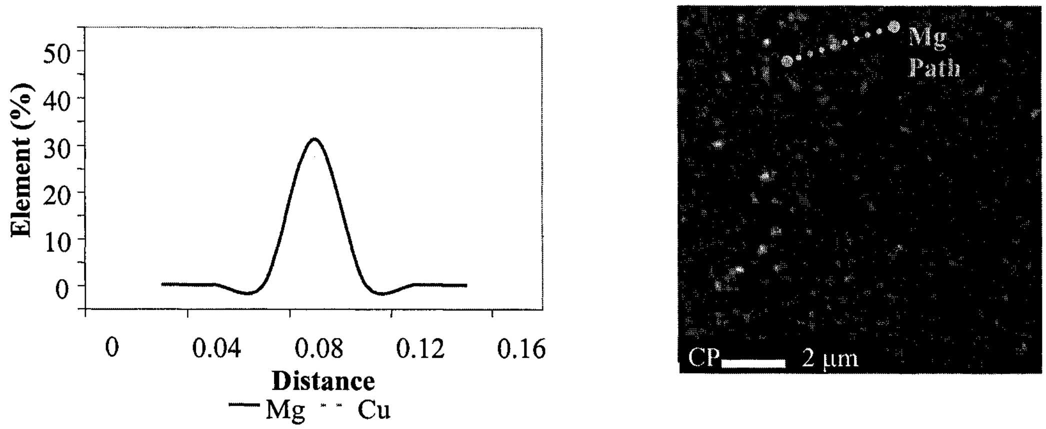

(c) After 24 h Solution Heat Treatment

Figure 5.2 – Concentration Profile Along the Path Shown in the Figure at the Right in Alloy M of Cu and Mg in $CuAl_2$ and $Al_5Mg_8Si_6Cu_2$ Particles Respectively

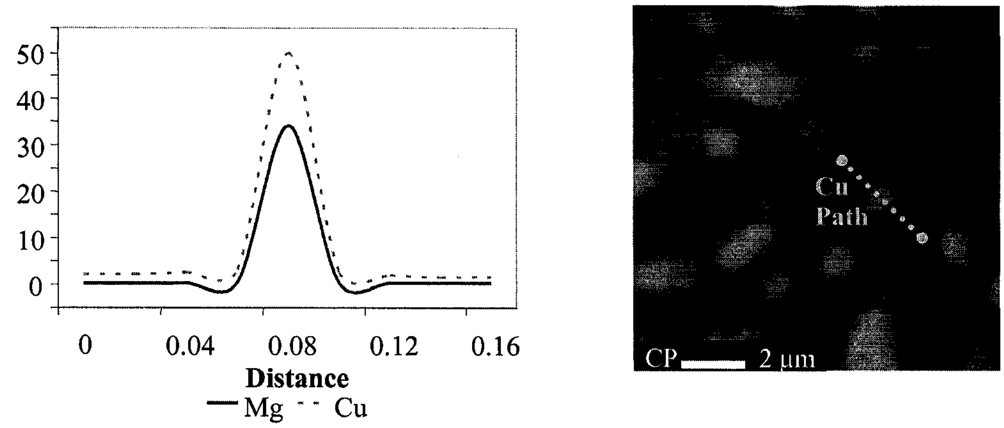

1

(a) As-Cast

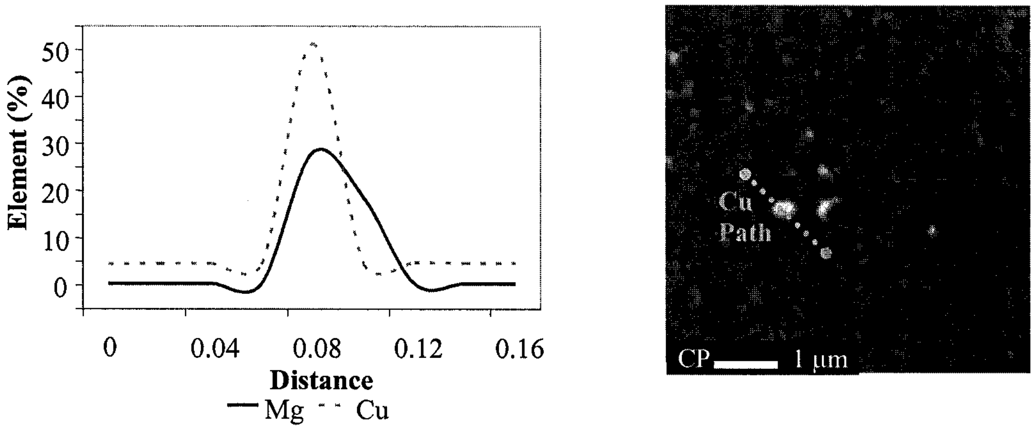

(b) After 4 h Solution Heat Treatment

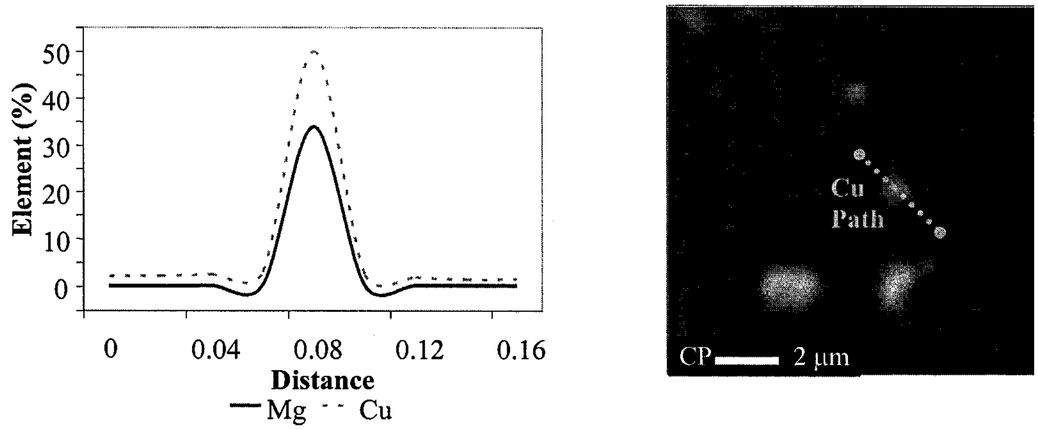

(c) After 24 h Solution Heat Treatment

Figure 5.3 – Concentration Profile Along the Path AB Shown in the Figure at the Right in Alloy MS of Cu and Mg in $CuAl_2$ and $Al_5Mg_8Si_6Cu_2$ Particles Respectively

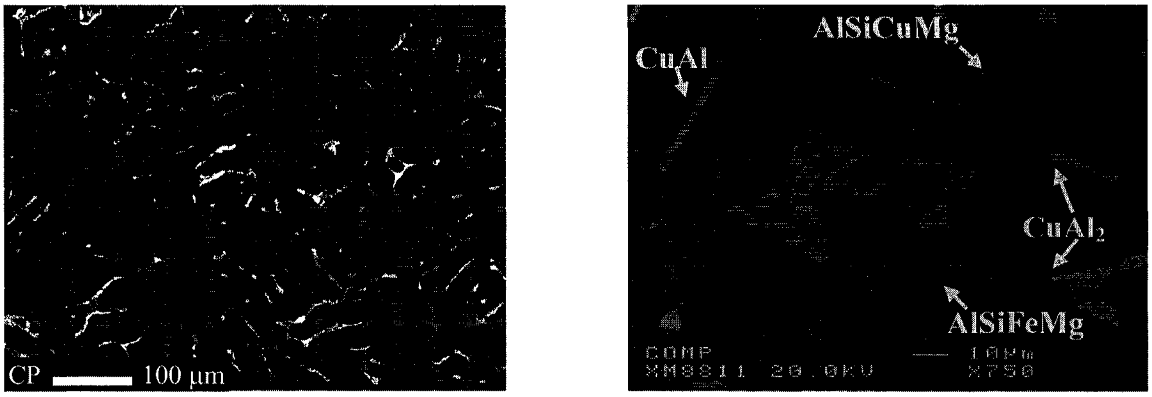

(a) (b) Backscattered Image

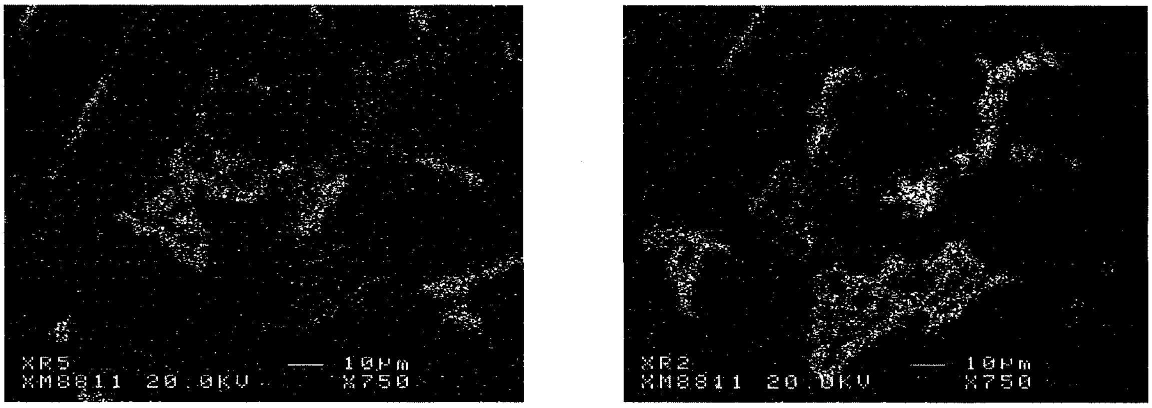

(c) Cu (d) Mg

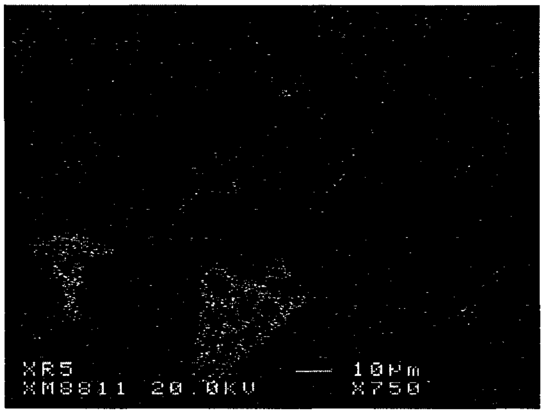

(e) Fe

Figure 5.4 – Alloy MS in the As-Cast Condition, Showing:

(a) Segregation of $Al_5Mg_8Si_6Cu_2$ and $CuAl_2$,
(b) Backscattered Image of Blocky Copper Phase ($CuAl_2$)
(c, d, e) X-Ray Images Showing Cu, Mg and Fe Distributions Respectively

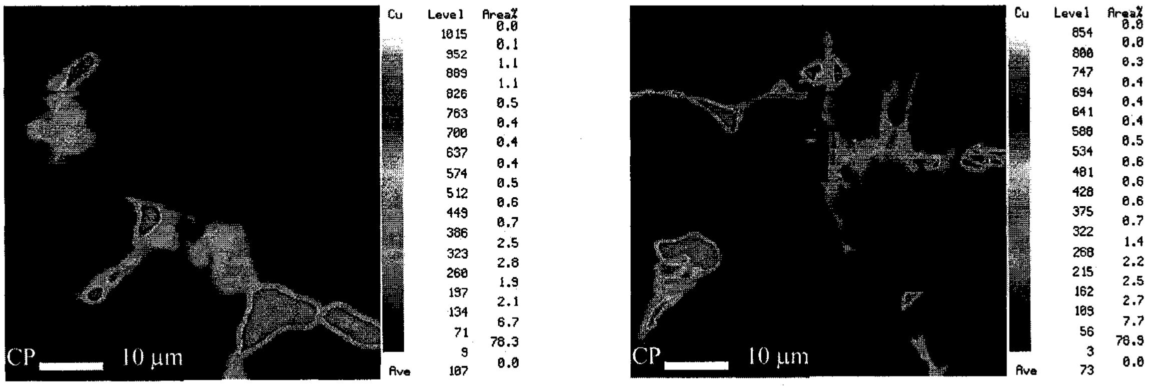

(a) 0 h (d) 0 h

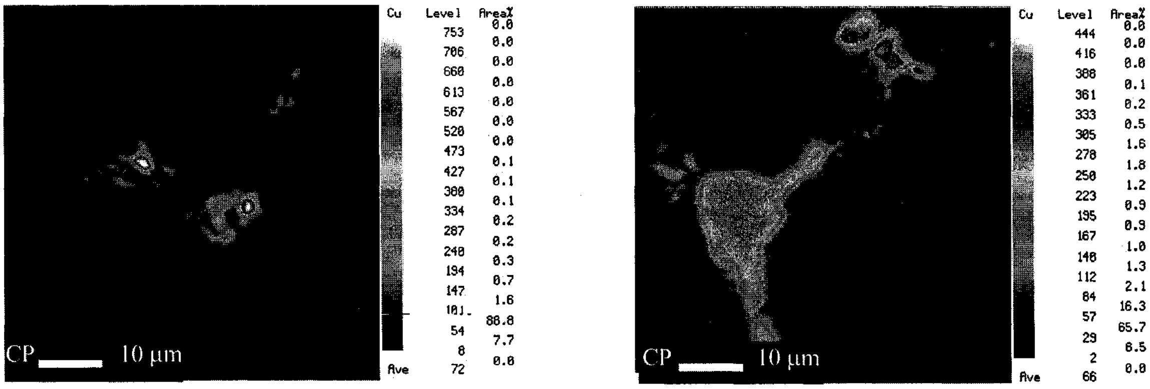

(b) 4 h (e) 4 h

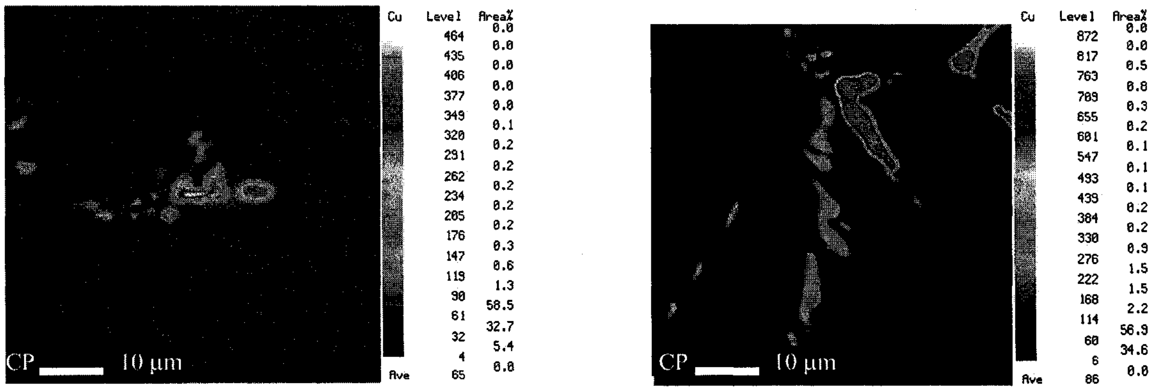

(c) 24 h (f) 24 h

Figure 5.5 – Comparison Between X-Ray Images of Cu at Solution Temperature at 495 °C in: (a-c) Alloy M and (d-f) Alloy MS

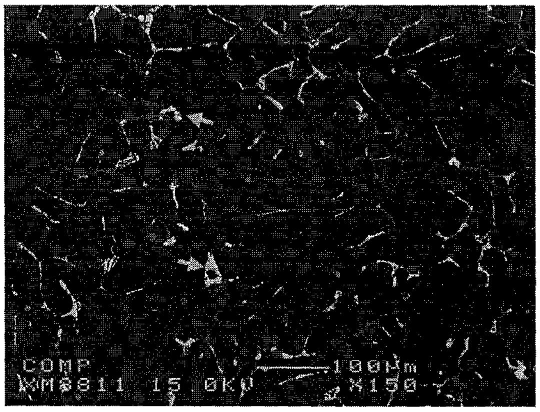

(a) 0 h

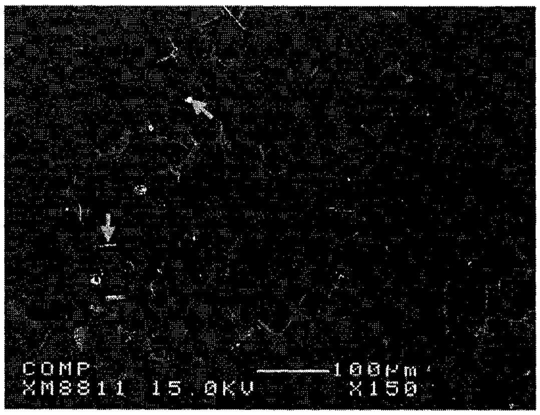

(b) 4 h

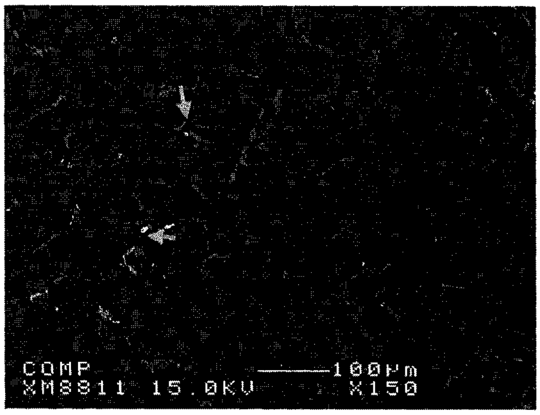

(c) 24 h

Figure 5.6 – Backscattered Image Taken From Alloy MS Showing Segregation of $Al_5Mg_8Si_6Cu_2$ (Red Arrowed) and $CuAl_2$ (Yellow Arrowed) due to Modification: (a) As-Cast, (b) After 4 h Solution Heat Treatment at 495 °C, (c) After 24 h Solution Heat Treatment at 495 °C

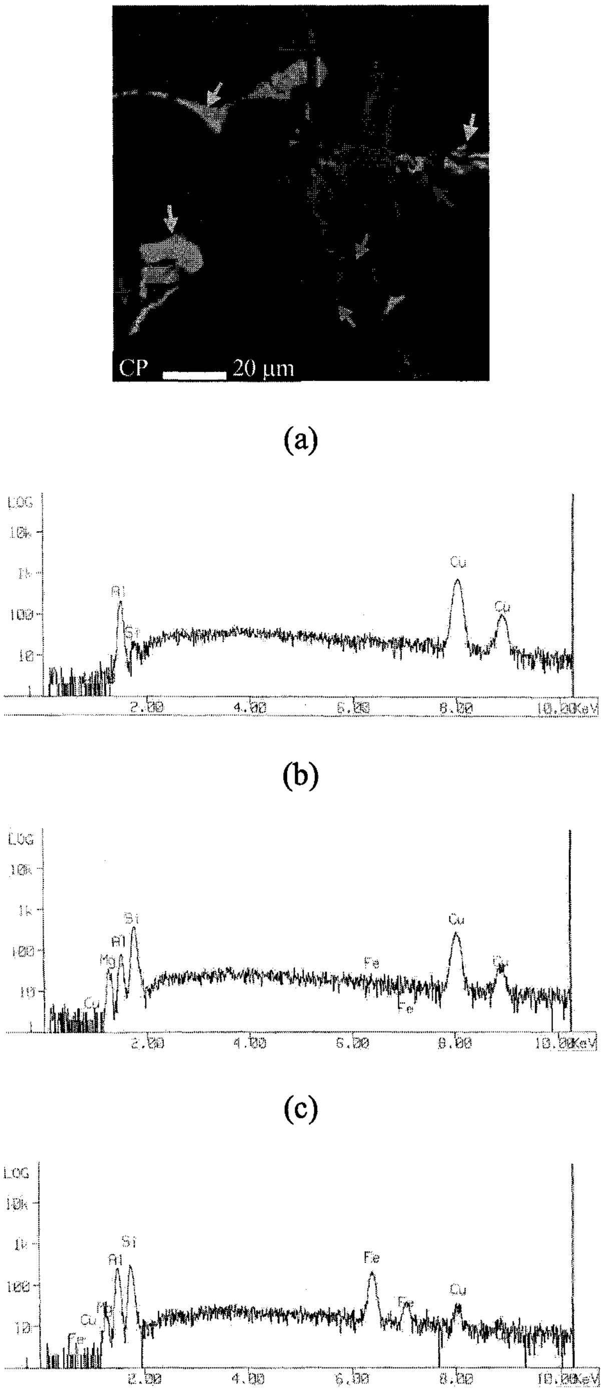

(a)

(b)

(c)

(d)

Figure 5.7 – Alloy MS in the As-Cast Condition, Showing:

(a) Backscattered Image of Precipitates Present,
(b, c, d) EDX Spectra Corresponding to $CuAl_2$ (Yellow Arrowed),
$Al_5Mg_8Si_6Cu_2$ (Red Arrowed) and AlMgSiFeCu (Green Arrowed) Respectively

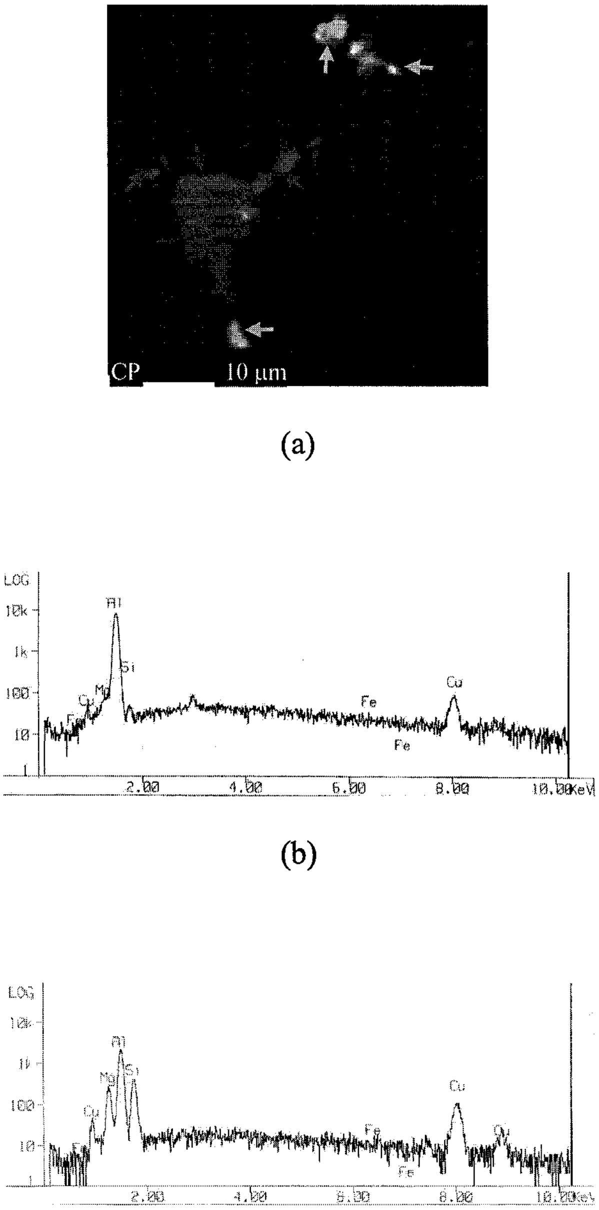

(a)

(b)

(c)

Figure 5.8 – Alloy MS After 4 h Solution Heat Treatment at 495 °C, Showing:

(a) Backscattered Image of Precipitates Present,
(b, c) EDX Spectra Corresponding to $CuAl_2$ (Yellow Arrowed) and $Al_5Mg_8Si_6Cu_2$ (Red Arrowed) Respectively

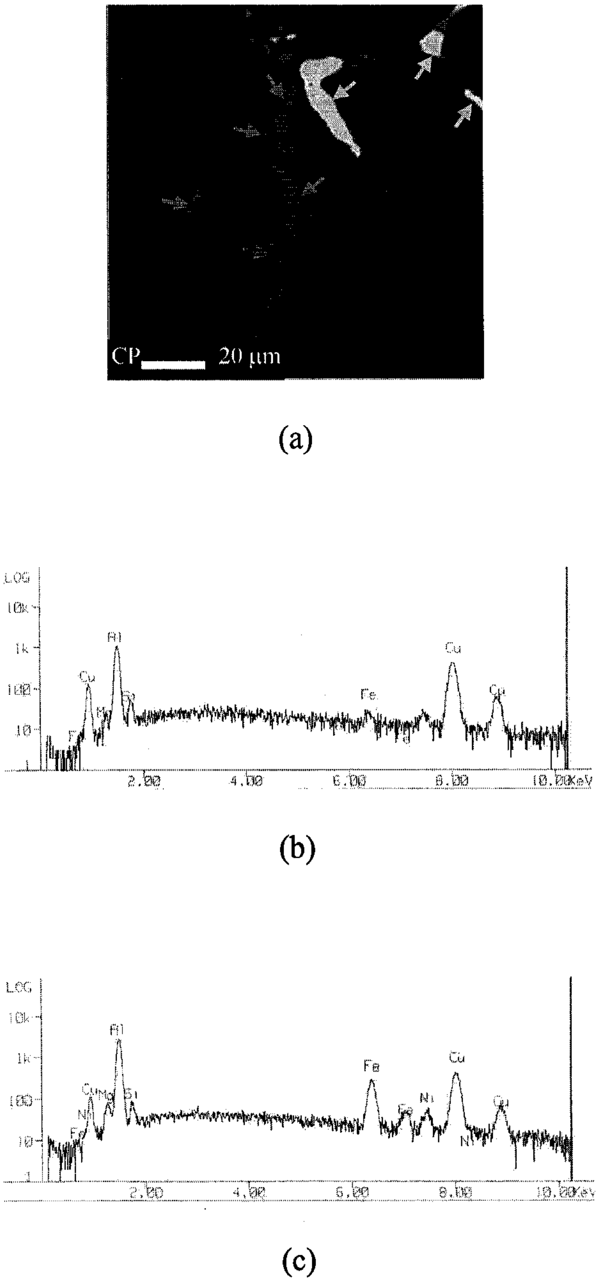

Figure 5.9 – Alloy MS After 24 h Solution Heat Treatment at 495 °C, Showing:

(a) Backscattered Image of Precipitates Present,
(b, c) EDX Spectra Corresponding to $CuAl_2$ (Yellow Arrowed) and AlMgSiFeCu (Green Arrowed) Respectively

The Cu concentration in the $CuAl_2$ phase remains stable during the dissolution, as can be seen in Table 5.3.

Table 5.3 – Volume Fractions of Cu and Elements (Mg, Fe, Si, Cu), as a Function of Alloy Compositions and Solution Treatment Time

Alloy	Solution Time (h)	Elements (wt %)	Cu (wt %)
M (A319.2 + 0.4%Mg)	0	3.85 ± 0.34	2.6 ± 0.65
	4	1.16 ± 0.28	0.28 ± 0.08
	24	1.11 ± 0.24	0.36 ± 0.11
MS (A319.2 + 0.4%Mg + 160 ppm Sr)	0	3.76 ± 0.79	2.33 ± 0.50
	4	2.08 ± 0.33	0.30 ± 0.09
	24	2.29 ± 0.56	0.32 ± 0.10

During aging, co-precipitation of second particles (mainly Cu~ and Mg~ rich phases) takes place. Figure 5.10 and 5.11 shows the backscattered images of alloy MS under different heat treatments. At high magnification, it clearly shows that samples aged at higher temperatures have coarser precipitates independent of solution times.

The wavelength-dispersive X-ray maps showing the Al, Si, Cu, Mg and Fe distributions taken from the polished surfaces of the heat treated samples corresponding to the alloy M are shown in Figures 5.12 to 5.15. From the figures, it can be seen that higher aging temperatures promotes higher amounts of $CuAl_2$ and $Al_5Mg_8Si_6Cu_2$ precipitation. For alloys MS, the wavelength-dispersive X-ray maps are represented in Figures 5.16 to 5.19. The artificial aging time for both alloys was constant at 4h.

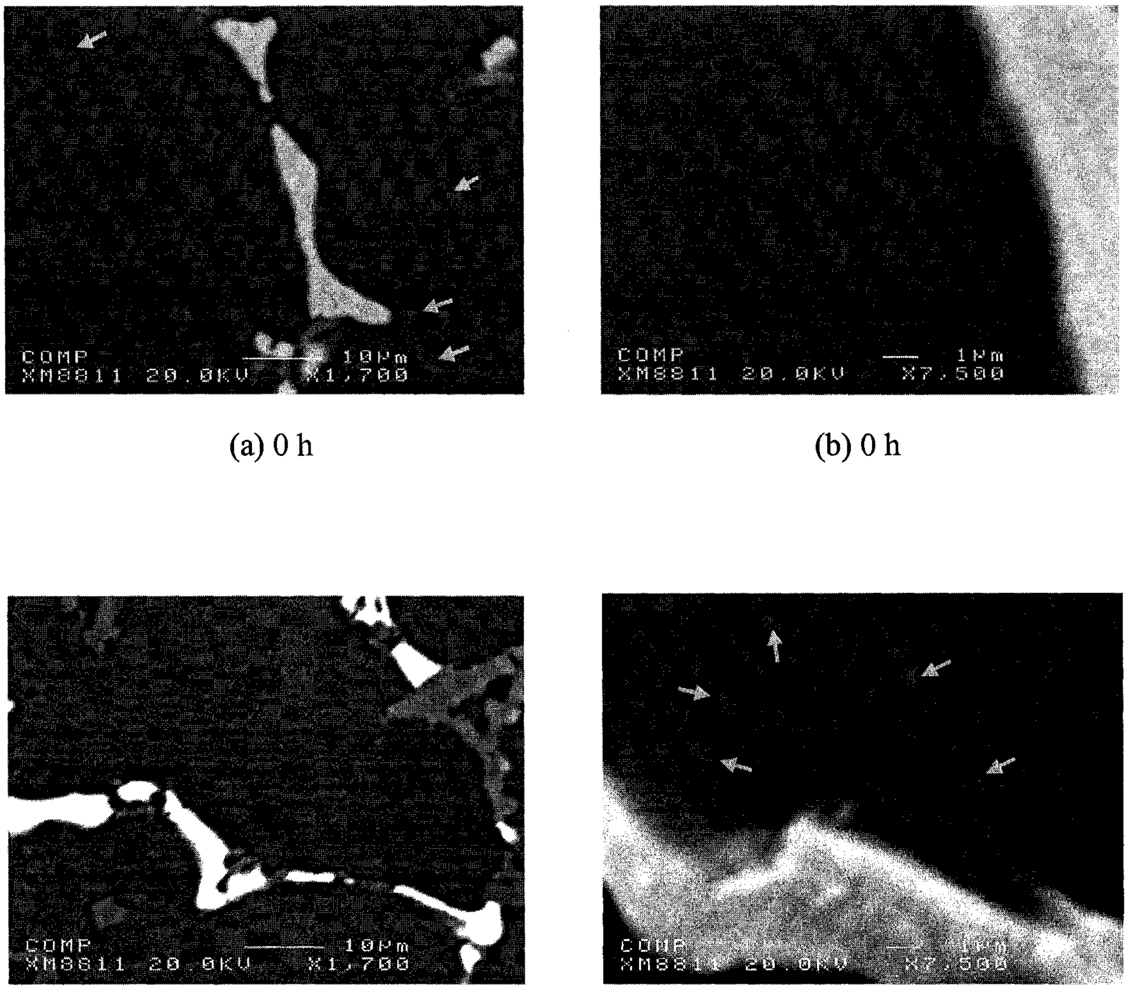

(a) 0 h (b) 0 h

(c) 4 h (d) 4 h

Figure 5.10 – Backscattered Images Showing Co-Precipitation (Yellowed Arrowed) in the Surroundings of $CuAl_2$ in Alloy MS at Solution Temperature 495 °C for 4 h and Aging Time 4 h:

(a, b) 180 °C Aging Temperature
(c, d) 220 °C Aging Temperature

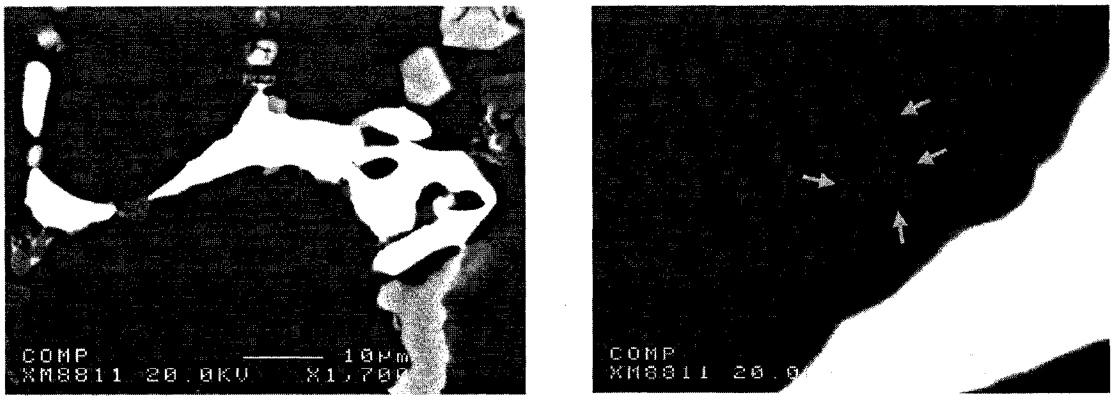

(a) 0 h (b) 0 h

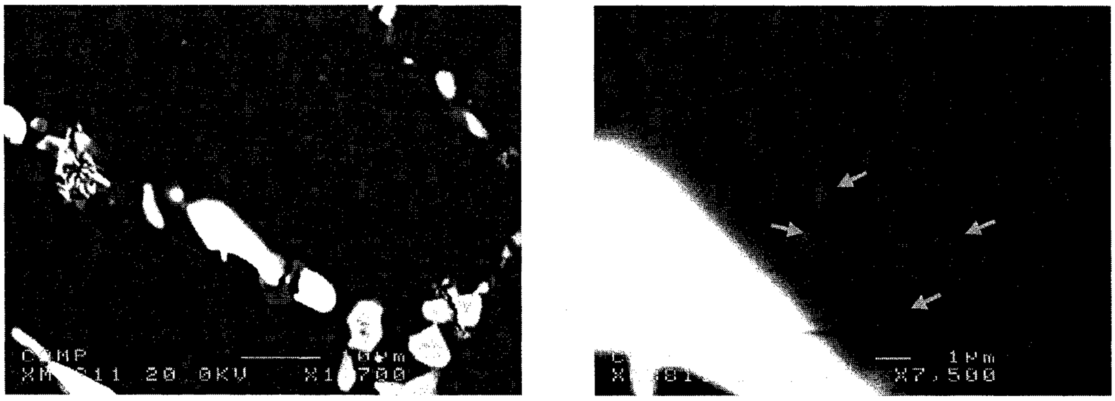

(c) 4 h (d) 4 h

Figure 5.11 – Backscattered Images Showing Co-Precipitation (Yellowed Arrowed) in the Surroundings of $CuAl_2$ in Alloy MS at Solution Temperature 495 °C for 24 h and Aging Time 4 h:

(a, b) 180 °C Aging Temperature
(c, d) 220 °C Aging Temperature

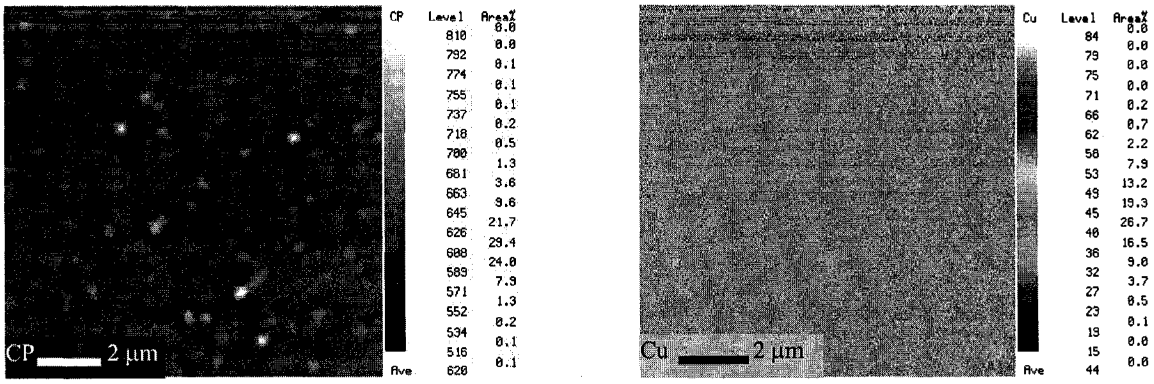

(a) Backscattered Electron Image (d) Cu

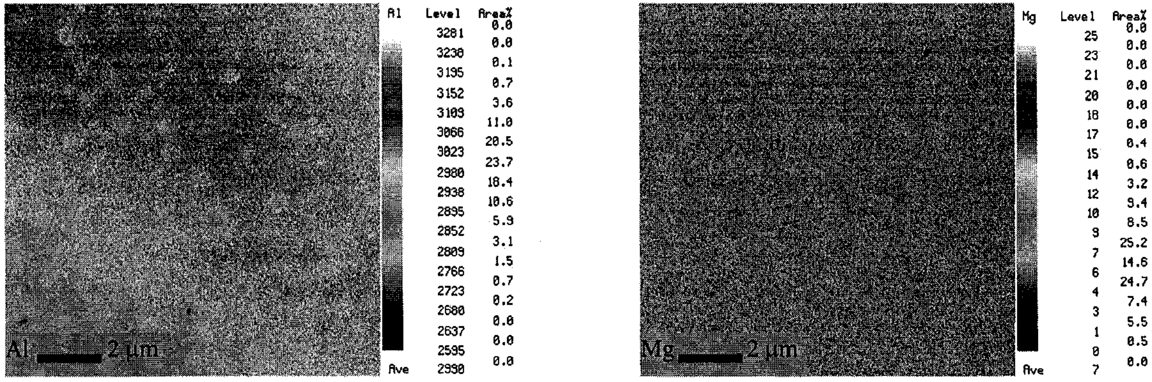

(b) Al (e) Mg

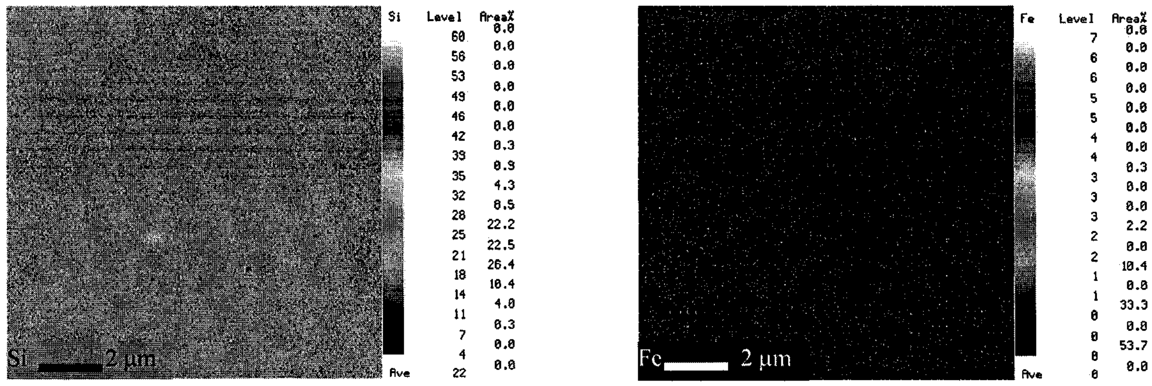

(c) Si (f) Fe

Figure 5.12 – Wavelength-Dispersive X-Ray Maps in Alloy M at Solution Temperature 495 °C for 4 h and Aging Temperature 180 °C for 4 h Showing Distributions of: (a) Compositional, (b) Al, (c) Si, (d) Cu, (e) Mg and (f) Si

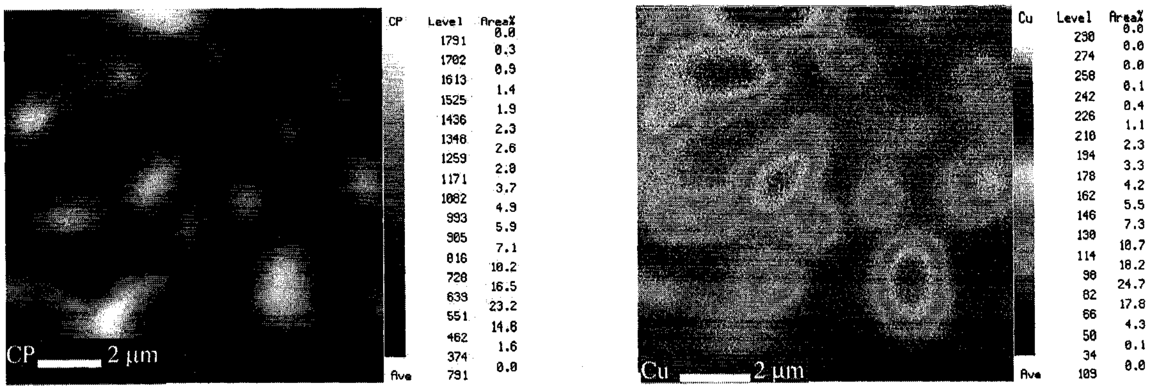

(a) Backscattered Electron Image

(d) Cu

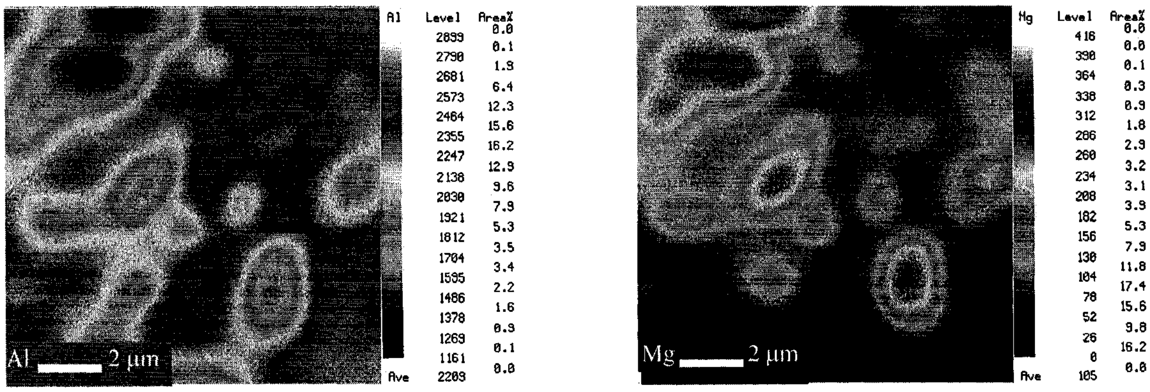

(b) Al

(e) Mg

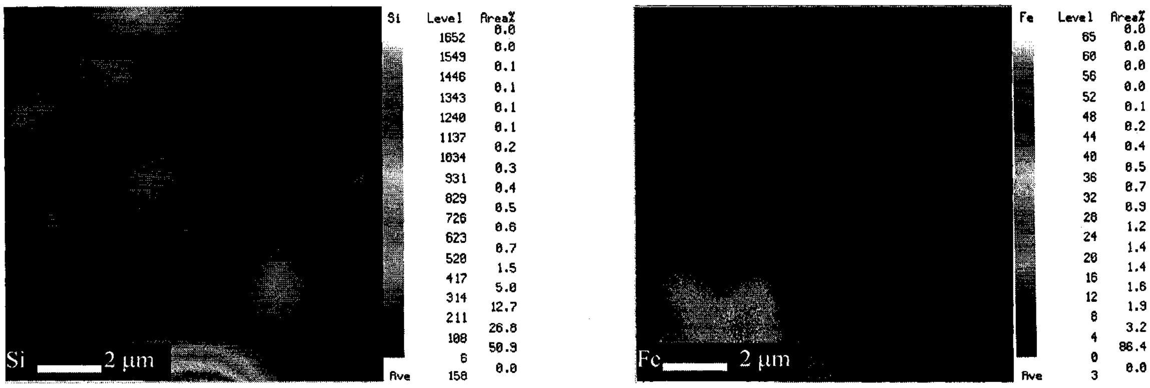

(c) Si

(f) Fe

Figure 5.13 – Wavelength-Dispersive X-Ray Maps in Alloy M at Solution Temperature 495 °C for 4 h and Aging Temperature 220 °C for 4 h Showing Distributions of: (a) Compositional, (b) Al, (c) Si, (d) Cu, (e) Mg and (f) Si

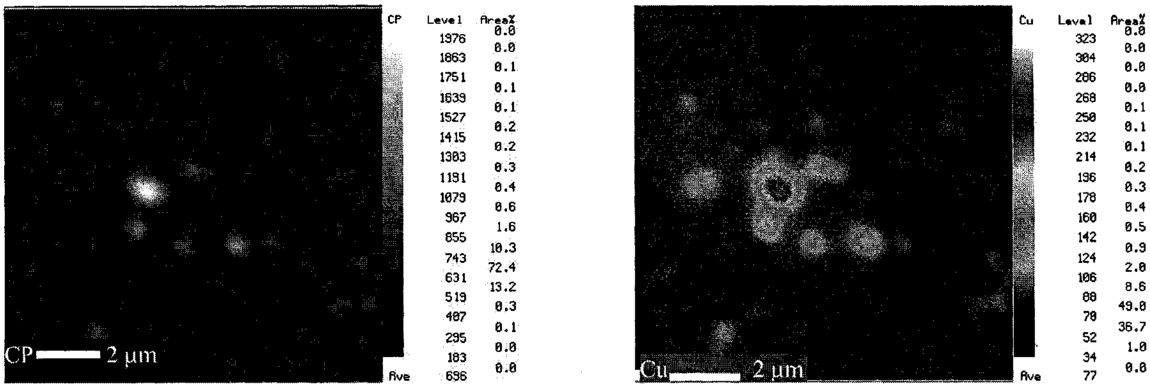

(a) Backscattered Electron Image (d) Cu

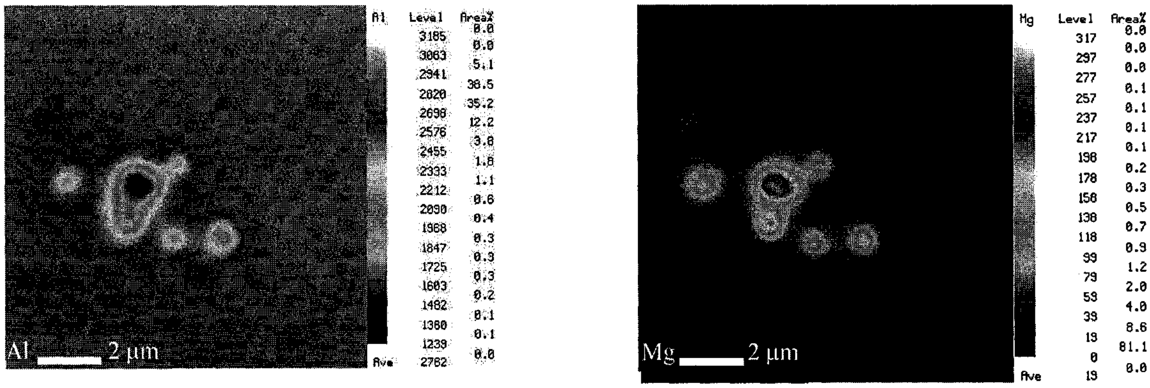

(b) Al (e) Mg

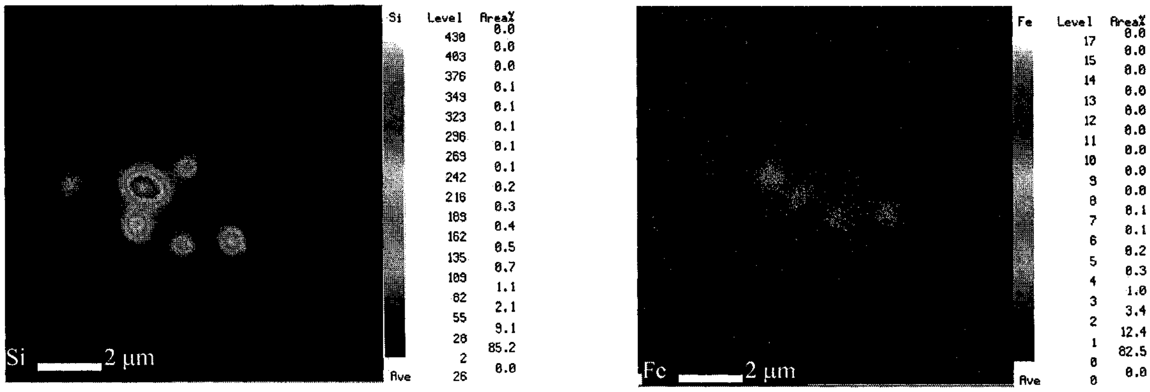

(c) Si (f) Fe

Figure 5.14 – Wavelength-Dispersive X-Ray Maps in Alloy M at Solution Temperature 495 °C for 24 h and Aging Temperature 180 °C for 4 h Showing Distributions of: (a) Compositional, (b) Al, (c) Si, (d) Cu, (e) Mg and (f) Si

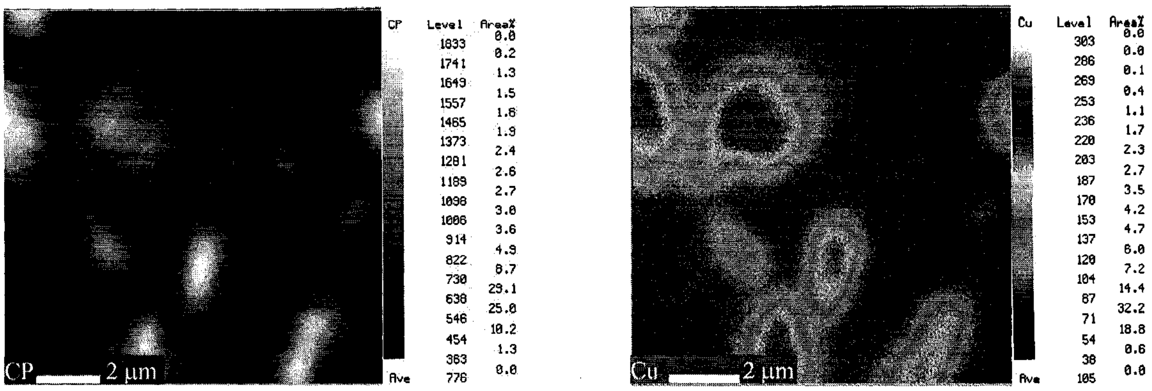

(a) Backscattered Electron Image

(d) Cu

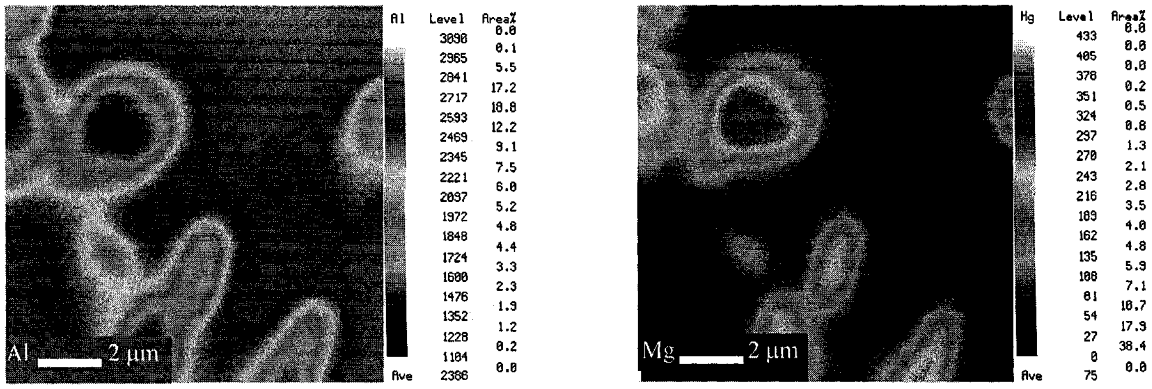

(b) Al

(e) Mg

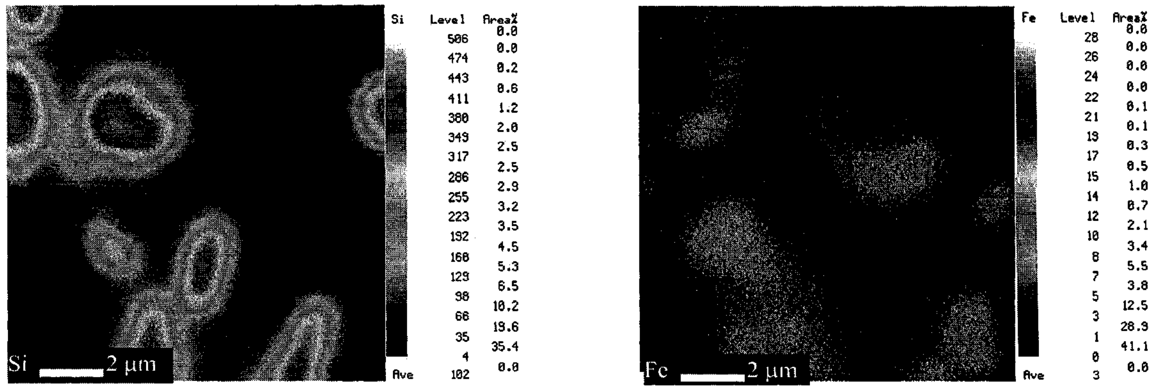

(c) Si

(f) Fe

Figure 5.15 – Wavelength-Dispersive X-Ray Maps in Alloy M at Solution Temperature 495 °C for 24 h and Aging Temperature 220 °C for 4 h Showing Distributions of: (a) Compositional, (b) Al, (c) Si, (d) Cu, (e) Mg and (f) Si

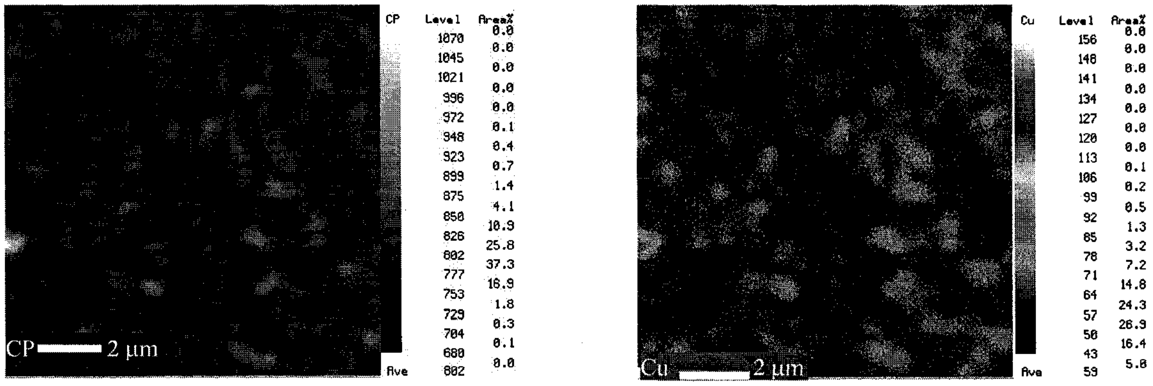

(a) Backscattered Electron Image (d) Cu

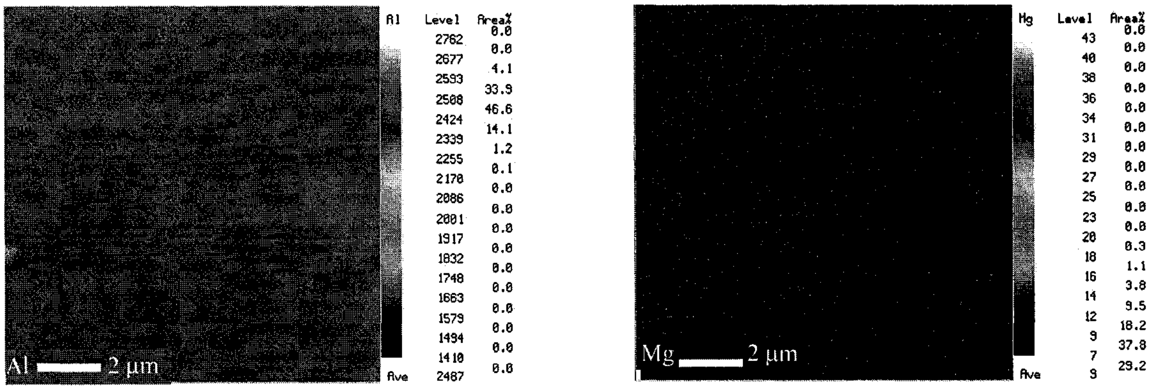

(b) Al (e) Mg

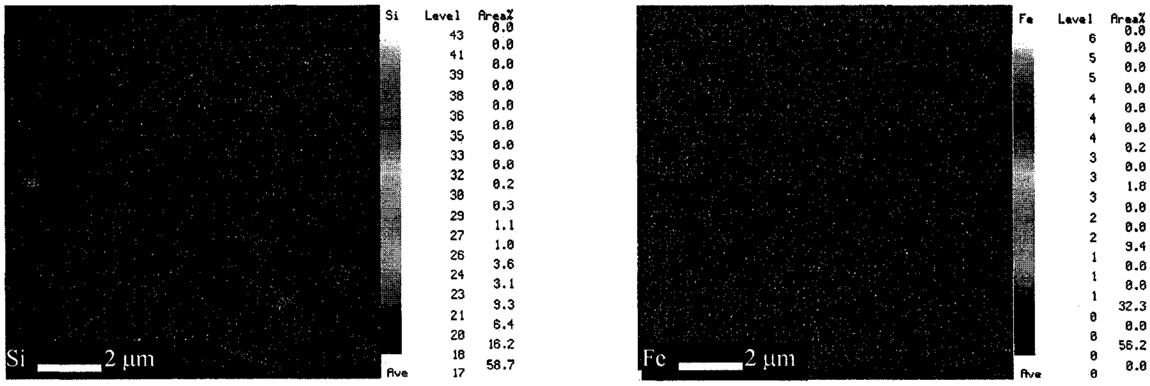

(c) Si (f) Fe

Figure 5.16 – Wavelength-Dispersive X-Ray Maps in Alloy MS at
Solution Temperature 495 °C for 4 h and Aging Temperature 180 °C for 4 h
Showing Distributions of: (a) Compositional, (b) Al, (c) Si, (d) Cu, (e) Mg and (f) Si

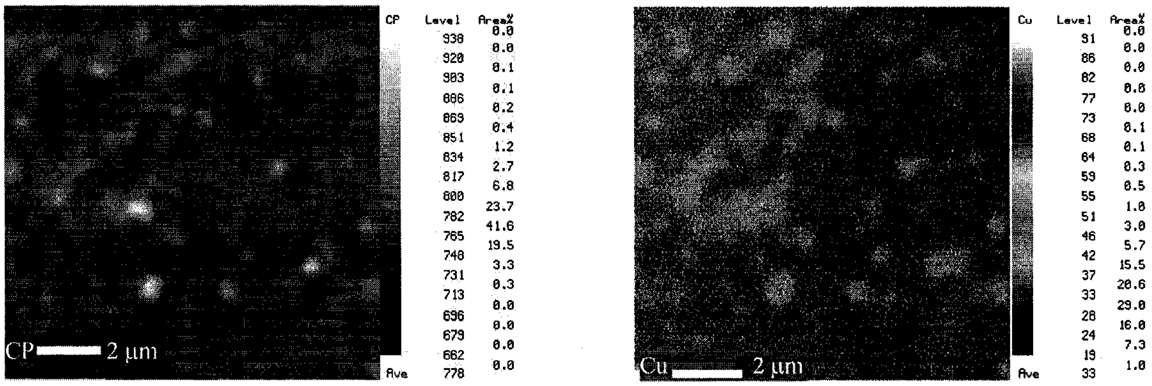

(a) Backscattered Electron Image (d) Cu

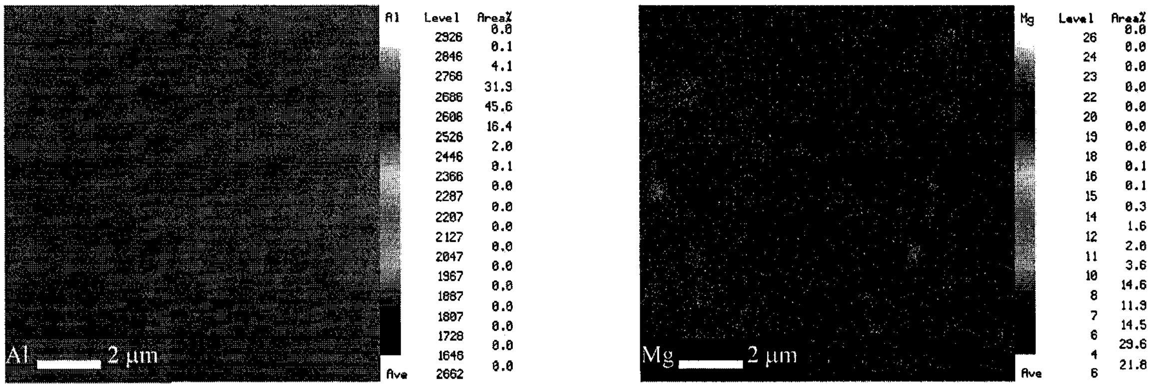

(b) Al (e) Mg

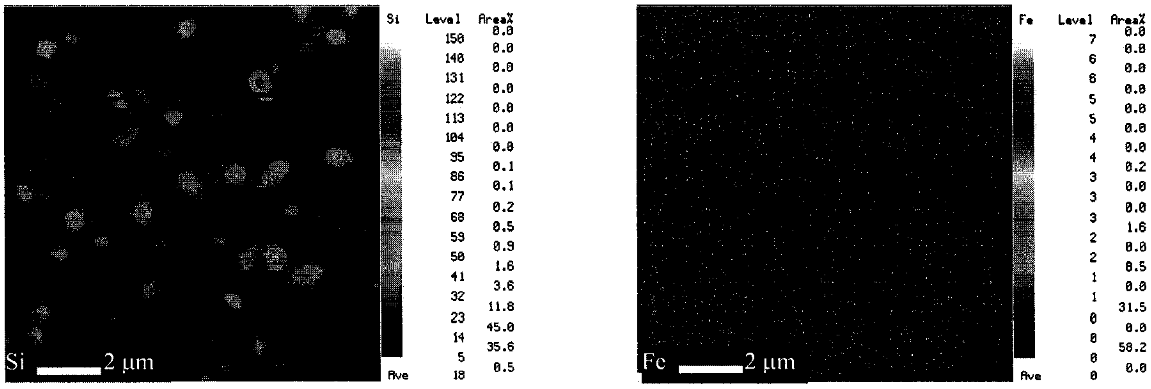

(c) Si (f) Fe

Figure 5.17 – Wavelength-Dispersive X-Ray Maps in Alloy MS at Solution Temperature 495 °C for 4 h and Aging Temperature 220 °C for 4 h Showing Distributions of: (a) Compositional, (b) Al, (c) Si, (d) Cu, (e) Mg and (f) Si

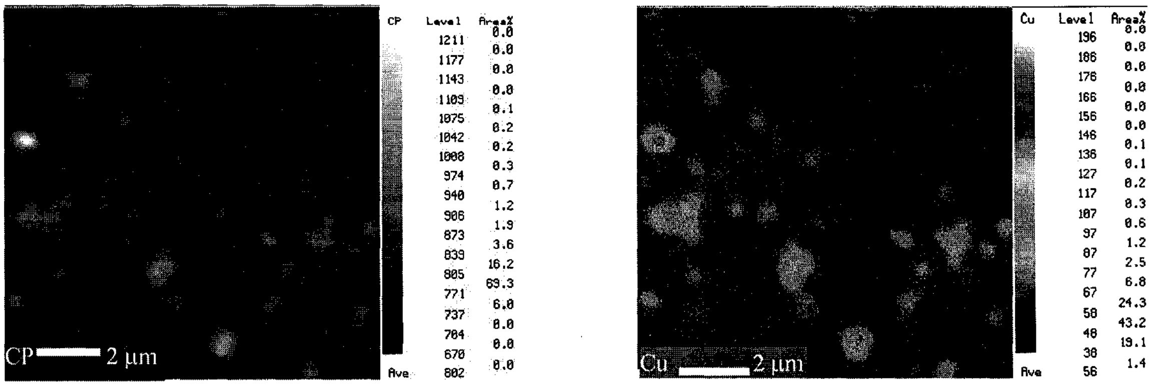

(a) Backscattered Electron Image

(d) Cu

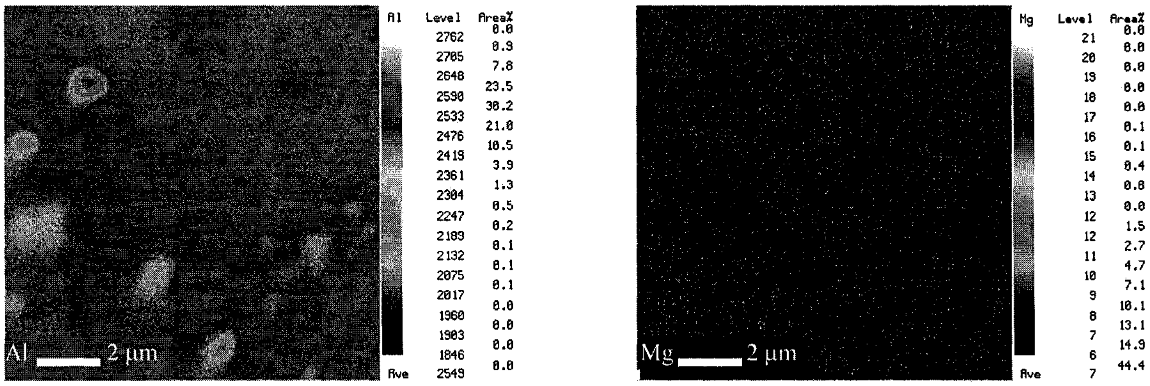

(b) Al

(e) Mg

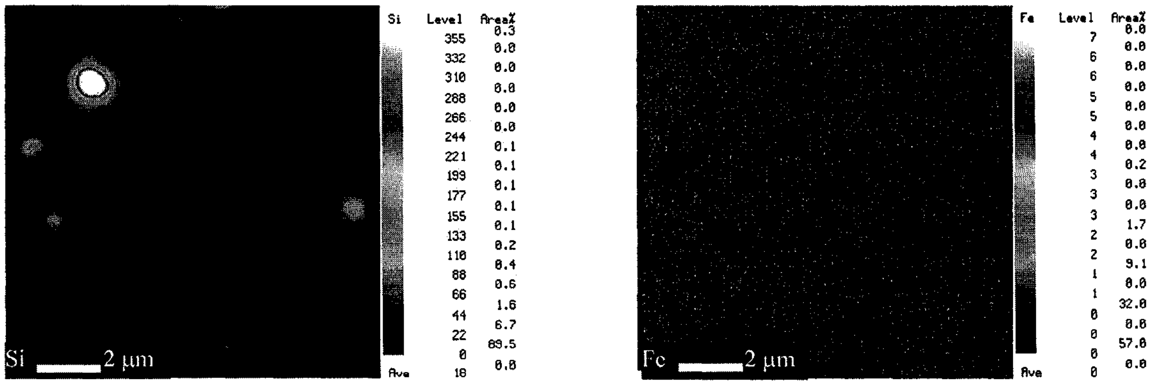

(c) Si

(f) Fe

Figure 5.18 – Wavelength-Dispersive X-Ray Maps in Alloy MS at
Solution Temperature 495 °C for 24 h and Aging Temperature 180 °C for 4 h
Showing Distributions of: (a) Compositional, (b) Al, (c) Si, (d) Cu, (e) Mg and (f) Si

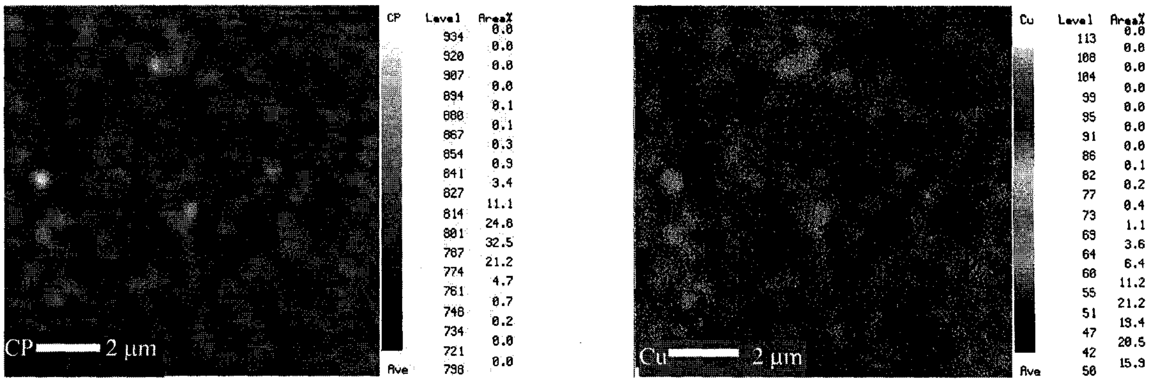

(a) Backscattered Electron Image

(d) Cu

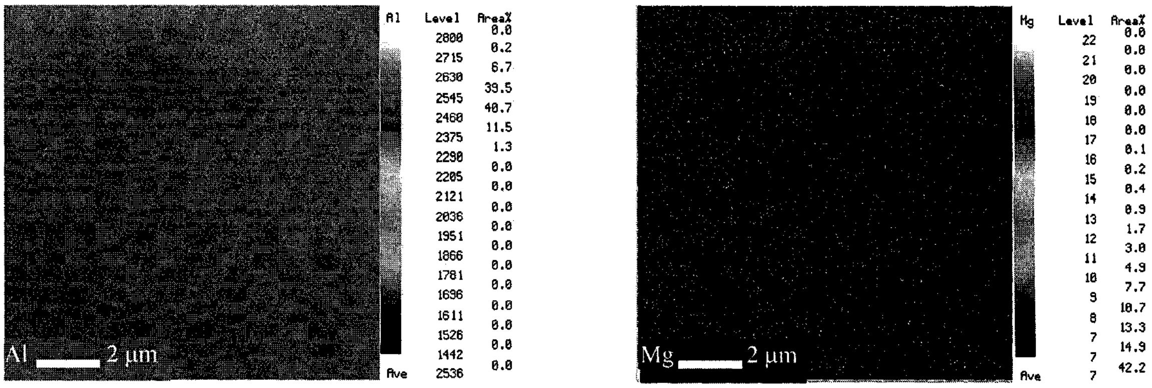

(b) Al

(e) Mg

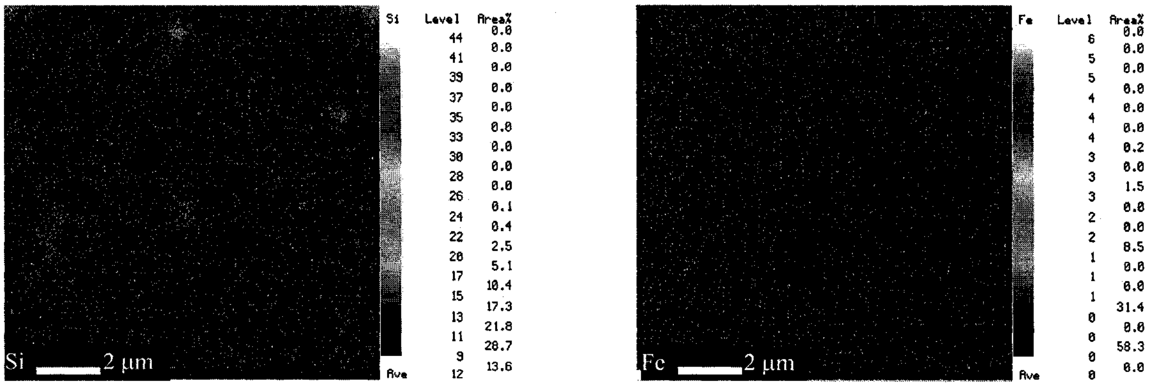

(c) Si

(f) Fe

Figure 5.19 – Wavelength-Dispersive X-Ray Maps in Alloy MS at Solution Temperature 495 °C for 24 h and Aging Temperature 220 °C for 4 h Showing Distributions of: (a) Compositional, (b) Al, (c) Si, (d) Cu, (e) Mg and (f) Si

A general view of the microstructure of alloy MS (0.40 wt % Mg + 160 ppm Sr) is seen in Figure 5.20 in the different T6 conditions. Figure 5.20 d shows that even after 24 h of solution treatment at 495 °C and aged at a high temperature (220 °C), there is not a complete dissolution of the $CuAl_2$ phase, and a few particles are still observed in the matrix. Figures 5.21 to 5.24 show high magnification backscattered images of alloy MS showing Cu~ and Mg~ rich precipitates, along with their corresponding EDX spectra in different T6 conditions.

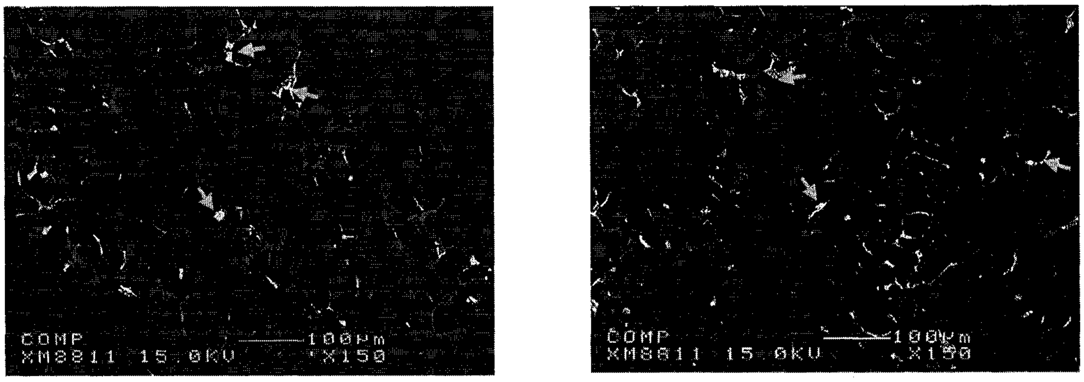

(a) Aged at 180 °C (b) Aged at 220 °C

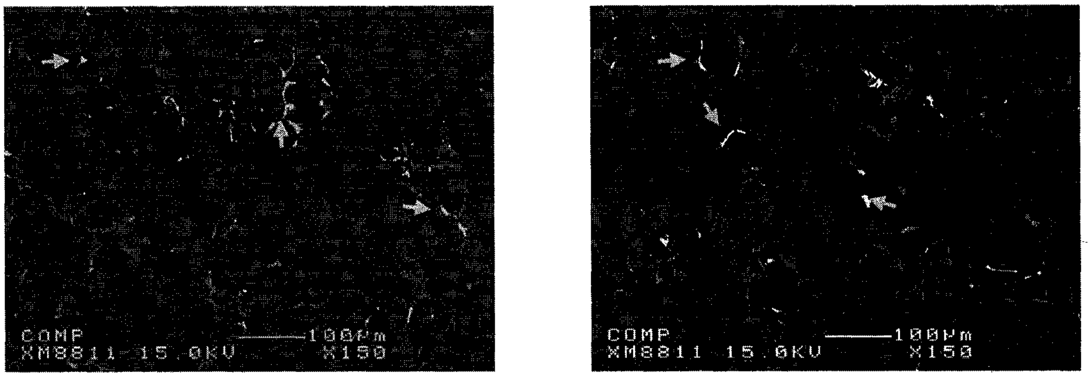

(c) Aged at 180 °C (d) Aged at 220 °C

Figure 5.20 – Backscattered Image Taken From Alloy MS Showing Segregation of $Al_5Mg_8Si_6Cu_2$ (Red Arrowed) and $CuAl_2$ (Yellow Arrowed) due to Modification Solution Temperature 495 °C and Aging Time 4 h:

(a, b) After 4 h Solution Heat Treatment
(c, d) After 24 h Solution Heat Treatment

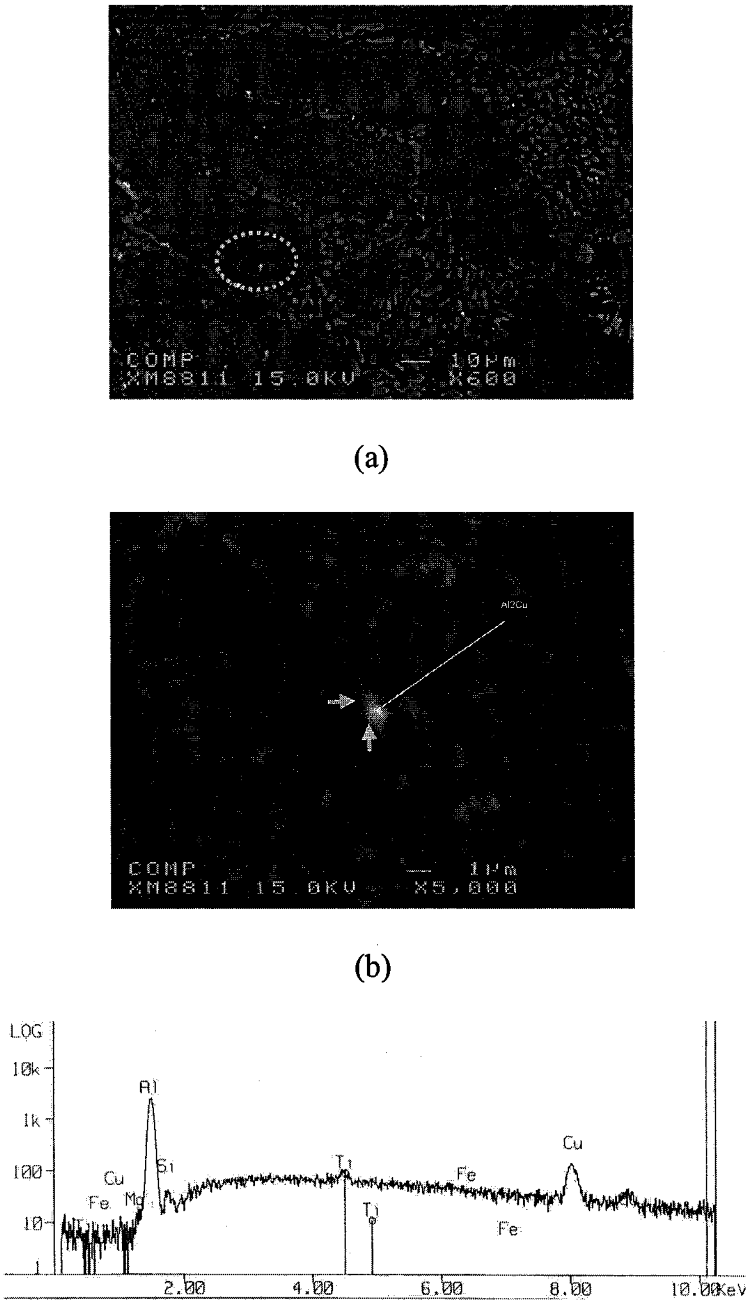

(c)

Figure 5.21 – Alloy MS Showing:
(a) Backscattered Image of Mg~ (Red Arrowed)
and Cu~ (Yellowed Arrowed) Rich Precipitates
(b) Magnified View of the Circled Area Showed in (a)
(c) EDX Spectra Corresponding to the Phases Present

Solution Heat Treatment at 495 °C for 4 h and Aged at 180 °C for 4 h

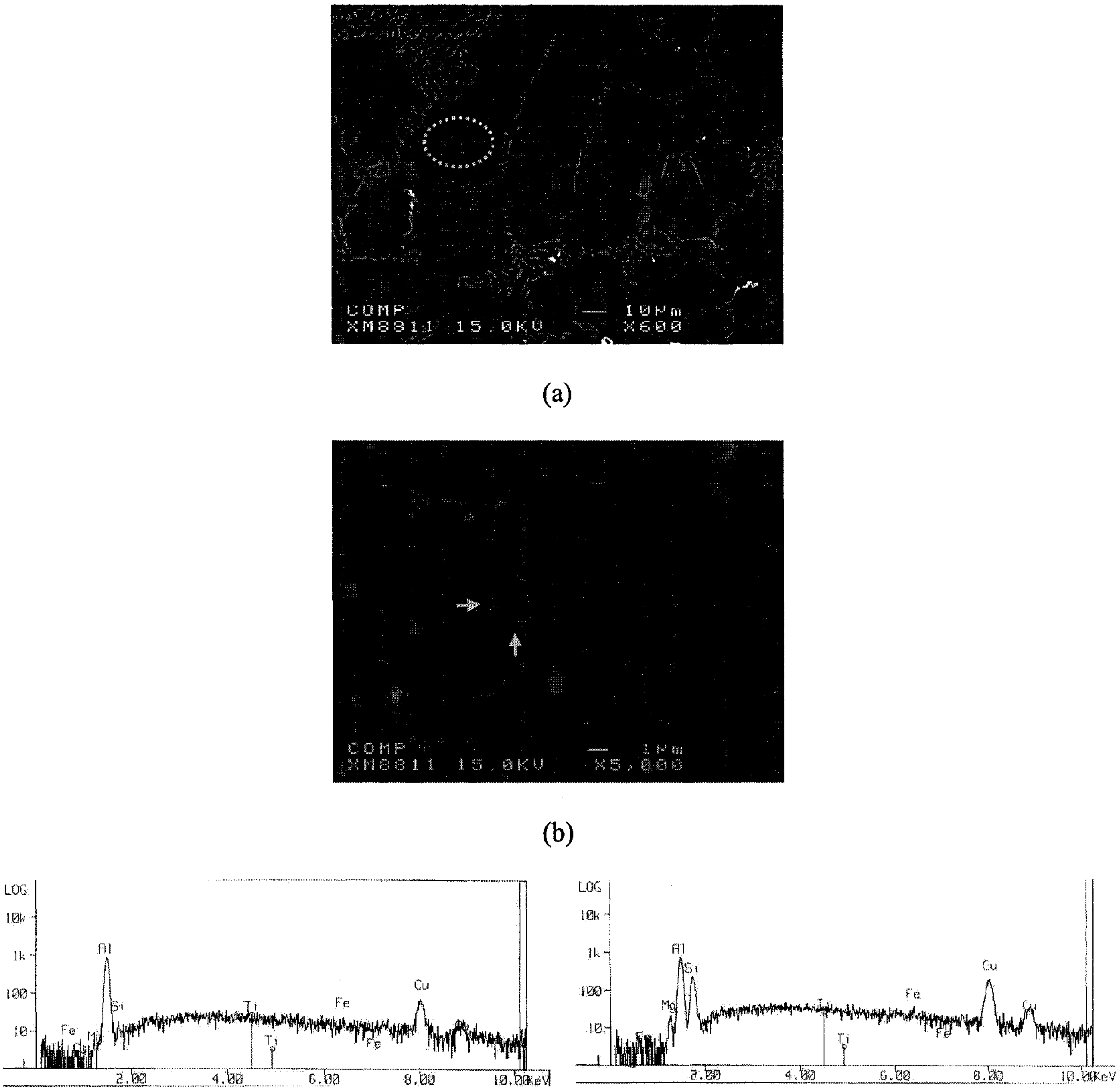

(a)

(b)

(c)

Figure 5.22 – Alloy MS Showing:
(a) Backscattered Image of Mg~ (Red Arrowed)
and Cu~ (Yellowed Arrowed) Rich Precipitates
(b) Magnified View of the Circled Area Showed in (a)
(c) EDX Spectra Corresponding to the Phases Present

Solution Heat Treatment at 495 °C for 4 h and Aged at 220 °C for 4 h

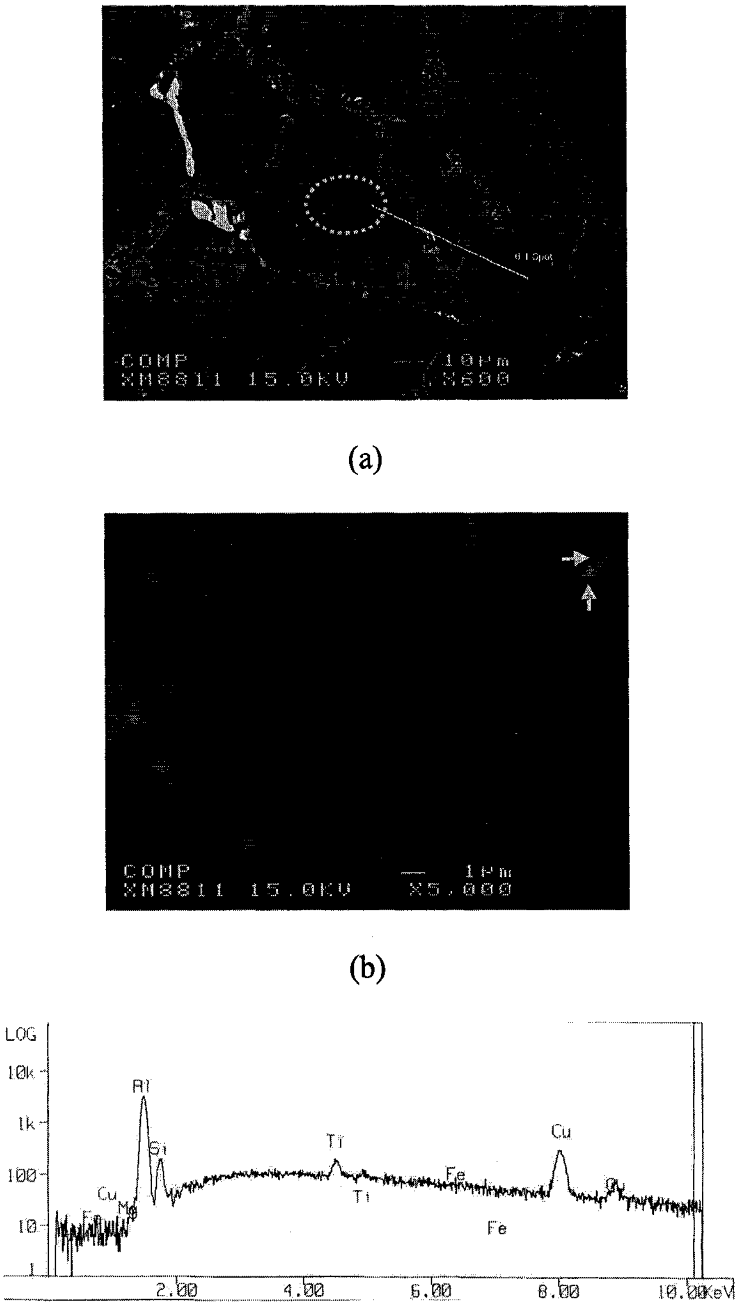

(a)

(b)

(c)

Figure 5.23 – Alloy MS Showing:
(a) Backscattered Image of Mg~ (Red Arrowed)
and Cu~ (Yellowed Arrowed) Rich Precipitates
(b) Magnified View of the Circled Area Showed in (a)
(c) EDX Spectra Corresponding to the Phases Present

Solution Heat Treatment at 495 °C for 24 h and Aged at 180 °C for 4 h

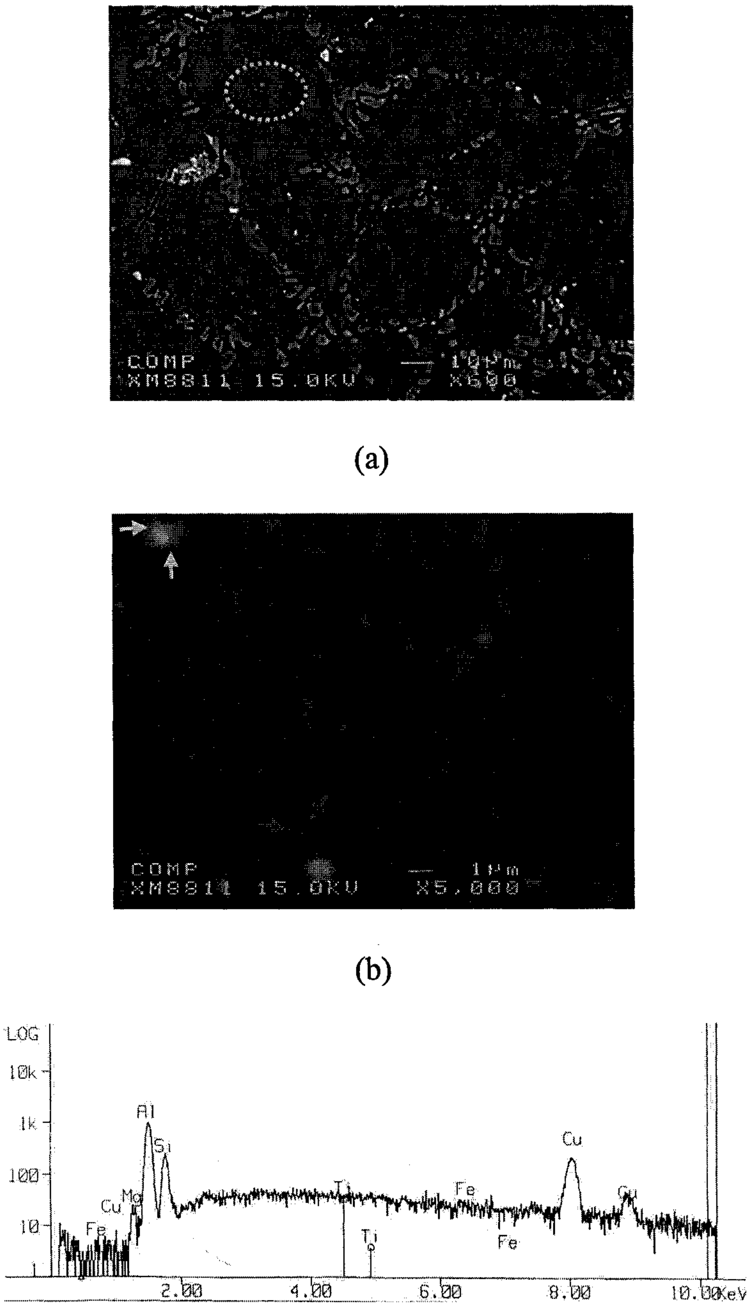

(a)

(b)

(c)

Figure 5.24 – Alloy MS Showing:
(a) Backscattered Image of Mg~ (Red Arrowed)
and Cu~ (Yellowed Arrowed) Rich Precipitates
(b) Magnified View of the Circled Area Showed in (a)
(c) EDX Spectra Corresponding to the Phases Present

Solution Heat Treatment at 495 °C for 24 h and Aged at 220 °C for 4 h

The results of the WDS analysis carried out on the different phases present in the alloy M are summarized in Table 5.4, and correspond to the backscattered images shown in this chapter. Table 5.5 shows the WDS analysis of the different phases present in alloy MS. From these tables, it can be seen that Sr modification slows down the rate of $Al_5Mg_8Cu_2Si_6$ dissolution due to its effects on the segregation and morphology of Cu phases during solidification.

Table 5.4 – WDS Analysis of Phases Observed in Alloy M

Composition (wt %)						Stoichometry	Phase
Al	Si	Cu	Mg	Fe	Mn + Cr		
					As-Cast		
47.61	1.09	48.69	0.35	0.18	0.007	$Al_{2.30}CuSi_{0.05}Mg_{0.01}$	$CuAl_2$
46.82	26.79	1.16	16.07	10.18	0.097	$Al_{8.14}Si_{4.47}Fe_{0.85}Mg_{3.10}$	$Al_8FeMg_3Si_5$
48.18	0.79	51.27	0.15	0.04	0.000	$Al_{2.21}CuSi_{0.03}$	$CuAl_2$
58.67	22.76	1.86	10.79	6.31	0.169	$Al_{15.21}Si_{5.66}Fe_{0.79}Mg_{3.10}$	$Al_{15}FeMg_3Si_5$
20.71	29.71	19.38	31.82	0.04	0.005	$Al_{5.03}Cu_2Si_{6.93}Mg_{8.58}$	$Al_5Mg_8Cu_2Si_6$
46.49	0.76	52.23	0.11	0.05	0.000	$Al_{2.09}CuSi_{0.03}$	$CuAl_2$
57.10	23.43	1.40	11.38	7.16	0.131	$Al_{14.81}Si_{5.83}Fe_{0.89}Mg_{3.27}$	$Al_{15}FeMg_3Si_5$
20.75	29.98	18.83	31.92	0.04	0.012	$Al_{5.19}Cu_2Si_{7.20}Mg_{8.86}$	$Al_5Mg_8Cu_2Si_6$
					T4 – 4 h		
50.00	0.73	48.44	0.12	0.07	0.016	$Al_{2.43}Cu$	$CuAl_2$
51.35	1.29	34.01	0.82	11.36	0.121	$Al_{6.99}Cu_{1.97}Fe_{0.75}$	Al_7FeCu_2
					T4 – 24 h		
41.07	0.73	52.61	0.13	0.09	0.012	$Al_{1.84}Cu$	$CuAl_2$
30.89	30.04	17.76	28.27	0.05	0.000	$Al_{4.10}CuSi_{3.83}Mg_{4.16}$	$Al_4Mg_5CuSi_4$

Table 5.5 – WDS Analysis of Phases Observed in Alloy MS

Composition (wt %)						Stoichometry	Phase
Al	Si	Cu	Mg	Fe	Mn + Cr		
					As-Cast		
17.05	30.20	19.93	34.73	0.07	0.005	$Al_{4.12}Cu_2Si_{6.86}Mg_{9.11}$	$Al_5Mg_8Cu_2Si_6$
48.25	0.74	51.28	0.13	0.09	0.006	$Al_{2.22}CuSi_{0.03}$	$CuAl_2$
45.24	26.74	2.13	17.15	9.44	0.071	$Al_{9.92}Si_{5.63}FeMg_{4.17}$	$Al_{10}FeMg_4Si_6$
					T4 – 4 h		
48.14	0.67	50.83	0.09	0.04	0.007	$Al_{2.23}CuSi_{0.03}$	$CuAl_2$
16.39	29.11	20.08	34.60	0.04	0	$Al_{4.85}Cu_2Si_{9.56}Mg_9$	$Al_5Mg_8Cu_2Si_6$
					T4 – 24 h		
48.64	0.65	50.88	0.10	0.06	0.014	$Al_{2.25}CuSi_{0.03}$	$CuAl_2$
15.84	30.74	20.41	35.20	0.01	0.010	$Al_{3.66}Cu_2Si_{6.81}Mg_9$	$Al_5Mg_8Cu_2Si_6$

5.2. Transmission Electron Microscopy (TEM) Results

Figure 5.25a shows the precipitation in an untreated sample of alloy M, which was cooled at a rate of around ~ 8 $^{\circ}C \cdot s^{-1}$ (corresponding to a dendrite arm spacing ~ 20-30 μm). A characteristic that was detected in foils from these samples was the absence of Mg and Cu rich precipitates, but the existence of Si particles.

The microstructure of samples solution treated at 495 °C for 4 h and water quenched consisted of helical dislocations produced by the quenching of vacancies during the water quench (Figure 5.25b). After 24 h of solution, precipitates coarsen and most of the constituents are completely dissolved (Figure 5.25c).

In the series of micrographs and diffraction patterns of Figure 5.26, the effect of increasing aging time at 185 °C is evident. After aging for ½ h (Figures 5.26a and 5.26b), elongated precipitates (20 x 1 nm) appear aligned along the two orthogonal <100> directions together with smaller (2.5 nm) equiaxed precipitates. After 2 h (Figures 5.26c and 5.26d) and 12 h (Figures 5.26e and 5.26f) of aging, the needle-like precipitates coarsen, and discrete diffraction maxima for the precipitates appear in the different diffraction patterns indicating the presence of θ'-$CuAl_2$.

Figure 5.27 shows the bright-field image for a sample aged for 4 h (the second aging peak); where besides a few silicon particles the high-density fine precipitates (appearing as short lines) homogenously precipitate on the α matrix parallel to each other.

After 6 h of aging (the second plateau), along with the high-density fine precipitates in the matrix which are parallel to each other; collateral precipitation takes place on a 90° angle from the fine precipitates (Figure 5.28).

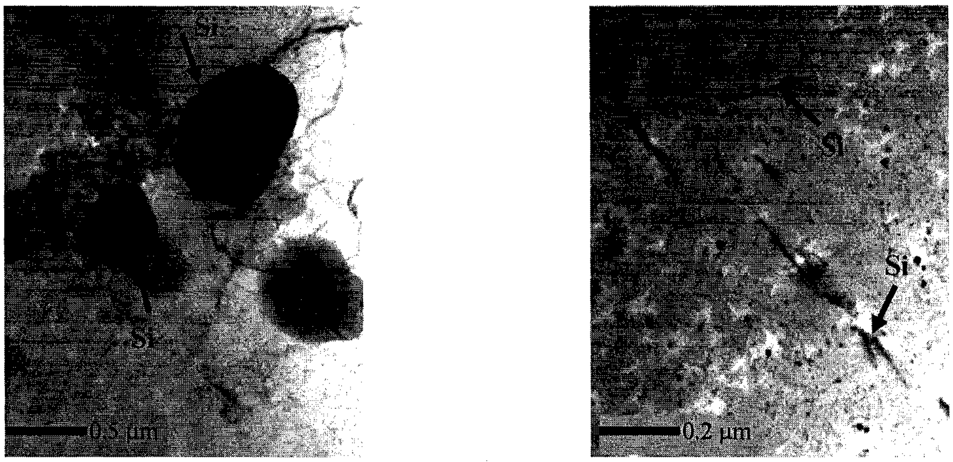

(a) As-Cast Condition

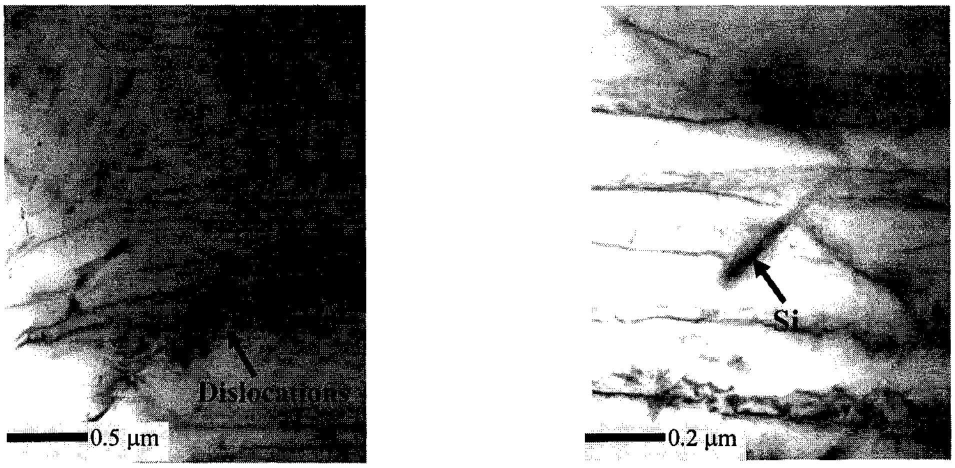

(b) After 4 h of Solution at 495 °C

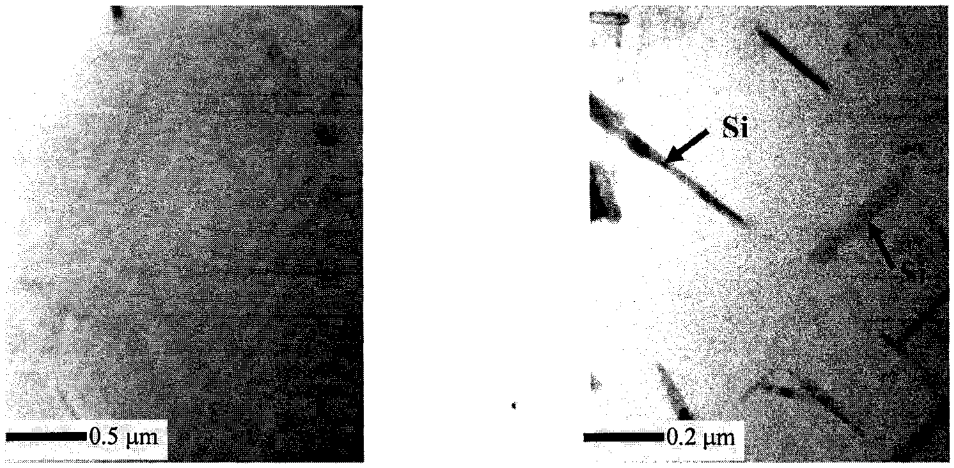

(c) After 24 h of Solution at 495 °C

Figure 5.25 – Effect of Solution Time on the Size of the Age-Hardening Precipitates

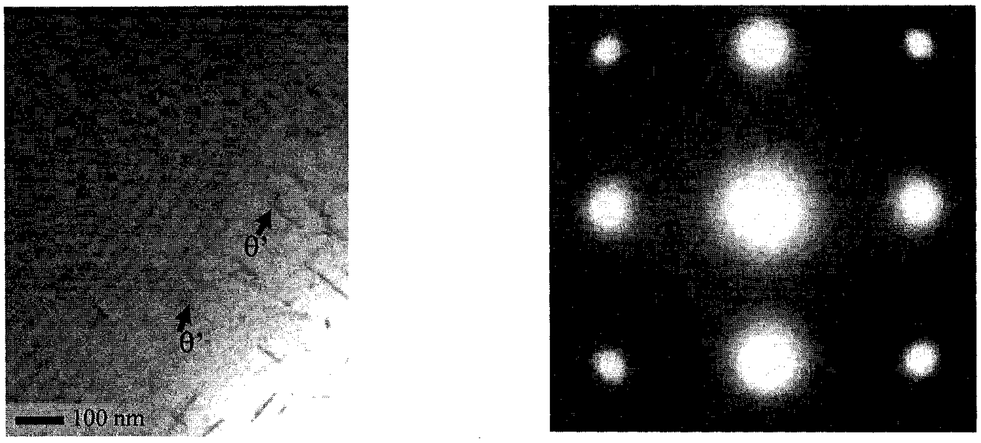

(a) After 0.5 h of Artificial Aging (b) Corresponding SAD Pattern

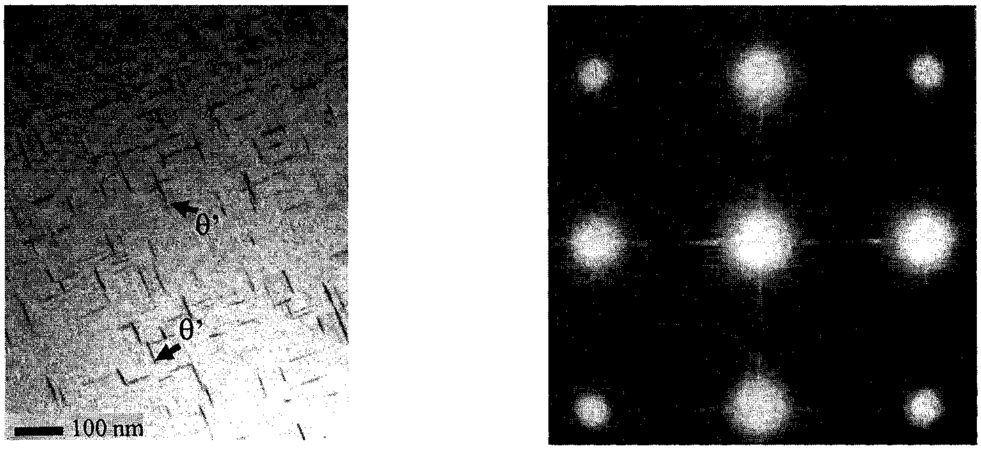

(c) After 2 h of Artificial Aging (d) Corresponding SAD Pattern

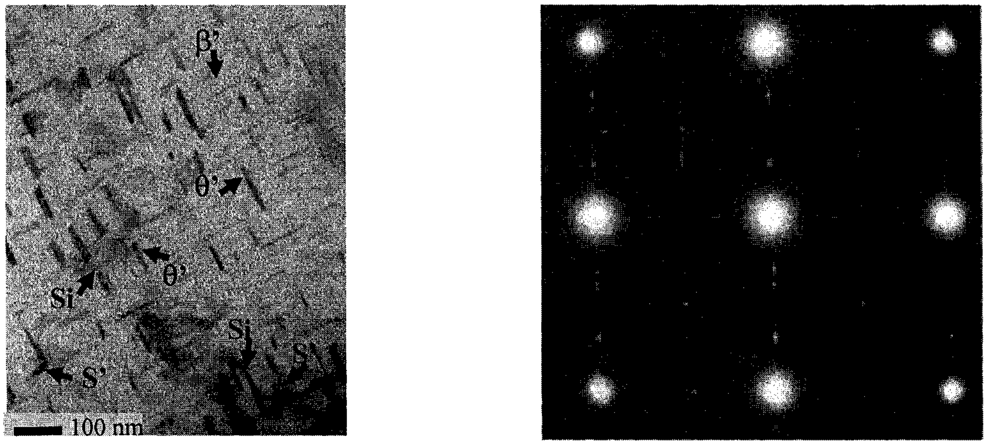

(e) After 12 h of Artificial Aging (f) Corresponding SAD Pattern

Figure 5.26 – Effect of Aging Time at 180 °C on the Size of the Age-Hardening Precipitates Samples were Solution-Heat Treated at 495 °C for 4 h

Figure 5.27 – High-Density Fine Precipitates Homogenously on the α Matrix
Sample was Solution Heat Treated at 495 °C for 4 h
and Aged for 4 h at 180 °C

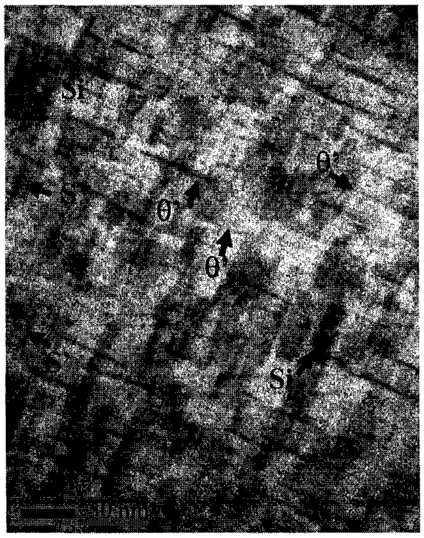

Figure 5.28 – High-Density Fine Precipitates Homogenously on the α Matrix
Coexisting with a Bulk-Shadowed Second Phase Perpendicularly Oriented
Sample was Solution Heat Treated at 495 °C for 4 h
and Aged for 6 h at 180 °C

The bright field image of precipitates aged for 24 h at 180 °C is shown in Figure 5.29. After tilting the sample near a <011> zone axis the morphology of the θ'-$CuAl_2$ is evident. Two variants of θ'-$CuAl_2$ are diffracting: one set is in the edge on orientation, and the other variant is inclined at 45°. The plate-shaped and disc-shaped precipitates grow up. This aging treatment was chosen to produce an over-aged microstructure.

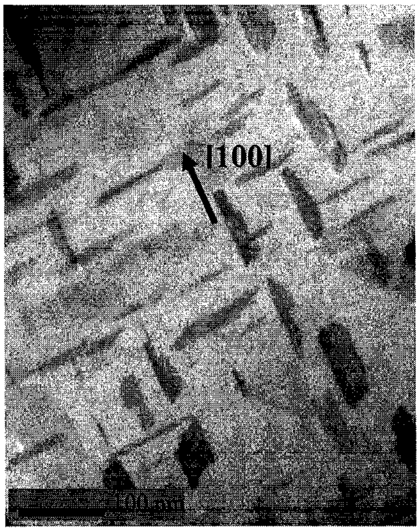

Figure 5.29 – Plate-Shaped θ'-$CuAl_2$ View from Near the [011] Aluminium Axis Sample was Solution Heat Treated at 495 °C for 4 h and Aged for 24 h at 180 °C

From the TEM observations, it is found that silicon forms precipitates in the aluminum matrix with four distinct morphologies, as illustrated by the transmission electron micrographs in Figure 5.30. Strengthening precipitates have been identified; namely Si plates and particles, $CuMgAl_2$ and Mg_2Si. Minor species do not contribute significantly to strength, among them: the two quaternary precipitates (Q phase or $Al_5Cu_2Mg_7Si_7$ and AlCuMgSi), the Si rods, the Si laths, and the $CuAl_2$ precipitates.

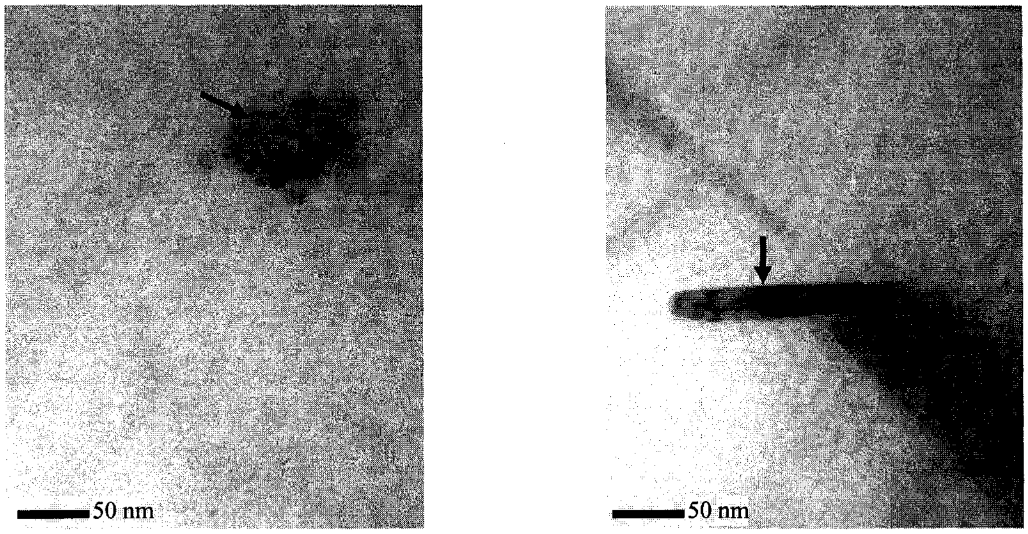

(a) Spherical Si Particle After Solution Treated at 495 °C for 4 h and Quenched in Water at 90 °C

(b) Si Rods After Solution Treated at 495 °C for 4 h and Quenched in Water at 90 °C

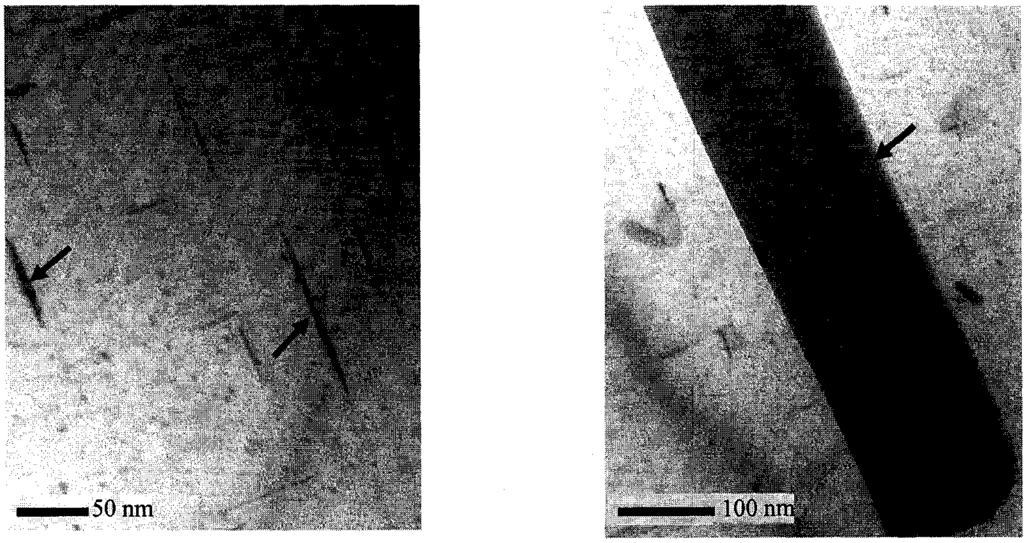

(c) Si Plates After 12 h of Aging at 180 °C

(d) Lath of Si After 12 h of Aging at 180 °C

Figure 5.30 – Bright Field Transmission Electron Micrographs of Precipitates in Alloy M

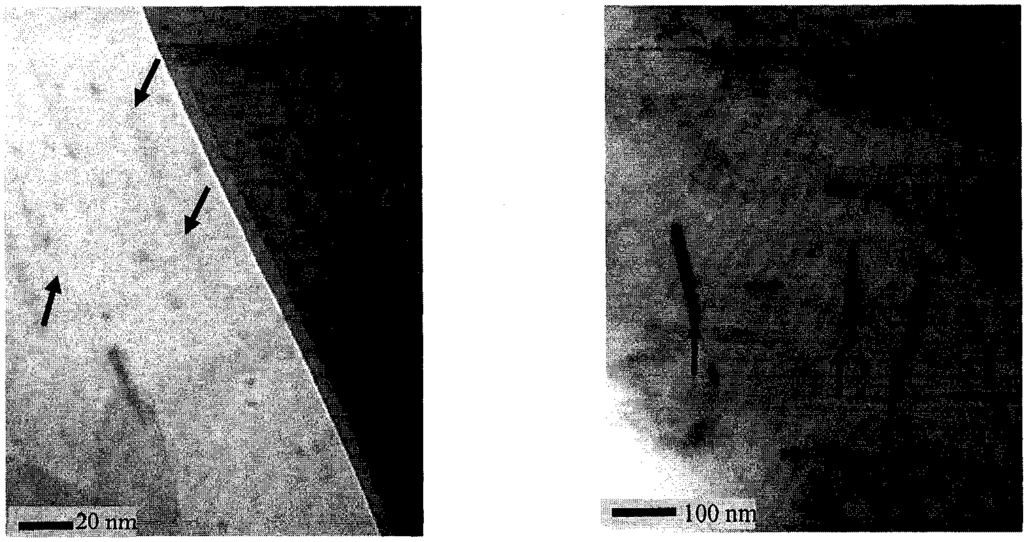

(e) Precipitation of θ' and θ After 12 h of Aging at 180 °C

(f) $CuMgAl_2$ (S') Precipitates After 2 h of Aging at 180 °C

Figure 5.30 – Bright Field Transmission Electron Micrographs of Precipitates in Alloy M (Continued)

Table 5.6 gives the analysis of the average length and diameter of at least 50 silicon precipitates of different morphologies.

Table 5.6 – Average Length and Diameter of the Si Precipitates and $CuAl_2Mg$(S') Present in the Aluminum Matrix (Alloy M)

Precipitate	Average Length (nm)	Average Diameter (nm)
Spherical Si	50-100	50-100
Si Rods	200-300	10-15
Si Plates	500-1000	10-30
Si Lath	3000-5000	1000-2000
$CuAl_2Mg$ (S')	100-200	5-10

CHAPTER 6

DISCUSSION

6.1. Microstructural Results

A series of parameters can be employed to describe the metallurgical microstructure of aluminum castings. Separation between dendritic arms is affected by the solidification rate, distribution and aspect of the eutectic aggregate. As well grain size, can be controlled by addition of elements or compounds and by the cooling rate. Size and distribution of intermetallic phases is much more complex, since care has to be taken with respect to impurity content as well as other solidification conditions.

6.1.1. Microstructure

Alloy 319.2 contains both high concentrations of copper and silicon. Copper contributes to strength by precipitation hardening and silicon improves castability. Solidification starts with the formation of equiaxed dendritic α-aluminum crystals. The dendrites grow at a high velocity and become coherent very early. In the period of dendrite arm coarsening, iron-containing phases α-$Al_{15}(Fe, Mn)_3Si_2$ or β-Al_5FeSi may precipitate. During the main eutectic reaction, Al, Si and β-Al_5FeSi phases precipitate together. When the temperature is below 515 °C, $CuAl_2$, $Al_5Mg_8Cu_2Si_6$ and Mg_2Si phases start to precipitate through some low temperature eutectic reactions. These late reactions have no bearing on coherency or rigidity points [13].

The increased Mg content (up to 0.4 %) in some of the samples, will not significantly change the solidification process, (and hence the precipitates), except that an increased amount of $Al_5Mg_8Cu_2Si_6$ phase will be present.

Microstructures of unmodified samples (alloy A and alloy M) in the as-cast condition were shown in Figures 4.2a and 4.2b. In commercial casting processes, the metal solidifies dendritically into the liquid solution. The cells contained within the dendritic structure correspond to the dimensions separating the arms of the primary dendrites which are rich in aluminum and are outlined by the eutectic structure. The eutectic structure consists of silicon flakes and needles without preferential orientation in an aluminum matrix. Although the Si platelets generally appear as isolated needles in two dimensions, the placement of the eutectic silicon particles indicates a three dimensional structure of a continuous platelet network. The unmodified microstructure is acicular, where the silicon represents the hard phase that causes a discontinuity of the soft and ductile matrix of aluminum. It is the presence of these large brittle Si flakes in the unmodified alloys which causes the castings to exhibit lower tensile properties.

The eutectic microstructure strongly depends on the composition and the casting process of the alloy. The presence of certain elements (such as Sr among others) even in very small amounts may have a dramatic effect. On the other hand, very high solidification rates may give modified structures, even in the absence of chemical modifiers. Higher cooling rates (for example when using a permanent mold), promote a finer eutectic structure, smaller dendritic cells and smaller arm spacing.

Microstructures of modified samples (alloy MS) in the as-cast condition are shown in Figures 4.2c. The morphology of the Si flakes changed and became finely divided and fibrous. The modified eutectic is connected in a coral or seaweed-like structure. The structural transformation from acicular to fibrous Si causes an improvement of the tensile properties in the modified samples. Figure 6.1 shows the structural differences between the unmodified and modified alloys.

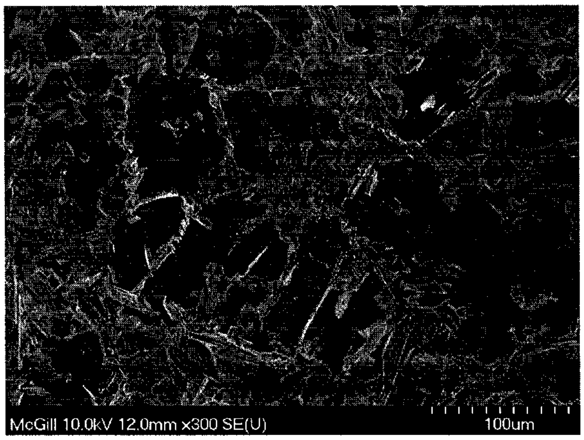

(a) Alloy M

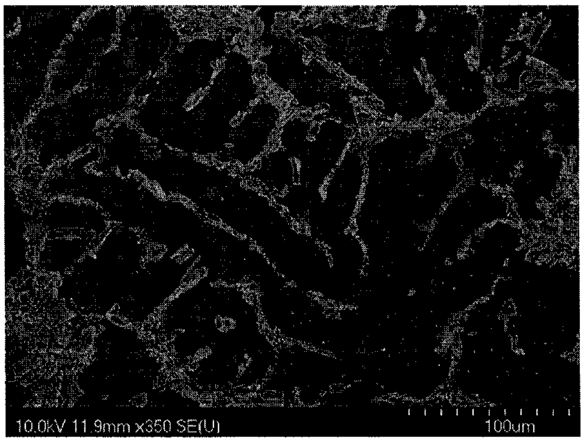

(b) Alloy MS

Figure 6.1 – Scanning Electron Micrograph Showing the Structural Differences Between Unmodified and Modified Alloys:

(a) Large Plates of Si Phase with Sharp Sides and Ends
(b) Si Fibers Forming an Interconnected Network

The two heat treatments used in this work are solution treatment (T4 condition) and aging treatment (T6 condition). As was explained in previous chapters, the T4 condition includes solution heat treatment and a subsequent quenching; whereas in the T6 condition an artificial aging was done after the quenching. During the solution treatment, several metallurgical processes take place: homogenization of the as-cast structure, dissolution of intermetallic phases and morphological changes of the Si phase. During the artificial aging, precipitation hardening occurs. The quenching treatment has no effect on the Si microstructure, although during aging $CuAl_2$, AlMgSi and Mg_2Si precipitate within the aluminum-rich dendrites, initially as GP zones and later as fine particles.

The effect of different solution heat treatment times on the microstructure of unmodified and modified samples with and without Mg additions are shown in Figures 4.3 and 4.5. As is well known, under normal cooling conditions, the eutectic silicon forms a network of interconnected irregular flakes. Thermal treatments can also alter the Si morphology. The change in size and morphology of the Si phase directly influences the mechanical properties.

When the unmodified samples (alloy A and alloy M) are solution heat treated for 4 h, the Si needles break up into smaller particles. As the treatment continues for 24 h, the Si particles spheroidize and coarsen. In the modified samples (alloy S and alloy MS), after 4 h of solution treatment, a large quantity of the Si has spheroidized and coarsening has begun. After 24 h of solution treatment, further coarsening of the Si takes place.

As is seen in Figures 6.2 and 6.3, solution treatment causes spheroidization and coarsening in unmodified and modified eutectic phases. During solution heat treatment, modification facilitates fragmentation and promotes eutectic Si phase breakdown and branching, allowing a higher spheroidization rate due to the size of the fragmented Si segments. Other authors report similar observations [9, 11, 94-97, 99, 101].

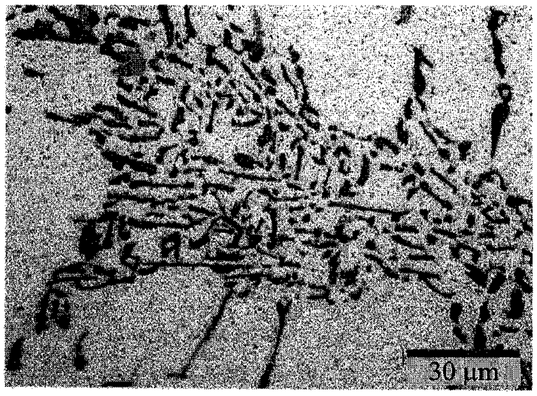

(a) 0 h

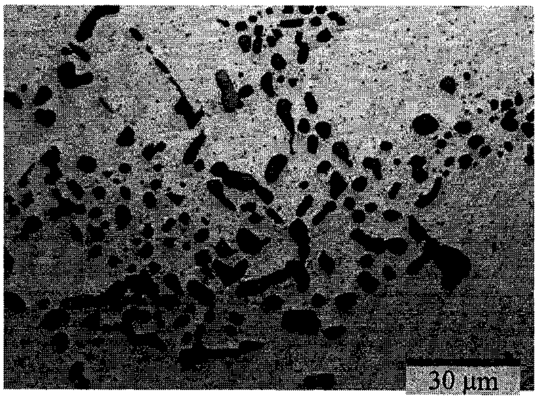

(b) 4 h

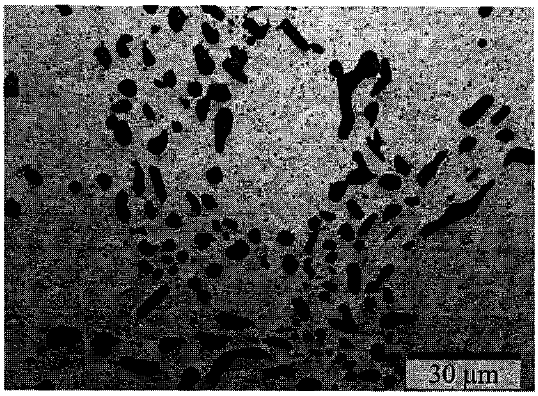

(c) 24 h

Figure 6.2 – High Magnification Micrographs Showing Effect of Solution Treatment Time on the Unmodified Microstructure in Alloy A:

(a) As-Cast, (b) After 4 h Solution Heat Treatment at 495 °C,
(c) After 24 h Solution Heat Treatment at 495 °C

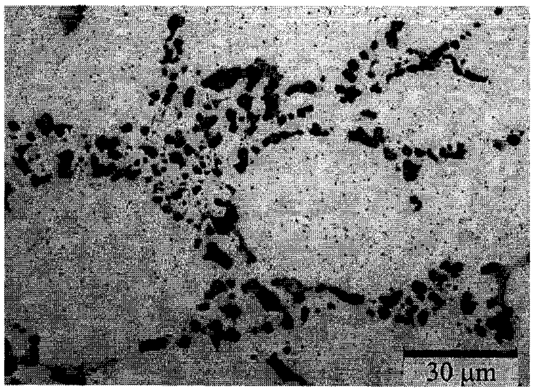

(a) 0 h

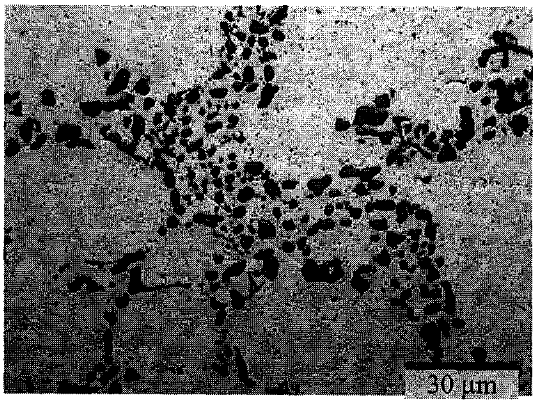

(b) 4 h

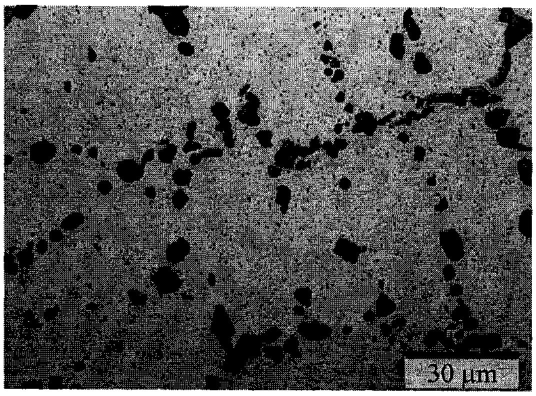

(c) 24 h

Figure 6.3 – High Magnification Micrographs Showing Effect of Solution Treatment Time on the Modified Microstructure in Alloy S:

(a) As-Cast, (b) After 4 h Solution Heat Treatment at 495 °C,
(c) After 24 h Solution Heat Treatment at 495 °C

The microstructural differences between unmodified and modified microstructures were greatly diminished with a longer solution treatment time (24 h). The prolonged solution heat treatment up to 24 h, led to a significant coarsening of the Si particles. The process by which the second phase particles coarsen and become larger is defined by Ostwald ripening [13]. This process involves the growth of larger particles at the expense of smaller ones. Consequently, the number of second phase particles decreases while their average size and spacing increases.

During solution heat treatment, incipient melting (Figure 4.4) can occur when the alloy composition exceeds the critical composition and the alloy is treated at a temperature higher than the eutectic temperature. In alloys with segregation of the alloying elements, the composition may locally exceed the critical composition, even though the mean composition is lower, and incipient melting will again occur [98, 100].

The subsequent artificial aging at 180 and 220 °C had relatively no effect on the Si microstructure in unmodified or modified samples. Figure 6.4 presents the different modified microstructures obtained after 4 h of solution heat treatment at 495 °C and an artificial aging of 2 h and 10 h at 180 °C and 220 °C. Figure 6.5 shows the different modified microstructures obtained after 24 h of solution heat treatment at 495 °C and an artificial aging of 2 h and 10 h at 180 °C and 220 °C.

Because the most common intermetallic phases found in these alloys are related to contamination with iron, which has a limited solubility in liquid aluminum, the iron level in this work was controlled (< 0.15 wt %). A short summary of the intermetallic phases encountered in this alloy is presented in Table 6.1. The composition of the major interdendritic phases obtained from energy dispersive X-ray (EDX) analysis is shown in Tables 5.4 and 5.5. The data are in general agreement with the results obtained by previous studies [96].

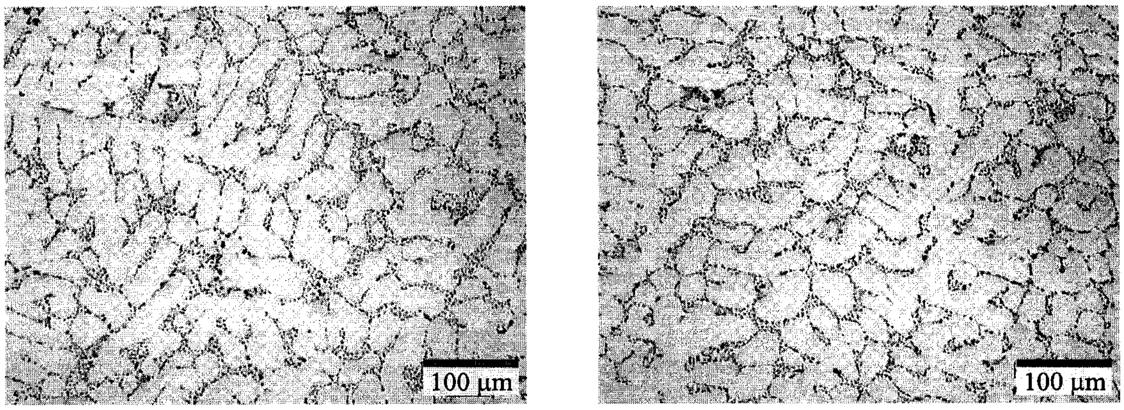

(a) After 2 h of Aging (b) After 10 h of Aging

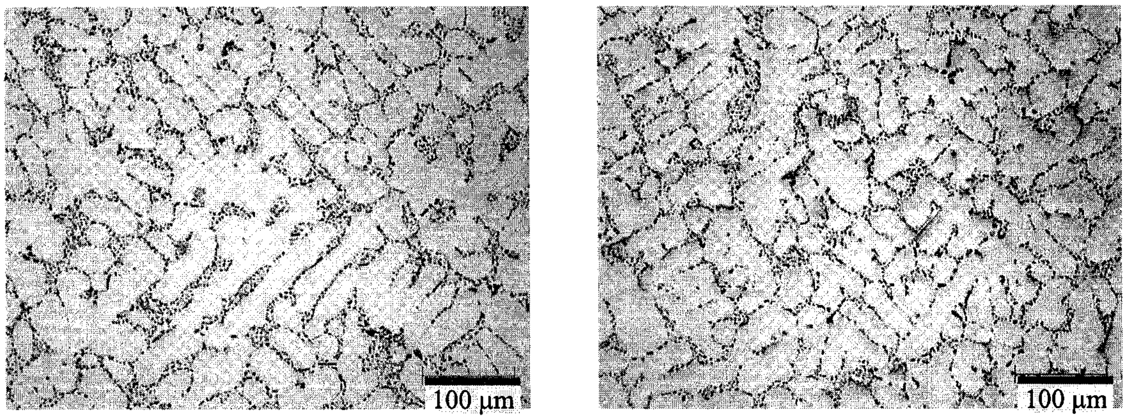

(c) After 2 h of Aging (d) After 10 h of Aging

Figure 6.4 – Microstructure of Alloy S Treated at 495 °C for 4 h, Showing:

(a, b) 180 °C Aging Temperature
(c, d) 220 °C Aging Temperature

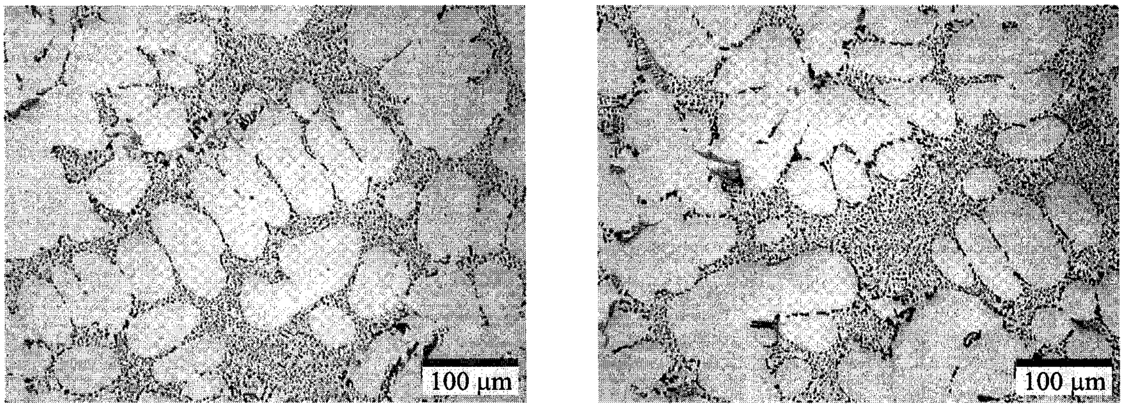

(a) After 2 h of Aging (b) After 10 h of Aging

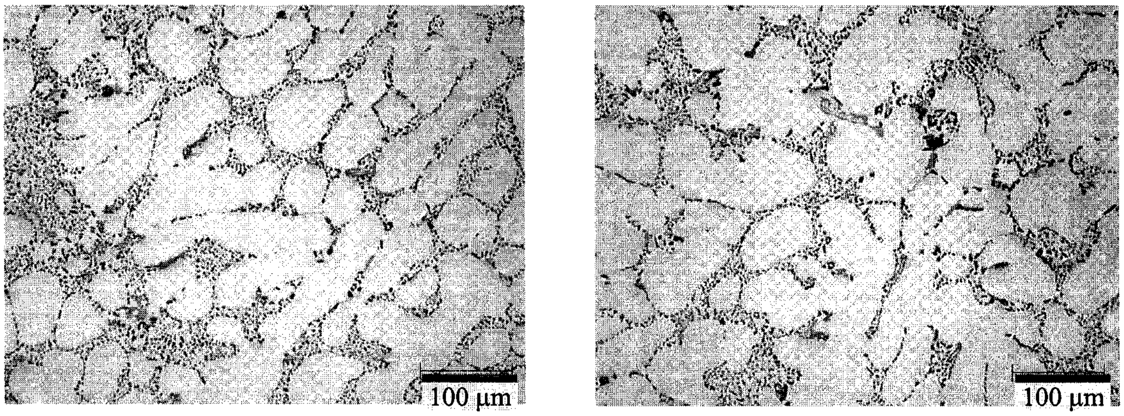

(c) After 2 h of Aging (d) After 10 h of Aging

Figure 6.5 – Microstructure of Alloy S Treated at 495 °C for 24 h, Showing:

(a, b) 180 °C Aging Temperature
(c, d) 220 °C Aging Temperature

In cast alloys, the morphology and nature of the intermetallics are controlled by the solidification rate and the chemical composition [7, 8, 30-42]. The solidification rate has a great impact on the kinetics and amount of iron-rich phases present in the microstructure. Higher cooling rates favor the formation of α-$Al_{15}(Fe, Mn)_3Si_2$ phase (commonly referred to as Chinese script type), whereas at lower cooling rates the formation of β-Al_5FeSi needles takes place [30-42, 61].

Figure 6.6 shows the morphology of the iron-rich phases present in alloy S. The transition between β-Al_5FeSi to α-$Al_{15}(Fe, Mn)_3Si_2$ takes place at slower rates as the amount of iron is reduced [37]. Several studies [7, 8, 30-42] have shown that such transition depends on the amount of Fe, Mn and Cr. Fe promotes β-Al_5FeSi formation, while Mn and Cr contribute to the stabilization of α-$Al_{15}(Fe, Mn)_3Si_2$ particles.

Table 6.1 – Intermetallic Phases in 319 Alloys

Reaction	Phases
Pre-dendritic	$Al_{15}(Fe, Mn)_3Si_2$
Post-dendritic	$Al_{15}(Fe, Mn)_3Si_2$, β-Al_5FeSi
Eutectic	β-Al_5FeSi, Mg_2Si
Post-eutectic	$Al_5Mg_8Cu_2Si_6$, $CuAl_2$

As the castings are heat treated, the solubility of the precipitated phases is not the only feature which changes. The morphology of intermetallic phases changes when the alloy is treated at high temperature for long periods of time. The morphology of β-phase platelets changes through concurrent fragmentation and dissolution at the plate tips, whereas the α-$Al_{15}(Fe, Mn)_3Si_2$ phase does not undergo any change. The Fe needles fragment and undergo gradual dissolution with prolonged solution treatments (24 h). The blocky Cu phase dissolves with increasing solution time and its dissolution rate decreases when modified.

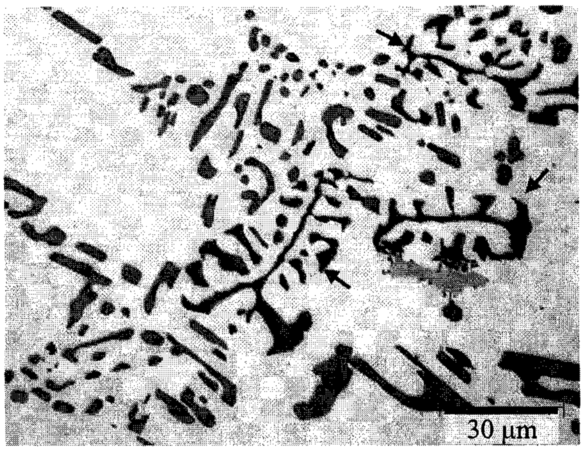

(a)

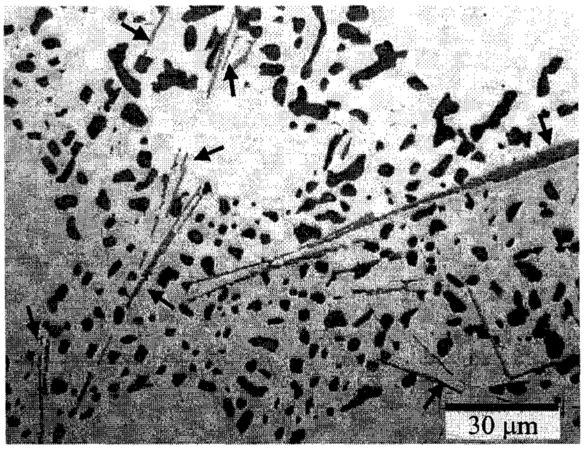

(b)

Figure 6.6 – High Magnification Micrographs Showing the Morphology of the Iron Rich Phases in Alloy S:

(a) Chinese Script Type α-$Al_{15}(Fe, Mn)_3Si_2$ Phase (Red Arrowed)
(b) Needles of β-Al_5FeSi Phase (Blue Arrowed)

The solution temperature is more critical than the solution time. A high solution temperature (over 530 °C) might be too high for an alloy containing any amount of the complex $Al_5Mg_8Cu_2Si_6$-$CuAl_2$, eutectic. Other authors [36, 102, 103] have reported an increase in porosity as well.

6.1.2. Secondary Dendrite Arm Spacing (SDAS)

Engineering castings can be improved by optimization of the secondary dendritic arm spacing (SDAS), since both mechanical and physical properties are enhanced when this parameter diminishes [28, 29]. The SDAS results of the as-cast and heat-treated coupons were shown in Tables 4.1 to 4.4. The SDAS results with their corresponding standard deviations are shown in Figures 6.7 to 6.10. It is seen that SDAS increases when increasing the solution heat treatment time. After 4 h of solution heat treatment, samples with Sr additions have higher SDAS than those without Sr additions (compare alloy A or M with alloy S or MS in Figure 6.7 and 6.8). On the other hand, this effect is not seen after longer solution heat treatment times (compare the same alloy but in Figures 6.9 and 6.10). Aging does not have a remarkable effect on the SDAS. At longer solution times and higher aging temperatures, the SDAS varies more and higher standard deviations are present (Figure 6.10).

6.1.3. Grain Size

The grain size results of the as-cast and heat-treated coupons were shown in Tables 4.5 to 4.8. The grain size results with their corresponding standard deviations are shown in Figures 6.11 to 6.14. Alloy S presents larger grains than the rest of the alloys. Longer solution heat treatment times promote grain growth. The latter effect is stronger in samples with Mg additions (alloy M), where the grain size increased 2 % after 4 h of solution heat treatment and increased 32 % after 24 h of solution heat treatment, whereas in alloy A, the grain size increased only 8 % after 24 h of solution heat treatment. The grain size increases linearly when aging time increases.

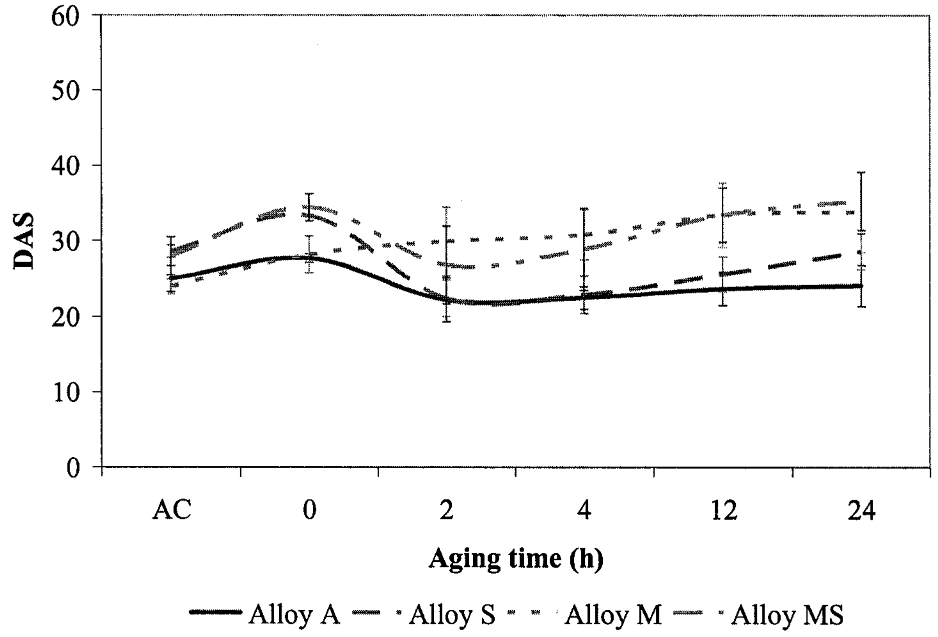

Figure 6.7 – Secondary Dendrite Arm Spacing Obtained from the Coupons (Solution Temperature 495 °C for 4 hours – Aging Temperature 180 °C)

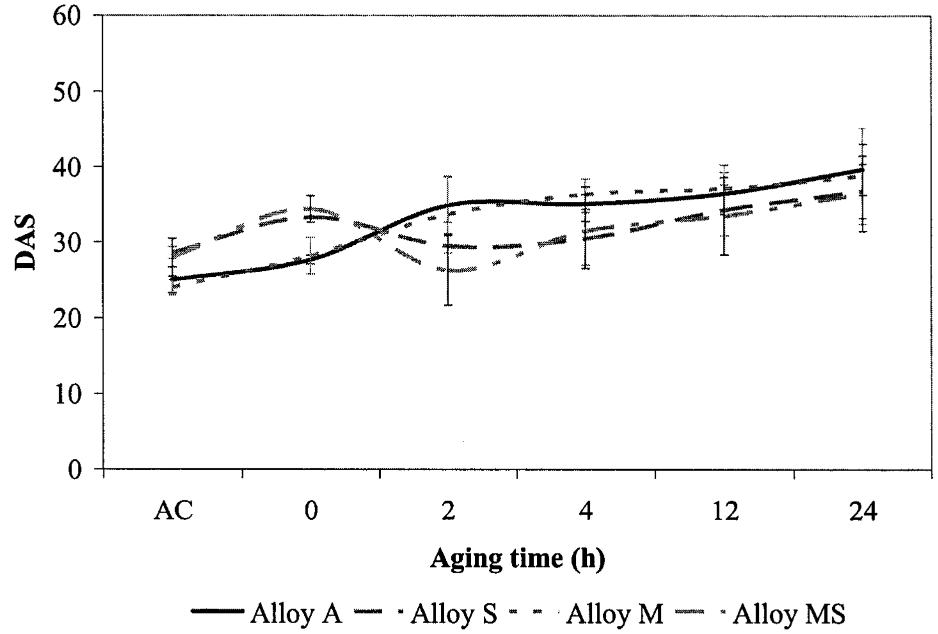

Figure 6.8 – Secondary Dendrite Arm Spacing Obtained from the Coupons (Solution Temperature 495 °C for 4 hours – Aging Temperature 220 °C)

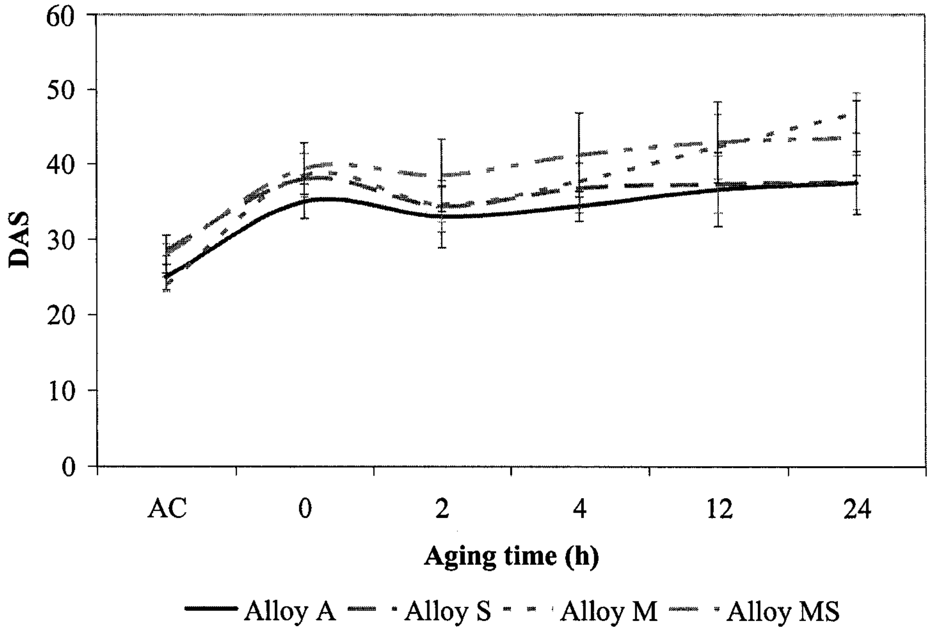

Figure 6.9 – Secondary Dendrite Arm Spacing Obtained from the Coupons (Solution Temperature 495 °C for 24 hours – Aging Temperature 180 °C)

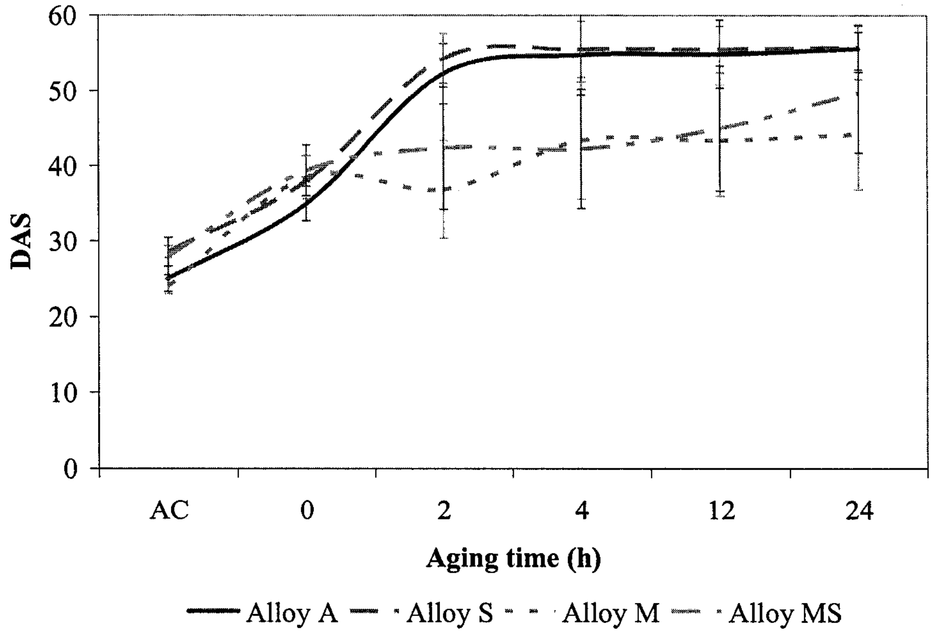

Figure 6.10 – Secondary Dendrite Arm Spacing Obtained from the Coupons (Solution Temperature 495 °C for 24 hours – Aging Temperature 220 °C)

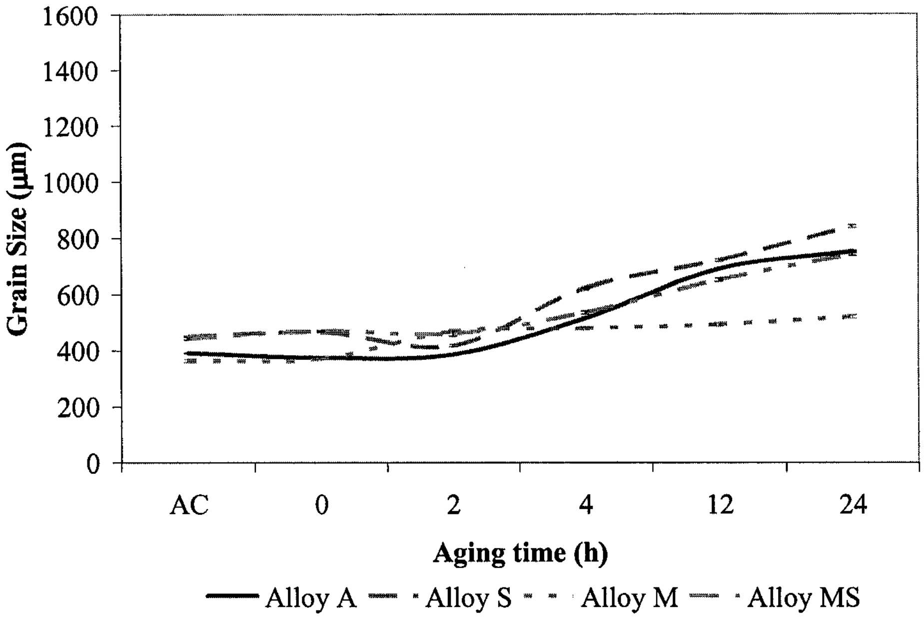

Figure 6.11 – Grain Size Obtained from the Coupons
(Solution Temperature 495 °C for 4 hours – Aging Temperature 180 °C)

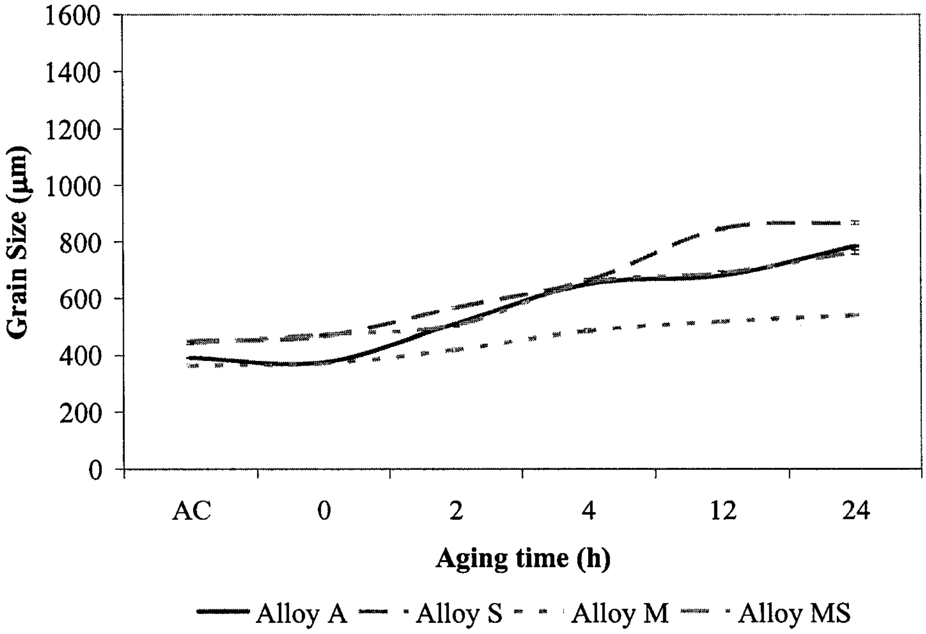

Figure 6.12 – Grain Size Obtained from the Coupons
(Solution Temperature 495 °C for 4 hours – Aging Temperature 220 °C)

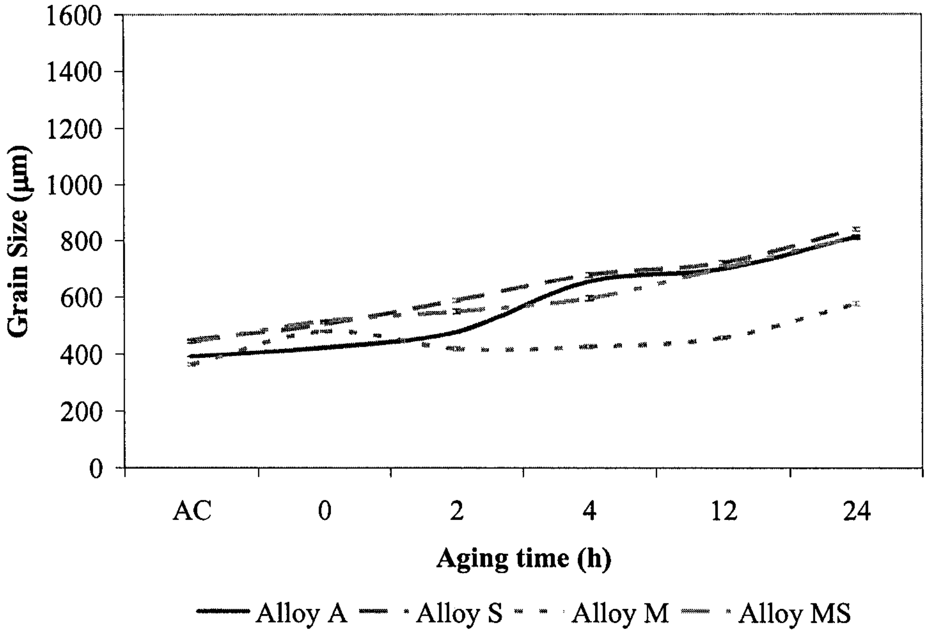

Figure 6.13 – Grain Size Obtained from the Coupons
(Solution Temperature 495 °C for 24 hours – Aging Temperature 180 °C)

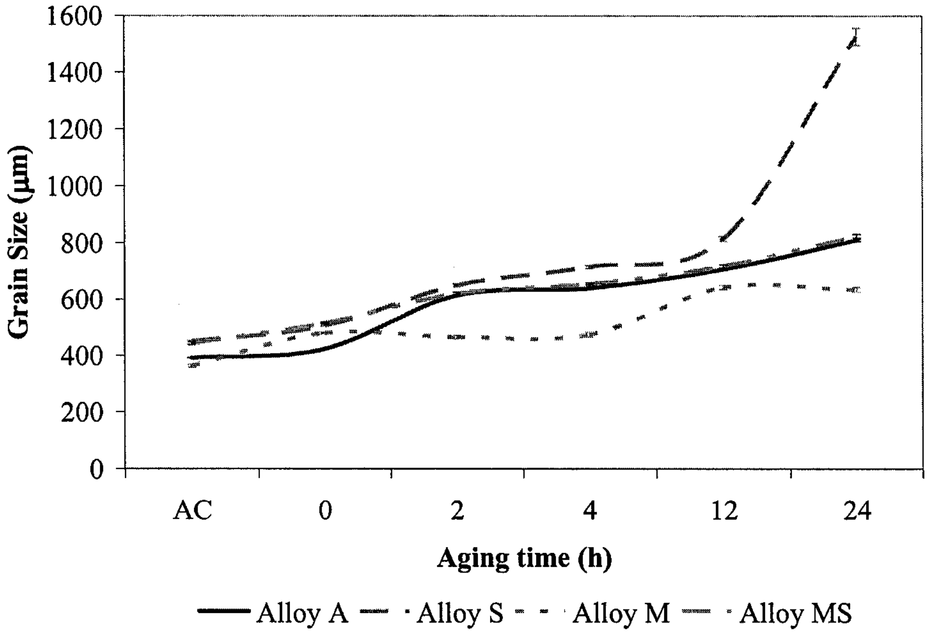

Figure 6.14 – Grain Size Obtained from the Coupons
(Solution Temperature 495 °C for 24 hours – Aging Temperature 220 °C)

6.2. Mechanical Properties

Many variables affect the mechanical properties in aluminum alloy castings, such as: the variation in the chemical composition within the specific limits of the alloy (especially Mg content); the casting soundness; the metallurgical characteristics (like grain size, constituent distribution and eutectic modification); the solidification rate and the heat treatment. Because it is possible to control grain size, constituent distribution and eutectic modification, then the major variations in mechanical properties come from the ability to control shrinkage and solidification rates in a casting.

6.2.1. Casting Soundness

To detect the presence of casting/solidification defects mainly associated with shrinkage and porosity in the tensile bars, all samples were X-rayed. The gage length was carefully examined to detect the presence of porosity or inclusions. The X-ray films facilitated the selection of sound samples. Most of the test bars were sound with negligible gas porosity (rated "slight" according to ASTM standards). The results indicated that porosity increased with modification.

6.2.2. Hardness

The 319.2 base alloy exhibits three main phases in addition to the aluminum solid solution: Si, $CuAl_2$ and β-Al_5FeSi. This alloy does not exhibit the common peak and overaged conditions associated with classical precipitation hardening processes. The complex metallurgy of 319 alloy likely leads to a series of precipitates which form sequentially, and become coherent or incoherent at different times. Thus, the hardening curves exhibit a series of peaks and valleys. The peaks correspond to times when one or more of these precipitates are able to add hardness to the alloy; the valleys correspond to conditions of overaging with respect to these particular precipitates. Subsequent precipitation of a different species is then able to add hardness resulting in another peak.

The maximum hardness during age hardening is obtained by partly incoherent precipitation (or intermediate phases). Larger particles tend to break away from the aluminum lattice, forming small crystals sometimes with aluminum atoms (such as $CuAl_2$) or intermetallic compounds of the foreign atoms such as $MgZn_2$ or Mg_2Si. In this case, the lattice structure of this precipitate is completely divergent from that of the aluminum matrix. The diameter of these precipitates and heterogeneities measures between 0.02 μm and 5 μm. Particles larger than approximately 1 μm in diameter are visible under an optical microscope.

The results indicate that modification has an influence in the Al matrix, as well as on the eutectic Si (Figures 4.12 and 4.13). The shorter the solution heat treatment, the smaller the difference existing between the unmodified and modified alloys. Spheroidization and coarsening of the eutectic Si occur at the elevated temperature of solution heat treatment or at prolonged times. The change in size and morphology of the discontinuous Si phase is significant since it directly influences the hardness. Thus, the modifier does have some effect on the metallurgy of the heat treatment process. The modified alloys (alloys S and MS) remain softer after artificial aging.

To determine the effectiveness of aging temperature and time on the hardness of alloy M (high Mg content, high volume fraction of intermetallics) coupons were treated similarly (same solution heat treatment conditions and aging times), as can be seen in Table 4.9. Prolonged aging treatment at 220 °C brought about significant changes in hardness. When the aging treatment temperature is raised from 210 to 220 °C, a remarkable aging response (decrease in VH by ~10 %) is exhibited by the unmodified high Mg-containing alloys.

Also, although the modified high Mg alloy apparently displays slightly lower hardness parameters compared to those obtained from the high Mg alloy, the consistency in the data is better. Due to improvement in the silicon particle spheroidization process, coupled with a greater dissolution of the $CuAl_2$ phase in the aluminum matrix, the hardness of the high magnesium alloy also decreases.

6.2.3. Tensile Properties

After solution heat treatment (4 h at 495 °C) and quenching, the alloy A possessed a YS of 177 MPa (Figure 4.18a). Aging either at 180 °C or at 220 °C slightly enhanced the YS level to 219 MPa only after 10 h. Other authors have reported that aging in the temperature range of 180-220 °C is characterized by the presence of peak-aging [55]. However, the maximum yield stress value diminished with the increase in the aging temperature. A noticeable softening was observed in samples with Sr additions when aged at 220 °C.

In cast samples with Mg additions, the YS was 228 MPa, and increased to 237 MPa under the T4 condition. As can be seen from Figures 4.18 and 4.19, each aging temperature reveals a peak aging. The maximum YS and aging time decreased with the increase in aging temperature. The maximum YS value (345 and 375 MPa) was obtained when the high Mg alloy was aged either for 0.5 h at 220 °C or 10 h at 180 °C.

In cast samples with Mg and Sr additions the YS was 213 MPa. After solution treatment, the YS value was 227 MPa. When the alloy was aged for 8 h at 180 °C, an increase by about 50 % was seen. Lower aging temperatures caused hardening in samples with Mg and Sr additions, although the obtained YS values were lower than in samples with Mg additions.

For the 319.2 alloy the UTS value for samples that were solution treated was about 310 MPa. A somewhat linear hardening resulted when using an aging temperature of 220 °C, with a decrease in the slope with decrease in aging temperature. The maximum UTS value was 320 MPa at 180 °C for 0.5 h. When adding Mg, there is a strong response to aging conditions and peak-aging was clearly distinguished. In the T4 condition a value of the order of 339 MPa was obtained. Peak-aging was clearly distinguished, but aging at higher temperature led to a more linear hardening. The maximum UTS level reached was 370 MPa, corresponding to either 4 h at 180 °C or 0.5 h at 220 °C.

As mentioned previously, the alloy with Mg and Sr additions had tensile properties lower than those with Mg. Prior to aging, the UTS value was 313 MPa. When aging at 220 °C a substantial increase to 349 MPa was observed, followed by an overaging effect. An inverse phenomenon was seen at 180 °C. The minimum UTS level (270 MPa) was obtained when aging at 220 °C for 5 h. In order to reach the peak-hardness, the time required decreased with the increase in aging temperature. The maximum UTS value was around 350 MPa, obtained at 180 °C for 4 h or at 220 °C for 0.5 h.

From the results, it can be seen that the addition of 0.40 % Mg to A319.2 alloy enhances the YS in the as-cast condition, maintaining a good level of UTS. When aged either at 180 °C or 200 °C for 8 h, the Mg additions increased the YS and UTS by 5 % and 44 %, respectively. For samples in the T4 condition, addition of Mg enhances the YS and UTS by ~31 % and ~2 %, upon aging at 180 °C or 220 °C for 8h.

Samples with Sr additions did not exhibit a remarkable difference in UTS, although other authors have reported a negative effect of Mg addition on the modification efficiency of Sr in 319 alloys [102-104]. Aging the samples with Mg and Sr additions at 180 °C and 220 °C for 4 h, showed increases in the YS and UTS by ~79 % and ~10-27 %, respectively, in comparison to the values obtained from the 319 alloy.

The decreases in hardness and tensile values with increasing aging time and temperature can be explained by the increased rate of growth of the precipitates at higher temperatures. As temperatures increase, so does the diffusion rate, which is defined as the atom's ability to move within the crystal lattice. For hardness, as the precipitates grow, the aluminum crystal lattice is strained, creating a hardening effect. Once the precipitates exceed a critical size, the lattice will shear and the crystal lattice strain will be reduced. When this occurs, the condition is termed "overaging" and lower hardness values are recorded [102, 105].

Tensile strength is also impacted when the precipitates exceed a critical size, but in this case it is related to the quantity and distribution of precipitates. Let us make the assumption that, initially, the precipitates are evenly distributed and uniformly sized. As a preferential precipitate grows, it draws atoms from the surrounding precipitates, which in turn reduces the total number of precipitates, which in turn reduces the total number of precipitates within the aluminum crystal lattice. With fewer precipitates present, the average distance or spacing between neighboring precipitates increases, and thus it is easier for slip plane movement to occur. This is an important point, due to the fact that the force required to cut through a precipitate is inversely proportional to the precipitate spacing. Once this critical size and precipitate spacing is reached, tensile strengths will begin to decrease.

Thus, UTS and hardness are optimum at low aging temperatures due to an increase in the number of precipitates being nucleated at lower temperatures. In the case of hardness as the precipitates grow, the increased quantity of them provides a uniform strain of the crystal lattice, resulting in higher hardness. Due to the lower aging temperatures, diffusion is slowed and maximum hardness is achieved at longer aging times.

For tensile strength, as opposed to what was previously stated for increased aging time and temperature, the greater the quantity of precipitates, the smaller the interparticle spacing and the greater the force required to cut through the precipitates. In addition, the greater quantity of precipitates will interface with the slip-planes by pinning the grain boundaries, thereby resulting in higher UTS.

From Tables 6.2 and 6.3, it is seen that the yield strength is unaffected by the microstructural changes associated with solution treatment or modification and depends primarily on the Mg content and the aging conditions. It is significant that heat treatment yields a somehow larger improvement in tensile properties than does modification.

Table 6.2 – Effect of the Composition on Tensile Properties and Vickers Hardness (VH) in As-Cast Condition Samples

Composition	UTS (MPa)	YS (MPa)	VH (5 Kgf)
A	279.28 ± 9.20	177.31 ± 2.23	68.75 ± 2.71
S	251.53 ± 1.39	161.20 ± 0.68	65.60 ± 4.88
M	313.16 ± 8.77	228.27 ± 6.69	87.54 ± 1.01
MS	269.45 ± 1.01	213.11 ± 0.98	82.55 ± 2.49

Table 6.3 – Effect of the Composition on Tensile Properties and Vickers Hardness (VH) in T4 Condition Samples

Composition	UTS (MPa)	YS (MPa)	VH (5 Kgf)
A	310.32 ± 6.95	178.61 ± 8.44	85.69 ± 0.46
S	291.09 ± 3.92	163.20 ± 1.99	84.60 ± 0.42
M	339.12 ± 0.84	237.22 ± 5.36	100.70 ± 2.36
MS	312.83 ± 8.88	227.29 ± 3.30	96.32 ± 1.81

6.3. Electron Probe Microanalyzer (EPMA) Results

The distribution of various elements within the aluminium dendrites was determined by performing quantitative line scans (5- or 10- µm steps) across aluminium dendrites. Figure 5.1 shows an example of this analysis for a modified high-Mg as-cast sample. The quantitative line scans were done along the major and minor axes of the dendrites (Table 5.1). The Cu concentration is a minimum (0.95 wt %) near the center of the dendrites, and increases (up to 3.7 wt %) at the edges.

A non uniform concentration across the aluminum dendrites was observed for Si, although its maximum concentration was at the center of the dendrite (1.18 wt %) and its minimum at the dendrite eutectic boundary (0.5 wt %). This non uniform distribution results from the non equilibrium solidification or coring [31]. The effect of coring seems to disappear after solution heat treatment.

After 4 h of solution treatment, the Cu concentration in the matrix around the $CuAl_2$ particles is ~4 wt %, whereas after 24 h of solution the Cu concentration is ~ 3.5 wt %. So, during the solution heat treatment, the Cu atoms diffuse in the matrix far away from the remaining $CuAl_2$ during the solution heat treatment. This is in agreement with other authors [3, 13, 98-100], that even after solution at 495 °C for 24 h, the dissolution of $CuAl_2$ occurs by diffusion of the Cu atoms in the outer layer of the $CuAl_2$ phase particles into the surrounding matrix, without changing the chemical composition of the remaining portions of the particles.

In alloy M and MS, the Si concentration in the matrix after 4 h of solution treatment decreases by 27 %. Prolonging the solution time does not seem to have an influence on the Si concentration in the matrix around $CuAl_2$ particles. On the other hand, in alloy M, the Mg concentration in the matrix doubled after 4 h of solution treatment. When the high Mg alloy is modified, the Mg concentration increases by 55 %. Further solution treatment has little influence on the Mg concentration in the matrix.

The effect of solution treatment time and aging temperature on the element content at the center of dendrites for alloys M and MS aged for 4 h is presented in Table 5.2. The presence of Sr in alloy MS promotes the precipitation of Cu- and Mg-rich phases and Si particles. In high Mg samples solution heat treated for 4 h, higher aging temperatures promote the precipitation of Cu, Mg and Si phases within the dendrites. When high Mg samples are modified and after solution heat treated for 4 h, higher aging temperatures do not promote the precipitation of Cu, Mg and Si phases within the dendrites. When high Mg samples are solutionized for longer times, there is an increase in the amount of elements distributed within the dendrites. An inverse phenomenon is seen when these samples are modified. Overall higher aging temperatures slightly decrease the element content at the center of the dendrites, except in high Mg samples solution heat treated for 4 h.

The line scans corresponding to alloy M in the as-cast and T4 condition (Figure 5.2) reveal the concentration gradients of Cu and Mg across the area containing the Cu- and Mg- phase particles. After 4 h of solution, the concentration gradient of Cu around $CuAl_2$ particles decreases 16 %, whereas that of Mg around $Al_5M_8Si_6Cu_2$ particles decreases ~39 % and increases again after 24 h of solution due to coarsening of the Mg phase particles. After 24 h of solution, the $CuAl_2$ phase was very small and dispersed, making its detection impossible.

The line scans for alloy MS (Figure 5.3), show that the concentration gradient of Cu around $CuAl_2$ particles remains stable during solution treatment, whereas that of Mg around $Al_5M_8Si_6Cu_2$ particles decreases ~20 % and increases after 24 h of solution due to coarsening of the Mg phase particles. The stable concentration gradient of Cu around $CuAl_2$ particles is attributable to the presence of Sr, since the rate of dissolution decreases with Sr concentration (compare Figure 5.5 b and e).

Figure 5.4 and later Figure 5.20 show that in modified high-Mg alloys segregation of $Al_5M_8Si_6Cu_2$ and $CuAl_2$ phase particles exists in areas away from the advancing interfaces of the eutectic silicon colonies. This results in a blocky morphology of the $CuAl_2$ phases, making their dissolution in the aluminum matrix very slow during solution heat treatment, as can be seen in Figure 5.5 and 5.6. The EDX spectra of the corresponding phases in samples in the as-cast and T4 conditions are seen in Figure 5.7, 5.8 and 5.9 respectively.

During aging, precipitation of second phase particles containing mainly Cu and Mg takes place (Figures 5.10 and 5.11). Such precipitated particles are too fine to be clearly examined by optical microscopy and even hard to detect by the beam of the electron probe.

Wavelength-dispersive X-ray maps analyzed the Al, Si, Cu, Mg and Fe distribution in alloy M and MS after 4 h of aging (Figures 5.12 to 5.15). Figures 5.16 to 5.19 show the Cu and Mg precipitates in alloy MS under different T6 heat treatments. It appears that at higher aging temperatures these precipitates are slightly larger independent of the solution time. However, it must be appreciated that the diameter of the beam limits the analysis of such fine precipitates.

The effect of solution treatment time and aging temperature on the precipitation of second phase particles for alloy MS aged for 4 h is presented in Figures 5.21 to Figure 5.24. From the figures, it is seen that when samples are solution heat treated for 4 h and aged at a higher temperature, Cu, Mg and Si precipitates are coarser but fewer in number. When samples are solution heat treated for longer times, there is a decrease in the amount of the second phase particles.

The results of the WDS analysis carried out on different phases found in the modified and unmodified high Mg alloys are summarized in Table 5.4 and 5.5.

6.4. Field Emission Scanning Electron Microscopy (FE-SEM) Results

To characterize the fine precipitates in the alloy M, an imaging technique capable of achieving good resolution and contrast at a magnification of roughly x100k was necessary. For such application, the selection of an appropriate detector is a significant factor in determining how charging, contrast and contamination will occur. As was pointed out by other authors [106], the FE-SEM can analyze small particles (below 50 nm) but the analysis in 'bulk' samples must be carried out at low voltages to preserve volume resolution, resulting in very weak signals. Thin foils were analyzed using relatively high voltages since the interaction volume effect is no longer a problem. Since an accelerating voltage of 10 kV gave the best results for the EDS analysis, this voltage was used to analyze smaller particles.

As was explained previously, hardening in this alloy occurs by cooperative precipitation of $CuAl_2$ and Mg_2Si phase particles. In the peak-aged conditions, the $CuAl_2$ and β'-Mg_2Si are metastable phases, coherent with the matrix. The size of these metastable phases increases with increase in either the time or temperature of the aging.

As a result, equilibrium θ ($CuAl_2$) and β' (Mg_2Si) phases in the form of incoherent particles are responsible for the observed drop in the alloy strength. The precipitated particles in the peak-aged condition are too fine to be clearly analyzed by optical microscopy. In the over-aged condition, the particles are visible and can be distinguished from the other dissolved phases.

The size and distribution of the precipitation in alloy M in the as-cast condition is presented in Figure 6.15, where large (300nm x 100nm) and small (50 nm x 25 nm) Si particles were detected. After solution heat treatment of the alloy, almost all particles remain in solution (Figure 6.16). When prolonged times are used, coarsening of Si, $CuAl_2$ and AlMgSiFeCu phases takes place (compare Figure 6.16b and 6.17b).

The size and distribution of the precipitation in alloy M after being solution heat treated at 495 °C for 4 h and aged at 180 °C for 2, 4, 6, 12 and 24 h is presented in Figures 6.18, 6.19, 6.20, 6.21 and 6.22, respectively.

The homogeneous distribution of the precipitated particles throughout the matrix, when the tensile properties were in the peak-aged condition and represent a maximum, can be seen in Figure 6.19 and 6.21. These figures correspond to samples solutionized for 4 h at 495 °C and aged at 180 °C for 4 h and 12 h, respectively. The size of the particles varies between 5 μm x 500 nm x 50 nm (length x width x diameter) when aged for 4h and 500 nm x 100nm x 100 nm (length x width x diameter) after 12 h of aging.

The increase in the number and the distribution of the very fine Cu and Mg precipitates after 4 h of aging, can explain the increase in strength reported for this condition. After 12 h of aging, strength can be explained due to the large amount of Cu and Mg precipitation throughout the sample and the existence of large coherent $CuAl_2$ phase particles. No definite particle boundaries can be seen and the corresponding EDX spectrum (Figure 6.23) reveals diffused Mg and Cu reflections, indicating the coherency of the particles with the matrix.

Samples that report a minimum on the hardening curve can be seen in Figures 6.18 and 6.20, and correspond to samples aged for 2 h and 6 h, respectively. After 2 h of aging, there is no detectable fine precipitation within the matrix, but coarse Si particles of ~ 1 μm and Cu particles of 40-80 nm are present. When aged for 6 h, the size of the particles varies between 500 nm x 100 nm x 100 nm (length x width x diameter). A remarkable increase in the size and number of small precipitates (~40 to 80 nm of diameter) was seen after 6 h of aging.

When the sample is overaged (Figure 6.21 and 6.22), two phases were identified, namely $CuAl_2$ and Mg_2Si. The large $CuAl_2$ phase particles have defined boundaries indicating their coherency with the matrix. The associated EDX spectrum reveals strong Mg and Cu reflections compared to the ones of the peak-aged condition (Figure 6.23).

Figure 6.24 shows the effect of Sr on the high Mg alloy after solution at 495 °C for 4 h and aging at 180 °C for 4 h. An increased amount of precipitation is seen in modified samples, along with a segregation of $Al_5Mg_8Si_6Cu_2$ and $CuAl_2$ phases.

FE-SEM was used to successfully characterize Cu and Mg precipitates as fine as 50 nm (comparable to the capabilities of a TEM). It was found that increasing the accelerating voltage from 5 kV to 30 kV improved the EDS acquisition. This improvement is due to its advantage on the high peak-to-background ratio inherent in thin specimens, such as in thin foils, due to their small interaction volume.

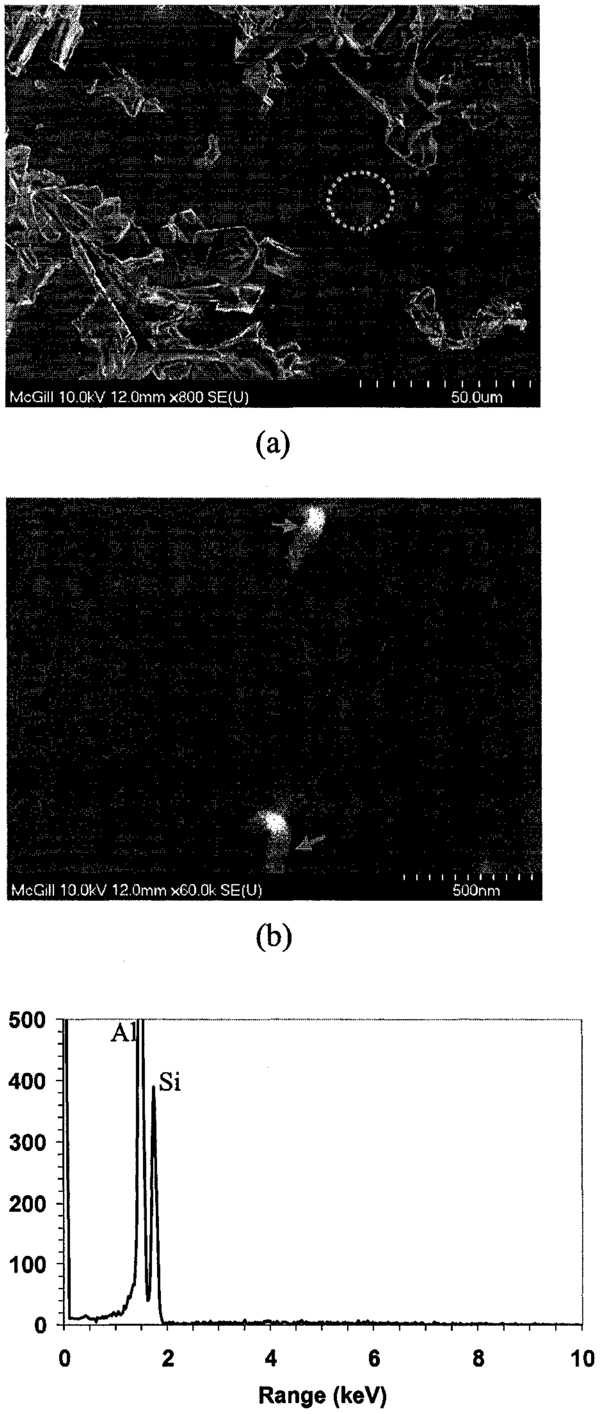

(a)

(b)

(c)

Figure 6.15 – Alloy M Showing:
(a) Si Containing Phase (Blue Arrowed) Precipitation
(b) Magnified View of the Circled Area Showed in (a)
(c) EDS Spectra Corresponding to the Phases Present

In the As-Cast Condition

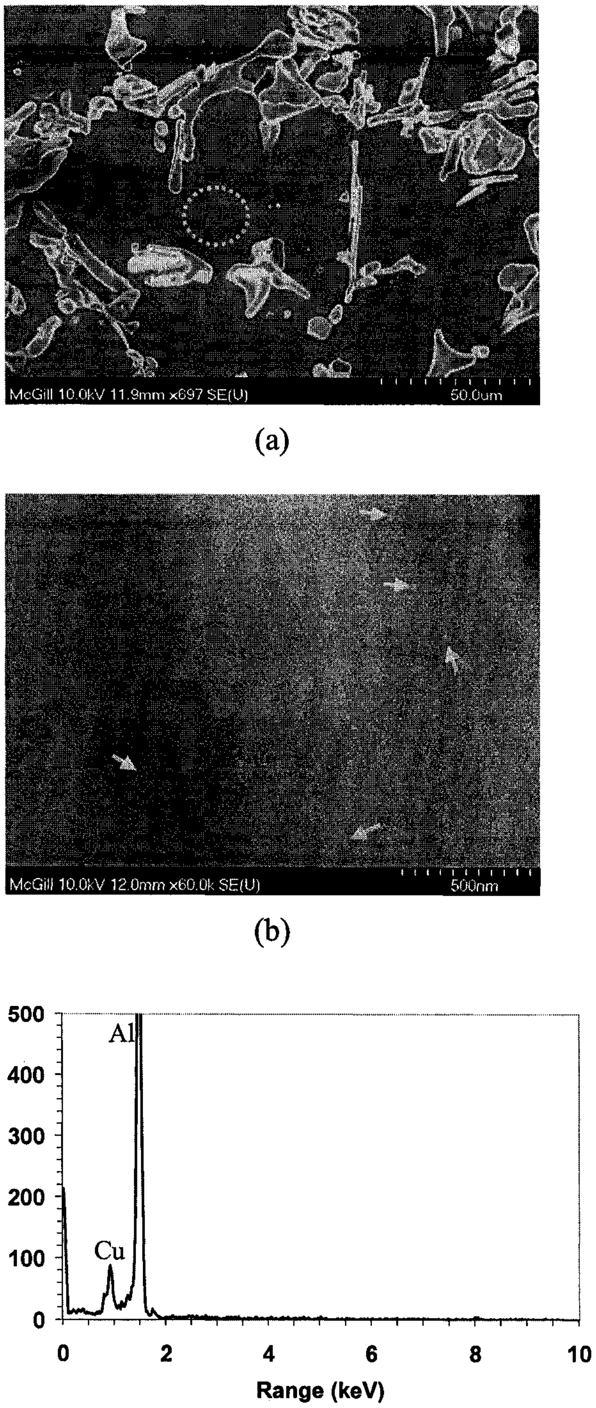

(a)

(b)

(c)

Figure 6.16 – Alloy M Showing:
(a) Cu Containing Phase (Yellow Arrowed) Precipitation
(b) Magnified View of the Circled Area Showed in (a)
(c) EDS Spectra Corresponding to the Phases Present

After Solution Heat Treated at 495 °C for 4 h

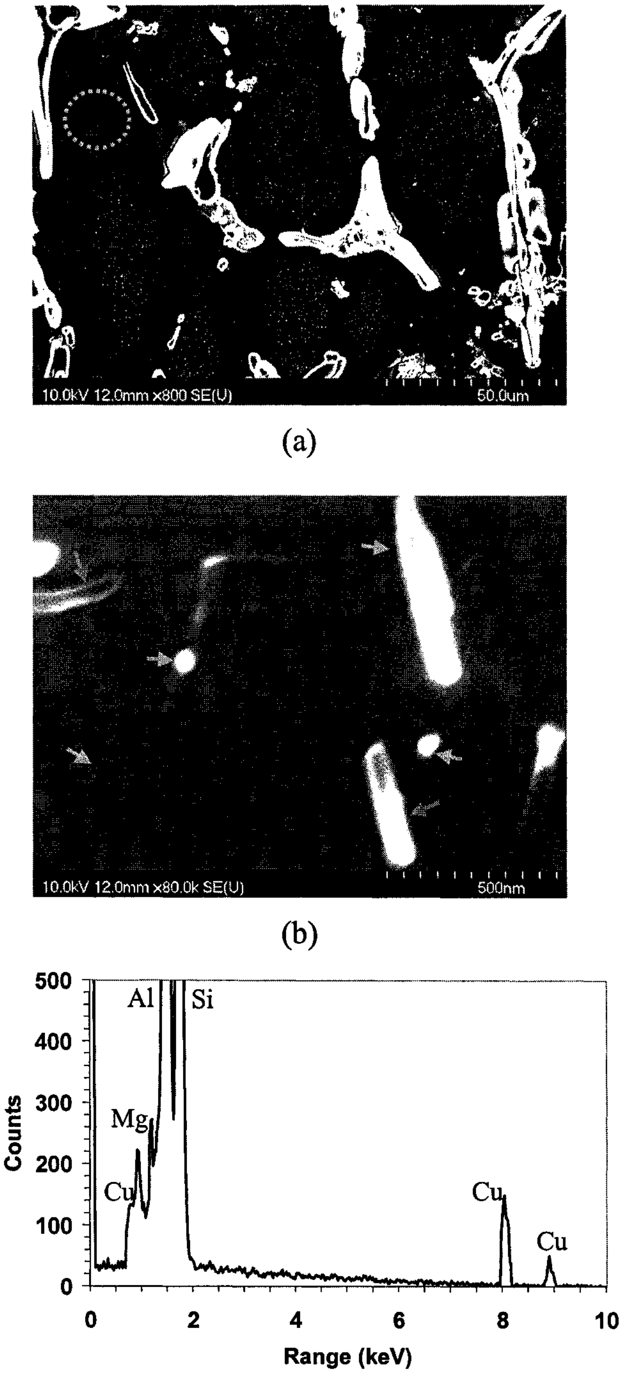

(a)

(b)

(c)

Figure 6.17 – Alloy M Showing:

(a) Cu Containing Phase (Yellow Arrowed), Mg Containing Phase (Red Arrowed) and Si Containing Phase (Blue Arrowed) Precipitation

(b) Magnified View of the Circled Area Showed in (a)

(c) EDS Spectra Corresponding to the Phases Present

After Solution Heat Treated at 495 °C for 24 h

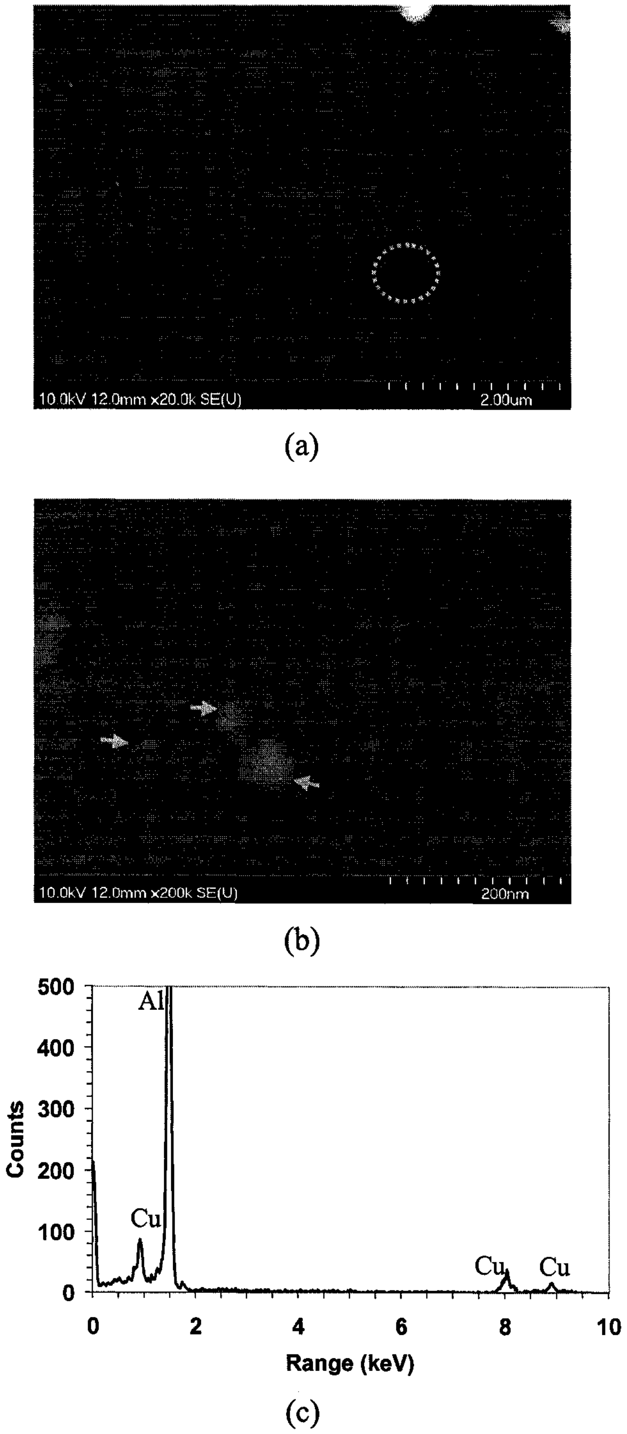

Figure 6.18 – Alloy M Showing:
(a) Cu Containing Phase (Yellow Arrowed) Precipitation
(b) Magnified View of the Circled Area Showed in (a)
(c) EDS Spectra Corresponding to the Phases Present

After Solution Heat Treated at 495 °C for 4 h and Aged at 180 °C for 2 h

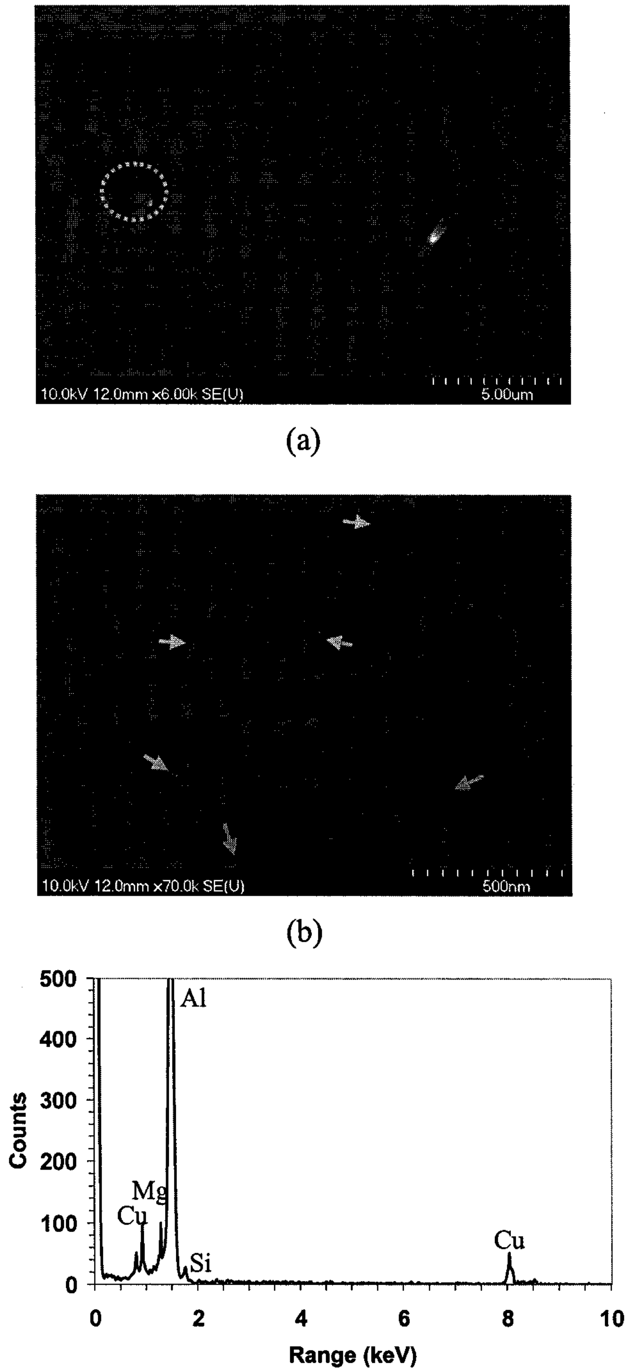

(a)

(b)

(c)

Figure 6.19 – Alloy M Showing:
(a) Cu Containing Phase (Yellow Arrowed), Mg Containing Phase (Red Arrowed) and Si Containing Phase (Blue Arrowed) Precipitation
(b) Magnified View of the Circled Area Showed in (a)
(c) EDS Spectra Corresponding to the Phases Present

After Solution Heat Treated at 495 °C for 4 h and Aged at 180 °C for 4 h

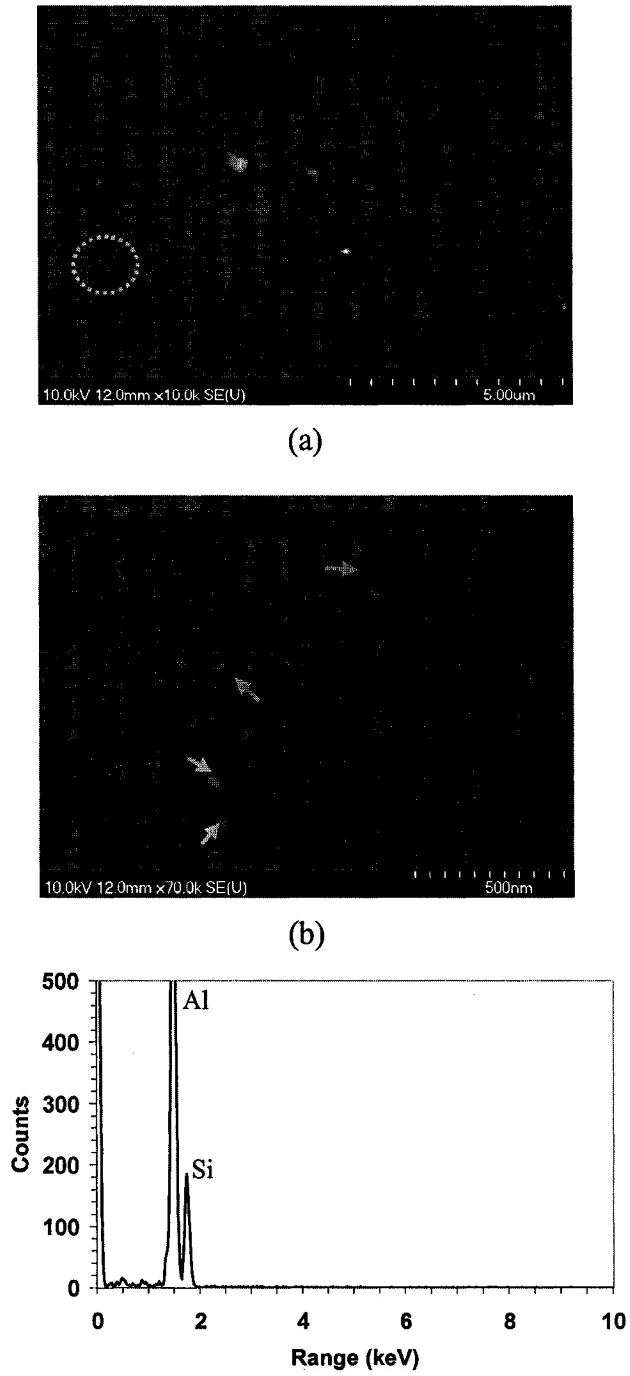

(a)

(b)

(c)

Figure 6.20 – Alloy M Showing:
(a) Cu Containing Phase (Yellow Arrowed), Mg Containing Phase (Red Arrowed) and Si Containing Phase (Blue Arrowed) Precipitation
(b) Magnified View of the Circled Area Showed in (a)
(c) EDS Spectra Corresponding to the Phases Present

After Solution Heat Treated at 495 °C for 4 h and Aged at 180 °C for 6 h

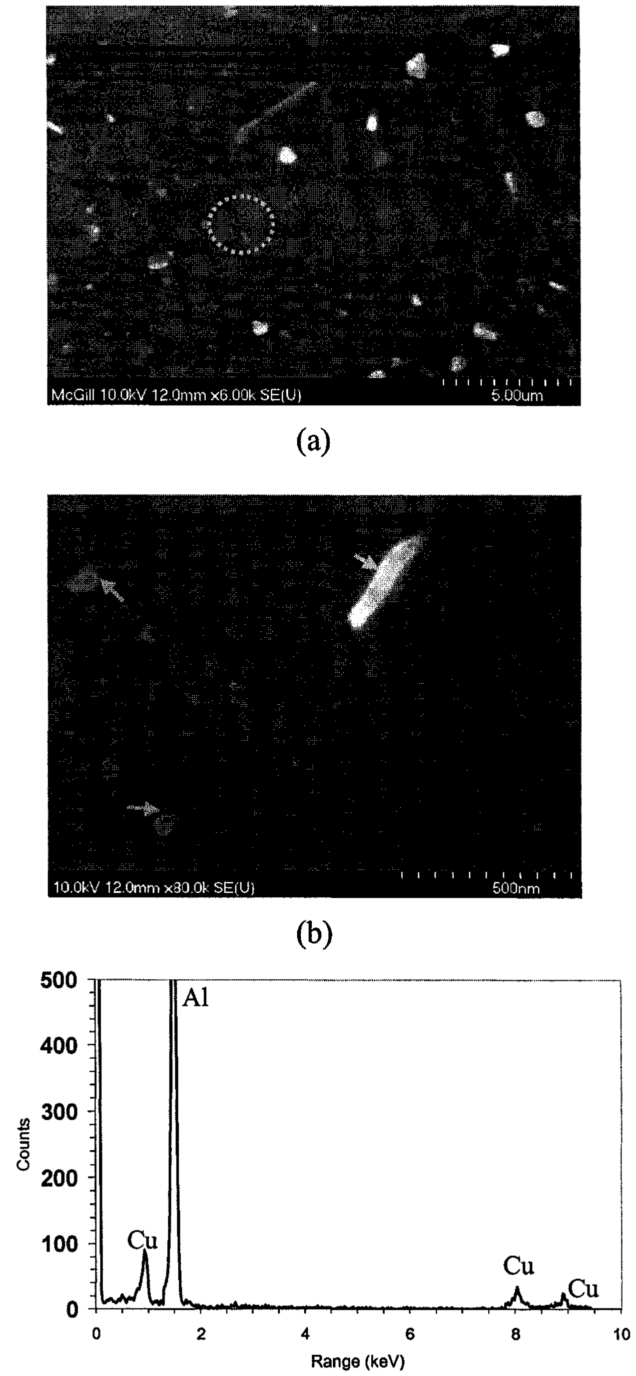

(a)

(b)

(c)

Figure 6.21 – Alloy M Showing:
(a) Cu Containing Phase (Yellow Arrowed), Mg Containing Phase (Red Arrowed) and Si Containing Phase (Blue Arrowed) Precipitation
(b) Magnified View of the Circled Area Showed in (a)
(c) EDS Spectra Corresponding to the Phases Present

After Solution Heat Treated at 495 °C for 4 h and Aged at 180 °C for 12 h

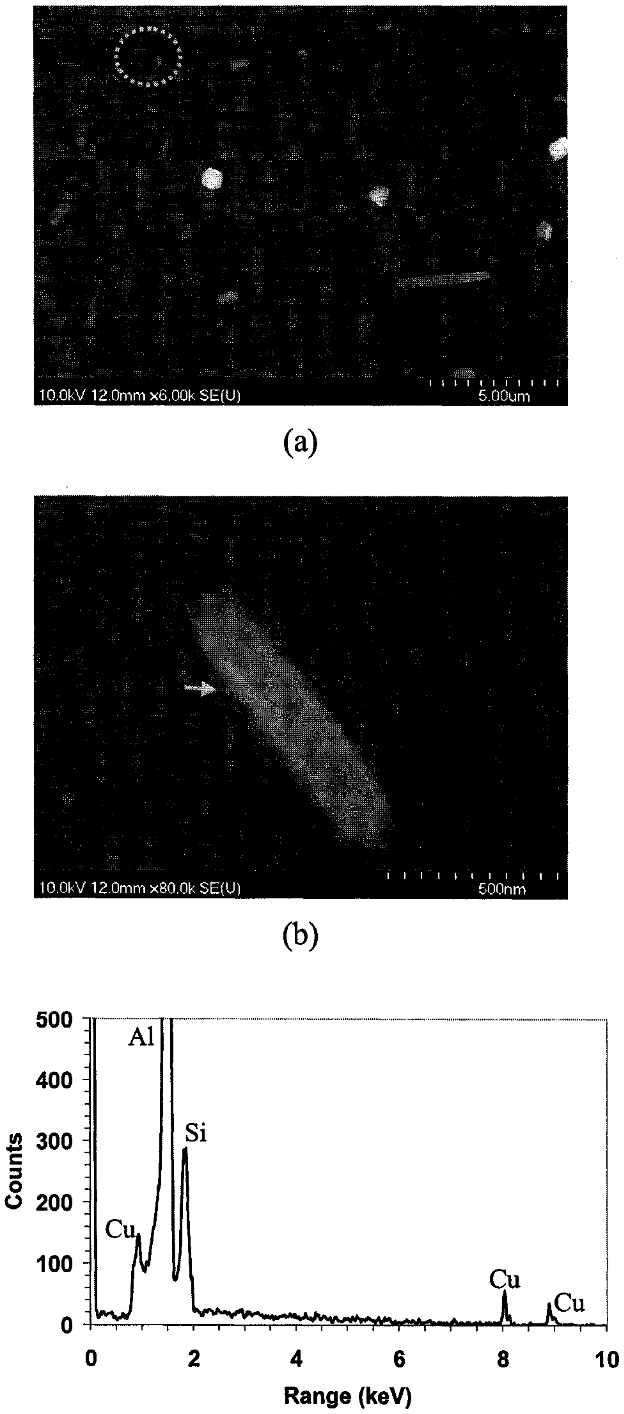

(a)

(b)

(c)

Figure 6.22 – Alloy M Showing:
(a) Cu Containing Phase (Yellow Arrowed) Precipitation
(b) Magnified View of the Circled Area Showed in (a)
(c) EDS Spectra Corresponding to the Phases Present

After Solution Heat Treated at 495 °C for 4 h and Aged at 180 °C for 24 h

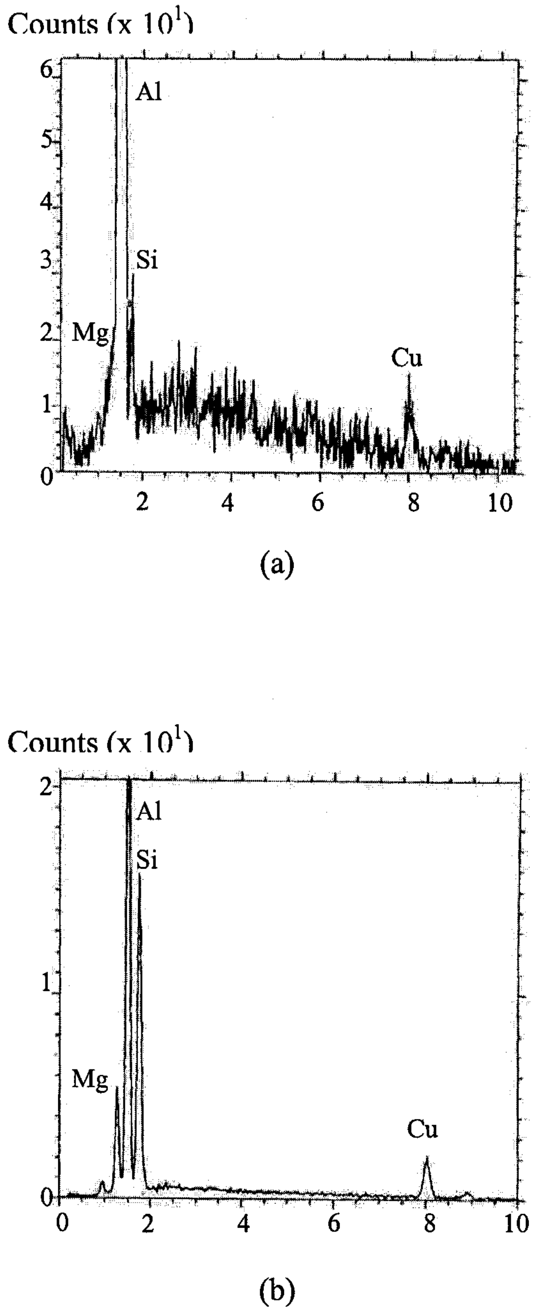

Figure 6.23 – EDXs Corresponding to Precipitation in Alloy M After Solution Heat Treated at 495 °C for 4 h and Aged at 180 °C, Showing:

(a) Peak-Aged Condition After 4 h of Aging
(b) Over-Aged Condition After 24 h of Aging

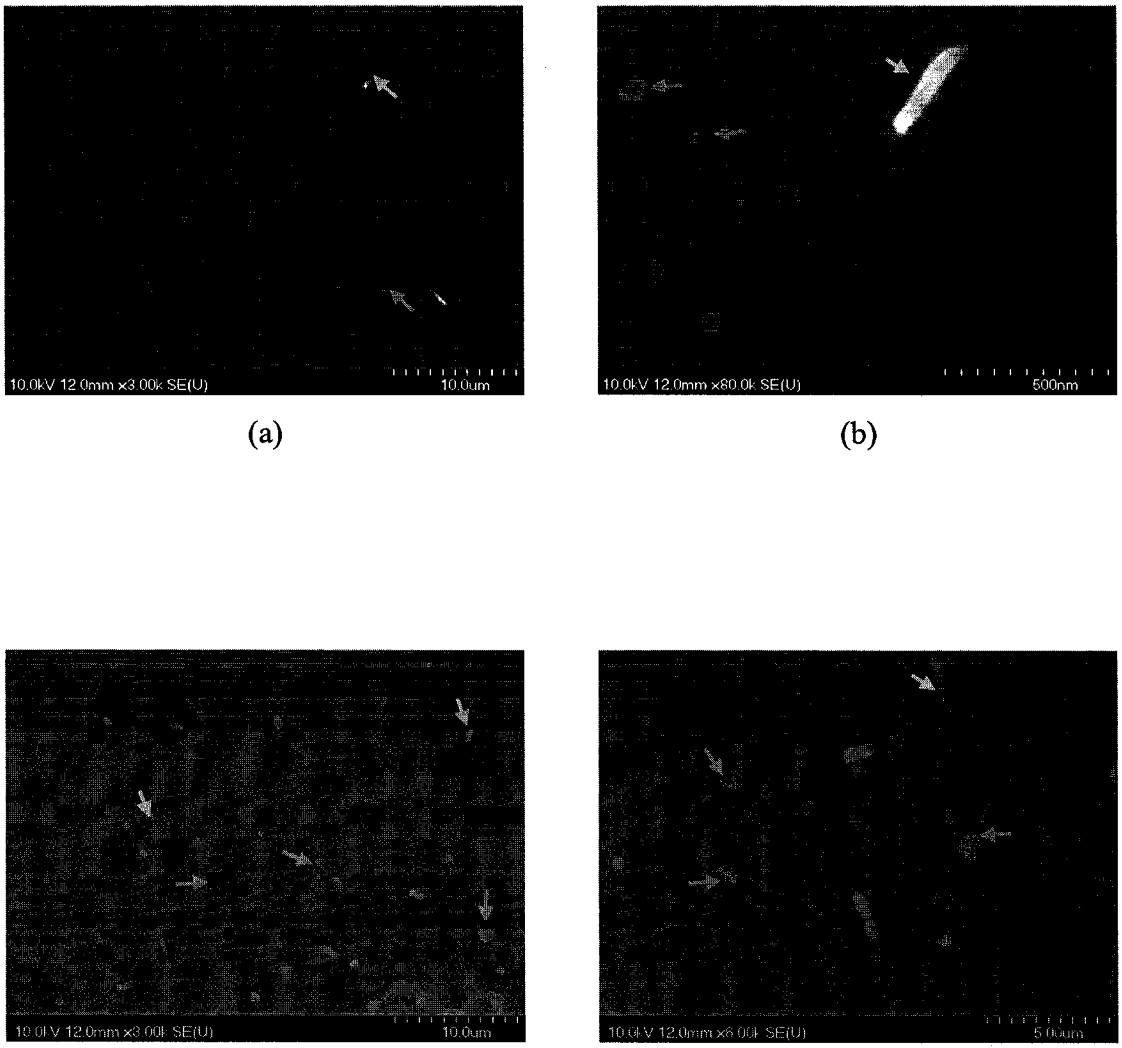

(a) (b)

(c) (d)

Figure 6.24 –Size and Distribution of Cu Containing Phase (Yellow Arrowed), Mg Containing Phase (Red Arrowed) and Si Containing Phase (Blue Arrowed) Precipitation

After Solution Heat Treated at 495 °C for 4 h and Aged at 180 °C for 4 h Showing:

(a, b) Alloy M
(c, d) Alloy MS

6.5. Transmission Electron Microscopy (TEM) Results

Understanding the age-hardening curves requires TEM analysis of the aluminum dendrites. It is apparent from the microstructural observations, that 319 alloy is complex, with a variety of particles and precipitates which exceed that normally encountered in most cast aluminum alloys. Along with the existence of large particles of silicon and intermetallics -which has long been recognized-, this alloy exhibits the presence of smaller precipitates in the aluminum matrix. Such small precipitates can contribute to the strength of the alloy to some degree. In the age-hardening process of Al-Si-Cu-Mg alloy, GP zones and metastable phases can strengthen alloys and lead to the aging peak.

Fine and profuse GP zones are distributed homogeneously in the matrix in the early stage of aging, and their strengthening effects are significant. Metastable phases at intermediate aging in semi-coherency with the matrix, are resistant to the movement of dislocations, and thus have a certain strengthening effect [8, 13, 97, 98]. However, the GP zones dissolve before the metastable phase formation in the precipitation sequence of Al-Si-Cu-Mg alloy [3]. Other authors have reported that the θ phase has been nucleated on dislocations [3, 99, 100]. These plate-like metastable phases are nucleated and grow on dislocations at the expense of fine and uniformly dispersed GP zones.

In the transition from GP zones to metastable phases, the number of GP zones decreases significantly by dissolution, while the metastable precipitates have not grown enough and their size is too small to resist the movement of dislocations. Therefore, the age-hardening effect of the alloy is low at this stage, and this can explain the lower hardness in valleys between two aging peaks.

The continuous transition from GP zones to the metastable phase may be responsible for the hardness plateau presented along the aging-curve.

From the TEM observations and measurements of tensile strength, important strengthening precipitates have been identified; namely Si plates and particles, $CuMgAl_2$ and Mg_2Si. The relative contributions of these precipitates depend very strongly upon the Mg concentration in the aluminum matrix which is in turn controlled by the thermal history. Minor species do not contribute significantly to strength, among them: the two quaternary precipitates (Q phase or $Al_5Cu_2Mg_7Si_7$ and AlCuMgSi), the Si rods, the Si laths, and the $CuAl_2$ precipitates.

Additionally to θ' precipitation, very small precipitates can be seen in the form of dark points or small needles. The diffraction pattern from these precipitates is similar to that from θ', but the streaks are stronger and some additional maxima can be identified within them. They result most probably from the presence of S' ($CuAl_2Mg$) phase. Computer simulations of the S' reflections done by other studies [6, 102-106] show that S' reflections are hidden within the streaks of θ'. Eskin et al. [2-6, 55. 105] suggested that the small plates are the β" phase, but his supposition was based only on the morphology, not the diffraction evidence.

Silicon forms precipitates in the aluminum matrix with four distinct morphologies, as illustrated by the transmission electron micrographs in Figure 5.30. The most common form of Si consists of small almost *spherical particles* ~50 nm in diameter. These precipitates seldom grow any larger than 50 nm in diameter even after aging for 24 h at 220 °C. They consist of multiple domains due to the intersecting twins which impinge on each other and arrest further growth of the particle (Figure 5.30a).

Silicon *rods* were observed as a minor constituent, typically 200 nm long and 10 nm in diameter and aligned along the <100> axis of the aluminum lattice (Figure 5.30b).

Silicon can be present in the form of *plates* 500-1000 nm long and 10-30 nm thick, oriented almost parallel to the [100] plane of the aluminum lattice (Figure 5.30c).

Another minor form of Si consists of very *large laths* with a rod-like morphology typically 5 μm long and 1 μm thick. These large precipitates are internally twinned on planes parallel to their length (Figure 5.30d).

The high concentration of Cu in the 319 aluminum alloys promotes the binary precipitate $CuAl_2$ (θ') to a major role in the T6 temper. These plates are typically 50-100 nm in diameter and 10 nm thick and are oriented parallel to the [100] plane of the aluminum lattice. In the overaged condition some of the θ' converts to θ particles (Figure 5.30e).

The binary precipitate Mg_2Si (β') is found only as a very minor species. These needles are typically 50 nm long and 5 nm in diameter, oriented parallel to the <100> direction of the aluminum lattice. The only ternary precipitate observed is the $CuMgAl_2$ (S') phase in the form of rods typically 100 nm long and 10 nm thick oriented parallel to the <100> axis of the aluminum. They nucleate heterogeneously on either dislocations or on very small particles of a quaternary phase (Figure 5.30f).

6.6. Precipitation Processes

It was believed previously that natural aging occurred in heat-treatable aluminum alloys together with zone formation, while artificial aging brought about incoherent precipitation.

The structural changes during the age-hardening process, in reality, are not so easy to distinguish. With increasing aging temperatures, different decomposition and precipitation processes take place in sequence, in some cases, and simultaneously in others. This can be shown in detail by considering the 319 alloy of this study. In this alloy, five stages of structural changes can be determined during the heat-treating operations. These are summarized in Table 6.4.

Table 6.4 – Age Hardening Behavior of Alloy M

Stage	Heat Treatment	Phases
I	None	Mostly precipitated as equilibrium $CuAl_2$ phases (point A)
II	Solution treatment and rapid cooling	All Cu in solution Most Mg phases in solution (point B)
III	Natural aging at room temperature	Segregation into GP I zones (coherent)
IV	Age hardening at 180 °C	Dissolution of GP I zones Segregation into GP II zones (coherent) Precipitation of S' phase ($CuAl_2Mg$) (point C)
	Further age hardening at 180 °C	Increased diffusion into GP II zones and precipitation as θ phase (partially coherent) (point D and E) Precipitation of S' phase ($CuAl_2Mg$) (point E and F) Precipitation of β" phase (Point E and F) Precipitation of traces of Si (Point G)
V	Overaging resulting from treatment time too long	Precipitated as θ phase, the equilibrium phase (incoherent) (Point G and H)

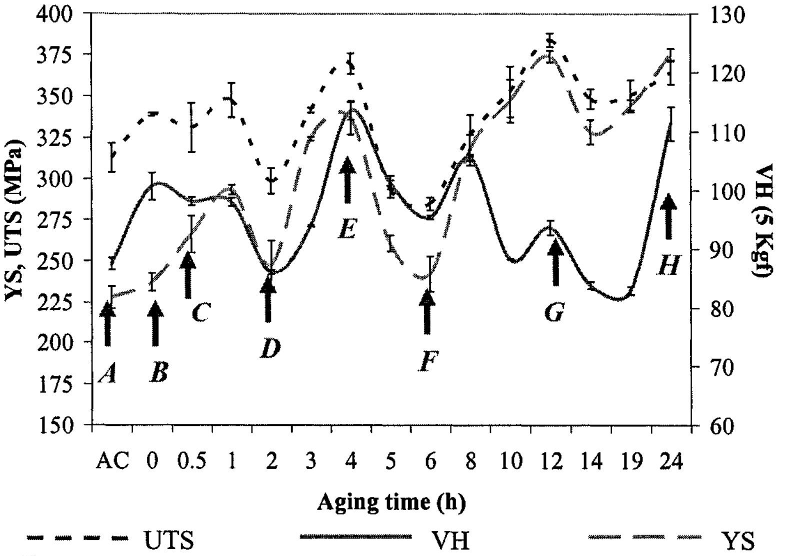

Tensile Properties and Vickers Hardness (VH) After 4 h of Solution Treatment at 495 °C and Aged at 180 °C

The first stage represents the structure prior to solution heat treatment. The precipitates may originate either in the cast structure or in any previous thermal treatment. In the second stage, the copper atoms that had precipitated previously are taken into solution at 500 °C. This solution heat treatment also removes any previous cold work or precipitation hardening. The material is then quenched from the solution-treatment temperature to room temperature, developing helical dislocations.

During natural aging, the dissociation of the supersaturated solid solution begins by coherent precipitation of copper-rich GP zones only a few atoms thick. These precipitates stress the aluminum lattice, and because of their great number, form a dense network that impedes the movement of dislocations during deformation. The extremely small zones that originate at room temperature are called GP I zones and do not grow more during subsequent artificial aging, but actually re-dissolve in a short time at temperatures between 150 to 200 °C, leading to a temporary reduction in hardness. This regression suggests that the arrangement of the strengthening atoms, after artificial aging, is basically different from that after natural aging. Artificial aging at elevated temperatures causes new enrichment of copper atoms in GP II zones soon after the end of the reversion.

As the artificial aging continues at approximately 180-220 °C, the formation of a metastable phase, θ, takes place, which corresponds to the equilibrium phase $CuAl_2$ in composition, but has a different crystal lattice. Maximum hardness is obtained during the appearance of the GP II zones and sometimes for a mixture of GP II, θ' and a mixture of S' + θ' + β" and precipitating Si.

Some authors [2-6], have reported that they observed Q' phase, but these precipitates have electron diffraction patterns very close to that of the β" (or β') phase. Copper and excess silicon refine β" precipitates, Mg facilitates the formation of the θ' phase instead of θ" [5, 6].

As soon as only θ' particles are present, the stage of overaging is attained, characterized by a reduction in hardness, tensile strength, and elongation. When aged at longer times, the equilibrium phase $CuAl_2$ forms a relatively coarse precipitate, which is visible under the optical microscope.

The change of phase composition affects the aging response and mechanical properties of alloys. Impurities and small additions can considerably affect the hardening effect of Al-Si-Cu-Mg alloys, mainly due to the binding of main alloying elements in insoluble particles and to the decreasing content of copper and magnesium in the supersaturated solid solution.

From this study it can be seen that multiple aging peaks in the age hardening curves of 319-type alloys are present. Although some of the minor peaks will tend to be overlooked when plotting these curves within the 95 % confidence limit, the major peaks stay and are very well distinguished on the age hardening curves. Multiple aging peaks have not been studied in deep previously partly because aging phenomena is not seen in long time frames and partly because sometimes these multiple peaks tend to be overlooked.

CHAPTER 7

CONCLUSIONS

The Al-Si-Cu alloy system is of great importance in the casting industry. The addition of Mg increases considerably the strength of the alloy after aging treatment. The mechanisms of strengthening are challenging due to several alloying additions and resulting complexity of phase transitions. Based on the theoretical and experimental investigation the conclusions that can be drawn from this research are summarized as follows:

- The alloy does not exhibit the common peak-overaging conditions normally found in the literature. This is due to the presence of sequential precipitation of different species during the aging process.

- Except for the modification of the Si phase, Sr has few influences on the hardening mechanisms.

- The increased Mg content (up to 0.40 wt %) in some of the samples results in higher hardness. This may be due to the increased amount of $Al_5Mg_8Cu_2Si_6$ phase presented.

- Hardness is less sensitive to overaging at lower aging temperatures.

- Higher solution times promote higher hardness in samples with high Mg content, but an inversed phenomenon is seen for the unmodified and modified alloys.

- In the unmodified and modified alloys, hardness decreases with increasing aging time and temperature.

- In samples solution heat treated at 495 °C, the highest hardness occurs:

    - A319.2
      Solution heat treated for 24 h and artificially aged at 220 °C for 2 h
    - A319.2 + Sr
      Solution heat treated for 24 h and artificially aged at 180 °C for 3 h
    - A319.2 + Mg
      Solution heat treated for 4 h and artificially aged at 220 °C for 2 h
    - A319.2 + Mg + Sr
      Solution heat treated for 4 h and artificially aged at 220 °C for 6 h

- In the age-hardening curves of Al-Si-Cu-Mg alloys, multiple aging peaks are present.

- Hardness plateau and weaker peaks are present in age-hardening curves of modified and unmodified Al-Si-Cu alloys.

- In the case of the high Mg content alloy, after 4 h of solution heat treatment at 495 °C, virtually all the $CuAl_2$ phase was dissolved in the matrix.

- Prolonged solution treatments tend to put the rest of the copper into the surrounding aluminum matrix.

- Sr modification slows down the rate of $CuAl_2$ and $Al_5Mg_8Cu_2Si_6$ dissolution due to its effects on the segregation and morphology of Cu phases during solidification.

- The age hardening peaks are related to their precipitation sequence. The first hardness peak of the age-hardening curve is attained depending on the high GP zones, while the second one is acquired in terms of metastable particles [2]. The transition from GP zones to metastable phases due to dissolution of GP zones and the nucleation of metastable phases on dislocations is the reason for the formation of double aging peaks.

- In the Al-Si-Cu alloys only binary θ' phases contribute to the hardening and no ternary Si nor Mg containing phases were found.

- Additions of 0.40 wt % Mg caused the precipitation of S phase ($CuAl_2Mg$) in addition of θ' plates. The presence of both kinds of precipitates was confirmed using electron diffraction phase analysis.

- The precipitation of θ'', θ' due to the presence of Cu and S' and β'' (Mg_2Si) due to the addition of Mg and presence of Si has been reported.

- Plate shaped $CuAl_2$ forms stable θ and metastable θ' precipitates.

- Mg refines θ' particles and increases their precipitation density, thus improving hardening.

- The needle-shaped Mg_2Si is rare and forms only as a minor precipitate in T6 condition.

- The Si phase is present in the form of plates, needles, laths and particles. Si plates and Si particles are the most numerous and are heavily twinned.

- The best combination of mechanical properties corresponds to the presence of all hardening phases: θ', S' and β'.

STATEMENT OF ORIGINALITY

The following aspects of the present work are considered to be original contributions to knowledge:

- The effect of Sr modifications and Mg additions on the heat treatment of A319 aluminum alloy has been further understood. The use of macrohardness, matrix microhardness measurements, tensile testing and electron microscopy helped to identify the different precipitates and phases present in the Al-Si-Cu and Al-Si-Cu-Mg alloys.

- The alloy does not exhibit the common peak-overaging conditions normally found in the literature. This is due to the presence of sequential precipitation of different species during the aging process.

- For the first time it has been shown that, in the age-hardening curves of Al-Si-Cu-Mg alloys, multiple aging peaks are present. Hardness plateaus and weaker peaks are present in the age-hardening curves of modified and unmodified Al-Si-Cu alloys.

- The influence of artificial aging time on the properties of heat-treated A319 aluminum alloy was studied and relationships with artificial aging temperature have been established. It is seen that hardness is less sensitive to overaging at lower aging temperatures. In the unmodified and modified alloys, hardness decreases with increasing aging time and temperature.

- For the first time in aluminum casting alloys, a technique was developed to examine fine precipitates using FE-SEM techniques, by using thin specimens that would normally be used in TEM, such as thin foils.

- The nature of the precipitates in the Al-Si-Cu-Mg alloys was characterized using FE-SEM techniques, which was ascertained in this work to be as effective as TEM methods in resolving the dimensional and composition features of the particles with the added benefits of simplicity and statistical confidence.

- A transmission electron microscopy study involving all the stages of the heat treatment of the A319 aluminum alloy has been done. An influence of the artificial aging time on the precipitate distribution was found. The precipitation of θ", θ' due to the presence of Cu and S' and β" (Mg_2Si) due to the addition of Mg and presence of Si has been reported. Based on the precipitate morphology, it was found that the best combination of mechanical properties corresponds to the presence of all hardening phases: θ', S' and β'.

REFERENCES

[1] J.F. Hernandez Paz, "Heat Treatment and Precipitation in A356 Aluminum Alloys", Ph.D. Thesis, McGill University, 2003.

[2] R.X. Li, R.D. Li, Y.H. Zhao, L.Z. He, C.X. Li, H.R. Guan and Z.Q. Hu, "Age-Hardening Behavior of Cast Al-Si Base Alloy", Materials Letters, 58, 2004, 2096-2101.

[3] R.K. Mishra, G.W. Smith, W.J. Baxter, A.K. Sachdev and V. Franetovic, "The Sequence of Precipitation in 339 Aluminum Castings", Journal of Materials Science, 36, 2001, 461-468.

[4] G.W. Smith, W.J. Baxter and R.K. Mishra, "Precipitation in 339 and 2124 Aluminum: A Caveat for Calorimetry", Journal of Materials Science, 35, 2000, 3871-3880.

[5] R.K. Mishra, A.K. Sachdev and W.J. Baxter, "Strengthening Precipitates in Cast 339 Aluminum Alloy", AFS Transactions, 2004.

[6] W. Reif, J. Dutkiewicz, R. Ciach, S. Yu and J. Krol, "Effect of Ageing on the Evolution of Precipitates in Al-Si-Cu-Mg Alloys", Materials Science and Engineering, Vol. A234-236, 1997, 165-168.

[7] H.K. Kang, M. Kida and H. Miyahara, AFS Transactions, 27, 1999, 507.

[8] S. Zafar, N. Ikram, M.A. Shaikh and K.A. Shoaib, Journal of Materials Science, Vol. 25, 1990, 259.

[9] C. Kammer, Ed., Aluminum Handbook – Vol. 1 Fundamentals and Materials, 1st Edition, Aluminium-Verlag Marketing & Kommunikation GmbH, Littmanndruck, Oldenburg, Germany, 1999, 117, 181, 236, 257-259.

[10] J. Hatch, Ed., Aluminum – Properties and Physical Metallurgy, 8th Edition, The American Society for Metals, Metals Park, OH, USA, 1998, 320-321, 345, 351-352.

[11] L. Backerud, G. Chai and J. Tamminen, Solidification Characteristics of Aluminum Alloys – Vol. 2 Foundry Alloys, The American Foundrymen's Society and Skanaluminium, 1990.

[12] L. Heusler, W. Schneider, "Recent Investigations of Influence of P on Na and Sr Modification of Al-Si Alloys", AFS Transactions, Vol. 97, 1997, 915-921.

[13] P.D. Hess and E.V. Blackmun, "Strontium as Modifying Agent for Hypoeutectic Aluminum-Silicon Alloys", AFS Transactions, 1975, 87-90.

[14] B. Closset and J.E. Gruzleski, "Mechanical Properties of A356.0 Alloys Modified with Pure Strontium", AFS Transactions, 1982, 453-464.

[15] W. Khalifa, F.H. Samuel and J.E. Gruzleski, "Iron Intermetallic Phases in the Al Corner of the Al-Si-Fe System", Metallurgical and Materials Transactions, 34A, 3, 2003, 807-825.

[16] C. Villeneuve, A.M. Samuel, F.H. Samuel, H.W. Doty and S. Valtierra, "Role of Trace Elements in Enhancing the Performance of 319 Aluminum Foundry Alloys", AFS Transactions, 109, 2001, 1-14.

[17] C. Kammer, Ed., Aluminum Handbook – Vol. 2 Forming, Casting, Surface Treatment, Recycling and Ecology, 1st Edition, Aluminium-Verlag Marketing & Kommunikation GmbH, Littmanndruck, Oldenburg, Germany, 2003, 263, 388, 390, 403.

[18] D. Gloria-Ibarra, "Control of Grain Refinement of Al-Si Alloys By Thermal Analysis", Ph.D. Thesis, McGill University, 1989.

[19] D.L. Zalensas, Ed., Aluminum Casting Technology, 2nd Edition, The American Foundrymen's Society, Des Plaines, IL, USA, 1993, 31, 50, 66-67, 289-294.

[20] Metalcaster's Reference and Guide, 2nd Edition, The American Foundrymen's Society, Des Plaines, IL, USA, 189.

[21] J.E. Gruzleski, Microstructural Development During Metalcasting, 1st Edition, The American Foundrymen's Society, Des Plaines, IL, USA, 2000, 109-115, 230-232.

[22] G.E. Totten, D.S. MacKenzie, Handbook of Aluminum – Vol. 1 Physical Metallurgy and Processes, Marcel Dekker Inc., New York, NY, USA, 2003, 601, 606, 622-626.

[23] R. Elliot, Eutectic Solidification Processing: Crystalline and Glassy Alloys, Butterworths and Co, 1993.

[24] P.B. Crosley and L.F. Mandolfo, "The Modification of Aluminum-Silicon Alloys", Modern Casting, Vol. 49, 1966, 53-64.

[25] M. Shamsuzzoha, L.M.Hogan and J.T. Berry, AFS Transactions, 1993, 101, 999.

[26] S. Lu and A. Hallowell, Solidification Processing, Institute of Metals, London, England, 1987, 131.

[27] J.E. Gruzleski and B.M. Closset, The Treatment of Liquid Aluminum-Silicon Alloys, The American Foundrymen's Society, Des Plaines, IL, USA, 1990.

[28] B. Closset and J.E. Gruzleski, "A Study on the Use of Pure Metallic Strontium in the Modification of Al-Si Alloys", AFS Transactions, Vol. 89, 1981, 801-808.

[29] C. Depuis and R. Dumont, "The Impact of LiMCa Technology on the Optimization of Metal Cleanliness", Light Metals, Met. Soc. AIME, 1993, 997-1002.

[30] G.K. Sigworth, Int. Molten Aluminum Conference Proceedings, AFS, 1986, 75.

[31] D.V. Neff and E.P. Stankiewictz, "The Multicast Filtration System", Light Metals, Metallurgical Society AIME, 1986, 821-836.

[32] J. Campbell, Castings, Butterworth Heinemann, Oxford, England, 1991, 174-175.

[33] J. Campbell, The Solidification of Metals, The Iron and Steel Institute, London, England, 1967, 18.

[34] K. Kubo and R.D. Pehlke, Metallurgical Transactions B, 1985, 16B, 359.

[35] S. Srivkumar and D. Apelian, "Materials Processing in the Computer Age", TMS, 1991, 389.

[36] X.G. Chen and S. Engler, 98th Casting Congress, AFS, 1994.

[37] N. Andrade-Gonzalez, "Variation of the Mechanical Properties in an Al-Si-Mg Alloy as a Function of the Secondary Dendrite Spacing and the Heat Treatment Parameters", MSc. Thesis, Instituto Tecnologico de Saltillo, 2001, 63-65.

[38] R.E. Spear and G.R. Gardner, AFS Transactions, 1963, 71, 209.

[39] D.M. Stefanescu, G.J. Abbaschian and R.J. Bayuzick, Eds., Structures in Directionally Solidified Aluminum Foundry Alloy A356, TMS, 1998.

[40] J.C. Jaquet and W. Hotz, Cast Metals, 1992, 4, 200.

[41] Q.S. Hamed and R. Elliot, Cast Metals, 1993, 6, 36.

[42] C.H. Caceres, C.J. Davidson and J.R. Grififiths, ''The Deformation and Fracture Behavior of an Al-Si-Mg Casting Alloy'', Materials Science & Engineering, 1995, A197, 171-179.

[43] S. Cano, MEng. Thesis, Universidad Autonoma de Nuevo Leon, 1996.

[44] G. Bracale, AFS Transactions, 1962, 70, 228.

[45] J.T. Berry, AFS Transactions, 1970, 78, 421.

[46] O. Vorre, J.E. Evensen and T.B. Petersen, AFS Transactions, 1985, 92, 459.

[47] E.W. Miguelucci, AFS Transactions, 1986, 93, 913.

[48] K. Radhakrishna and S. Seshan, AFS Transactions, 1992, 100, 667.

[49] C. Huitron, S. Valtierra, J.F. Mujica, E. Valdez and R. Colas, Heat Treating, ASM Internacional, 1997, 237.

[50] C. Vazquez-Lopez, A. Calderon, M.E. Rodríguez, E. Velasco, S. Cano, R. Colas and S. Valtierra, Journal of Materials Research, 2000, 15, 85.

[51] M.C. Flemings and S. Metz, AFS Transactions, 1970, 78, 453.

[52] J.G. Kaufman, E.L. Rooy, Aluminum Alloy Castings – Properties, Processes, and Applications, The American Foundry Society and The American Society for Metals, Materials Park, OH, USA, 2004, 62-64, 137-138.

[53] "Heat Treating of Non Ferrous Metals: Heat Treating of Aluminum Alloys", Metals Handbook, 9th Edition, Vol. 4, 675-718.

[54] ASTM Standard B917/B917M-2001, "Standard Practice for Heat Treatment of Aluminum Alloys Castings from All Processes", 7.

[55] J.L. Murray and A.J. McAlister, Bull Alloy Phase Diagrams, 1984, Vol. 5, 74-84.

[56] M.Y. Drits, E.S. Kaaner and V.I. Kuzmina, "Solubility of Silicon and Zirconium in Aluminum", Russ. Metall., Vol. 1, 1968, 102-105.

[57] M.H. Mulazimoglu, "Electrical Conductivity Studies of Cast Al-Si and Al-Si-Mg Alloys", Ph.D. Thesis, McGill University, 1988.

[58] H.J. Li, S. Shivkumar, X.J. Luo and D. Apelian, "Influence of Modification on the Solution Heat Treatment Response of Cast Al-Si-Mg Alloys", Cast Metals, Vol. 1, 1989, 227-234.

[59] F. Paray, J.E. Gruzleski, "Microstructure – Mechanical Property Relationships in a 356 Alloy. Part 1: Microstructure", Cast Metals, Vol. 7, No. 1, 1994, 29-40.

[60] C.W. Meyers, "Solution Heat Treatment in A357 Alloys", AFS Transactions, Vol. 93, 1985, 741-750.

[61] G.K. Sigworth, AFS Transactions, 1987, 95, 73.

[62] M. Tiryakioglu and J. Campbell, Eds., Advances in Aluminum Casting Technology, The American Society for Metals, Materials Park, OH, USA, 1998, 127.

[63] E.L. Rooy, "Aluminum and Aluminum Alloys", ASM Handbook, Vol. 15, The American Society for Metals, Materials Park, OH, USA, 1998, 743-770.

[64] J. Gauthier, P.R. Louchez and F.H. Samuel, Cast Metals, 1996, 8, 91.

[65] P.Y. Zhu, Q.Y. Liu and T.X. Hou, AFS Transactions, 1985, 95, 609.

[66] J.W. Martin, Precipitation Hardening, Butterworth Heinemann, 2nd Edition, Oxford, England, 1998.

[67] J.T. Stanley, "Quench Factor Analysis of Aluminum Alloys", Materials Science and Technology, Vol. 3, 1987, 923-935.

[68] P. Brenner, "Properties and Uses of a Hardenable and Weldable Al-Zn-Mg Alloy", Aluminum, 37, 1961, 633-644.

[69] P. Ouellet and F.H. Samuel, "Effect of Mg on the Ageing Behavior of Al-Si-Cu 319 Type Aluminum Casting Alloys", Journal of Materials Science, 34, 1999, 4671-1697.

[70] L.J.D. Sully, "Castings", ASM Handbook, Vol. 15, The American Society for Metals, Materials Park, OH, USA, 1998, 286.

[71] I.J. Polmear, Light Alloys, Metallurgy of the Light Metals, 3rd Edition, NY, USA, 1998, 144-168.

[72] E. Velasco, R. Colas, S. Valtierra and J.F. Mojica, ''A Model for Termal Fatigue in an Aluminum Casting Alloy'', International Journal of Fatigue, 1995, 17, 6, 399-406.

[73] J.I. Goldstein, D.E. Newbury, P. Echlin, D.C. Joy, A.D. Romig, C.E. Lyman, C. Fiori and E. Lifshin, Scanning Electron Microscopy and X-Ray Microanalysis, 2nd Edition, New York, NY, USA, Plenum Press, 1992.

[74] Z.R. Li, Ed., Industrial Applications of Electron Microscopy, Marcel Dekker Inc., New York, NY, USA, 2003, 1-29.

[75] C.R. Brundle, C.A. Evans Jr. and S. Wilson, Eds., Encyclopedia of Materials Characterization – Surfaces, Interfaces, Thin Films, Butterworth-Heinemann, Stoneham, MA, USA, 1992, 57-59, 70-83, 99-115, 175-191

[76] D. Brandon and W.D. Kaplan, Microstructural Characterization of Materials, John Wiley & Sons, New York, NY, USA, 1999, 59-106, 177-250.

[77] P.B. Hirsch, A. Howie, R.B. Nicholson, D.W. Pashley and M.J. Whelan, Electron Microscopy of Thin Crystals, Butterworth-Heinemann, London, England, 1965.

[78] D.B. Williams and C.B. Carter, Transmission Electron Microscopy, New York, NY, USA, Plenum Press, 1996.

[79] W.F. Miao and D.E. Laughlin, "A Differential Scanning Calorimetry Study of Aluminum Alloy 6111 with Different Pre-Aging Treatments", Journal of Materials Science Letters, Vol. 19, 2000, 201-203.

[80] S.J. Anderson, "Quantification of the Mg_2Si β" and β' Phase in Al-Mg-Si Alloys by Transmission Electron Microscopy", Metallurgical and Materials Transactions, Vol. 26A, 1995, 1931-1937.

[81] K. Matsuda, S. Ikeno, T. Sato and A. Kamio, "Classification of Metastable Phases in Al-Mg_2Si Alloys by HRTEM", Materials Science Forum, Vol. 217-222, 1996, 707-712.

[82] M.H. Mulazimoglu, A. Zaluska, F. Paray and J.E. Gruzleski, "The Effect of Strontium on the Mg_2Si Precipitation Process in 6201 Aluminum Alloy", Metallurgical and Materials Transactions, Vol. 28A, 1996, 1289-1295.

[83] R. Mathiesem, "Precipitation Hardening and Microstructure Characterization of Aluminum Alloys", Heat Treatment Fundaments Project, 2004, SINTEF.

[84] J.L. Cavazos and R. Colas, "Precipitation in a Heat-Treatable Aluminum Alloy Cooled at Different Rates", Materials Characterization, Vol. 47, 2001, 175-179.

[85] D.G. Eskin, Z. Metallkd, 8, 1992, 10.

[86] D.G. Eskin, Z. Metallkd, 86, 1995, 1.

[87] M. Kaczorowski and J. Bindas, Aluminium, 59, 1893, 17.

[88] D.G. Altenpohl, Aluminum – Technology, Applications and Environment, 6th Edition, Warrendale, PA, USA, The Minerals, Metals & Materials Society, 1998, 356-360.

[89] Buehler Microhardness Manual and Conversion Tables, Buehler Ltd., Lake Bluff, ILL, USA.

[90] A. Elwazri, "Processing and Properties of High Carbon Microalloyed Steels", Ph.D. Thesis, McGill University, 2004, 52-54.

[91] Z. Li, A.M. Samuel, F.H. Samuel, C. Ravindran, S. Valtierra and H.W. Doty, "Parameters Controlling the Performance of AA319-Type Alloys: Part I Tensile Properties", Materials Science and Engineering A, 367, 2004, 96-110.

[92] Z. Li, A.M. Samuel, F.H. Samuel, C. Ravindran, S. Valtierra and H.W. Doty, "Factors Affecting Dissolution of $CuAl_2$ Phase in 319 Alloys", AFS Transactions, 2003, Vol. 1111, 1-14.

[93] Z. Li. A.M. Samuel, F.H. Samuel, C. Ravindran, S. Valtierra and H.W. Doty, "Effect of Alloying Elements on the Segregation and Dissolution of $CuAl_2$ Phase in Al-Si-Cu 319 Alloys", Journal of Materials Science, 38, 2003, 1203-1218.

[94] S.P. Ringer and K. Hono, "Microstructural Evolution and Age Hardening in Aluminum Alloys: Atom Probe Field-Ion Microscopy and Transmission Electron Microscopy Studies", Materials Characterization, 44, 2000, 101-131.

[95] F. Paray, "Heat Treatment and Mechanical Properties of Aluminum Silicon Modified Alloys", Ph.D. Thesis, McGill University, 1992.

[96] J. Charbonnier, J.J. Perrier and R. Portalier, "Recent Developments in Al-Si Alloys Having Guaranteed Structures or Properties", AFS International Journal, 3, 1983, 17-26.

[97] PY. Zhu and Q.Y. Liu, "Kinetics of Granulation of Discontinuous Phase in Eutectic Structures", Materials Science and Technology, Vol. 2, 1986, 500-507.

[98] F.H. Samuel, "Incipient Melting of $Al_5Mg_8Si_6Cu_2$ and Al_2Cu Intermetallics in Unmodified and Strontium-Modified Al-Si-Cu-Mg (319) Alloys During Solution Heat Treatment", Journal of Materials Science, 33, 1998, 2283-2297.

[99] L.A. Narayan, F.H. Samuel and J.E. Gruzleski, Metallurgical and Materials Transactions A., 1995, 26A, 2161.

[100] S. Murali, K.S. Raman and K.S.S. Murthy, ''The Formation of β-FeSiAl_5 and Be-Fe Phases in Al-7Si-0.3Mg Alloy Containing Be'', Materials Science and Engineering A, 1995, 190A, 165-172.

[101] A.M. Samuel, P. Ouellet, F.H. Samuel and H.W. Doty, AFS Transactions, 1997, 105, 951.

[102] M.L. Purtee, "Aging Effects of an Aluminum Based 319 Alloy", Foundry Management and Technology, 126, 10, 1998, 40-44.

[103] M. Takeda, F. Ohkubo, T. Shirai and K. Fukui, "Precipitation Behavior of Al-Mg-Si Ternary Alloys", Materials Science Forum, 217-222, 1996, 815-820.

[104] J.H. Sokolowski, X.C. Sun, G. Byczynski, D.O. Northwood, D.E. Penrod, R. Thomas and A. Esseltine, "The Removal of Copper-Phase Segregation and the Subsequent Improvement in Mechanical Properties of Cast 319 Aluminum Alloys by a Two-Stage Solution Heat Treatment", Journal of Materials Processing Technology, 53, 1995, 385-392.

[105] H. Ye, "An Overview of the Development of Al-Si Alloy Based Material for Engine Applications", Journal of Materials Engineering and Performance, 12, 3, 2003, 288-297.

[106] A.M. Elwazri, R. Varano, F. Siliciano, D. Bai and S. Yue, "Characterization of Precipitation of Niobium Carbide Using Carbon Extraction Replicas and Thin Foils by FESEM", Materials Science and Technology, 22, 5, 537-541.

APPENDIX A

MECHANICAL PROPERTIES

ALLOY A

Artificially Aged at 180 °C

Aging Time (h)	UTS (MPa)	YS (MPa)	VH (5 Kgf)
As-Cast	279.3 ± 9.2	177.3 ± 2.2	68.7 ± 2.7
0*	310.3 ± 6.9	178.6 ± 8.4	85.7 ± 0.5
0.5	319.7 ± 2.6	186.4 ± 5.4	89.0 ± 0.8
1	282.9 ± 2.1	180.9 ± 8.2	88.5 ± 0.8
2	285.5 ± 14.1	164.0 ± 11.0	82.6 ± 0.9
3	282.9 ± 2.3	159.8 ± 15.7	79.5 ± 0.7
4	295.5 ± 12.3	172.1 ± 14.2	88.8 ± 1.9
5	274.1 ± 12.8	153.0 ± 7.2	89.2 ± 1.1
6	264.1 ± 14.5	151.5 ± 4.9	90.2 ± 1.1
8	258.4 ± 6.7	154.3 ± 8.9	89.7 ± 1.0
10	321.3 ± 7.5	204.3 ± 9.0	87.2 ± 0.7
12	306.7 ± 3.8	204.4 ± 6.2	90.9 ± 1.5
14	298.0 ± 4.0	194.5 ± 8.5	91.0 ± 0.8
19	316.9 ± 10.7	217.0 ± 0.7	88.9 ± 1.3
24	316.8 ± 0.2	207.6 ± 2.8	89.6 ± 1.1

* Solution Heat Treated for 4 h at 495 °C

ALLOY B

Artificially Aged at 180 °C

Aging Time (h)	UTS (MPa)			YS (MPa)			VH (5 Kgf)		
As-Cast	251.5	±	1.4	161.2	±	0.7	65.6	±	4.9
0*	291.1	±	3.9	163.2	±	2.0	84.6	±	0.4
0.5	305.4	±	15.4	194.6	±	8.8	87.5	±	3.7
1	313.5	±	8.2	191.2	±	15.0	88.5	±	1.6
2	290.7	±	0.8	181.1	±	6.7	80.1	±	0.7
3	286.2	±	4.7	180.6	±	5.0	88.5	±	3.8
4	293.8	±	10.4	184.9	±	6.1	83.0	±	5.2
5	285.8	±	7.2	168.6	±	8.7	83.8	±	0.9
6	272.4	±	9.6	169.5	±	4.9	79.3	±	0.9
8	278.1	±	8.5	176.3	±	3.1	83.3	±	0.7
10	299.1	±	0.5	208.0	±	10.5	91.4	±	2.9
12	289.0	±	6.9	191.1	±	0.3	85.8	±	2.1
14	284.9	±	0.4	185.1	±	4.1	89.0	±	1.2
19	279.3	±	4.7	192.3	±	4.9	89.2	±	1.6
24	305.7	±	5.9	228.6	±	4.7	82.7	±	3.5

* Solution Heat Treated for 4 h at 495 °C

ALLOY C

Artificially Aged at 180 °C

Aging Time (h)	UTS (MPa)	YS (MPa)	VH (5 Kgf)
As-Cast	313.2 ± 8.8	228.3 ± 6.7	87.5 ± 1.0
0*	339.1 ± 0.8	237.2 ± 5.4	100.7 ± 2.4
0.5	331.1 ± 14.7	266.3 ± 11.1	98.2 ± 0.7
1	347.6 ± 10.4	293.3 ± 3.0	98.0 ± 0.7
2	298.9 ± 7.7	248.1 ± 14.2	86.1 ± 0.4
3	341.4 ± 1.5	324.6 ± 1.2	93.9 ± 0.1
4	369.8 ± 6.3	336.6 ± 9.7	113.5 ± 1.6
5	293.8 ± 5.2	260.8 ± 4.9	101.4 ± 1.2
6	284.9 ± 3.9	242.2 ± 10.6	95.4 ± 0.4
8	326.2 ± 12.4	317.5 ± 9.3	105.6 ± 0.6
10	352.8 ± 15.3	347.3 ± 12.9	88.2 ± 0.1
12	384.1 ± 4.2	374.2 ± 3.5	93.6 ± 1.2
14	348.3 ± 6.1	328.6 ± 7.3	83.9 ± 0.6
19	350.7 ± 9.1	344.1 ± 3.7	83.0 ± 0.7
24	364.2 ± 7.0	375.4 ± 3.6	111.3 ± 2.8

* Solution Heat Treated for 4 h at 495 °C

ALLOY D

Artificially Aged at 180 °C

Aging Time (h)	UTS (MPa)	YS (MPa)	VH (5 Kgf)
As-Cast	269.5 ± 1.0	213.1 ± 1.0	82.6 ± 2.5
0*	312.8 ± 8.9	227.3 ± 3.3	96.3 ± 1.8
0.5	300.4 ± 14.9	209.2 ± 10.8	80.6 ± 0.2
1	330.7 ± 11.5	244.9 ± 10.4	94.0 ± 0.4
2	308.8 ± 5.0	209.6 ± 3.8	90.2 ± 0.0
3	329.7 ± 15.6	316.6 ± 1.3	97.9 ± 0.5
4	354.5 ± 14.0	320.1 ± 8.8	96.5 ± 0.2
5	280.3 ± 12.9	207.5 ± 0.2	72.7 ± 0.9
6	341.9 ± 1.2	334.3 ± 1.7	105.7 ± 0.6
8	353.3 ± 1.5	348.1 ± 6.2	106.8 ± 0.4
10	360.5 ± 0.5	365.9 ± 12.4	93.6 ± 2.3
12	348.7 ± 7.4	332.9 ± 5.7	96.3 ± 4.0
14	357.9 ± 8.3	349.3 ± 11.4	97.5 ± 0.5
19	364.3 ± 9.8	353.0 ± 12.0	107.0 ± 2.0
24	366.0 ± 6.1	343.3 ± 8.6	98.1 ± 0.3

* Solution Heat Treated for 4 h at 495 °C

ALLOY A

Artificially Aged at 220 °C

Aging Time (h)	UTS (MPa)	YS (MPa)	VH (5 Kgf)
As-Cast	279.3 ± 9.2	177.3 ± 2.2	68.8 ± 2.7
0*	310.3 ± 7.0	178.6 ± 8.4	85.7 ± 0.5
0.5	311.5 ± 4.3	173.4 ± 1.3	92.5 ± 1.4
1	299.2 ± 6.9	174.8 ± 5.1	88.3 ± 0.7
2	299.7 ± 13.4	157.8 ± 0.6	88.0 ± 0.7
3	282.7 ± 0.3	174.5 ± 4.3	80.8 ± 1.2
4	293.6 ± 9.9	172.5 ± 3.3	85.6 ± 0.9
5	260.3 ± 6.6	166.9 ± 8.5	79.5 ± 1.0
6	285.9 ± 6.9	177.5 ± 6.3	79.0 ± 0.9
8	273.8 ± 1.3	164.3 ± 0.5	78.6 ± 2.0
10	351.0 ± 5.4	233.6 ± 4.6	76.7 ± 1.1
12	316.4 ± 0.0	234.1 ± 15.3	75.7 ± 1.0
14	288.2 ± 1.5	222.5 ± 13.0	75.6 ± 1.7
19	336.8 ± 2.1	234.1 ± 5.2	71.6 ± 0.8
24	312.2 ± 14.8	229.6 ± 10.8	69.4 ± 1.1

* Solution Heat Treated for 4 h at 495 °C

ALLOY B

Artificially Aged at 220 °C

Aging Time (h)*	UTS (MPa)	YS (MPa)	VH (5 Kgf)
As-Cast	251.5 ± 1.4	161.2 ± 0.7	65.6 ± 4.9
0	291.1 ± 3.9	163.2 ± 2.0	84.6 ± 0.4
0.5	300.8 ± 8.9	201.7 ± 3.5	82.9 ± 0.3
1	265.8 ± 8.2	199.3 ± 3.8	79.9 ± 1.0
2	286.4 ± 6.3	174.6 ± 6.5	81.9 ± 0.3
3	275.3 ± 6.6	187.1 ± 6.7	72.2 ± 0.6
4	289.0 ± 0.9	195.5 ± 4.4	86.7 ± 0.3
5	269.6 ± 7.6	178.2 ± 7.4	79.3 ± 0.9
6	280.0 ± 5.5	189.1 ± 5.5	84.3 ± 0.3
8	263.7 ± 10.3	176.7 ± 3.7	72.4 ± 0.3
10	318.1 ± 1.4	225.7 ± 2.4	70.1 ± 0.4
12	304.5 ± 9.5	215.5 ± 12.1	68.7 ± 1.2
14	285.9 ± 2.4	211.7 ± 10.6	63.4 ± 0.5
19	294.8 ± 4.8	213.8 ± 10.9	63.9 ± 1.5
24	303.0 ± 6.7	212.8 ± 6.0	63.5 ± 1.4

* Solution Heat Treated for 4 h at 495 °C

ALLOY C

Artificially Aged at 220 °C

Aging Time (h)	UTS (MPa)	YS (MPa)	VH (5 Kgf)
As-Cast	313.2 ± 8.8	228.3 ± 6.7	87.5 ± 1.0
0*	339.1 ± 0.8	237.2 ± 5.4	100.7 ± 2.4
0.5	369.8 ± 5.7	341.5 ± 2.7	96.2 ± 0.3
1	332.8 ± 9.7	337.4 ± 0.8	89.4 ± 1.4
2	351.8 ± 8.6	301.9 ± 5.8	126.7 ± 0.9
3	337.0 ±	336.0 ± 1.1	127.6 ± 1.1
4	323.6 ± 1.7	316.9 ± 2.0	110.2 ± 2.0
5	304.1 ± 9.5	298.8 ± 8.6	104.5 ± 0.6
6	329.7 ± 4.0	324.7 ± 6.6	120.3 ± 1.4
8	328.9 ±	300.7 ± 13.8	108.6 ± 2.1
10	349.7 ± 14.8	327.4 ± 1.4	88.9 ± 1.7
12	321.2 ± 4.3	313.3 ± 0.3	93.6 ± 0.9
14	309.9 ± 6.8	280.6 ± 7.3	83.9 ± 1.9
19	340.4 ± 2.6	289.5 ± 9.2	83.0 ± 1.7
24	310.1 ± 0.1	288.0 ± 8.0	111.3 ± 1.6

* Solution Heat Treated for 4 h at 495 °C

ALLOY D

Artificially Aged at 220 °C

Aging Time (h)	UTS (MPa)	YS (MPa)	VH (5 Kgf)
As-Cast	269.5 ± 1.0	213.1 ± 1.0	82.6 ± 2.5
0*	312.8 ± 8.9	227.3 ± 3.3	96.3 ± 1.8
0.5	348.9 ± 0.6	326.2 ± 1.3	84.7 ± 0.5
1	347.4 ± 2.1	327.8 ± 1.0	83.2 ± 0.0
2	302.8 ± 2.3	275.0 ± 7.6	88.9 ± 0.2
3	338.1 ± 9.7	308.9 ± 12.0	121.3 ± 0.5
4	308.6 ± 2.0	317.1 ± 9.2	112.2 ± 0.6
5	270.1 ± 5.0	252.4 ± 14.7	95.8 ± 3.3
6	298.6 ± 14.5	274.6 ± 3.5	107.8 ± 0.9
8	298.6 ± 13.9	234.2 ± 12.4	107.1 ± 1.7
10	287.2 ± 4.8	273.7 ± 15.5	91.3 ± 1.5
12	298.8 ± 10.4	269.3 ±	107.9 ± 1.9
14	300.8 ± 1.2	277.5 ± 2.1	71.3 ± 0.5
19	319.9 ± 2.6	287.0 ± 2.2	100.2 ± 1.1
24	301.3 ± 9.3	279.5 ± 1.5	66.0 ± 1.9

* Solution Heat Treated for 4 h at 495 °C

APPENDIX B

MACROHARDNESS VICKERS

(5 Kgf)

AFTER T6 (W)

Solution Heat Treated for 4 h at 495 °C & Artificially Aged at 180 °C

Aging Time (h)	Alloy A	Alloy S	Alloy M	Alloy MS
As-Cast	68.8 ± 2.7	65.6 ± 4.9	87.5 ± 1.0	82.6 ± 2.5
0	85.7 ± 0.5	84.6 ± 0.4	100.7 ± 2.4	96.3 ± 1.8
0.5	89.0 ± 0.8	87.5 ± 3.7	98.2 ± 0.7	80.6 ± 0.2
1	88.5 ± 0.8	88.5 ± 1.6	98.0 ± 0.7	94.0 ± 0.4
2	82.6 ± 0.9	80.1 ± 0.7	86.1 ± 0.4	90.2 ± 0.0
3	79.5 ± 0.7	88.5 ± 3.9	93.9 ± 0.1	97.9 ± 0.5
4	88.8 ± 2.0	83.0 ± 5.2	113.5 ± 1.6	96.5 ± 0.2
5	89.2 ± 1.1	83.8 ± 0.9	101.4 ± 1.2	72.7 ± 0.9
6	90.2 ± 1.1	79.3 ± 0.9	95.4 ± 0.4	105.7 ± 0.6
8	89.7 ± 1.0	83.3 ± 0.7	105.6 ± 0.6	106.8 ± 0.4
10	87.2 ± 0.7	91.4 ± 2.9	88.2 ± 0.1	93.6 ± 2.3
12	91.0 ± 1.5	85.8 ± 2.1	93.6 ± 1.2	96.3 ± 4.0
14	91.0 ± 0.8	89.0 ± 1.2	83.9 ± 0.6	97.5 ± 0.5
19	88.9 ± 1.3	89.2 ± 1.6	83.0 ± 0.7	107.0 ± 2.0
24	89.6 ± 1.1	82.7 ± 3.5	111.3 ± 2.8	98.1 ± 0.3

AFTER T6 (X)

Solution Heat Treated for 4 h at 495 °C & Artificially Aged at 220 °C

Aging Time (h)	Alloy A	Alloy S	Alloy M	Alloy MS
As-Cast	68.8 ± 2.7	65.6 ± 4.9	87.5 ± 1.0	82.6 ± 2.5
0	85.7 ± 0.5	84.6 ± 0.4	100.7 ± 2.4	96.3 ± 1.8
0.5	92.5 ± 1.4	82.9 ± 0.3	96.2 ± 0.3	84.7 ± 0.5
1	88.3 ± 0.7	79.9 ± 1.0	89.4 ± 1.4	83.2 ± 0.0
2	88.0 ± 0.7	81.9 ± 0.3	126.7 ± 0.9	88.9 ± 0.2
3	80.8 ± 1.2	72.2 ± 0.6	127.6 ± 1.1	121.3 ± 0.5
4	85.6 ± 0.9	86.7 ± 0.3	110.2 ± 2.0	112.2 ± 0.6
5	79.5 ± 1.0	79.3 ± 0.9	104.5 ± 0.6	95.8 ± 3.3
6	79.0 ± 0.9	84.3 ± 0.3	120.3 ± 1.4	107.8 ± 0.9
8	78.6 ± 2.0	72.4 ± 0.3	108.6 ± 2.1	107.1 ± 1.7
10	76.7 ± 1.1	70.1 ± 0.4	88.9 ± 1.7	91.3 ± 1.5
12	75.7 ± 1.0	68.7 ± 1.2	93.6 ± 0.9	107.9 ± 1.9
14	75.6 ± 1.7	63.4 ± 0.5	83.9 ± 1.9	71.3 ± 0.5
19	71.6 ± 0.8	63.9 ± 1.5	83.0 ± 1.7	100.2 ± 1.1
24	69.4 ± 1.1	63.5 ± 1.4	111.3 ± 1.6	66.0 ± 1.9

AFTER T6 (Y)

Solution Heat Treated for 24 h at 495 °C & Artificially Aged at 180 °C

Aging Time (h)	Alloy A	Alloy S	Alloy M	Alloy MS
As-Cast	68.8 ± 2.7	65.6 ± 4.9	87.5 ± 1.0	82.6 ± 2.5
0	80.1 ± 2.3	75.0 ± 0.1	102.0 ± 2.9	99.9 ± 4.7
0.5	87.6 ± 0.2	87.7 ± 0.4	99.0 ± 1.1	95.2 ± 0.5
1	89.9 ± 0.0	90.7 ± 0.5	99.8 ± 0.6	87.6 ± 0.1
2	86.8 ± 0.2	84.4 ± 0.4	122.9 ± 0.3	92.7 ± 0.2
3	84.4 ± 0.2	96.2 ± 0.2	117.5 ± 0.6	120.2 ± 1.1
4	84.1 ± 0.3	83.5 ± 0.2	104.6 ± 0.3	92.9 ± 0.1
5	84.3 ± 0.3	83.8 ± 0.3	108.3 ± 2.6	107.1 ± 0.4
6	86.3 ± 0.1	83.6 ± 0.2	106.4 ± 0.7	91.2 ± 0.5
8	82.6 ± 0.0	83.6 ± 0.1	118.0 ± 1.2	97.2 ± 0.6
10	85.7 ± 0.2	83.5 ± 0.5	123.3 ± 0.2	98.2 ± 0.5
12	85.1 ± 0.0	80.3 ± 0.1	110.1 ± 1.3	95.2 ± 0.7
14	80.0 ± 0.3	80.0 ± 0.6	90.3 ± 1.5	89.6 ± 0.7
19	79.8 ± 0.3	75.6 ± 0.4	88.9 ± 0.8	84.4 ± 0.4
24	77.8 ± 0.6	74.3 ± 0.9	85.1 ± 0.8	83.4 ± 0.5

AFTER T6 (Z)

Solution Heat Treated for 24 h at 495 °C & Artificially Aged at 220 °C

Aging Time (h)	Alloy A			Alloy S			Alloy M			Alloy MS		
As-Cast	68.8	±	2.7	65.6	±	4.9	87.5	±	1.0	82.6	±	2.5
0	80.1	±	2.3	75.0	±	0.1	102.0	±	2.9	99.9	±	4.7
0.5	93.2	±	0.5	75.4	±	0.4	96.3	±	0.5	97.3	±	0.9
1	84.7	±	0.3	82.4	±	0.2	105.7	±	0.5	100.4	±	1.3
2	99.9	±	1.5	80.6	±	0.6	124.0	±	0.7	95.5	±	0.1
3	82.1	±	0.2	65.1	±	0.7	115.5	±	0.3	109.5	±	0.4
4	83.2	±	0.4	83.4	±	0.1	123.7	±	0.2	105.4	±	0.4
5	75.0	±	0.3	76.3	±	0.0	113.7	±	0.2	101.6	±	0.9
6	75.5	±	0.7	81.7	±	0.4	115.3	±	0.1	104.0	±	1.3
8	71.8	±	1.0	65.9	±	0.2	96.8	±	0.3	100.3	±	1.8
10	73.8	±	0.3	80.0	±	0.3	94.4	±	0.5	99.2	±	0.3
12	71.8	±	0.3	77.2	±	1.2	90.0	±	0.8	92.2	±	0.9
14	70.0	±	0.2	69.7	±	1.0	85.8	±	0.2	87.6	±	1.4
19	66.7	±	0.6	65.9	±	0.7	83.4	±	0.3	84.3	±	1.3
24	65.4	±	0.1	64.1	±	0.5	77.7	±	0.5	74.7	±	0.6

APPENDIX C

MICROHARDNESS VICKERS

(50 gf)

MICROHARDNESS

Solution Heat Treated at 495 °C

Aging Time (h)	Alloy A	Alloy S	Alloy M	Alloy MS
As-Cast	75.6 ± 4.3	74.3 ± 1.9	81.9 ± 4.5	81.7 ± 4.4
T4 (4 h)	87.5 ± 0.6	85.0 ± 1.5	95.8 ± 2.2	90.9 ± 1.3
T4 (24 h)	82.2 ± 3.0	75.1 ± 0.9	90.7 ± 2.5	85.7 ± 3.2